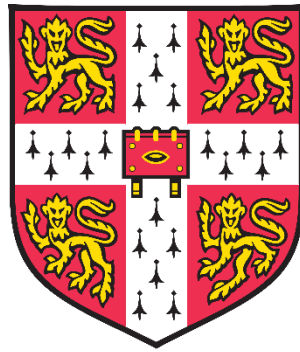


# **Novel diagnostic techniques for investigations into energy and matter transport in dynamic systems**



Nadeem El Gabbani  
Darwin College  
University of Cambridge

14<sup>th</sup> June 2021

This thesis is submitted for the degree of  
Doctor of Philosophy

## **Declaration**

This thesis is the result of my own work and includes nothing which is the outcome of work done in collaboration except as declared in the Preface and specified in the text. I further state that no substantial part of my thesis has already been submitted, or, is being concurrently submitted for any such degree, diploma or other qualification at the University of Cambridge or any other University or similar institution except as declared in the Preface and specified in the text. It does not exceed the prescribed word limit for the Engineering Degree Committee.

Signed: Nadeem El Gabbani

Date: 23<sup>th</sup> June 2021

# Novel diagnostic techniques for investigations into energy and matter transport in dynamic systems

Nadeem El Gabbani

## Abstract

Light-matter interactions are fundamental to many technologies used today. They are complex, non-linear processes sensitive to the properties of the source, material, mechanisms, and environment in which they interact. In order to control a process, its key features must be measurable and characterised. To date, most efforts in doing so follow either empirical or theoretical approaches, requiring existing or potential users of laser technology to invest significant time and money in their attempted use.

In this work a novel diagnostics platform is theorised for the study of light-matter interactions by assessing energy transfer within a process relative to certain performance attributes e.g. ablation efficiency (kg/W), coupling momentum efficiency (N.s/W) and kinetic energy ratio (plume energy over pulse energy) with the aim of producing widely relatable results which significantly lessen the need for heavily empirical or theoretical work. The missing element of the diagnostic platform, a torsion balance, capable of measuring impulsive forces and mass loss, was designed, constructed, and calibrated to the ultra-precision standards required to measure nano-scale forces including a force and mass-loss resolution of nN and  $\mu\text{g}$  respectively.

The tool was then used to characterise the behaviour of some 'generic' pulsed nano-second light matter interactions with varying source parameters such as total energy input (58.6 mJ to 468.8 mJ), repetition rate (5 kHz to 40 kHz), temporal pulse shape (up to 500 ns duration and 50 kW peak power), and materials (aluminium, silicon, and PVC), as well different environments (air and vacuum) and processing strategies (scanning and single point drilling). Three dimensional processing maps were then produced using the torsion balance, laser, environment, and material data to represent the quantitative and qualitative nature of results.

When convoluted or stitched together, the maps uniquely enable the optimisation of process specific performance with respect to laser, material, and environmental parameters, to which the torsion balance data was very sensitive (ablation efficiencies from  $10^{-7}$  to  $10^{-13}$  kg/W, coupling momentum efficiency from  $10^{-4}$  to  $10^{-9}$  N/W and kinetic energy ratios from  $10^{-5}$  to 437 %). Regions of high or low performance, could be easily identified using the qualitative

map elements, whilst being relatable to quantitative data such as total energy, repetition rate and pulse shape, which are in turn relatable to theory using conventional methods. A single data set, for example, ablation efficiency plotted against total number of pulses and repetition rate for a given pulse shape, material, and environment, could be captured and processed in 16 minutes.

In this work the ability to generically optimise a laser based process or technology very easily, quickly, and efficiently was demonstrated. For the first time, this has enabled high parameter resolution, light-matter-environmental parameter sweeps to be produced within hours, instead of months or years. This is important because it could revolutionize the way light-matter interactions are approached and completely change where time, energy and financial resources are spent in academia and industry. The end result could be the production of a well-defined process map for any given laser, material, and environment.

# Acknowledgements

I dedicate this thesis to you all.

First and foremost to my wife Pooja, whose support, love, and courage enabled this work and has made me a better person than I ever hoped to become. I am so happy that I got to go through this experience with you by my side.

To my family, who have seen me grow through the process of this thesis and have always been there cheering me on, and sometimes pretending to understand what I have been rambling on about.

To my supervisor and dear friend Krste. When you were first introduced to me as my supervisor, I had no idea what to expect. I could not imagine doing a PhD anywhere else, with anyone else. I got more than just a supervisor – I got a mentor, best friend and someone who truly believes in me. This thesis was enabled by you.

To my advisors, Bill, and Martin. I often find myself thinking back and reflecting on how lucky I have been as a member of your research group. You always encouraged me to follow my interests, always supported my efforts and always gave help when it was needed, even when you had a million other more urgent things to do. The group itself is unique, and I have never seen or heard of another place with such wonderful attitude, character, and genius.

To my cohort Lily, Katjana, and James - you are brilliant people! I enjoyed sharing this adventure and growing up with you during the last 5 years. We experienced a lot of the good and bad times together, not forgetting the occasional madness. I am lucky to have had you as my colleagues, and now friends for life. To the people outside my cohort, particularly Maxime and Peter, thank-you for making this an extremely exciting, rewarding, stimulating and adventurous experience. So much so that some of you have now become close friends and business partners. The Institute for Manufacturing is the setting in which all of this took place. None of the above would be possible without this unique institution.

To my friends outside of Cambridge, you have continued to keep me wildly entertained, energised, and encouraged to do the best I possibly can. Thank-you for being there for me again.

Thank-you to the Engineering and Physical Sciences Research Council (EPSRC) and Air Force Office of Scientific Research (AFOSR) for supporting this work.

# Table of Contents

1. Introduction.....	1
1.1. Background.....	1
1.2. Relevance.....	2
1.3. Research Question .....	4
1.4. Research Objectives.....	5
2. Review of Light-Matter Interactions.....	6
2.1. Light Delivery Parameters.....	7
2.1.1. Wavelength.....	7
2.1.2. Intensity and Fluence.....	7
2.1.3. Spatial Profile.....	7
2.1.4. Temporal Profile .....	8
2.1.5. Polarisation Profile.....	9
2.2. Optical Properties of Materials .....	9
2.2.1. Transmission, Reflectance, and Absorption .....	9
2.2.2. Optical Penetration .....	10
2.2.2.1. Effect of Temperature .....	12
2.2.2.2. Effect of Surface Films.....	12
2.2.2.3. Effect of Surface Roughness .....	12
2.3. Mechanisms, Timescales, and Material Responses.....	12
2.3.1. Energy Coupling and Thermodynamic Response .....	13
2.3.2. Dynamic Material Response .....	15
2.3.2.1. Melting.....	15
2.3.2.2. Vaporisation, Boiling and Phase explosions.....	16
2.3.2.3. Laser Induced Plasmas and Compressibility.....	16
2.4. Discussion .....	17
3. Review of Diagnostics for Light-Matter Interactions.....	18
3.1. Magnetic Diagnostics.....	18
3.2. Plasma Particle Flux .....	19
3.3. Refractive Index Measurements.....	20
3.3.1. Schlieren.....	21
3.3.2. Holographic Interferometry.....	22
3.3.3. Reflectometry.....	23
3.3.4. Ellipsometry .....	23
3.4. Neutral Atom Diagnostics.....	23
3.5. Emission and Scattering of Electromagnetic Radiation .....	24

3.6.	Photography and Microscopy.....	25
3.7.	Discussion .....	25
4.	Force Balances as Diagnostic Tools .....	28
4.1.	Configurations, Capabilities, and Limitations.....	29
4.1.1.	Pendulum .....	30
4.1.2.	Torsion.....	32
4.1.3.	Effective Zero-Stiffness.....	33
4.1.4.	Resonant .....	34
4.2.	Discussion .....	34
5.	System Design.....	36
5.1.	Nano-Impulse and Mass-Flow Rate Balance .....	36
5.1.1.	Balance Theory and Modelling.....	36
5.1.2.	Displacement Measurement Theory .....	40
5.1.3.	Calibration Techniques .....	43
5.1.4.	Design .....	45
5.1.4.1.	Mechanical .....	45
5.1.4.2.	Optical .....	46
5.1.4.3.	Electrical.....	48
5.1.4.4.	Vacuum .....	48
5.1.4.5.	System .....	48
6.	Experimental Design.....	50
6.1.	Calibration and Characterisation.....	50
6.1.1.	Resolution.....	51
6.1.2.	Sensitivity .....	51
6.1.3.	Noise Floor .....	51
6.1.4.	Repeatability .....	53
6.1.5.	Range.....	54
6.1.6.	Accuracy.....	54
6.2.	Materials for Processing.....	60
6.2.1.	Aluminium.....	60
6.2.2.	Polyvinylchloride (PVC) .....	61
6.2.3.	Silicon .....	62
6.3.	Environment.....	63
6.3.1.	Vacuum .....	64
6.3.2.	Atmospheric Pressure.....	64
6.3.3.	Temperature .....	64
6.4.	Laser Systems .....	64

6.4.1.	SPI G4 200 W Nanosecond Fibre Laser .....	64
6.4.2.	Laser Parameters .....	65
6.4.2.1.	Waveform and Pulse Energy .....	65
6.4.2.2.	Repetition Rate .....	66
6.4.2.3.	Total Energy .....	66
6.5.	Processing Strategies .....	66
6.5.1.	Single Point Processing .....	67
6.5.2.	Area Processing .....	69
6.6.	Additional Analysis Tools .....	69
6.6.1.	Optical Microscopy.....	69
6.6.2.	Scanning Electron Microscopy.....	70
6.7.	Summary of Key Measurement Parameters.....	70
6.8.	Experiment 1, Multi-shot Laser Drilling.....	70
6.9.	Experiment 2, Large Area Scanning .....	70
7.	Results and Analysis.....	72
7.1.	Effect of Repetition Rate and Pulse Shape .....	72
7.1.1.	Aluminium.....	72
7.1.2.	Silicon .....	75
7.1.3.	PVC .....	78
7.2.	Effect of Total Energy Input and Pulse Shape.....	81
7.2.1.	Aluminium.....	81
7.2.2.	Silicon .....	84
7.2.3.	PVC .....	87
7.3.	Effect of Total Energy Input and Environment.....	90
7.3.1.	Aluminium.....	90
7.3.2.	Silicon .....	93
7.3.3.	PVC .....	96
7.4.	Effect of Processing Strategy .....	99
7.4.1.	Aluminium.....	99
7.4.2.	Silicon .....	102
7.4.3.	PVC .....	105
8.	Discussion .....	108
9.	Conclusions .....	119
10.	Future Work.....	121
	References .....	123
	Appendices.....	136

# List of Figures

<b>Figure 1.</b> Applications of lasers in materials processing [1], [2].....	1
<b>Figure 2.</b> Parameters and processes in light-matter interactions. ....	6
<b>Figure 3.</b> Overview of laser TEM modes 00, 01, 02, 10, 11 and 12. ....	8
<b>Figure 4.</b> A range of useful temporal pulse profiles.....	9
<b>Figure 5.</b> Optical absorption depth against wavelength for a range of materials [4], [38]. ...	11
<b>Figure 6.</b> An overview of mechanisms within ultrashort light-matter interactions [39].....	13
<b>Figure 7.</b> A schematic of a magnetic pickup coil. ....	18
<b>Figure 8.</b> A schematic of a Langmuir probe with a varying voltage source and filter [55]. ...	19
<b>Figure 9.</b> A schematic of a single mirror, digital schlieren imaging system [57].....	21
<b>Figure 10.</b> Schliere showing refractive index change in the environment due to heat rising from a hand. Image source: University of Brighton, Advanced Engineering Centre.....	21
<b>Figure 11.</b> A schematic of a digital holographic interferometer. ....	22
<b>Figure 12.</b> A schematic of a neutral atom detector. ....	23
<b>Figure 13.</b> Experimental results from Pangovski et. al, a work published on designer pulses for controlling material transport [75].. ....	26
<b>Figure 14a, left.</b> A free body diagram of a simple pendulum.	
<b>Figure 14b, right.</b> A free body diagram of an inverted pendulum. ....	30
<b>Figure 15a, left.</b> A free body diagram of a horizontal torsion balance.	
<b>Figure 15b, right.</b> A free body diagram of a vertical torsion balance. ....	32
<b>Figure 16.</b> A free body diagram of a folded pendulum experiencing an unknown force. ....	33
<b>Figure 17.</b> Force/impulse derivation for underdamped mass-spring-damper systems [93]..	36
<b>Figure 18.</b> Mass loss on underdamped mass-spring-damper systems [93]. ....	37
<b>Figure 19.</b> A deflection trace created using the MATLAB model. ....	38
<b>Figure 20.</b> The iterative process used to optimise balance parameters using MATLAB.....	39
<b>Figure 21.</b> Example of how to form a quadrature encoder signal.....	41
<b>Figure 22.</b> A schematic for an angular homodyne interferometer [97].....	41
<b>Figure 23.</b> An arctan signal suitable for linear interpolation.....	42
<b>Figure 24.</b> Diagram of an electrostatic comb pair used for producing calibration forces.....	43
<b>Figure 25.</b> A theoretical comparison between parallel plates and electrostatic fins.....	44
<b>Figure 26.</b> A CAD model of the balance assembly. ....	45
<b>Figure 27.</b> A CAD model of the chamber assembly. ....	46
<b>Figure 28.</b> Schematic of the interferometer optical train.....	47
<b>Figure 29.</b> A CAD model of the mechanical and optical assemblies. ....	49
<b>Figure 30.</b> Simplified balance system schematic. ....	49
<b>Figure 31.</b> An image of the partially assembled balance and interferometer assembly.....	50
<b>Figure 32.</b> An image of the assembled balance with feedthrough connections.....	51

<b>Figure 33.</b> Balance noise floor measurements, taken .....	52
<b>Figure 34.</b> A force and impulse measurement taken with the balance. ....	53
<b>Figure 35.</b> Interferometer laser wavelength and stability measurement. ....	56
<b>Figure 36.</b> An image of the electrostatic fin pairs mounted and engaged.....	57
<b>Figure 37.</b> A plot of force against voltage at different electrostatic fin engagement heights.	58
<b>Figure 38.</b> A plot of force against engagement height at fixed voltages. ....	59
<b>Figure 39.</b> Aluminium sample with mounting holes for the force balance arm.....	61
<b>Figure 40.</b> Aluminium sample with mounting holes for the force balance arm.....	62
<b>Figure 41.</b> A 2" silicon wafer mounted to the force balance. ....	63
<b>Figure 42.</b> A plot showing a subset of pulse shapes measured from the SP-200P-A-EP-M-L-Y laser. ....	66
<b>Figure 43.</b> A diagram of the proposed processing strategies. ....	67
<b>Figure 44.</b> An image of beam delivery system for single point processing. ....	68
<b>Figure 45.</b> An image of beam delivery system for area processing.....	69
<b>Figure 46.</b> A plot of momentum coupling coefficient against waveform and repetition rate for aluminium in air exposed to 160 pulses, or 469 mJ.....	72
<b>Figure 47.</b> A plot of ablation efficiency coefficient against waveform and repetition rate for aluminium in air exposed to 160 pulses, or 469 mJ.....	73
<b>Figure 48.</b> A plot of kinetic energy ratio against waveform and repetition rate for aluminium in air exposed to 160 pulses, or 469 mJ.....	74
<b>Figure 49.</b> A plot of momentum coupling coefficient against waveform and repetition rate for silicon in air exposed to 160 pulses, or 469 mJ. ....	75
<b>Figure 50.</b> A plot of ablation efficiency against waveform and repetition rate for silicon in air exposed to 160 pulses, or 469 mJ.....	76
<b>Figure 51.</b> A plot of kinetic energy ratio against waveform and repetition rate for silicon in air exposed to 160 pulses, or 469 mJ.....	77
<b>Figure 52.</b> A plot of momentum coupling coefficient against waveform and repetition rate for PVC in air exposed to 160 pulses, or 469 mJ.....	78
<b>Figure 53.</b> A plot of ablation efficiency against waveform and repetition rate for PVC in air exposed to 160 pulses, or 469 mJ.....	79
<b>Figure 54.</b> A plot of kinetic energy ratio against waveform and repetition rate for PVC in air exposed to 160 pulses, or 469 mJ.....	80
<b>Figure 55.</b> A plot of momentum coupling coefficient against number of pulses and waveform for aluminium exposed to air. ....	81
<b>Figure 56.</b> A plot of ablation efficiency against number of pulses and waveform for aluminium exposed to air. ....	82
<b>Figure 57.</b> A plot of kinetic energy ratio against number of pulses and waveform for aluminium exposed to air. ....	83
<b>Figure 58.</b> A plot of momentum coupling coefficient against number of pulses and waveform for silicon exposed to air. ....	84
<b>Figure 59.</b> A plot of ablation efficiency against number of pulses and waveform for silicon exposed to air. ....	85

<b>Figure 60.</b> A plot of kinetic energy ratio against number of pulses and waveform for silicon exposed to air. ....	86
<b>Figure 61.</b> A plot of momentum coupling coefficient against number of pulses and waveform for PVC exposed to air. ....	87
<b>Figure 62.</b> A plot of ablation efficiency against number of pulses and waveform for PVC exposed to air. ....	88
<b>Figure 63.</b> A plot of kinetic energy ratio against number of pulses and waveform for PVC exposed to air. ....	89
<b>Figure 64.</b> A plot of momentum coupling coefficient against number of pulses and environment for aluminium. ....	90
<b>Figure 65.</b> A plot of ablation efficiency against number of pulses and environment for aluminium. ....	91
<b>Figure 66.</b> A plot of kinetic energy ratio against number of pulses and environment for aluminium. ....	92
<b>Figure 67.</b> A plot of momentum coupling coefficient against number of pulses and environment for silicon. ....	93
<b>Figure 68.</b> A plot of ablation efficiency against number of pulses and environment for silicon. ....	94
<b>Figure 69.</b> A plot of kinetic energy ratio against number of pulses and environment for silicon. ....	95
<b>Figure 70.</b> A plot of momentum coupling coefficient against number of pulses and environment for PVC. ....	96
<b>Figure 71.</b> A plot of ablation efficiency against number of pulses and environment for PVC. ....	97
<b>Figure 72.</b> A semi-log plot of kinetic energy ratio against number of pulses and environment for PVC. ....	98
<b>Figure 73.</b> A semi-log plot of momentum coupling coefficient against repetition rate and processing type for aluminium in vacuum. ....	99
<b>Figure 74.</b> A semi-log plot of ablation efficiency against repetition rate and processing type for aluminium in vacuum. ....	100
<b>Figure 75.</b> A semi-log plot of kinetic energy ratio against repetition rate and processing type for aluminium in vacuum. ....	101
<b>Figure 76.</b> A semi-log plot of momentum coupling coefficient against repetition rate and processing type for silicon in vacuum. ....	102
<b>Figure 77.</b> A semi-log plot of ablation efficiency against repetition rate and processing type for silicon in vacuum. ....	103
<b>Figure 78.</b> A semi-log plot of kinetic energy ratio against repetition rate and processing type for silicon in vacuum. ....	104
<b>Figure 79.</b> A semi-log plot of ablation efficiency against repetition rate and processing type for PVC in vacuum. ....	105
<b>Figure 80.</b> A semi-log plot of ablation efficiency against repetition rate and processing type for PVC in vacuum. ....	106
<b>Figure 81.</b> A semi-log plot of kinetic energy ratio against repetition rate and processing type for silicon in vacuum. ....	107

<b>Figure 82.</b> A stitched array of SEM images taken using the system described in 5.4.6.3..	110
<b>Figure 83 (above).</b> A filled contour plot of $C_m$ against repetition rate and number of pulses on the aluminium target in air using waveform SW0.	
<b>Figure 83 (below).</b> A filled contour plot of the $C_m$ value against repetition rate and number of pulses on the aluminium target in vacuum using waveform SW0. ....	113
<b>Figure 84 (above).</b> A filled contour plot of the $C_l$ value against repetition rate and number of pulses on the aluminium target in air using waveform SW0.	
<b>Figure 84 (below).</b> A filled contour plot of the $C_l$ value against repetition rate and number of pulses on the aluminium target in vacuum using waveform SW0. ....	114
<b>Figure 85 (above).</b> A filled contour plot of the $C_m$ value against repetition rate and number of pulses on the aluminium target in air using waveform SW3.	
<b>Figure 85 (below).</b> A filled contour plot of the $C_m$ value against repetition rate and number of pulses on the aluminium target in vacuum using waveform SW3. ....	115
<b>Figure 86 (above).</b> A filled contour plot of the $C_m$ value against repetition rate and number of pulses on the silicon target in air using waveform SW0.	
<b>Figure 86 (below).</b> A filled contour plot of the $C_m$ value against repetition rate and number of pulses on the silicon target in vacuum using waveform SW0. ....	116
<b>Figure 87.</b> An overlay of figures 81 and 82, showing the combination of qualitative data from the force balance and quantitative data from the SEM. ....	117
<b>Figure 88.</b> A photograph showing early integration testing of the balance system and Falcon GHz digital holographic system developed by Pangovski et al. [47], [73], [128].....	122

## List of Tables

<b>Table 1.</b> A summary of diagnostic techniques used to study light-matter interactions. ....	25
<b>Table 2.</b> An uncertainty budget for the balance and electrostatic fin system for calibration. ....	54
<b>Table 3.</b> An uncertainty budget for balance and logarithmic decrement methods for calibration. ....	54
<b>Table 4.</b> A summary of materials and their properties to be used in experimental light-matter interaction trials [109]–[111]. ....	60
<b>Table 5.</b> A summary of processing environments used in experimental light-matter interaction trials. ....	63
<b>Table 6.</b> Experiment 1, single-spot, parameter summary. ....	70
<b>Table 7.</b> Experiment 2, large-area, parameter summary. ....	71

## Key Nomenclature

Symbol	Description	Units
$\beta$	Kinetic energy ratio of a light-material interaction	-
$E_{\text{plume}}$	Plume kinetic energy of a light-matter interaction	J
$E_{\text{pulse}}$	Laser pulse energy	J
$V_e$	Plume velocity of a light-matter interaction	m/s
$\delta m$	Mass ejected from a light-matter interaction	kg
$I_{\text{SP}}$	Specific Impulse of a light-matter interaction.	s
$I_T$	Total Impulse of a light-matter interaction	N.s
$C_I$	Ablation efficiency coefficient	kg/J
$C_m$	Momentum coupling coefficient	N/W

# 1. Introduction

## 1.1. Background

The interaction of light and matter can produce a myriad of fascinating and useful phenomenon which are fundamental to many technologies and processes used today. As such, a wide range of laser technology has become available across a wide range of light intensities and interaction times to satisfy industrial and academic needs as shown in figure 1.

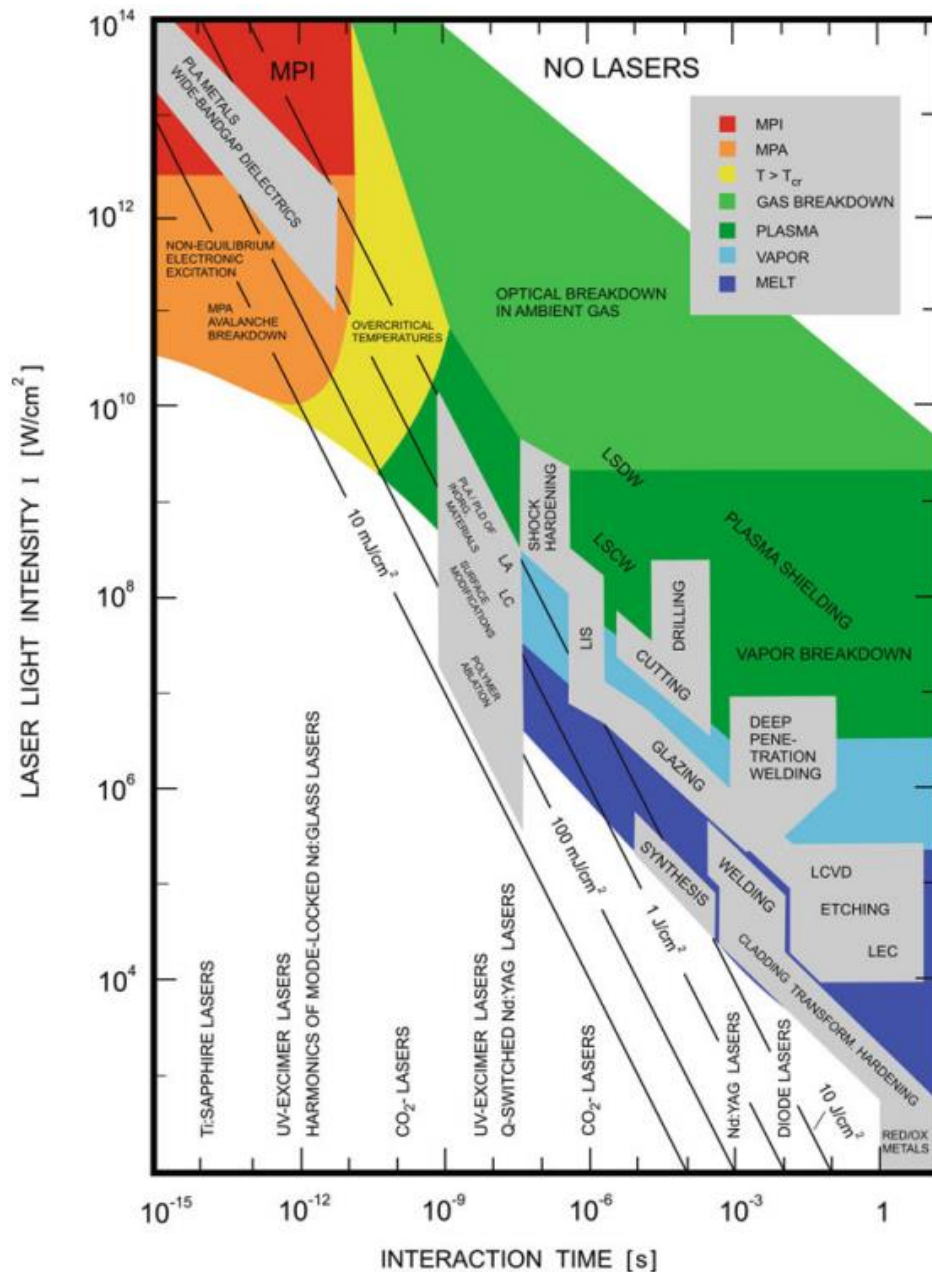


**Figure 1.** Applications of lasers in materials processing [1], [2]. Operations such as cutting, drilling, and etching generally occur on timescales longer than microseconds at low to moderate intensities. Operations such as laser ablation, surface modification and deposition occur on timescales approaching nanoseconds at high intensity. No single laser can perform across the range of intensity and interaction time – performance is mainly limited by the geometry, gain medium and conditioning optics of the laser. The grey boxes shown are more like ‘grey areas’, as many more laser parameters, material properties and interaction pathways have to be considered.

## Introduction

The qualitative and quantitative results produced by light-matter interactions are determined by the properties of the source, material, and mechanisms by which they interact [3]. To achieve a desired result, there must be measurement and control of as many parameters as possible so that optimisation can occur. Due to limitations in source technology combined spatial, temporal and polarisation pulse shaping has yet to be realised, and due to limitations in the understanding of interactions between light and matter, material specific responses have yet to be sufficiently characterised and thus applications must still be designed around the laser and empirically assessed for suitability. This means that for each combination of laser and material, the correct parameter space, which includes many more parameters than just intensity and interaction time, must be found [4].

Bridging the gap between brute force empirical trials and fundamental theory toward a practical applications framework has become the goal of many academic and industrial stakeholders as an immense amount of time, money and energy has been spent on seemingly similar yet unrelatable applications [5], [6]. The general approach to overcome these challenges has been to develop and test theories through simulation and experimentation using traditional plasma diagnostic techniques [7], [8]. However due to the complexity or limited span of most theories, they are not yet of practical use. This work aims to form the early basis of a new practical framework based on the measurement of energy pathways by looking at the types of energy in a system and how/where they are transferred. Whilst this may not produce the fundamental theory behind processes it could ease the empirical nature of light-matter interactions by high-level characterisation of processes by performance in their specific application.

### 1.2. Relevance

Laser technology has become an integral part of modern society, owing to the great number of operations lasers can perform, from surface modifications such as etching, welding and shock hardening to material removal operations such as drilling and ablation [9], [10]. Each unique operation can be defined by a unique combination of interactions which vary with the parameters of the source and material being processed. Many fields depend on the understanding of these interactions as they form the basis for many technologies and processes including:

- Medical science: tissue diagnosis capability, optical coherence tomography or ablative modifications of tissue [11], [12].
- Superconductor science: technologies utilising superconductivity in their function [13].

## Introduction

- Material science: material analysis in analytical chemistry [14], [15].
- Energy research: laser based fusion and diagnostic technologies [16], [17].
- Manufacturing: Additive and subtractive, including photolithography [18], [19].

Much interest is being shown in lasers with short and ultra-short pulse durations and high peak powers. These regimes have allowed for new types of applications to be realised in surface processing and material removal as summarised in figure 1, where surface processing could involve surface structuring/patterning or altering material properties. Subtractive processes using ultrafast lasers can uniquely be applied to almost every type of material: polymers, semiconductors, metals and dielectrics [6].

- Spacecraft propulsion: next generation laser propulsion systems for moderate thrust and efficiency [20]–[23].

The regimes sought after in manufacturing also enable applications in different sectors, such as in-space propulsion. Recent advances in electric thruster architectures and power processing units give modern electric propulsion systems the ability to outperform chemical thrusters in many different scenarios, including deep space exploration, geo-stationary station keeping, constellation phasing, and low altitude orbit drag compensation. However, the worldwide EP portfolio presents significant operational gaps.

The main gap is in the lack of efficient and compact technologies operating with low power (<1 kW) for small satellites. The most promising solutions are Field Emission Electric Propulsion type system utilising liquid metals and colloids as propellants. They are generally limited by low thrust production per emitter [24]–[26], but researchers are trying to mitigate this by shrinking emitter size in order to obtain high density arrays. Established technologies such as Hall-Effect and Gridded-Ion thrusters suffer from limitations in propellant choice, are impaired by the need of an external neutraliser limiting propellant choice and lifetime, and provide low-efficiency at low-power, hindering miniaturization [27]. Other disruptive technologies (e.g. helicon, inertial electrostatic confinement thrusters etc.) presented in recent years have shown poor performance and thus their development has stopped at low technology readiness levels.

Over the past decade researchers have been working on using short and ultra-short pulsed lasers in propulsion systems [20], [28]. The propulsion principle is based on pulsed laser ablation and vaporization of a solid or liquid propellant to create an ionized cloud which is accelerated to high velocity. This configuration is desirable as it can be scaled up using multiple beams to provide variable thrust, efficiency and thrust vectoring and does not require moving parts or large and heavy fuel tanks for liquid/gaseous propellant. Pending feasibility,

## Introduction

laser propulsion could be a disruptive technology filling the above gap between electric and chemical propulsion systems.

- Energy savings: optimising industrial processes to save energy [29], [30].

As previously mentioned, laser based processes are inefficient with respect to time, cost, and energy consumption. As lasers are now widely and deeply embedded into manufacturing and processing plants worldwide, the case for energy saving is now defensible. If for example a typical pulsed laser with pulse energy of 100  $\mu\text{J}$  and repetition rate of 100 kHz operating on 24-hour days, 365 days a year, can be reduced to 90  $\mu\text{J}$  through a better understand of a process, the approximate energy saving would be 31.5 MJ or 3.6 kW per hour. If translated to a hundred thousand lasers worldwide, an energy saving of almost 400 MW per hour could be achieved, enough to power the Gaza Strip continuously [31].

### 1.3. Research Question

The overall goal of this project is to gain a better understanding of the energy and material transport mechanisms in light-matter interactions and enable the development of a framework for designing more energy efficient and effective technologies/processes. This goal can be addressed by the following questions:

- a. How are light-matter interactions affected by laser and material parameters such as temporal pulse shape, repetition rate, number of pulses, drilling vs. scanning, conductor vs. semiconductor vs. plastic, or even air vs. vacuum.
- b. What is the most effective technique for measuring the results from multiple parameter sets with energy efficiency and performance (e.g. material removal) in mind?
- c. Can results created by this technique be used to optimise a technology/process using a combination of empirical trials and fundamental theory in a generic way?
- d. Can these results contribute toward a framework for energy efficient and effective technologies/processes by creating and monitoring an energy budget? For example:

$$E_{\text{pulse}} - E_{\text{transmitted}} - E_{\text{reflected}} = E_{\text{absorbed}} = E_{\text{shockwave}} + E_{\text{plasma}} + E_{\text{kinetic}} + E_{\text{RF}} + E_{\text{material } \Delta T} + E_{\text{everything else}}$$

## 1.4. Research Objectives

The research question shall be addressed by the following objectives:

1. To develop a diagnostic system capable of characterising light-matter interactions.
  - a. Define the key mechanisms in light-matter interactions and how they relate to laser, material, environmental, and process parameters.
  - b. Define observable output parameters in light-matter interactions and the technologies required to measure them, covering the entire body of the interaction i.e. from beginning to end.
  - c. Define which technologies are most suitable for assessing energy efficiency and different kinds of performance parameters, along with their advantages, disadvantages, and applications.
  - d. Select which technologies are required, then design and construct an experimental system.
  
2. To measure the behaviour of varying laser, material, environmental, and process parameters with respect to energy efficiency and performance.
  - a. To design an experimental setup which widely varies laser, material, environmental, and process parameters.
  - b. Use the experimental results to optimise a technology/process in a generic way, but orders of magnitude more quickly - in minutes rather than weeks.
  - c. Determine if the experimental results can contribute toward a framework for energy efficient and effective technologies/processes.

## 2. Review of Light-Matter Interactions

The following chapter provides an overview of the source, material, and interaction properties for consideration in light-matter interactions as required by research objective 1a. Figure 2 provides an overview of the complexity and interdependent nature of these interactions by highlighting key parameters and interaction pathways which vary according to the properties of the source and material.

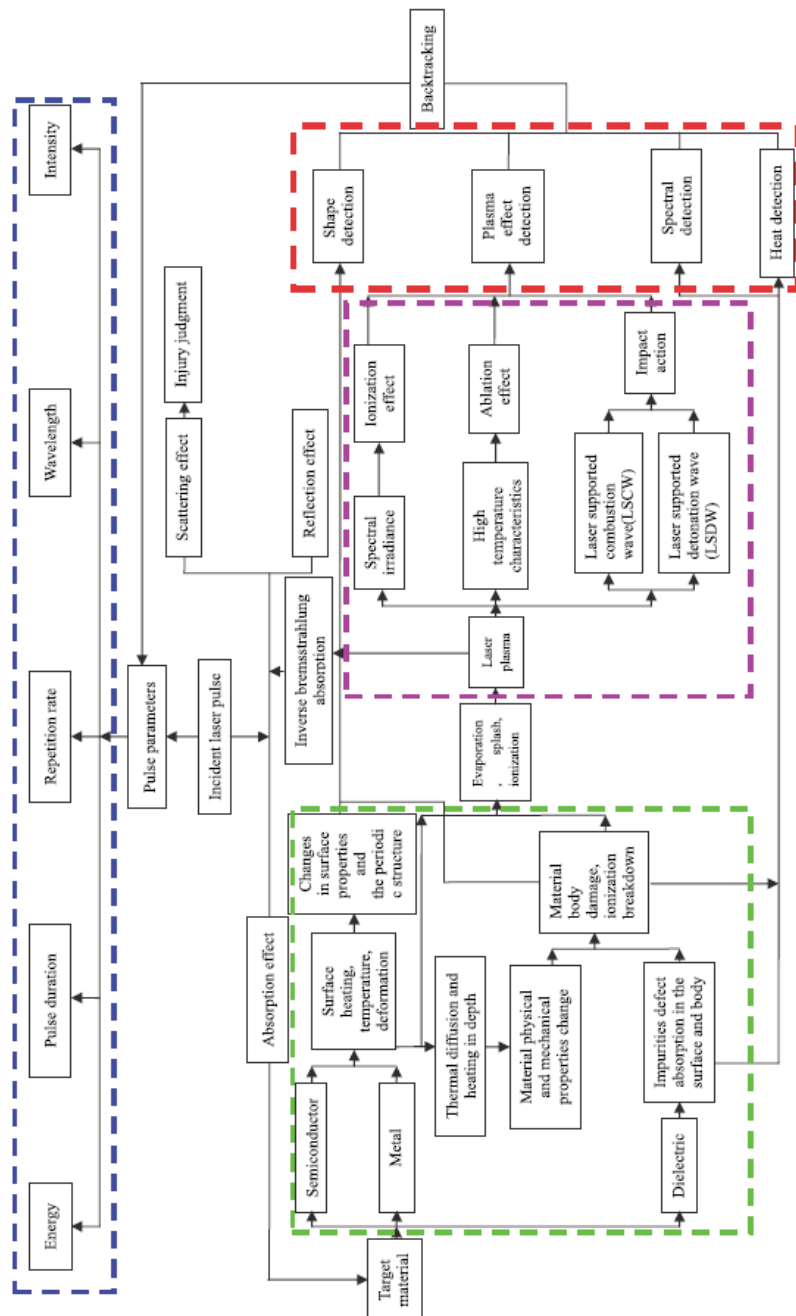


**Figure 2.** Parameters and processes in light-matter interactions. Light-matter interactions involve many complicated processes based on many different models and assumptions. All interactions can however be broken down into a few groups, which consist of laser parameters (blue), material parameters (green), material responses (purple), and their respective observation and measurement techniques (red) [3]. Environmental properties are not shown here, but can be equally important in many situations.

### 2.1. Light Delivery Parameters

In light-matter interactions the majority of energy delivered into a system is provided by the source, typically a laser. The following section defines the main parameters used to characterise laser light [1], [2], [4].

#### 2.1.1. Wavelength

The energy of photons produced by a laser are inversely proportional to their wavelength. The relationship between energy and wavelength can be described using equation 1, which relates the transition energy  $\Delta E$ , speed of light  $c$ , Planck constant  $h$  and laser wavelength  $\lambda$ .

$$\Delta E = \frac{hc}{\lambda} \quad (1)$$

For most materials, using incident light of shorter wavelengths and thus photons with more energy leads to greater absorption into a material. This is because more bound electrons are available to absorb them. This is why lasers with lower wavelengths (sub- $\mu\text{m}$ ) are often used for material modification processes [2].

#### 2.1.2. Intensity and Fluence

The intensity of a laser beam is the optical power exhibited per unit of area and is proportional to the square of the amplitude of the electric field of the beam. A higher intensity generally describes a case with a higher population of photons and or a higher energy associated with each photon. This optical energy is sometimes also described by fluence, which is the optical energy delivered per unit area. For pulsed lasers, the pulse energy is the total optical energy of a single pulse and fluence is then the optical energy delivered per unit of area per pulse. For CW lasers, the irradiation time is required to calculate the equivalent fluence.

#### 2.1.3. Spatial Profile

The spatial profile of a laser describes the spatial energy distribution exhibited by the laser beam. These are commonly known as Transverse Electro-Magnetic Modes (TEM modes) which are a result of standing waves interfering with each other within the gain medium and vary with the geometry of propagation medium. Figure 3 shows examples of TEM modes and their varying energy density as shown by the scale bar with arbitrary intensity. The TEM mode is therefore an important parameter in light-matter interactions as it defines the variation of energy density, which in turn is used to do work. The beam quality factor  $M^2$  is commonly used to measure the degree of variation a laser presents from an ideal Gaussian beam, which is represented by TEM00 in figure 3.

## Review of Light-Matter Interactions

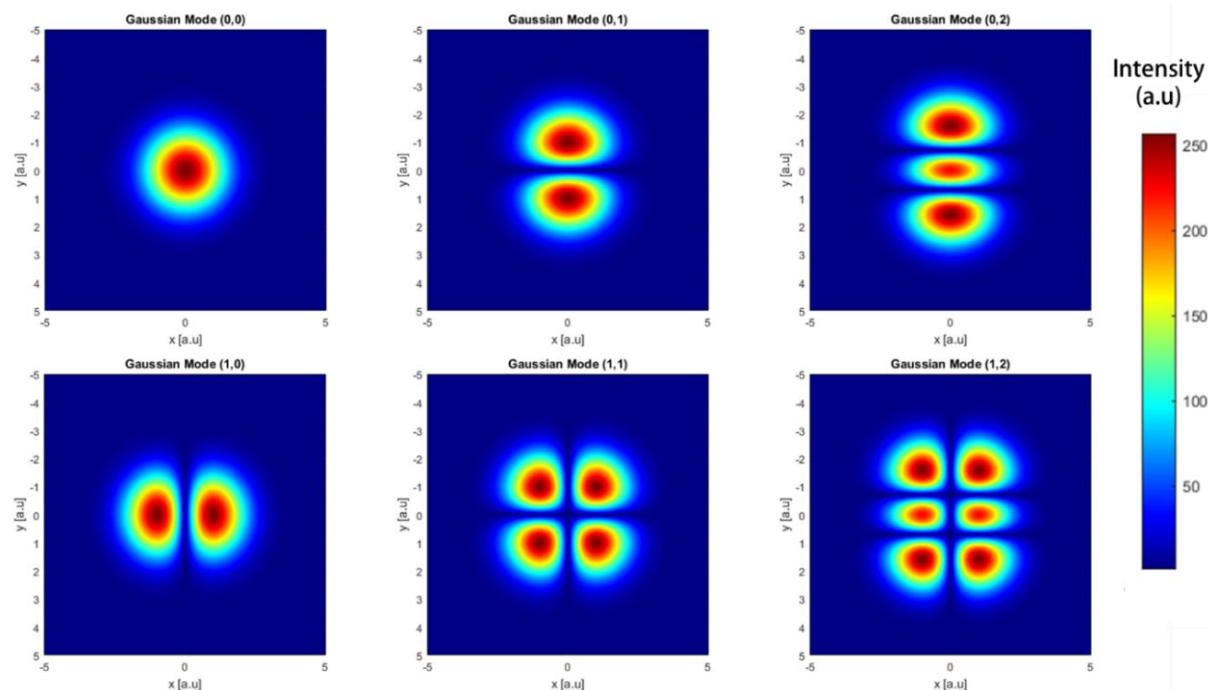


**Figure 3.** Overview of laser TEM modes 00, 01, 02, 10, 11 and 12. Most processing lasers operate with a mode pattern close to TEM00, but various low, high and multi-mode lasers can be found. The range and distribution of these various TEM modes makes beam geometry, such as diameter and waist difficult to characterise.

### 2.1.4. Temporal Profile

The temporal profile of a laser beam describes the pulse profile in the time domain. The temporal profile is an important parameter to understand and control as different interactions take place within a material depending on how much energy is provided and when it is provided. This is typically understood by considering the pulse duration or dwell time of the laser beam relative to the timescale of a material's atomic response. Different materials respond with specific reaction pathways according to the efficiency of electron generation and on the ability to release the energy into the lattice [32]. By carefully selecting the temporal pulse profile it may be possible to tailor processes toward maximum efficiency, lower residual stresses, and lower defect rates etc.

A range of temporal pulse profiles are shown in figure 4. Profile 1 shows the profile of single pulse from a pulsed laser. Profile 2 shows a double peak pulse profile where the temporal spacing between each pulse is tuneable. This configuration has been shown to improve microstructure quality for high fluence machining of metals such as aluminium, copper and steel [33] and has been attributed to the sudden relaxation and excitation of the electron-phonon interactions. Profile 4 shows a single pulse which is followed by a trailing energy bridge. This configuration has been show to improve material removal rates on silicon, which is attributed to the energy bridge continuing material removal through vapourisation and ejection of the molten material within ablation craters [34].

# Review of Light-Matter Interactions

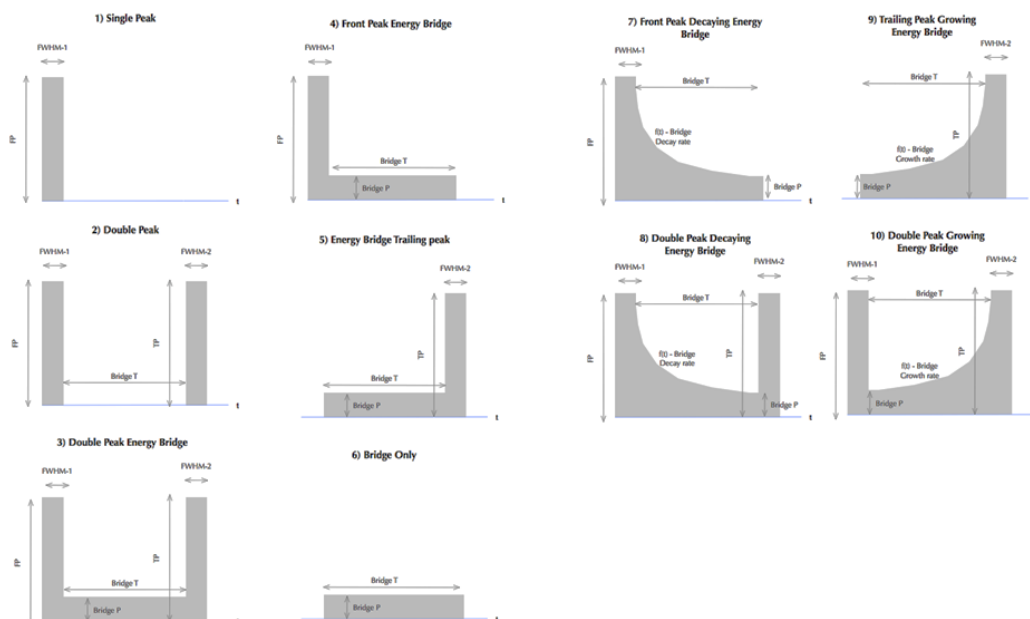


**Figure 4.** A range of useful temporal pulse profiles. Arbitrary intensity is shown on the Y axis and the pulse duration on the X axis. The pulse duration of each peak is shown to be equivalent to the full-width at half-maximum for a real pulse.

## 2.1.5. Polarisation Profile

The polarisation state of a laser describes the orientation of the electric field oscillations travelling perpendicular to the direction of propagation of the beam. Different polarisation states are produced in accordance with the inherent properties of the laser being used, such as geometry or gain medium, and by any optics which may alter this state, such as waveplates. The polarisation state is an important parameter to consider as the orientation of the electric field with respect to the material changes the absorption of energy into the material and therefore the efficiency of energy transfer. Knowing or controlling the polarisation state of a laser beam is useful in applications such as interferometry, spectroscopy or material surface modifications where it is possible to generate sub-micron scale features which vary according to the polarisation state [35], [36]. In the latter case, this is only typically considered for ultra-fast lasers with short pulse durations which operate outside of thermally dominated mechanisms.

## 2.2. Optical Properties of Materials

The following section defines the main parameters used to characterise the behaviour of light when incident on a material.

### 2.2.1. Transmission, Reflectance, and Absorption

At an interface between two materials, the electromagnetic radiation is said to transmit, absorb or reflect. For opaque materials, the reflectivity is  $1 - \text{Absorptivity}$ . For transparent materials,

## Review of Light-Matter Interactions

the reflectivity = 1 – Transmissivity + Absorptivity. The reflectivity at a simple two material interface, such as an air-metal can be described using the following equations [2], [37]:

$$R = \left| \frac{\tilde{n}_2 - \tilde{n}_1}{\tilde{n}_2 + \tilde{n}_1} \right|^2 \quad (2)$$

$$\tilde{n} = n + ik \quad (3)$$

$$n = \frac{c}{v} \quad (4)$$

Where  $\tilde{n}$  is the complex refractive index,  $n$  is the real refractive index,  $c$  is the speed of light in a vacuum and  $v$  is the speed of light in a medium. If we assume the refractive index of air is equal to 1, the reflectivity from different polarisation states can be approximated using equations 5, 6 and 7 which are polarisation dependent [37].

$$R_{\text{parallel}} = \frac{(n \cos \theta - 1)^2 + k^2 \cos^2 \theta}{(n \cos \theta + 1)^2 + k^2 \cos^2 \theta} \quad (5)$$

$$R_{\text{perpendicular}} = \frac{(n \cos \theta - 1)^2 + k^2}{(n \cos \theta + 1)^2 + k^2} \quad (6)$$

$$R_{\text{circular}} = \frac{1}{2}(R_{\text{parallel}} + R_{\text{perpendicular}}) \quad (7)$$

Where  $\theta$  is the incident beam angle,  $k$  is the extinction coefficient and  $n$  is the basic refractive index of the material. Circularly polarised light can be considered as the sum of two perpendicular linearly polarised waves travelling in the direction of propagation with a phase shift of 90 degrees between them. If the angle of incidence is 0, so that the beam is normal to the surface, the reflectivity becomes:

$$R_{\text{parallel}} = R_{\text{perpendicular}} = \frac{(n - 1)^2 + k}{(n + 1)^2 + k} \quad (8)$$

### 2.2.2. Optical Penetration

According to the Beer-Lambert law [2], [37], the propagation of an electromagnetic wave through a material can be described by the following simplified wave equation of the time dependent electric field propagation in a vacuum:

## Review of Light-Matter Interactions

$$E = E_0 e^{\left(\frac{-2\pi k d}{\lambda}\right)} \quad (9)$$

Where  $E$  is the amplitude of the varying electric field with depth  $d$ , and  $k$  is the extinction coefficient which describes the decay of the oscillation of the incident electric field amplitude [4]. The intensity can then be described as proportional to the square of the amplitude, so that:

$$I = I_0 e^{\left(\frac{-4\pi k d}{\lambda}\right)} \quad (10)$$

The absorption coefficient  $\alpha$  describes the attenuation of intensity occurring when light propagates along the  $Z$  axis:

$$\alpha = \left(\frac{4\pi k}{\lambda}\right) \quad (11)$$

The optical penetration depth  $\delta$  is the depth at which light intensity falls by a factor of  $1/e$  of the incident level:

$$\delta = \frac{1}{\alpha} \quad (12)$$

Figure 5 shows the change in optical penetration depth with wavelength for several materials. The optical penetration depths are usually small relative to typical material thicknesses so that energy absorption is confined within some thin layer. This means that materials with short absorption depths encourage local modification of surface properties as minimum energy is transferred to its surroundings, reducing the chances of residual stresses, defects, or other unwanted phenomenon.

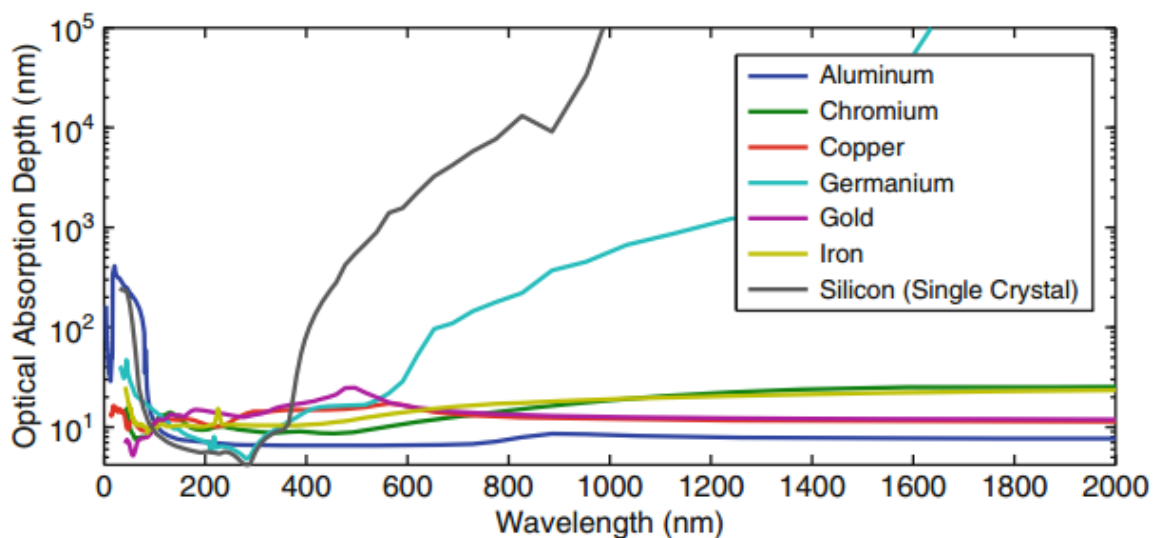


**Figure 5.** Optical absorption depth against wavelength for a range of materials [4], [38].

## Review of Light-Matter Interactions

### 2.2.2.1. Effect of Temperature

As a materials' temperature increases, there is typically an increase in optical absorption [2] due to an increased number of interactions between photons and electrons at higher levels of vibration/excitement of the materials' lattice structure.

### 2.2.2.2. Effect of Surface Films

The addition of a third interface can have a large effect on the optical properties of a material by changing the effective absorption [2]. Equation 13 defines the film thickness required for significant interference coupling so that this effect becomes notable. This effect can be useful for applications such as anti-reflection coatings, where the transmission through an optical element must be maximised. It should be noted that certain types of surface plasma formations can also be represented using the same equation.

$$t_{sf} = \left[ \frac{(2n+1)}{4} \right] \lambda \quad (13)$$

### 2.2.2.3. Effect of Surface Roughness

A rough surface can cause multiple reflections on the surface of a material and change the reflectivity, and therefore absorption by means of diffusion and interference [2]. For these effects to be noticeable the roughness must be of a similar magnitude to the wavelength of the incident light.

## 2.3. Mechanisms, Timescales, and Material Responses

Having briefly reviewed source and material parameters, the interactions and dynamic responses must now be assessed. The concentration shall be on short and ultrashort pulse duration events as these are the most relevant and interesting scientifically and commercially. This is highlighted by figure 1 which shows that most ablation and surface modifications occur at timescales at around  $10^{-9}$  seconds and below, and as such are a critical factor in the development of new processes, material structures, surfaces and interfaces [4].

For short ( $10^{-6}$  to  $10^{-9}$  s), and ultrashort ( $10^{-9}$  to  $10^{-15}$  s) pulse durations the interaction timescales can be summarised by figure 6. When the pulse reaches the material at  $t = 0$  we consider the amount of incident light that is reflected and absorbed. Only absorbed energy contributes to effects such as heating and melting of the material. Due to the properties of the material (e.g. absorption coefficient and refractive index) and incident laser light (e.g. wavelength, angle of incidence and intensity), most of the energy will theoretically be absorbed. Photons from the incident light are absorbed if their energy is greater than or equal

## Review of Light-Matter Interactions

to the band gap energy. At a timescale of  $10^{-15}$  s, the absorbed energy from the photons creates a large density of electron hole pairs which begin to transfer their kinetic energy to the ‘cold’ lattice via recombination and phonon generation once thermal equilibrium has been reached. At a timescale of  $10^{-12}$  s, the thermal energy has propagated within the volume of thermal absorption with energy flowing from high to low heat regions (thermal diffusion). Photons with energy greater than the band gap may form an ionisation front. The thermal transfer between the electrons and lattice at this stage is dependent on the pulse duration. At a timescale between  $10^{-9}$  s and  $10^{-6}$  s, the energy transfer is sufficient to cause phase explosions which are the main source of material removal. The ejected material is ionised, forming a plasma. Shockwaves are generated by recoil pressure of the plasma plume, causing plastic deformation and work hardening as well as creating a molten front within the volume of ejected material. At a timescale of  $10^{-6}$  s and beyond, re-solidification of the expelled material can occur, forming a rim around the ablated region with nano-particles in the surrounding regions.

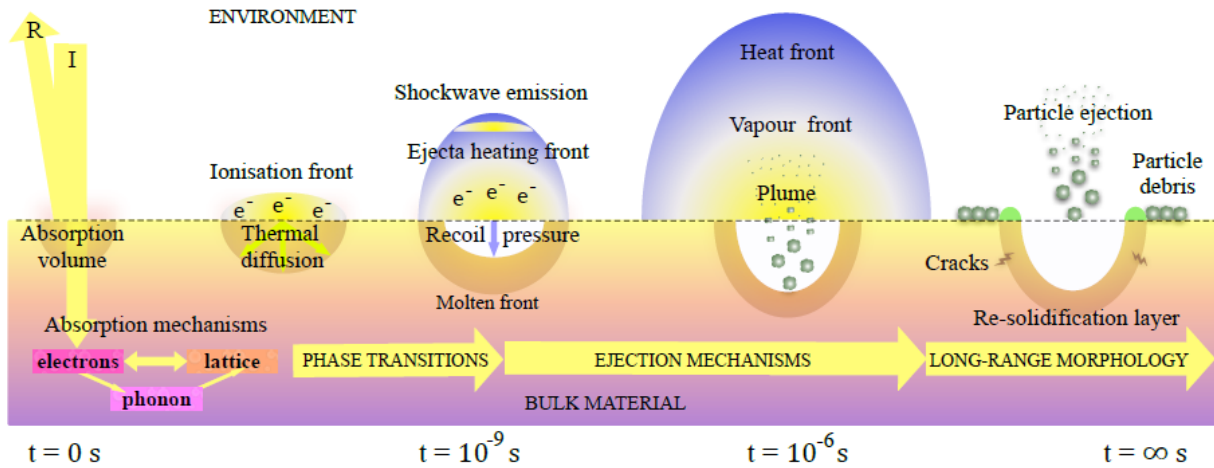


**Figure 6.** An overview of mechanisms within ultrashort light-matter interactions [39].

### 2.3.1. Energy Coupling and Thermodynamic Response

A thermal response for the interaction between a metal and short laser pulse can be described by the following two temperature thermal diffusion model in 1D, which describes thermal conductivity and thermal exchange within the lattice [40], [41]:

$$C_e \frac{\partial T_e}{\partial t} = k_e \frac{\partial^2 T}{\partial z^2} - \gamma_{e-1} (T_e - T_i) + S(z,t) \quad (14)$$

$$C_i \frac{\partial T_i}{\partial t} = \gamma_{e-1} (T_e - T_i) \quad (15)$$

## Review of Light-Matter Interactions

Where  $C_e$  and  $C_i$  are the electron and lattice heat capacities,  $T_e$  and  $T_i$  are the respective temperatures,  $\gamma_{e-1}$  describes electron-lattice coupling,  $k_e$  is the electron thermal conductivity and  $S(z, t)$  is the heating source term. The electron-lattice coupling coefficient can be estimated using the following equation, which holds for silicon as band gap transitions are not possible [42], [43]:

$$\gamma_{e-1} \simeq \frac{C_e n e^2 \rho}{m} \quad (16)$$

Where  $m$  is the effective electron mass,  $\rho$  is the material resistivity,  $e$  the electronic charge and  $n$  the charge carrier concentration. Three regimes can be described with the 1-D thermal diffusion model:  $\tau_L \ll \tau_e \ll \tau_i$ . Where  $\tau_L$  is the laser pulse duration,  $\tau_e$  the electron cooling time =  $C_e/\gamma_{e-1}$  and  $\tau_i$ , the lattice heating time =  $C_i/\gamma_{e-1}$ . In this first instance, when the pulse duration is shorter than the electron cooling and lattice heating times, the energy is delivered before any thermodynamic response is possible. The ablation depth  $l_T$  and mass  $m_T$  is then described by [40], [44]:

$$l_T \simeq \alpha^{-1} \ln \left( \frac{F_{abs}}{F_{th}} \right) \quad (17)$$

$$m_T \simeq N \rho A \alpha^{-1} \ln \left( \frac{F_{abs}}{F_{th}} \right) \quad (18)$$

$$F_{abs} = \text{Absorption} \times \text{Laser Fluence} \quad (19)$$

$$F_{th} = \alpha^{-1} \rho L_v \quad (20)$$

Where  $F_{abs}$  is the absorbed laser fluence and  $F_{th} = \rho L_v/\alpha$  is the threshold fluence condition for strong evaporation. Where  $N$  is the number of laser pulses,  $\rho$  is the material density and  $A$  is the focal spot area.  $L_v$  represents the latent heat of vaporisation. The electron and lattice temperature after pulse termination can also be approximated using the referenced literature [40]. When  $\tau_e \ll \tau_L \ll \tau_i$ , the pulse duration is longer than the electron cooling time, the expression for electron temperature changes but that for lattice does not, as a new quasi-stationary electron temperature is assumed. When  $\tau_e \ll \tau_i \ll \tau_L$ , the pulse duration is longer than the electron cooling and lattice heating times so that thermal equilibrium is assumed and  $T = T_e = T_i$ . The thermal penetration depth limit is now described as:

## Review of Light-Matter Interactions

$$l_T \approx 2 \left( \frac{k_T l_0}{\rho C_p} \right)^{1/2} \quad (21)$$

Where  $k_t$  is the thermal conductivity and  $C_p$  the bulk heat capacity. The absorbed energy creates a temperature increase by means of increasing vibrational energy in the lattice, which is related to the thermal and optical penetration depths. The surface and sub-surface temperatures can then be determined from a surface or volumetric heating source approximation [45].

### 2.3.2. Dynamic Material Response

The absorption of energy into the material is then distributed between multiple phases: solid, molten and vapour. Controlled moving in and out of different phases at different times can produce advantageous phenomenon useful in many processes such as sintering, doping, and at large temperature gradients which have been rapidly induced, work hardening. It should be noted that the physical and chemical properties of the material being irradiated e.g. heat capacity, absorptivity, and thermal conductivity, will change as increasing energy is absorbed, and are ultimately the result of an increase in temperature in the material. The absorbed energy usually manifests itself in the following pathway, where  $Q$  is the absorbed energy,  $m_a$  is the mass,  $c_p$  is the specific heat,  $L_m$  is the latent heat of melting,  $L_v$  is the latent heat of vaporisation, and  $T$  the respective temperature [37]:

1. Heating up the solid to the melting temperature,  $Q_1 = m_a \cdot c_p \cdot \Delta T_m$
2. Melting, which requires the latent heat of melting,  $Q_2 = m_a \cdot L_m$
3. Heating up the molten material to the vaporisation temperature,  $Q_3 = m_a \cdot c_p \cdot \Delta T_v$
4. Vaporisation, which requires the latent heat of vaporisation,  $Q_4 = m_a \cdot L_v$
5. Energy lost by conduction, convection, and radiation,  $Q_1$ .

#### 2.3.2.1. Melting

Once the material has been heated to the melting point and after absorption of the latent heat of melting, the time to melting can be estimated by rearranging:

$$T_s(t) = \begin{cases} T_\infty + \frac{2(1-R)I_0}{k_T} \left( \frac{D_{th}t}{\pi} \right)^{1/2} & \frac{l_T}{l_\alpha} \gg 1 \\ T_\infty + \frac{\alpha_{ext}(1-R)I_0}{\rho C_p} t & \frac{l_T}{l_\alpha} \ll 1 \end{cases} \quad (22)$$

## Review of Light-Matter Interactions

If the melted pool of material is constantly being ejected, the thermal penetration depth, and therefore melt depth calculated will become [46]:

$$l_{\text{melt}} \simeq \frac{D_{\text{th}}}{u_{\text{eject}}} \ln \left( \frac{T_s - T_{\infty}}{T_m - T_{\infty}} \right) \quad (23)$$

Where  $u_{\text{eject}}$  is the material ejection velocity. Surface melting is involved in many types of laser processing techniques, including surface finishing, structural modifications, sealing, alloying, engraving, marking and welding [1] and is therefore a crucial phenomenon to consider and observe.

### 2.3.2.2. Vaporisation, Boiling and Phase explosions

Once the material has been heated to the vaporisation temperature, and after absorption of the latent heat of vaporisation, mass removal may begin due to hydrodynamic instability in the molten liquid layer [47]–[49]. As fluence is further increased, the nucleation of vapor bubbles leads to normal boiling, and if this process occurs rapidly enough, rapid homogenous nucleation and expansion of vapor bubbles leads to phase explosions which are explosive boiling events, which eject a combination of solid and molten state material [4].

### 2.3.2.3. Laser Induced Plasmas and Compressibility

A plasma is generated when the incident laser light is of sufficient intensity, causing the vapour plume to interact with the laser light and ionise. The coupling relationship between the laser light and material is for the most part non-linear, which is an important consideration which affects material removal or modification rates, and is therefore important in understanding the mechanisms of phenomenon such as ablation or thin-film deposition.

The laser light intensity strongly defines the plasma's interaction with the material, as when the laser light intensities are just above plasma formation intensity, the plasma is confined to a region near the surface and the material removal rate is only slightly affected, remaining in a more linear regime. Whilst if the laser intensity is significantly above plasma formation intensity, the plasma becomes greater in volume and non-linear with respect to intensity.

Increase the laser intensity again, and the plasma decouples from the material surface and propagates away. After reaching a critical decoupling value, the plasma is entirely decoupled from the material surface. This is called plasma shielding, and is known to strongly affect material removal rates, as energy is further absorbed by the plasma and does not reach the material surface [1], [50].

## Review of Light-Matter Interactions

With sufficiently intense laser light, the energy will be both absorbed by the material and reflected. The air becomes ionised and turns into a plasma, whilst the material, if solid will be evaporated, ionised, and become a plasma. Both plasmas produced will have a high temperature and pressure which will cause a large expansion force which produces an impulsive force on the material. If the ejected material can react with the remainder of an incident or secondary pulse within this cycle, a laser-supported combustion (LSC) wave is created [51]. If the plasma created by the air causes significant shielding whilst the incoming laser pulses still interact, the ejected material reacts with the remainder of an incident or secondary pulse within this cycle to create a laser-supported detonation (LSD) wave, which is a result of the rapid temperature and pressure increase caused by significant shielding [52].

### 2.4. Discussion

The brief review of light-matter interactions highlights relevant interaction mechanisms and pathways as required by research objective 1a. Light-matter interactions are clearly very complex and interdependent, especially where short and ultra-short time scales and plasmas are concerned. It is also clear that to get a better understanding of a dynamic process there must be dynamic measurement exceeding the timescale of the phenomena trying to be observed. As a result, light-matter interactions require significant empirical study to achieve process optimisation or exploration of parameter space.

One reason for this is that many interaction models found in literature require assumptions and simplifications to be made. For example, many of the energy coupling and response equations are applied symmetrically e.g. surface and volumetric heating, melting and ablation geometry, and plasma/shockwave geometry. This is not ideal as many phenomenon that take place are non-symmetrical in nature. This also extends to outputs such as ablation depth or mass, where assumptions and simplifications must be made about the material parameters. For example, only properties such as density, absorption coefficient and threshold fluence are considered. These vary from material to material, batch to batch, sample to sample, and even between locations on the same sample.

### 3. Review of Diagnostics for Light-Matter Interactions

The following sections briefly review diagnostic parameters and techniques used in light-matter interactions as required by research objective 1b. These techniques are used to measure very specific aspects of light-matter interactions with respect to time, which can be considered as performance criteria e.g. magnetic flux or temperature change, and can be used to measure efficiency e.g. magnetic field flux per / pulse energy in. It is common to use multiple techniques in parallel, as no single technique is capable of measuring all parameters [41], [42].

#### 3.1. Magnetic Diagnostics

Magnetic diagnostics are concerned with the direct measurement of magnetic fields within an interaction volume usually containing a plasma. Magnetic diagnostics are important as the magnitude of such fields are elementary in the performance and understanding of many experiments where magnetic fields are present, and can be applied locally or macroscopically. The simplest and perhaps most commonly found magnetic probes are in the form of magnetic coils and Hall/Faraday effect probes, which can also be used to measure the AC or DC current passing in a target volume. The circuit equation for a simple magnetic pickup coil is:

$$V_0 = \frac{NAB}{RC} \quad (24)$$

Where R and C represent the resistance and capacitance of the integrating circuit, B is the magnetic field strength,  $V_0$  is the induced signal voltage proportional to the field and N is the number of turns in the coil of area A [53], [54]. Figure 7 is a schematic of a pickup coil.

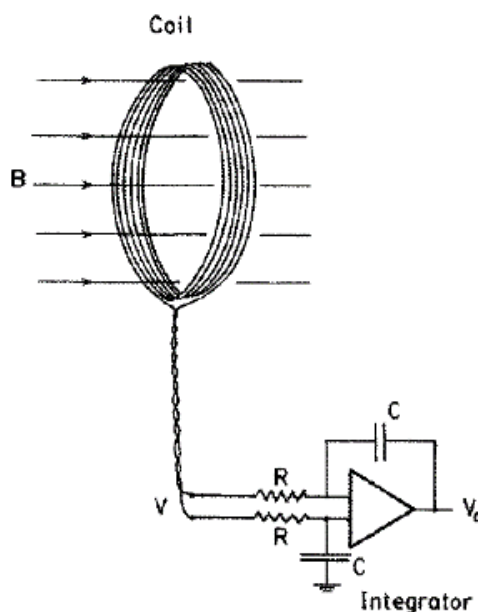


**Figure 7.** A schematic of a magnetic pickup coil. The integrating RC circuit and magnetic coil is shown to be experiencing a magnetic field B which changes with time [53].



probe voltage and current [53]. Another well-known probe of this type is the Faraday probe, which measures the flux in ion charge to estimate ion current.

### 3.3. Refractive Index Measurements

This section describes multiple techniques which are used to measure refractive index changes within an interaction area or volume containing a gas, plasma, transparent material or thin-film. Instead of physical probes, electromagnetic waves are used to probe an interaction area or volume by measuring the change in the properties of the electromagnetic wave itself, assuming the background intensity is not too high. Such techniques are therefore suitable for when the result must not be perturbed by probes. The change in refractive index (RI) can be related to key gas properties by the Gladstone-Dale equation which relates the refractive index and density [56]:

$$n - 1 = K\rho \quad (27)$$

$$n - 1 = \frac{KMP}{RT} \quad (28)$$

Where  $n$  is the refractive index,  $\rho$  is the gas density,  $R$  is the universal gas constant,  $T$  is the absolute temperature,  $M$  is the molecular mass of gas,  $P$  is the pressure and  $K$  is the Gladstone-Dale constant, which is a weak function of light probe wavelength and almost temperature and pressure independent. The effects of magnetic field changes on refractive index can be estimated using the Appleton-Hartree dispersion relation and looking at the two non-dimensional quantities:

$$X \equiv \omega_p^2 / \omega^2 \quad (29)$$

$$Y \equiv \Omega / \omega \quad (30)$$

Where  $\omega_p$  denotes the electron plasma frequency,  $\omega$  the group plasma frequency and  $\Omega$  the electron cyclotron frequency. The effect of magnetic field changes are typically considered negligible as  $Y$  is usually  $\ll 1$ , but when considered finite the Appleton-Hartree dispersion relation for refractive index becomes [53]:

$$n^2 \approx 1 - X \pm XY \cos \theta \quad (31)$$

Where the  $\pm XY \cos \theta$  term denotes the correction for magnetic field changes on refractive index. The electron density can be measured by determination of the phase shift  $\phi$ , if present.

## Review of Diagnostics for Light-Matter Interactions

One main advantage of refractive index techniques are that they are optical and can be digitally captured, and as such allow for visualisation of the observed process and phenomena across many different timescales.

### 3.3.1. Schlieren

Schlieren imaging is a well-established technique used to measure RI changes through a transparent media [57] such as a gas or transparent film. The RI change is experienced as the light source is slowed down during interaction with matter, producing refracted and deflected elements from the expected straight path called Schliere. As the wave travels a differential distance over a differential time it is refracted and deflected by an angle which is directly proportional to the change of RI with time. Schliere are typically imaged using shadowgraph and CCD techniques [58] as shown in figure 9 and 10.

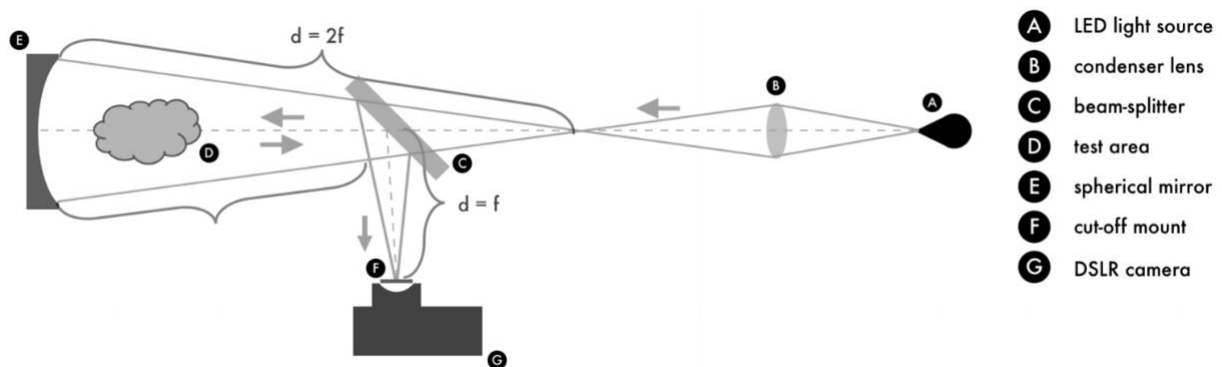


**Figure 9.** A schematic of a single mirror, digital schlieren imaging system [57].

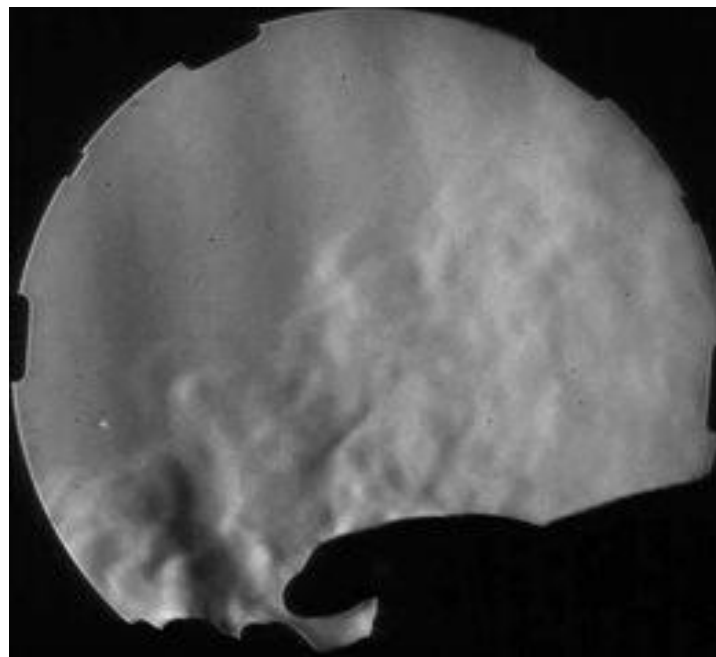


**Figure 10.** Schliere showing refractive index change in the environment due to heat rising from a hand. Image source: University of Brighton, Advanced Engineering Centre.

### 3.3.2. Holographic Interferometry

High-speed digital holography uses holographic interferograms to measure the refractive index history of an event within an interaction volume. It can be considered the state-of-the-art technique within holographic interferometry due to its high spatial and temporal resolution. One of the main advantages of high-speed digital holography is the ability to simultaneously retrieve quantitative and qualitative data as both amplitude and phase information is available. Comparatively, Schlieren only yields qualitative data whilst Synthetic Schlieren yields both qualitative and quantitative data at the cost of lower resolution and range [57]–[59]. Access to quantitative data makes both techniques suitable for process control, but pulsed digital holography more so due to the yield of simultaneous data with sufficient resolution [60], [61]. A simple digital holographic interferometer arrangement is shown in figure 11. Digital holography is mainly limited by the resolution and acquisition time of the CCD which defines the spatial [62] and temporal resolution [63] respectively. The asymmetric nature of many processes and phenomenon may require 3D visualisation, which has been demonstrated using tomographic reconstruction [64]–[66]. One of the main challenges with digital holography is that measurements of refractive index are made relatively through changes in phase and are therefore complex to traceably calibrate and directly relate to specific parameters of interest.

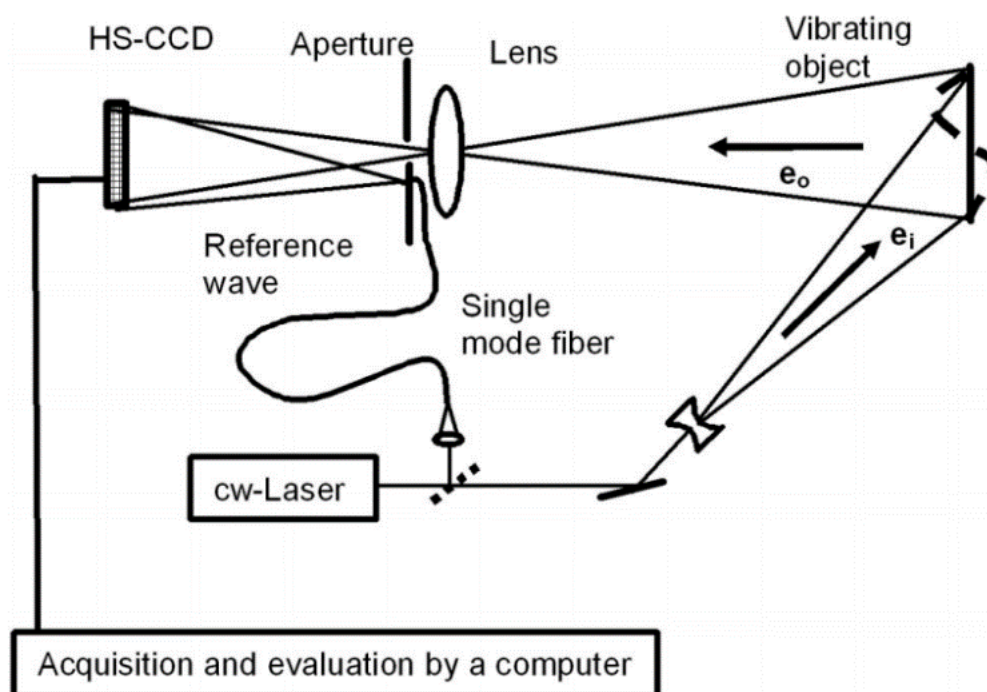


**Figure 11.** A schematic of a digital holographic interferometer. Light from the continuous wave laser is split between two paths, one to illuminate the object and one to act as a reference. Light will be scattered by the object toward the lens due to its illumination. The recombination of the object and reference arm at the CCD form an interferometric hologram, the phase of which can be unwrapped to output displacement as a function of time. This configuration is typically used for high speed vibration measurements [63].

### 3.3.3. Reflectometry

Reflectometry uses the transmission and reflection of particles and waves to probe the composition of plasmas and flat samples, such as biological membranes, polymers and thin-films. The technique works by comparing the density and frequency of a transmitted and reflected probe beam, usually neutrons, with respect to time as reflected neutrons will only reflect when the electron density is high enough [67]. The neutron density is directly related to the complex refractive index. The main advantages of reflectometry are the simplicity and low-cost nature of the devices, whilst the disadvantages are the sensitivity to intensity which can be triggered by temperature drifts, power fluctuations from source and surface roughness which cause scattering.

### 3.3.4. Ellipsometry

Ellipsometry measures the change of polar profile in a transmitted or reflected beam returning from a material or interaction volume. The change in polar profile and phase difference are then directly related to the optical properties of the material or interaction media by the complex refractive index [67]. The main advantage of ellipsometry is that the measurements are not intensity dependent, but phase dependent which gives rise to high sensitivity. The measurements can be highly accurate and repeatable as a ratio of measurements (Fresnel reflection coefficients, reflected vs. incident electric fields) are made.

## 3.4. Neutral Atom Diagnostics

Neutral atom diagnostics deal with the manipulation and measurement of neutral atoms within a plasma. Information on the plasma and its interior is provided by the neutral atoms which have no charge and therefore travel freely across the interaction volume until influenced by ionising and charge exchange collisions with electrons and ions [53], [54], [68]. See figure 12. Thus, this technique is useful for understanding the distribution function of electrons and ions from within the plasma for which no interactions have occurred.

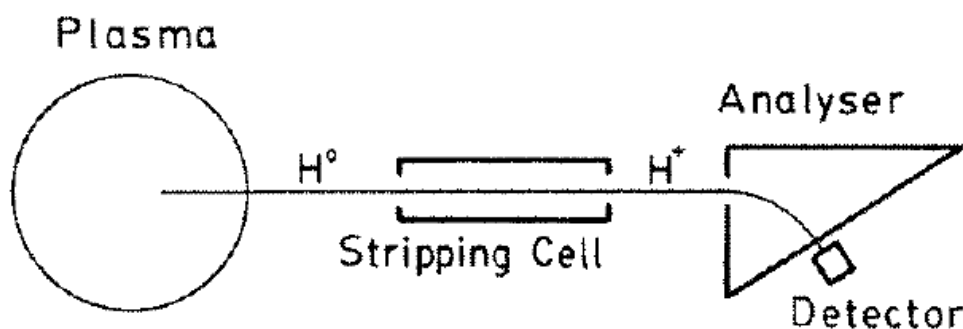


**Figure 12.** A schematic of a neutral atom detector. Neutral atoms from the plasma are ionised through a stripping cell and analysed using an electric or magnetic field to determine their specific energy [53].

A neutral beam of different species can also be introduced into the plasma to act as a diagnostic probe to measure attenuation, changes in charge or doping effects. Another use of neutral beams is in spectroscopy, as a neutral beam can form hydrogen like ions through charge exchange with impurities, which results in the emission of photons without any collisions. Due to their high complexity and specific operating conditions, neutral atom diagnostics are almost exclusively applied in the fields of fusion research.

### 3.5. Emission and Scattering of Electromagnetic Radiation

The radiation emitted from free electrons can be used to determine key parameters of a plasma [69], [70]. The radiation is related to the temperature and density of electrons, and therefore electron energy distribution which can be measured spatially and temporally. Emission of radiation from free electrons occurs due to acceleration in a magnetic or electric field, which is typically generated by cyclotrons, synchrotrons, bremsstrahlung and Cerenkov processes [53] and therefore not usually applicable to light-matter interactions. The radiation emitted from bound electrons is perhaps a more powerful technique than that using free electrons as the study of spectral lines has existed for a very long time and has an extensive database of energy level structures from which to work from [71].

Thomson scattering is the radiation emitted by a charged particle submitted to incident radiation. This phenomenon can also be used to find the electron, and in particular setups, the ion energy distribution within a plasma, making it one of the most powerful yet complicated diagnostic techniques available. The spectral distribution of light scattered through a plasma can be determined by the parameter  $\alpha$  [68]:

$$\alpha = \frac{\lambda}{4\pi\lambda_D \sin\left(\frac{\theta}{2}\right)} \quad (32)$$

Where  $\lambda$  is the probe wavelength,  $\lambda_D$  the Debye length and  $\theta$  the scattering angle. The Debye length is the scale over which charge carriers such as electrons screen out electric fields in plasmas. As a non-invasive technique the results attained are not obscured or limited by a probe, and as with RI techniques, must have a lower background intensity relative to the incident light source. This is a particular issue for Thomson scattering where the vast majority of photons are not scattered, and even fewer actually detected which means highly energetic and expensive lasers must be used. The main disadvantage of both techniques is that they must be applied locally with a relatively low measurement frequency due to exposure times and that realistically only the electron energy distribution functions are attainable, requiring other techniques to complement itself. Another well-known technique under this category is

laser induced fluorescence (LIF), which uses a laser to excite atoms or molecules to higher energy levels so that spontaneous light is emitted. The properties of the emitted light are then specifically related to the species present.

### 3.6. Photography and Microscopy

High-speed photography is often implemented to understand the temporal evolution of processes, as thousand to million frames per second cameras are available. Unfortunately, the information captured during such operations, such as colour and intensity, do not directly allow for calculation of many key thermo-fluidic or plasma properties, but are often used in addition to other techniques such as Schlieren to provide visual analysis usually in the form of images. Microscopy is often implemented in the analysis of material removal or modification, where the depth, area, position, condition etc. of events are important. Optical microscopes, interferometers or scanning electron microscopes are often selected according to the resolution and complexity of the measurement at hand, but are not generally used to capture time dependent process with great temporal resolution.

### 3.7. Discussion

The diagnostic approaches mentioned in the previous sections are summarised in table 1, as required by research objective 1c, by their measurable parameters: the electron charge distribution  $f_e$ , the ion charge distribution  $f_i$ , the electron charge density  $n_e$ , the ion charge density  $n_i$ , the mean group charge density  $n_0$ , the mean group velocity  $V_0$ , the electron temperature  $T_e$ , the ion temperature  $T_i$ , the mean group pressure  $p_0$ , the mean group density  $\rho_0$ , the mean group temperature  $T_0$ , the electric field strength  $E$ , and the magnetic field strength  $B$ .

**Table 1.** A summary of diagnostic techniques used to study light-matter interactions.

<b>Diagnostic Approach</b>	<b>Plasma only</b>	$f_e$	$f_i$	$n_e$	$n_i$	$n_0$	$V_0$	$T_e$	$T_i$	$p_0$	$\rho_0$	$T_0$	$E$	$B$
Magnetic								✓		✓			✓	✓
Particle Flux	✓	✓	✓	✓			✓	✓	✓				✓	
Refractive Index				✓		✓	✓	✓		✓	✓	✓		✓
Neutral Atom	✓		✓		✓	✓	✓		✓					✓
EM Emission	✓	✓		✓	✓	✓	✓	✓	✓					✓
EM Scattering	✓	✓		✓	✓			✓	✓					✓

## Review of Diagnostics for Light-Matter Interactions

Table 1 shows that no single technique can be used to measure all parameters, so that the observer must select the techniques accordingly. Measurement of electron temperature is the most important for measuring the energy coupling and dynamic response of interactions as shown in section 2.3.1, which many techniques can do. For light-matter interactions, a plasma only type measurement would restrict the diagnostic capabilities quite significantly as a plasma does not always exist, and even when it does, it does not constitute the entire body of the interaction as thermo-fluidic effects will carry on long after the plasma state has ended. As such, the electron temperature is well complimented with  $V_0$ ,  $p_0$ ,  $T_0$  and  $\rho_0$ , which will give an insight to the energy of bulk thermodynamic events occurring as discussed in 2.3.2.

The work presented by Pangovski et al [47], [72]–[75] applies state of the art high-speed digital holography to understand and improve laser-based manufacturing processes. The findings highlight the range of bulk parameters that can be extracted from the interaction volume and how they relate to the energy transport mechanisms described in chapter 2, as well as provide an excellent visual representation of events with high temporal resolution.

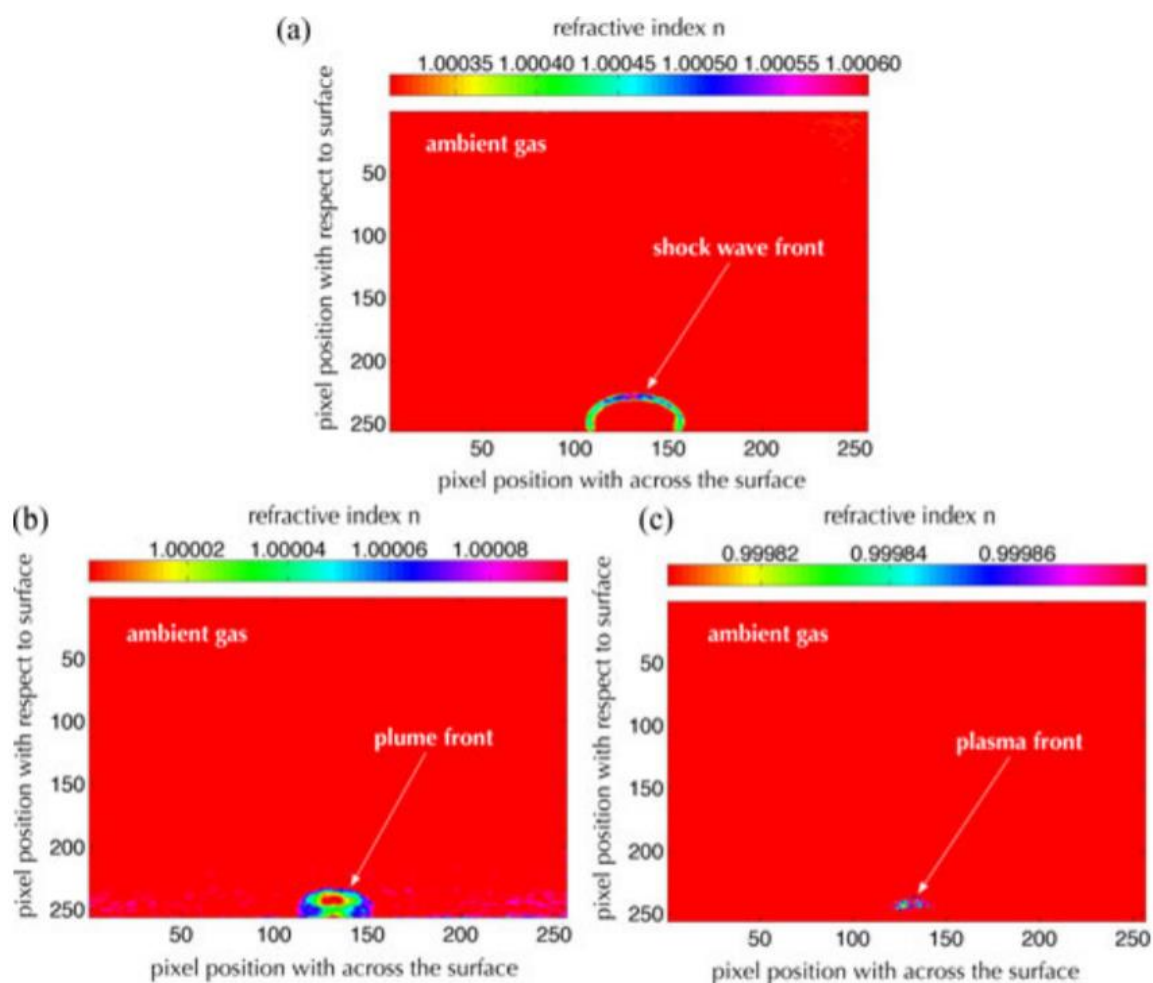


**Figure 13.** Experimental results from Pangovski et. al, a work published on designer pulses for controlling material transport [75]. The results show regions of (a) the shockwave, (b) the plume, and (c) the plasma with refractive index distributions. The field of view is 2.1 mm × 2.1 mm in each image.

## Review of Diagnostics for Light-Matter Interactions

Digital holography is therefore suitable for assessing energy efficiency and different kinds of performance and satisfies most of the diagnostic requirements for probing light-matter interactions but not all of them, as it is only capable of providing relative, indirect measurements e.g. using the Gladstone-Dale equations.

Most of the practical laser processing applications shown in figure 1 involve the addition or removal of material through melting and ablation, and set this as the primary goal (drilling, etching, ablating etc.). Therefore, the performance and efficiency of many of these applications can be linked to the mass loss. Current techniques for measuring material removal are usually all conducted post-process (e.g. using a mass balance), are extremely labour intensive (manual high precision measurements), or add additional uncertainties into measurements as they are made indirectly (e.g. using estimations from 2.3.1). As a practical technique does not yet exist it shall be the focus of the next chapters, with the intention of combining this new technique with digital holography to create a diagnostic platform capable of a wide range of measurements relative to light-matter interaction performance and efficiency.

## 4. Force Balances as Diagnostic Tools

If in addition to mass loss, the force of an interaction could be measured, it should be possible to measure how efficiently and effectively laser energy has been used in material ejection processes. Initially it is useful to consider the ratio of energy being used in force producing events relative to the total input energy, or kinetic energy ratio (KER),  $\beta$ . This can be done by comparing the plume kinetic energy  $E_{plume}$  against the laser pulse energy  $E_{pulse}$ , using equations 33 and 34.

$$\beta = \frac{E_{plume}}{E_{pulse}} \quad (33)$$

$$E_{plume} = \frac{\delta m V_e^2}{2} \quad (34)$$

Where  $\delta m$  is the mass-ejected and  $V_e$  is the plume exhaust velocity. The energy going into non-force producing events can then be found by subtracting the plume kinetic energy from the total input energy from the laser using equation 35.

$$E_{unused} = E_{pulse} - E_{plume} \quad (35)$$

This is a useful value to know as energy going to non-force producing events are likely to contribute significantly to the absorption of heat, which is undesirable as it can lead to the formation of melt pools which lead to low-quality geometries, or phase changes in materials which produce undesirable changes in material properties. The specific impulse or  $I_{SP}$  can then be used to measure the plume energy in terms of directly measurable parameters - force and mass loss.  $I_{SP}$  is a parameter important in propulsion testing as it defines propulsive efficiency. The formula is provided in equation 36.

$$I_{SP} = \frac{I_T}{\delta m g_0} = \frac{V_e}{g_0} \quad (36)$$

$I_T$  is the total impulse, or integral of force over time. Then combining equations 34 and 36.

$$E_{plume} = \frac{I_T^2}{2\delta m} \quad (37)$$

This can then be taken one step further. Assuming interactions are iso-energetic, a coefficient for ablation efficiency which shall be called  $C_l$ , can be determined by combining and equations 33 and 34 and rearranging.  $C_l$  can be assessed against different parameters to directly assess material removal efficiency.

$$E_{plume} = \beta E_{pulse} = \frac{1}{2} \delta m V_e^2 \quad (38)$$

$$C_l = \frac{2\beta}{V_e^2} = \frac{\delta m}{E_{pulse}} \quad (39)$$

## Force Balances as Diagnostic Tools

Interestingly this equation can be re-arranged to also depict the trend in plume exhaust velocity, as shown by re-arranging equation 39.

$$V_e = \sqrt{\frac{2\beta}{c_t}} \quad (40)$$

In addition to ablation efficiency, the momentum coupling coefficient  $C_m$ , can be used to assess how large an impulse is being produced per unit of energy consumed.

$$C_m = \frac{I_T}{E_{pulse}} = \frac{\delta m V_e}{E_{pulse}} \quad (41)$$

### 4.1. Configurations, Capabilities, and Limitations

Force balances capable of micro-newton measurements have been around for over a hundred years and have contributed greatly toward scientific knowledge such as estimation of the gravitational constant. It is only recently however that these balances have become accurate and repeatable enough to produce reliable nano-newton scale measurements. Such instruments are often implemented as thrust balances, high fidelity mass balances or in a multitude of ways in physics experiments. Even with the rapid advancement of MEMS, the larger mechanical balances are still favoured due to their predictable performance and mechanical simplicity. There are many different configurations a balance can take, each with different advantages, disadvantages and limitations which shall briefly be reviewed in the following sections. The following metrics can be used to assess a force balance [76]:

- Sensitivity – How much force is required to provide a certain linear or rotational displacement? This is usually expressed by the linear or angular spring rate, moment of inertia and damping coefficient of the moving balance assembly and limited by the zero-force noise or ‘noise floor’. Sensitivity is usually expressed in the form of N/m or N.m/rad.
- Resolution – What is the smallest change in force that can be reliably distinguished? The resolution is typically driven by the sensitivity and limited by the resolution of the displacement sensor and calibration techniques. The resolution is usually expressed in metres.
- Range – What is the minimum and maximum force the balance can measure and over what range is its behaviour linear? This range is typically limited on the low side by the noise floor and calibration technique, and by the displacement sensor range on the high side. The range is usually expressed in Newtons.

## Force Balances as Diagnostic Tools

- Noise Floor - How much noise is present when no force is applied to the balance? This is usually the limiting factor of measurements being made below micro-newton levels of force. The noise floor consists of multiple sources such as vacuum pumps, actuators, electronics, movement of people and vehicles, machinery and weather. The noise floor is usually evaluated in the form of a power spectral density graph which shows the noise levels at specific frequencies. The noise is usually expressed in  $N/\sqrt{\text{Hz}}$ .
- Repeatability - What are the range of measurement values being produced when repeating the same experiments under the same conditions? The repeatability is mainly affected by drifting and hysteresis caused by temperature change in mechanical and electrical components.
- Accuracy - What is the difference in value between the measured and actual force? Accuracy is greatly dependent on a repeatable system which has been calibrated to traceable standards.

### 4.1.1. Pendulum

A simple (SP) and inverted pendulum (IP) as shown in figure 14a and figure 14b respectively, can be used to relate displacement to the restoring force required to counteract an unknown force. This setup is commonly used due to its mechanical simplicity, high sensitivity and variable resolution which can be varied by changing the mass and length properties of the pendulum respectively [77]–[80].

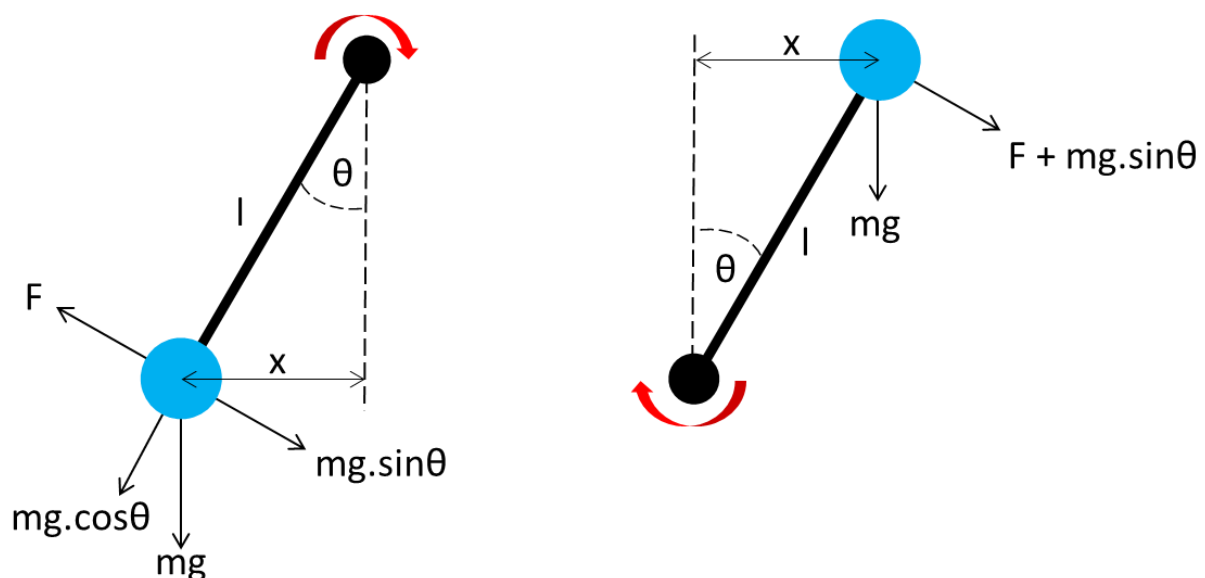


**Figure 14a**, left. A free body diagram of a simple pendulum. **Figure 14b**, right. A free body diagram of an inverted pendulum. Both pendulums have a mass  $m$  and length  $l$  which is displaced by an unknown force  $F$  and thus move by a small angle  $\theta$ .

## Force Balances as Diagnostic Tools

The motion of a simple pendulum can be represented by a mass-spring-damper system governed by a second order differential equation and evaluated to quite some depth. However, Hooke's law is sufficient for simple cases modelling steady state forces, so that the restoring force of the pendulum  $F_R$  opposes the unknown applied force:

$$F_R = -kx \quad (42)$$

With respect to figure 14a, the restoring force  $F_R$  would then equate to:

$$F_R = mg \sin \theta \quad (43)$$

For small angles  $\sin \theta \approx \theta$ , and therefore  $\theta = \frac{x}{l}$ . The restoring force then becomes:

$$F_R = mg \left( \frac{x}{l} \right) \quad (44)$$

The spring rate,  $k$  is then:

$$k = \left( \frac{mg}{l} \right) \quad (45)$$

The natural frequency of an undamped pendulum can then be given by:

$$\omega = \sqrt{\frac{k}{m}} \quad (46)$$

Therefore, to maximise the displacement created by some force  $F$ , a minimal value of  $k$  is required, which can be achieved by minimising the mass  $m$  and maximising the length  $l$ . Increasing the length of the pendulum also decreases the natural frequency when undamped, which is useful for frequency tuning with respect to noise. However, most enclosures and chambers present a limited volume so that the sensitivity cannot simply be increased by lengthening the pendulum arm.

The IP behaviour can be summarised as follows, so that relative to the SP, the IP presents a higher sensitivity and a reduced natural frequency relative to the length of the arm:

$$F_R = F + mg \sin \theta \quad (47)$$

$$\omega = \sqrt{\frac{k}{m} - \frac{g}{l}} \quad (48)$$

An IP as shown in figure 14b, is more sensitive than the simple pendulum as the gravitational force acts to assist rather than restore. The additional sensitivity reduces the effective spring rate compared to that of an SP with the same specification, which be seen by comparing

## Force Balances as Diagnostic Tools

equations 44 and 47. This type of system is inherently unstable as the restoring force no longer exists and therefore requires a feedback and control system to be used [76], [80]. Another disadvantage of this system is the attention required to pivot design, as the pendulum mass is above the pivot, making the restoring force and stability a function of the pivot stiffness which may change during an experiment due to thermal effects [80]. Both the SP and IP are therefore capable of measuring force and mass loss through analysis of displacement and angular velocity.

### 4.1.2. Torsion

Torsional balances can be modelled on the same principle as pendulums, with the exception that spring rate is determined by the stiffness of the torsional element which supplies the restoring force. This allows torsion balances to be configured vertically or horizontally as shown in figure 15a and figure 15b respectively.

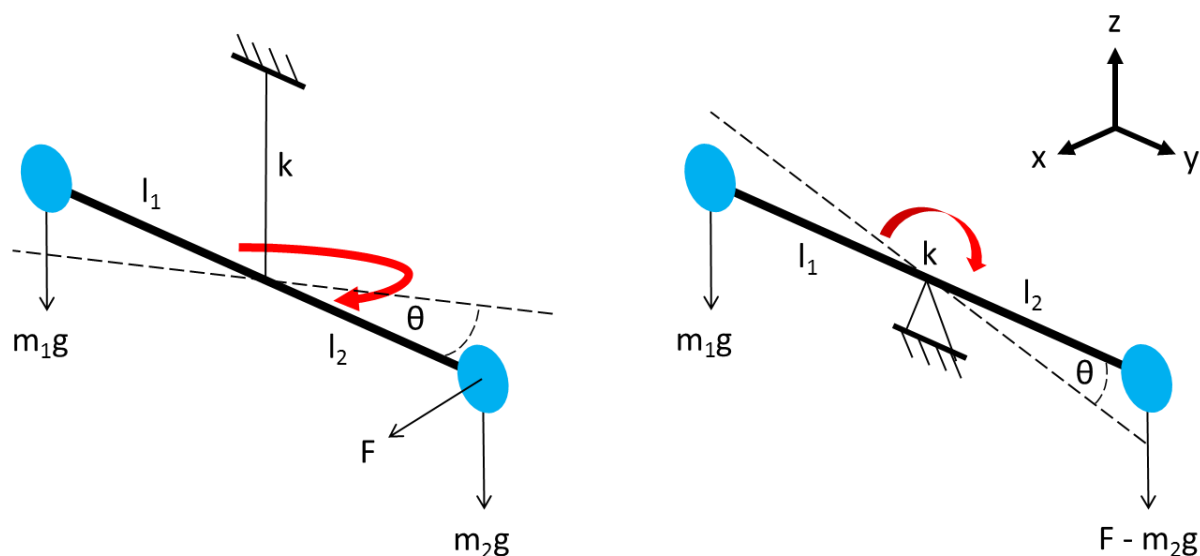


**Figure 15a, left.** A free body diagram of a horizontal torsion balance. **Figure 15b, right.** A free body diagram of a vertical torsion balance. Both balances balancing masses  $m_1$  and  $m_2$ , balancing lengths  $l_1$  and  $l_2$  and a torsional element with stiffness  $k$ . The whole arm is displaced by an unknown force  $F$  and thus moves by a small angle  $\theta$ .

The main difference between the vertical and horizontal setups are the dependency of mass and therefore gravity on the measurement axis. The horizontal setup is most desirable for force only measurements as gravity does not influence the measurement. However, using horizontal balances it is possible to simultaneously measure force and mass loss, as they act in opposite directions and change the equilibrium point of the balance according to the relative change in force = mass  $\times$  gravity [81]–[84].

## Force Balances as Diagnostic Tools

### 4.1.3. Effective Zero-Stiffness

A folded pendulum (FP), as shown in figure 16, is a concept taken from a laser interferometer gravitational wave detector which combines an SP with an IP [85], [86]. The positive and negative restoring forces of each pendulum counteract and create a very low effective stiffness and therefore very high sensitivity. This design was proposed as a force measurement system by Luna et al. [87] to take advantages of the high sensitivity and low frequency vibration isolation. The result is reported to be equivalent to a simple pendulum with 1 km arm length, but in a much smaller package. The design, which usually uses flexures instead of springs, is constructed from a monolithic block to mitigate issues from shear effects, repeatability and alignment issues associated by a multipart assembly.

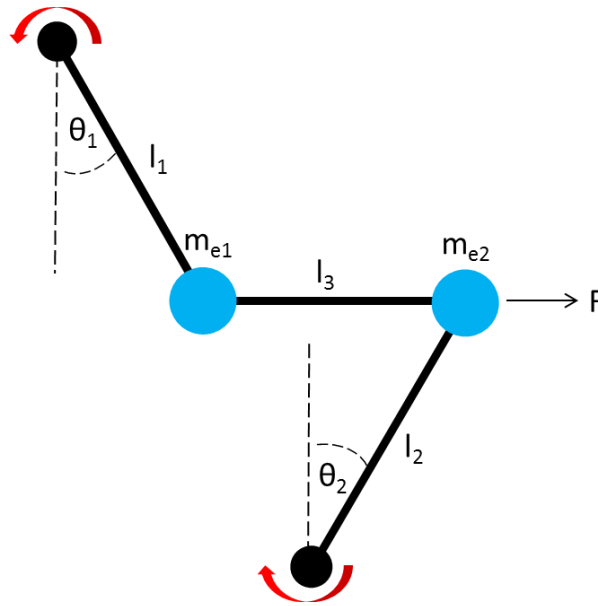


**Figure 16.** A free body diagram of a folded pendulum experiencing an unknown force.

Assuming the arms deflect through small angles so that  $\sin \theta \approx \theta$ :

$$F_R = m_1 g \theta_1 - m_2 g \theta_2 = \left( \frac{m_{e1} g}{l_1} - \frac{m_{e2} g}{l_2} \right) x = kx \quad (49)$$

$$m_{e1} = \frac{1}{2} m_1 + \left( 1 - \frac{x_c}{l_3} \right) m_c \quad (50)$$

$$m_{e2} = \frac{1}{2} m_2 + \left( \frac{x_c}{l_3} \right) m_c \quad (51)$$

$$M_e = m_{e1} + m_{e2} = \frac{1}{2} m_1 + \frac{1}{2} m_2 + m_c \quad (52)$$

Where  $l_1$ ,  $m_1$  and  $l_2$ ,  $m_2$  are the equivalent pendulum arm lengths and masses for the SP and IP respectively and  $k$  represents the effective spring rate of the system.  $M_e$  is the sum of

## Force Balances as Diagnostic Tools

equivalent bob masses,  $m_{e1}$  and  $m_{e2}$  and  $m_{l3}$  is the mass of the system pendulum excluding arms. The natural frequency is given by:

$$\omega = \sqrt{\frac{1}{M_e} \left( \frac{m_{e1}g}{l_1} - \frac{m_{e2}g}{l_2} \right) + \gamma} \quad (53)$$

The resonant frequency be expressed by equation 54, which is solved for a and b to find the critical mass centre position  $x_c$ , the position at which the system becomes unstable due to the positive pendulum contribution becoming less than the negative pendulum contribution. Due to horizontal orientation of such a system, it is unable to directly measure mass flow rate.

$$f = \frac{1}{2\pi} \sqrt{a - bx_c + \gamma} \quad (54)$$

$$x_c = \frac{a}{b} + \frac{\gamma}{b} \quad (55)$$

### 4.1.4. Resonant

Resonant balances based on the pendulum or torsion principle have demonstrated measurements of force and impulse in the micro-newton regime [88], [89]. They require an active control system consisting of an actuator and displacement sensor to apply a known force every half period relative to the systems natural period, which sets the system into resonance. The equilibrium amplitudes of each unknown force and resonant mode are proportional to the applied force. Such measurements are insensitive to random vibrational noise because of the resonant operation and long-term drift because the amplitude measurements are relative, rather than absolute.

## 4.2. Discussion

It can therefore be shown that force and mass flow-rate can be measured using certain configurations. Multiple studies on ultrafast laser ablation of aluminium, copper, stainless steel, Viton, Delrin, Teflon and Buna substrates using a vertical torsion balance were found in literature investigating transient forces due to laser ablation for spacecraft propulsion research [44], [81], [90]–[94]. These studies focused on maximizing the momentum coupling coefficient, so that the maximum amount of impulse could be produced from the smallest amount of energy. Studies conducted using a nanosecond laser at 1064 nm yielded total impulses in the range of  $10^{-3}$  N.s to  $10^{-8}$  N.s with pulse energies between 50 mJ and 400 mJ. Studies conducted using a picosecond laser of unspecified wavelength yielded total impulses in the range of  $10^{-7}$  N.s to  $10^{-9}$  N.s with pulse energies between 0.035 mJ and 0.05 mJ [89]. Due to

## Force Balances as Diagnostic Tools

the novelty of these experiments not much literature is available. Very little information is provided on laser and material parameters, interaction models, or balance noise conditions.

As these types of lasers and materials are widely relevant and accessible, a target total impulse in the range from  $10^{-3}$  N.s to  $10^{-8}$  N.s shall be set for the design of an impulse based diagnostic tool as required by search objective 1d.

Sub-micronewton impulse measurements will often only be achievable within a closed chamber or vacuum chamber where the effects of air currents and temperature change become less pronounced. Another difficulty in operating in this range is noise. If standard vibration isolation techniques do not work e.g. actively damped optical benches, a dual balance setup can be used to offer common-mode rejection whereby the noise of the dummy balance is subtracted from the active balance [77], [95]. This can also help compensate for thermal effects if the two balances are assumed to be experiencing the same thermal load.

## 5. System Design

### 5.1. Nano-Impulse and Mass-Flow Rate Balance

#### 5.1.1. Balance Theory and Modelling

The system is modelled on the second order differential equation of an underdamped mass-spring-damper system, representing a vertical torsion balance from 4.1.2. Equation 56 is used to model this behaviour, which incorporates the balance angular deflection  $\theta$ , the moment of inertia  $I$ , coefficient of damping  $C$ , torsional spring constant  $K$ , unknown force  $F$  and distance from centre of rotation to point of action  $r$ . Thus, if all these parameters are measured with respect to time, the unknown force or impulse can be determined as summarised by figure 17.

$$I\ddot{\theta}(t) + C\dot{\theta}(t) + K\theta(t) = F(t)r \quad (56)$$

With respect to the free body diagram in figure 15b, we can consider mass loss to act in the opposite direction of the force. The balance must therefore experience an effective change in force equal to some mass times gravity, which inevitably offsets the balance equilibrium position measured by the deflection trace. This effect is demonstrated in figure 18.

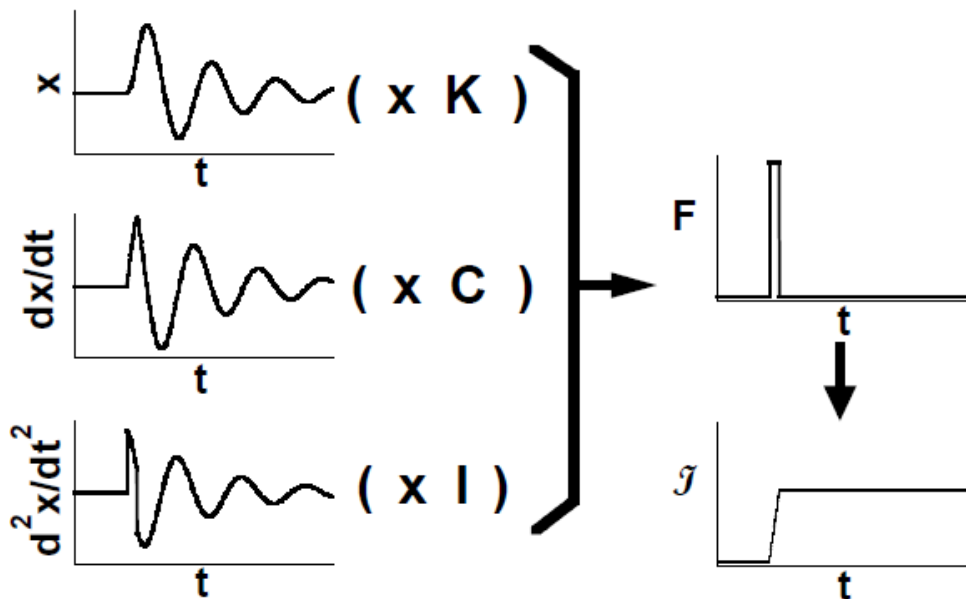


**Figure 17.** Force/impulse derivation for underdamped mass-spring-damper systems [93]. The angular deflection in this figure is represented by  $x$ .

If the angular deflection is measured, the resulting trace can be differentiated once to get the angular velocity and twice to get the angular acceleration. The spring constant and damping coefficient can then be extracted from the logarithmic decrement and period of the deflection trace. The moment of inertia and rotation to action distance can then be measured using CAD models during modelling, and metrology after manufacture. Reducing the number of individual measurements in general can reduce overall measurement error and uncertainty.

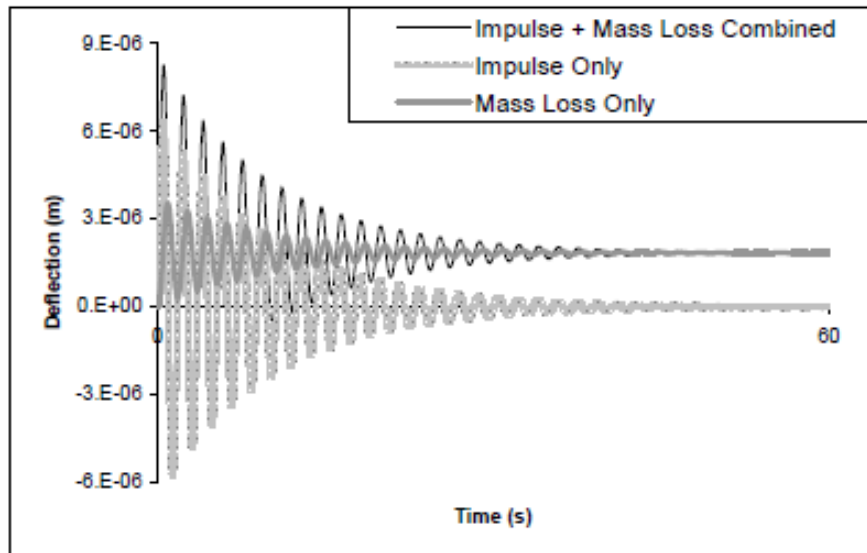


**Figure 18.** Mass loss on underdamped mass-spring-damper systems [93].

The logarithmic decrement  $\delta$  of the deflection trace can be used to calculate the damping coefficient  $C$  and spring constant  $K$  via the damping ratio  $\xi$ , period of oscillations  $T$  and moment of inertia  $I$ , using equations 57 – 63.

$$\delta = \log \left( \frac{\theta(T_n)}{\theta(T_{n+1})} \right) \quad (57)$$

$$\xi = \frac{\delta}{\sqrt{(2\pi)^2 + \delta^2}} \quad (58)$$

$$\omega_d = \frac{2\pi}{T} \quad (59)$$

$$\omega_n = \frac{\omega_d}{\sqrt{1 - \xi^2}} \quad (60)$$

$$C_{\text{critical}} = 2\sqrt{I\omega_n} \quad (61)$$

$$C = \xi C_{\text{critical}} \quad (62)$$

$$K = I\omega_n^2 \quad (63)$$

A MATLAB model was created to understand the time dependent behaviour of the balance when presented with unknown forces, impulses and mass flow rates. The torsion balance model can be found in appendix 1. The model solves equation 56 using a high-precision ordinary differential equation solver (ODE45 or ODE113) with absolute error tolerances set to  $10^{-13}$  and relative tolerances set to  $10^{-12}$ . The programme has 3 sets of input variables: The

## System Design

first set describe the forcing function with respect to time and magnitude as defined by the pulse shape, which is set as a square wave for simplicity. The second set define the mechanical properties of the balance, such as  $I$ ,  $C$ ,  $K$  and  $r$  which are used to change the balance performance. The final set define the duration and time steps used for each simulation. The model's primary output is the deflection trace  $\theta(t)$ , which is differentiated to find the angular velocity and acceleration. Example traces are shown in figure 19.

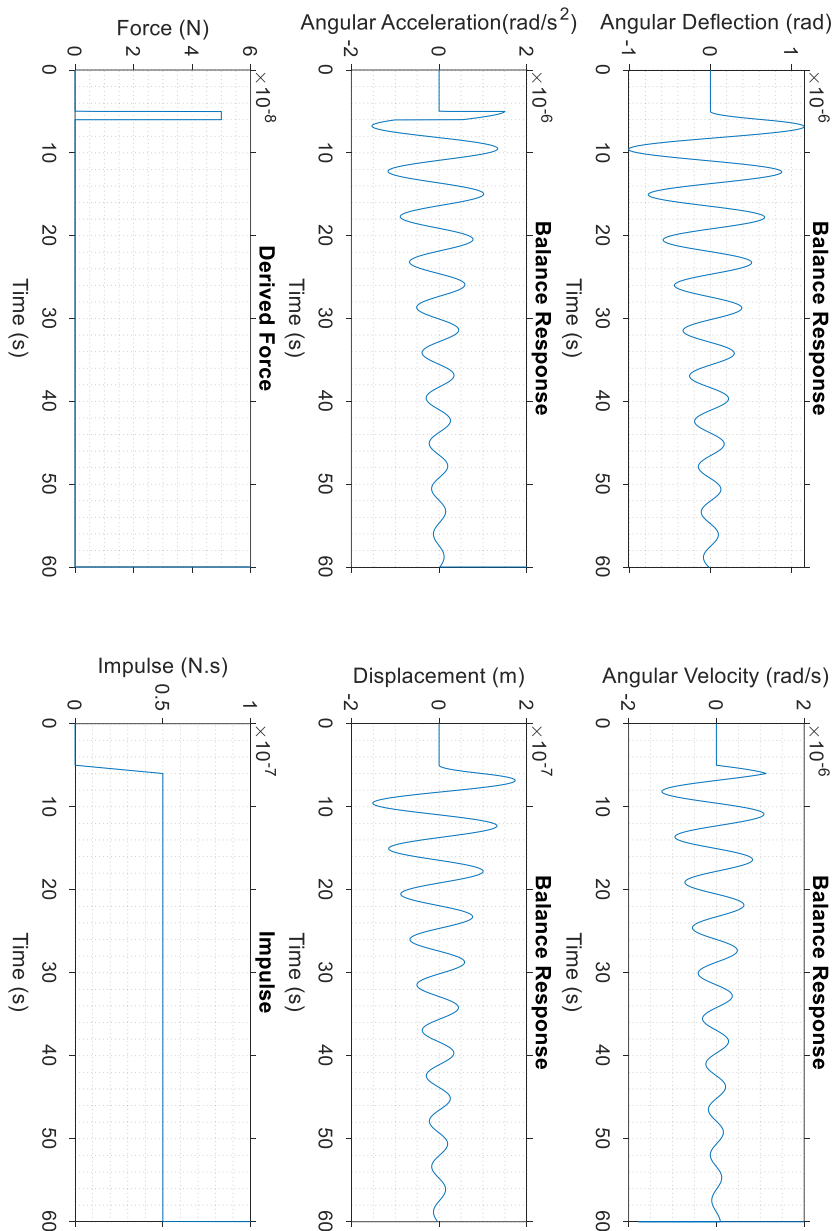


**Figure 19.** A deflection trace created using the MATLAB model. The response was forced using a  $5 \times 10^{-8}$  N.s impulse (top) with  $r = 0.15$  m,  $I = 0.005$  kg.m<sup>2</sup>,  $C = 0.0005$  kg.m<sup>2</sup>/s and  $K = 0.0066$  N.m/rad with no mass loss. The times steps are 50 ms. The measured force and impulse are also shown.

The input parameters can then be iteratively varied until a desirable response i.e. maximum deflection for a given force and optimum settling time, is produced across the range, resolution and natural frequencies, as highlighted by figure 20.

## System Design

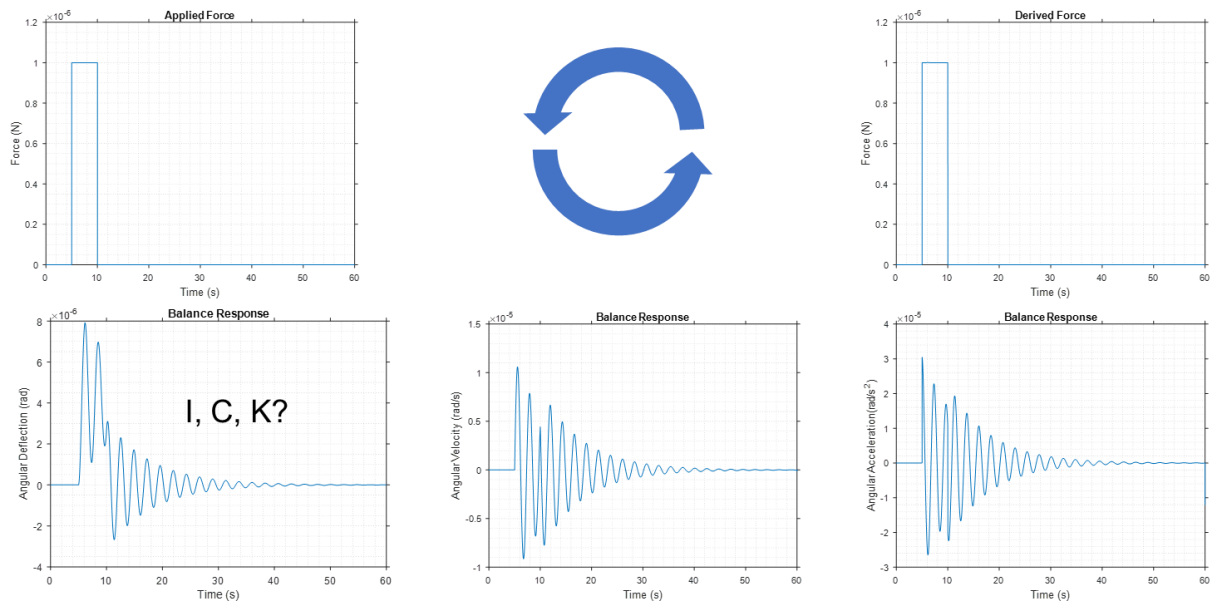


**Figure 20.** The iterative process used to optimise balance parameters using MATLAB. The applied force (top left) forces a balance response with respect to deflection (bottom left), which can be analysed to extract the scaling factors  $I$ ,  $C$  and  $K$ , as well as differentiated to get the angular velocity (bottom centre) and angular acceleration (bottom right). These can then be plugged into equation 56 with respect to time to derive the unknown force (top right). Other features such as settling time, resonant frequency, required deflection, and measurement resolution can be extracted from these datasets.

The model can then be used for comparison against the real balance. The following considerations must be made when optimising the balance response:

- Minimising  $K$  to maximise angular deflection  $\theta$  and thus lowering displacement sensor resolution requirements. This however increases susceptibility to noise and external forces, and increases error due to small angle approximation at larger displacements unless angular deflection is directly measured.
- The measurement range is then dependent on the range the displacement sensor is capable of. Typically, a sensor with a high resolution has a low range and vice-versa.
- The moment of inertia of the moving assembly should be minimised to improve response to low impulses, yet maximised to reduce the potential complexity and cost associated with low length and mass designs.
- Maximising arm length  $r$  to maximise the angular deflection  $\theta$ , and thus lowering displacement sensor resolution requirements. The moment of inertia of a simple rod halfway along its length is directly proportional to its mass and its length squared, so a balance between  $I$  and  $r$  must be sought. Arm length is an important consideration if the balance is to be placed within a chamber of limited volume.

## System Design

- The damping coefficient  $C$  must be tuned to provide an underdamped system. If tuned too low the pulses will not be damped within a reasonable period and may become influenced by noise and external forces. If tuned too high the deflection trace will contain too few peaks for accurate calculation of the logarithmic decrement and period.
- The damped resonant frequency  $\omega_d/2\pi$  should be minimised to avoid interference from noise and vibrations (which are typically present at and above 0.5 Hz), yet kept high enough so that individual pulses are damped within a reasonable period.

### 5.1.2. Displacement Measurement Theory

Upon completion, the model was found to perform in accordance with the results found in literature for propulsion studies e.g. work by D'Souza et al. The input variables, such as available balance length, spring sensitivity, balance moving mass were then varied to optimise the design based on achieving measurements in the order of  $10^{-9}$  N.s. Using the parameters listed in figure 19, the balance produces an angular deflection of  $6.6 \times 10^{-5}$  degrees or an equivalent linear deflection of  $\sim 173$  nm for a  $5 \times 10^{-8}$  N.s impulse. Similarly, a deflection of  $\sim 35$  nm is produced for a  $1 \times 10^{-8}$  N.s impulse.

The nm resolution required to accurately provide a time-resolved measurement on this scale can only be satisfied by interferometry, which uses the interference of electromagnetic waves and their relationship to the wavelength of the light source to extract information about changes in distance, area and volume. If using a simple Michelson interferometer in a homodyne (single frequency) configuration with a 632.8 nm light source, the linear displacement can be calculated as follows:

$$\Delta x = n \frac{\lambda}{2} \quad (64)$$

Where  $\Delta x$  is the linear displacement,  $\lambda$  is the laser source wavelength and  $n$  is the fringe count from the interference pattern, which for a single fringe would correspond to  $\lambda/2$  or 316.4 nm. The number of fringes that need to be resolved to achieve 35 nm resolution can be found by rearranging equation 64 for  $n$ , resulting in a required fringe resolution of  $\lambda/18$ . Most commercial interferometers in this configuration do not operate at a fringe resolution above  $\lambda/256$  due to hardware and noise limitations obscuring the true signal. If the original interference signal is phase shifted to produce 0, 90, 180 and 270 degree signals, they can be compared and counted using conventional quadrature signals as found in actuators and motors as shown in figure 21. A quadrature encoder is the system which produces the quadrature signal, and a quadrature decoder is the system which counts the signal.

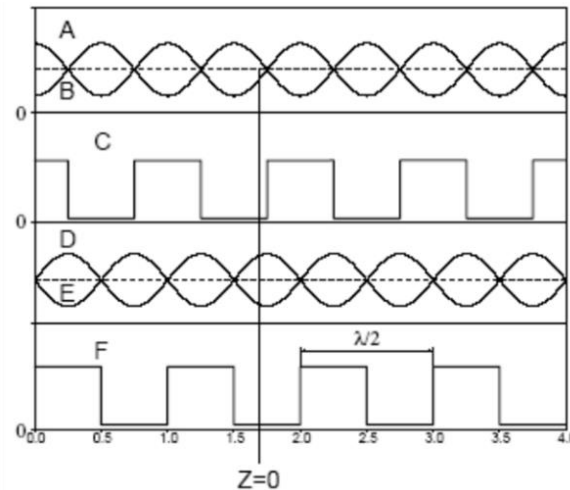


**Figure 21.** Example of how to form a quadrature encoder signal. Comparing 0 (A), 180 (B), 90 (C) and 270 (D) degree phase shifted signals to product a two channel signal for counting (C) and directional awareness (F) [96] with respect to time on the X axis and signal (a.u.) on the Y axis.

The main advantages of a quadrature system are as follows: the need for recording individual fringes for processing is eliminated, an operation which typically requires a large amount of hard disk space, computing power and expensive oscilloscopes if a high fringe rate needs to be measured. Modern decoders operate in x4 count mode, which means that  $\lambda/8$  resolution can be achieved without interpolation, as each leading and counting edge from signals C and F are used to produce four times the number of pulses for counting.

If an angular homodyne configuration is used as in figure 22, the angular deflection can be directly measured with a further increase in resolution. The angular interferometer differs from the Michelson as the reference mirror also moves, so that the system measures the relative changes between the two optical paths separated by some distance S, which increases the effective resolution and eliminates small angle approximations which is relevant for the desired balance configuration.

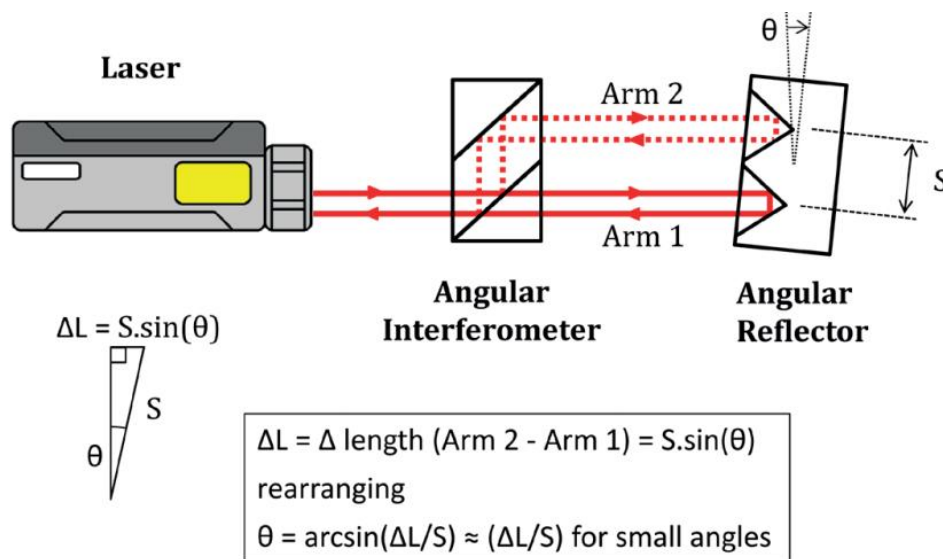


**Figure 22.** A schematic of an angular homodyne interferometer [97].

## System Design

If the light source remains at 632.8 nm and the separation distance  $S$  between the two retroreflectors from centre to centre =  $2r = 0.3$  m, the angular resolution becomes:

$$\theta = \sin^{-1}\left(\frac{\Delta x}{s}\right) \quad (65)$$

Where  $\theta = 1.3 \times 10^{-6}$  degrees, the number of fringes to be interpolated can be found by combining equations 64 and 65 and rearranging for  $n$ , resulting in an effective resolution of  $\lambda/16$  or 39.6 nm. This approximately meets the target resolution of 35 nm and does not require any interpolation to work.

If greater resolution is required interpolation must be used, as small improvements in balance properties or reduction of laser wavelength only produce small benefits to sensitivity or resolution. A 'rugged' type of interpolation method is desirable as the quality and stability of the signal with respect to amplitude is not yet known. An arctan or sine/cosine interpolator, which can be found in high precision optical and actuator technology, could be implemented, whereby two signals with a relative phase shift of 90 degrees (sine, cosine) are measured. The arctangent of the signals (sine/cosine) are then taken to produce a sawtooth waveform, which happens to produce a constant amplitude signal with linear trendline as in figure 23.

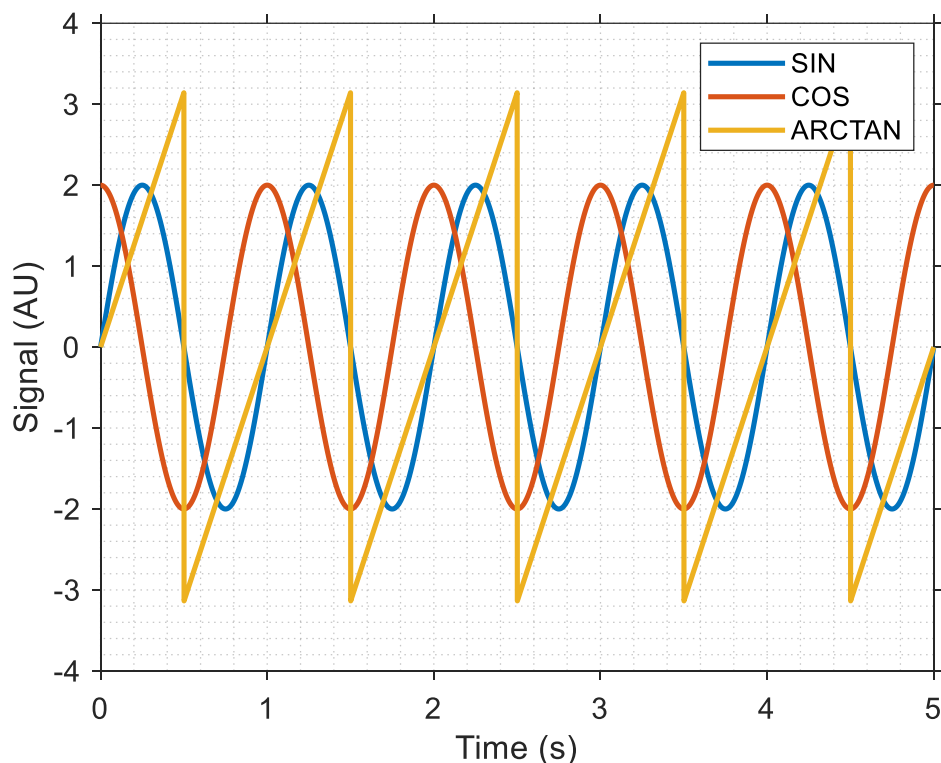


**Figure 23.** An arctan signal suitable for linear interpolation. A plot showing a sine (red) and cosine (blue) signal relative to their arctangent sawtooth function (yellow).

The amplitude of the waveform remains constant even when the signal varies in amplitude, however such variations do introduce a regular curvature to the slope of the signal which can

## System Design

be mitigated using a lookup table or non-linear interpolation method. The quadrature system previously mentioned is insensitive to such issues as it is a comparative method looking at low and high signal timings. The linear sawtooth signal is however ideal for the simplest kind of interpolation, linear interpolation, the resolution of which will be dependent on the signal quality and resolution of the analogue to digital conversion available. In this case, it is expected that 8-bit or  $1/256$  could theoretically be achieved.

### 5.1.3. Calibration Techniques

The application of a known force or impulse for calibration is important if measurements need to be accurate, reliable and repeatable [76]. Calibration for balances is typically used to assess the spring rate, which plays the most important role in force and impulse measurements. For use on a balance measuring such low forces the measurements must inherently be non-contact. The calibration must also be in the range of the forces or impulses that are expected to be measured during normal use, which in this case is between  $10^{-8}$  N.s and  $10^{-3}$  N.s as previously mentioned. Several methods for calibration have been developed by the spacecraft propulsion community, including orifice discharge [98], [99], impact methods (piezo or pendulum hammers) [100], electrostatic actuation [82], [101], [102] and electromagnetic actuation [103]. The orifice discharge and impact type techniques introduce a large uncertainty in measurements ( $>10\%$ ) and are therefore undesirable. The most favoured, state of the art technique uses electrostatic fins to provide forces and impulses directly proportional to an applied voltage. These techniques are favoured as the control and measurement of voltage can be done very accurately and precisely. An electrostatic comb concept is explained using figure 24. The amount of force exerted by the combs can be calculated using equation 66, which relates the permeability of free space  $\mu_0 \sim 8.85 \times 10^{-12}$  A<sup>2</sup>.s<sup>4</sup>/kg.m<sup>3</sup>, number of combs  $n$ , the comb width  $w$ , the engagement length  $l$  and applied voltage  $V$  [104].

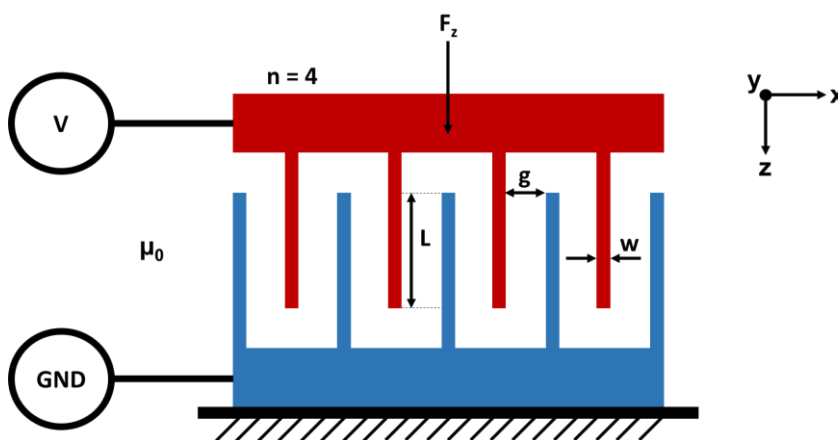


**Figure 24.** Diagram of an electrostatic comb pair used for producing calibration forces. The interlocking combs are separated by a small gap  $g$ , and engaged by a distance  $L$ . One comb is fixed into position (blue) and the other is attached to some moving element as required (red). The attractive force produced by the combs is a function of applied voltage, comb geometry and number of comb pairs [85].

## System Design

Likewise, the force exerted by parallel plates can be calculated using equation 67, which relates the plate area  $A$ , plate separation  $x$ , permeability of free space  $\mu_0$  and applied voltage  $V$ . The advantage of using combs or fins over parallel plates is that the comb geometry is independent of the gap  $g$  and engagement distance  $L$  so that the engagement distance must not be known with great accuracy and that the attractive force does not change throughout the moving combs motion [83]. Such setups have been demonstrated in literature to produce impulses as low as 7 nN.s [104], [105]. It would also be beneficial to calibrate the system to traceable standards so that laser-materials processing can be directly linked on the traceability chain. Figure 25 compares the performance of the two configurations with respect to force and voltage.

$$F_z = 2n\mu_0 V^2 \left( 1.0245 - \left( \frac{w/2}{\pi L} \right) \right) \quad (66)$$

$$F_z = \frac{1}{2} A \mu_0 \left( \frac{V}{x} \right)^2 \quad (67)$$

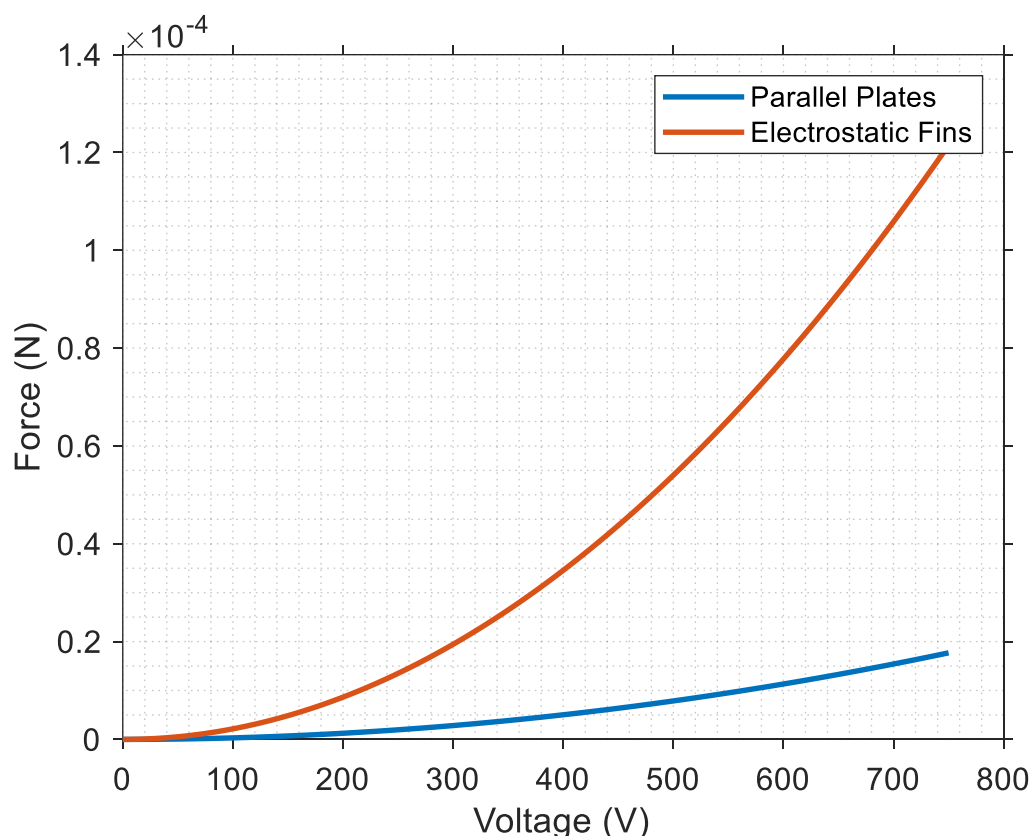


**Figure 25.** A theoretical comparison between parallel plates and electrostatic fins. With respect to force and applied voltage, the fins produce a greater force over an equivalent working area and voltage, where  $A = 0.0016 \text{ m}^2$ ,  $x = 0.003 \text{ m}$ ,  $L = 0.009 \text{ m}$ ,  $w = 0.001 \text{ m}$ ,  $g = w$  and  $n = 6$ .

## System Design

Another suitable approach not usually mentioned is the logarithmic decrement method, by which the natural frequency and moment of inertia of the balance are used to assess spring rate in accordance with equation 55 [83], [106]. As no additional force producing system is required for reference, the spring rate can be directly determined with fewer sources of uncertainty. The other advantage of this technique is that the spring rate could be determined in-situ and in a sense be self-calibrating, as no calibration force needs to be applied before or after measurements. The main disadvantage of this approach is that the system would not be linkable to any traceable standards. However, in the current configuration an interferometer is being incorporated, so that the wavelength of light could be made traceable. In any case, both methods shall be assessed.

### 5.1.4. Design

#### 5.1.4.1. Mechanical

The results from section 5.1.1, 5.1.2 and 5.1.3 were translated into a mechanical CAD model represented by figure 26. A vacuum chamber with optical and electrical feedthroughs was then designed to fit around the balance, the CAD model is shown in figure 27.

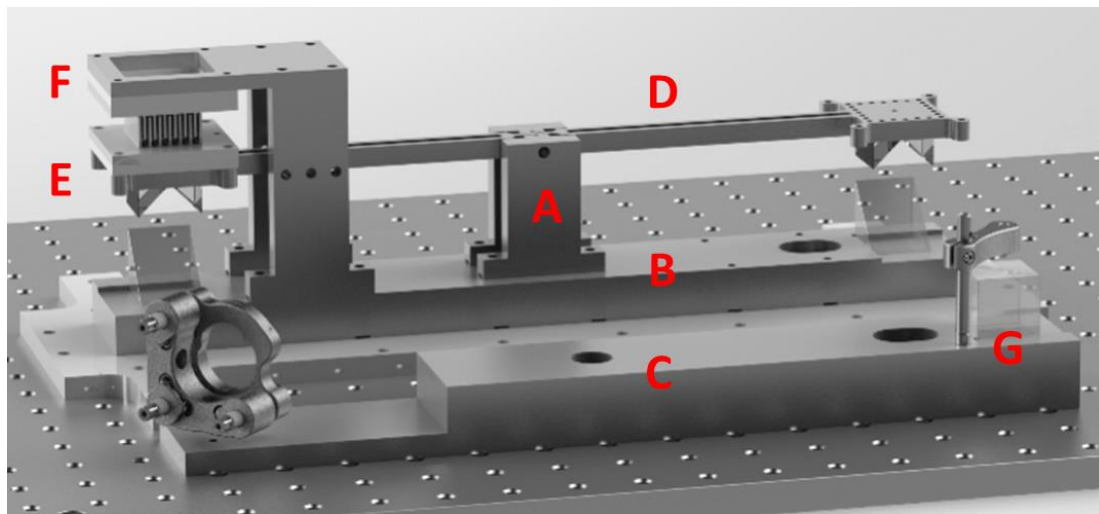


**Figure 26.** A CAD model of the balance assembly.

Position (A) in figure 25 shows the vertical mounting blocks which hold the torsional spring. The spring is mounted into the moving part of the assembly, the balance beam (D), which on the upper right hand side has a small mechanical breadboard for mounting substrates and systems under test and on the upper left hand side has the grounded electrostatic fin (E) mounted to it. The lower left and right hand parts of the beam hold retroreflectors which return beams from the two measurement arms (figure 22) at 180 degrees. The balance base plate (B) holds 90 degree mirrors on its left and right hand side to rotate the beams from the two measurements arms toward the rest of the optical assembly. The base plate has approximate dimensions of 350 mm x 50 mm x 18 mm. The base plate also holds two vertical blocks which

## System Design

mount the isolated, positively supplied electrostatic fin (F). The optics base plate (C) is used to recombine the two measurement arms at the beam splitter (G).

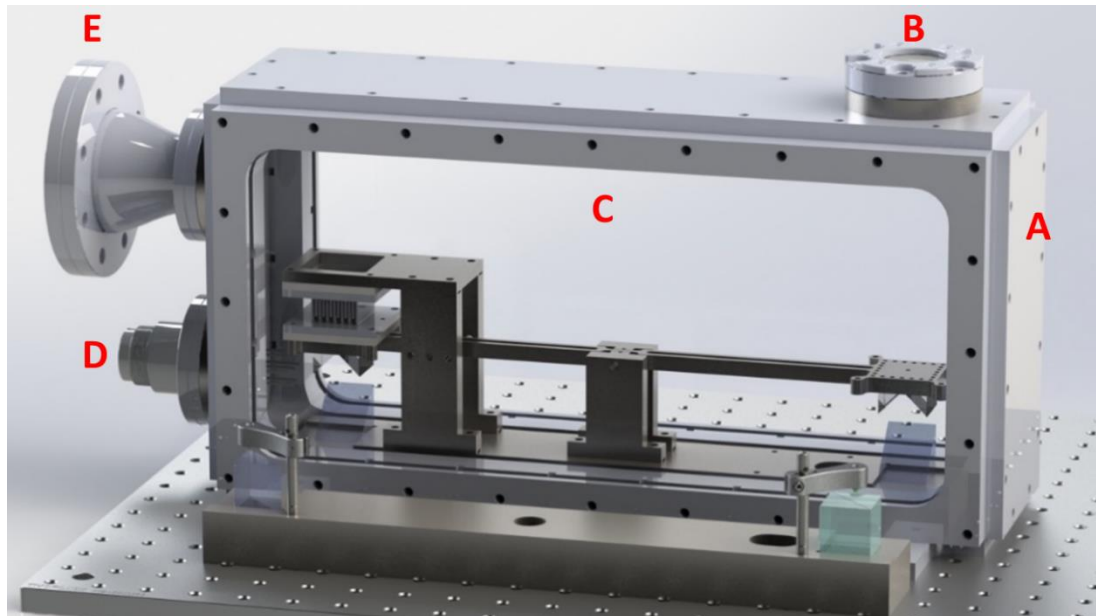


**Figure 27.** A CAD model of the chamber assembly.

Position (A) in figure 27 shows the front of the chamber assembly, which consists of a one piece aluminium structure with o-ring grooves machined into its external faces. The configuration can be seen looking inside the chamber assembly in figure 27, with approximate dimensions of 400 mm x 200 mm x 100 mm. The chamber assembly has been designed modularly, so that all of the sealing faces which consist of simple polished aluminium plates, can be exchanged on-demand. A 1.5" UHV window is installed at (B) for laser beam delivery onto the balance beam. (C) shows the position of the glass windows installed on the large chamber faces to allow the interferometer laser to pass through and holographic camera to image across any interaction volume as required. (D) shows the high-voltage, high-current instrumentation feedthrough initially dedicated to the calibration system. (E) shows the vacuum system inlet.

### 5.1.4.2. Optical

The angular interferometer optical design is shown in figure 28. A randomly polarised helium neon laser is used due to its excellent wavelength stability, a parameter critical for high precision fringe measurements. The beam is passed to the polarising beam splitter PBS1 mounted on the optics base which separates the S and P components to run along each measurement arm. Arm 1 going to retroreflector RR1 has additional mirrors to equalise its path length with arm 2 and RR2. A close to equal path length between measurement arm increases the fringe contrast, which essentially makes the fringe signal larger and therefore easier to measure. The beams in both arms travel to their respective retroreflectors and are

## System Design

returned - it is the relative change in distance between these arms that create the interference signal. The beam travelling along each measurement arm will vary between S and P state, but end up in the same state they left PBS1 in. The beams are returned to PBS1 encoded with the relevant information, but they cannot interfere as the S and P states cannot mix at a polarising beam splitter. This kind of arrangement is known as an optical isolator, which is being used to avoid creating the sensitive interference pattern until further downstream. From PBS1 the two beams are reflected off mirror M8 into a quarter wave plate, which creates a left handed and right handed circularly polarised beam from the S and P states respectively. Both beams are then split through a normal beam splitter NPBS with 50:50 intensity. One path, channel 1, reaches PBS2, which works as a polarising analyser and produces signals 1 (0 degrees) and 2 (180 degrees) which are picked up by photodetectors PD1 and PD2 respectively. PBS3 is angled at 45 degrees relative to PBS2 so that signals in channel 2 have a phase shift of 90 degrees relative to the other channel, producing signals 3 (90 degrees) and 4 (270 degrees), which are picked up by photodetectors PD3 and PD4 respectively.

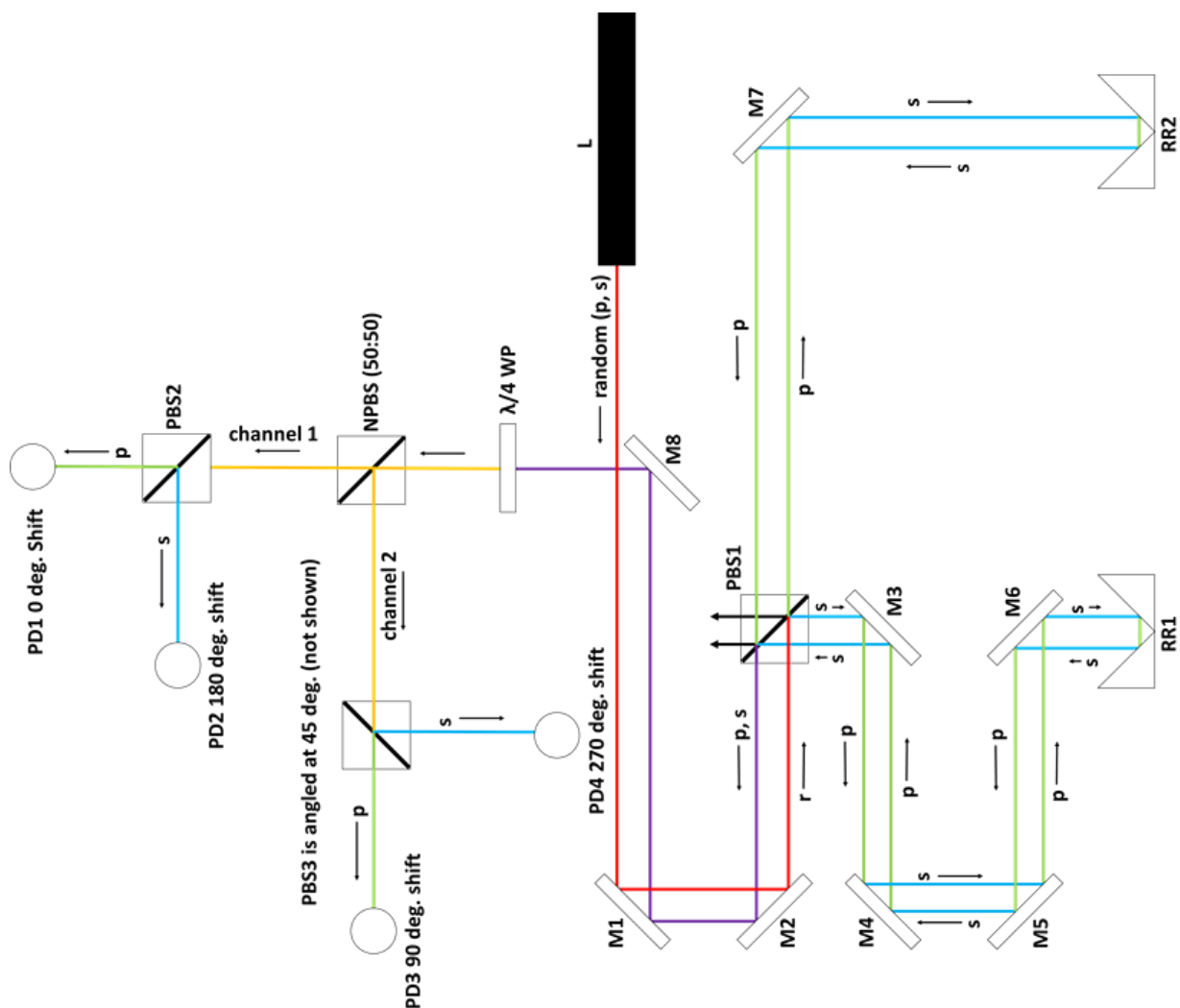


**Figure 28.** Schematic of the interferometer optical train.

## System Design

### 5.1.4.3. Electrical

Electronics are required to condition the signals produced by the interferometer for measurement. The electronics consist of four main sections; the quadrature encoder, which receives the signals, filters, amplifies and compares; the quadrature decoder, which produces a count from the encoded signal; the power supply, which provides power to all the components; and the microcontroller, which logs or sends data to a local PC. The electronics were developed using a prototyping board once the balance was assembled.

### 5.1.4.4. Vacuum

A three stage vacuum pumping system shall be installed so that vacuum applications, such as propulsion, and general low noise conditions without air currents can be reached. The pumping system shall consist of a roughing pump, turbomolecular pump and ion pump. The roughing pump is used to achieve base pressure of around  $10^{-3}$  mbar. The turbomolecular pump is designed to take over from around  $10^{-2}$  mbar up until around  $10^{-8}$  mbar. The ion pump shall be used from  $10^{-6}$  to  $10^{-8}$  mbar when the lowest noise conditions in vacuum are required, as it contains no moving parts and therefore does not contribute to noise. An assortment of vacuum pipes, fittings, valves, and gauges are required to operate such a system. The vacuum system design shall not be specified in this work as it can be considered standard practice

### 5.1.4.5. System

The CAD for the mechanical and optical components is shown in figure 29. A system schematic, shown in figure 30, was created to give an overall understand of how the system will work and what additional hardware and software might be required. The vacuum system has been designed to operate on a standalone circuit for simplicity. The vacuum pump electronics shall serve as a control unit for turning pumps on and off, monitoring the chamber pressure, monitoring environmental data and logging. The calibration system requires approximately 675 V to provide forces into the range of  $10^{-4}$  N.s. Power supplies can be externally commanded by a waveform generator to generate forces and impulses for calibration, however it is well known that the response time of high voltage power supplies are particularly slow, being on the order of tens of milliseconds. This would not allow for waveforms with periods less than the settling times to be produced, as waveforms would become increasingly distorted with decreasing period. A high voltage pulse generator can be used to mitigate this problem. The waveform generator can then be used to command the power supply and pulse generator whilst be controlled by a PC. The interferometer electronics shall also be output data to the PC in the form of the position count with respect to time. An oscilloscope shall also be incorporated for monitoring the alignment and speed of fringes as well as fault finding.

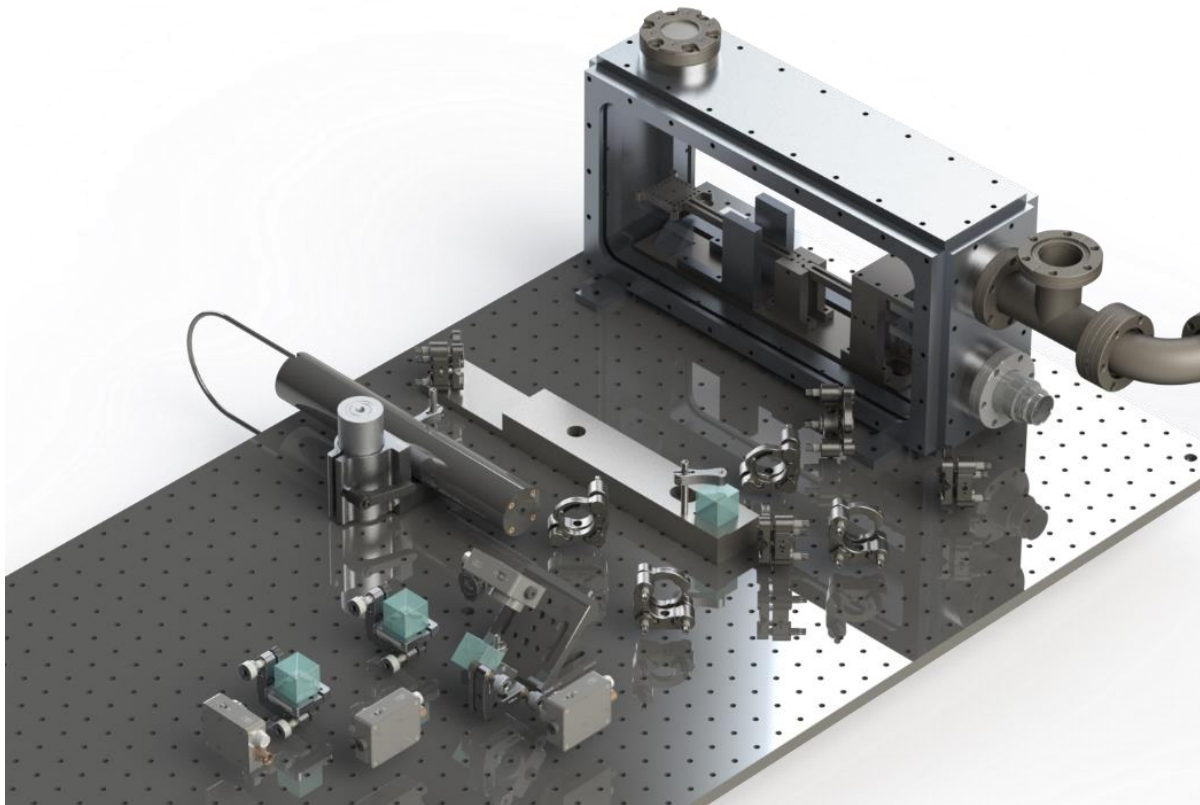


**Figure 29.** A CAD model of the mechanical and optical assemblies.

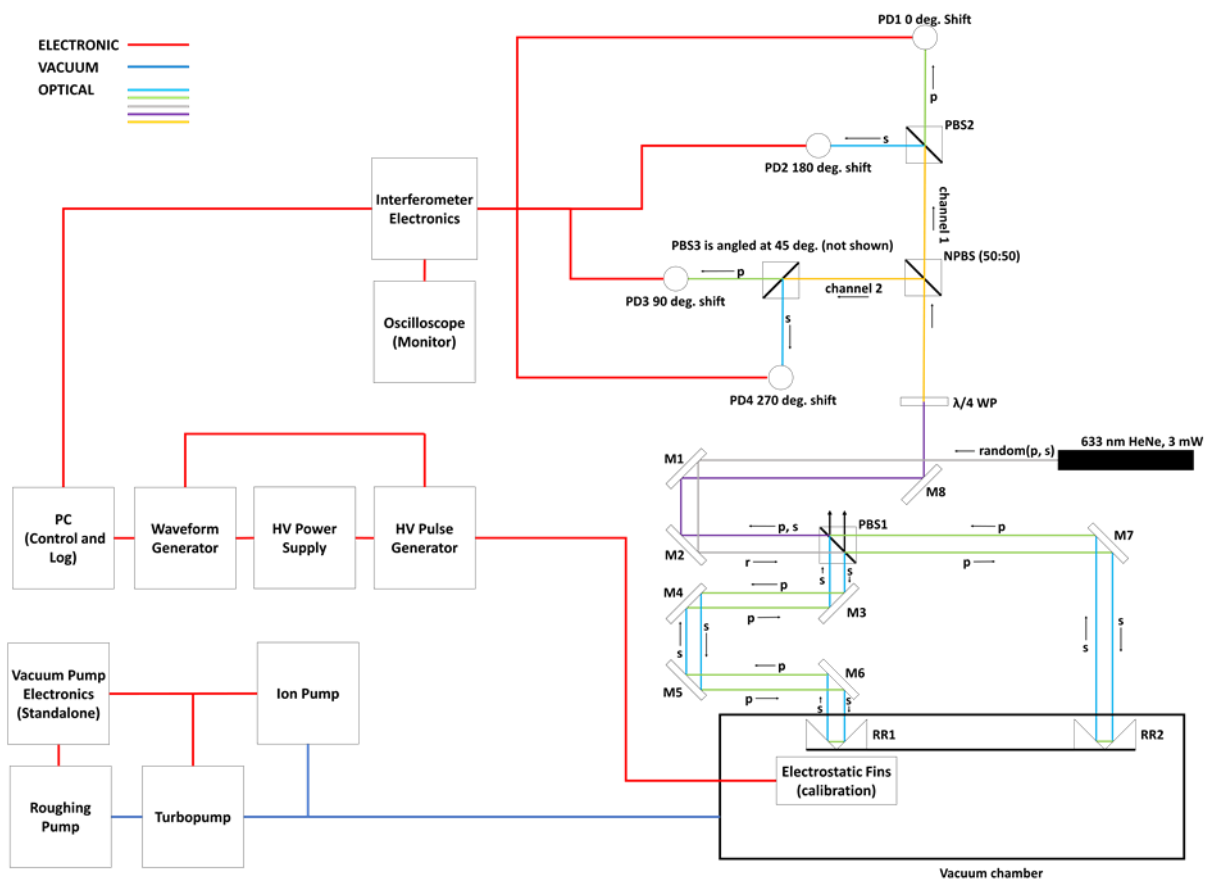


**Figure 30.** Simplified balance system schematic. Including key mechanical, optical, electronic, vacuum and auxiliary components.

## 6. Experimental Design

### 6.1. Calibration and Characterisation

The entire balance system, shown in figure 31 and 32, was assembled. The MATLAB code used to resolve force, impulse and mass flow rate is shown in appendix 2. The supporting electronics were developed in parallel - a circuit schematic, board design and bill of materials can be found in appendix 3a – 3d, 4 and 5 respectively. The code used to command the microcontroller in the electronic system is shown in appendix 6. Appendix 7 provides more detail about the design and development of the instrument. The balance performance can now be assessed in accordance with 4.1 and an experimental setup designed as required by research objective 2.

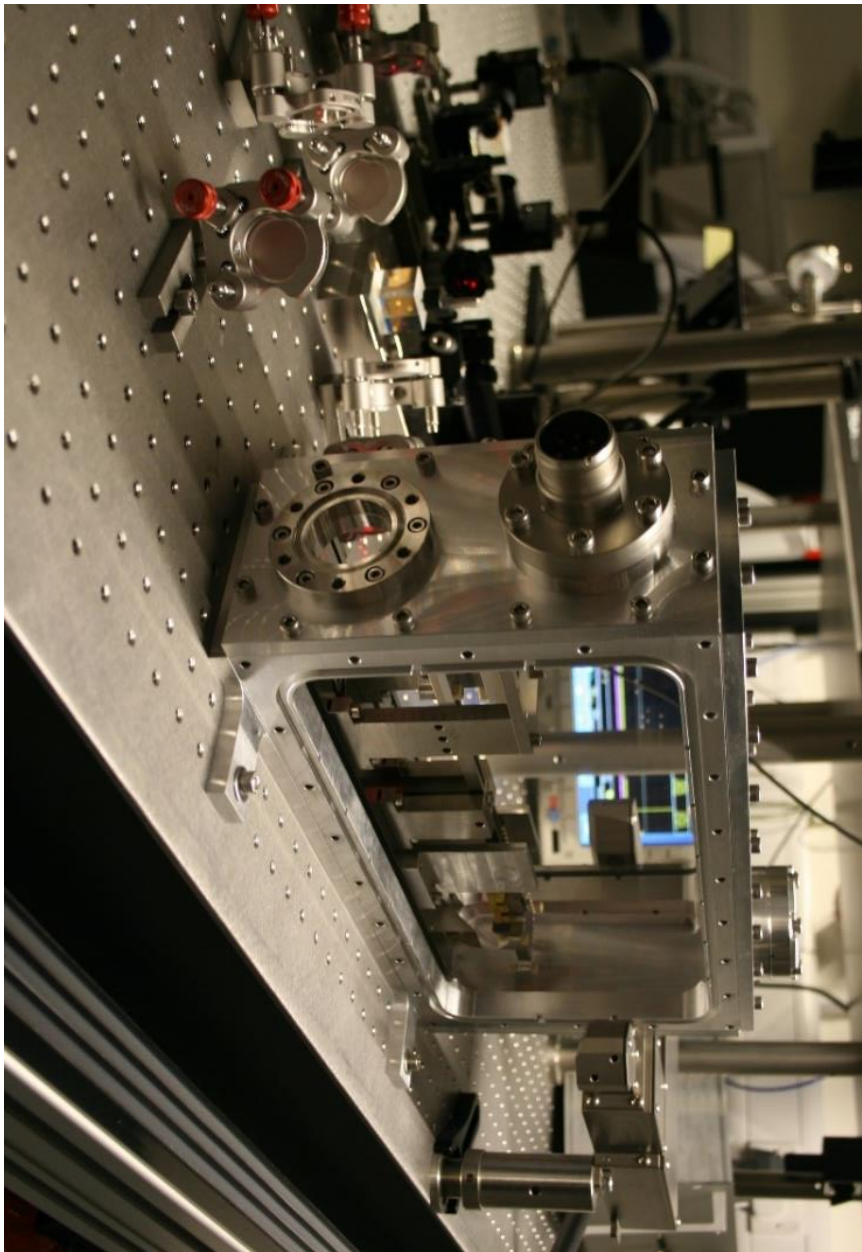


**Figure 31.** An image of the partially assembled balance and interferometer assembly.

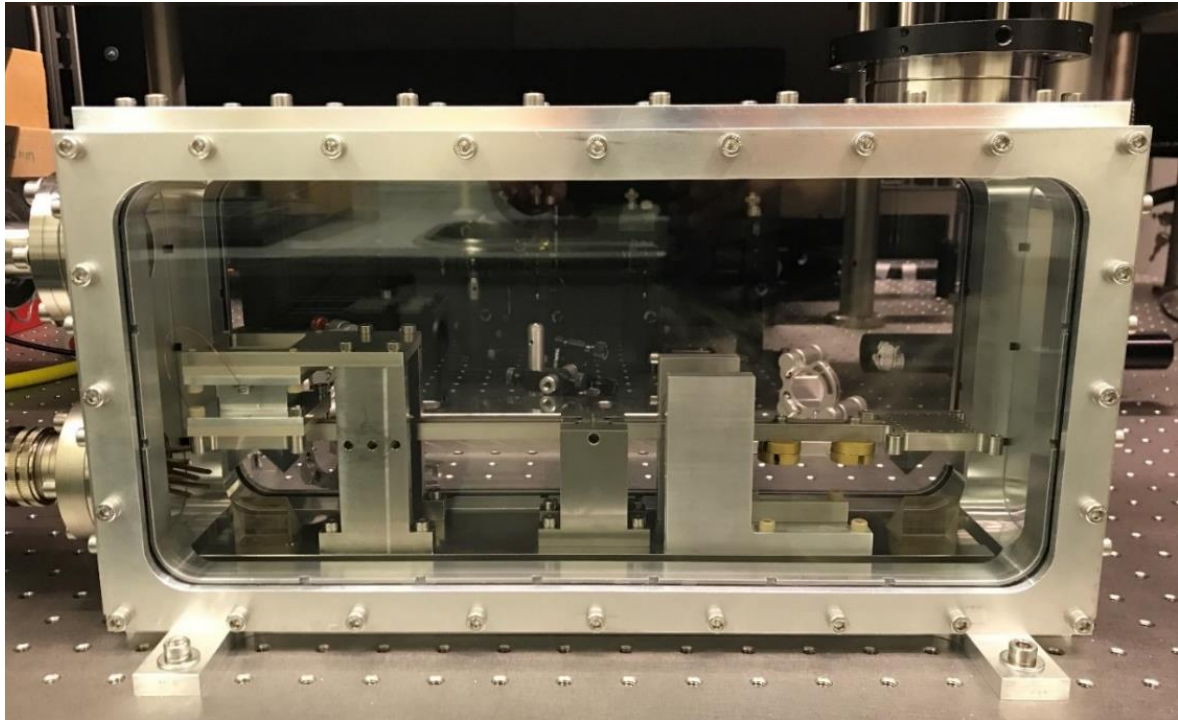


**Figure 32.** An image of the assembled balance with feedthrough connections.

### 6.1.1. Resolution

As described in 5.1.2, this corresponds to  $\lambda/16$  in quadrature mode resulting in  $39.5 \text{ nm} \pm 2\%$ .

### 6.1.2. Sensitivity

A C-Flex CD-20 torsional spring with a nominal torsional spring rate of  $0.03884 \text{ N.m/rad}$  was selected to mount the balance beam. Once mounted into the balance assembly with a beam with moment of inertia equal to  $0.00491 \text{ kg.m}^2$  the spring rate was measured at  $0.03237 \text{ N.m/rad} \pm 2.2\%$  using the logarithmic decrement method. This corresponds to  $1 \text{ m}$  of deflection for every  $1.225 \text{ N}$  of force experienced.

### 6.1.3. Noise Floor

This was measured under three different conditions; low vacuum with optical bench stabilisation on; low vacuum with optical bench stabilisation off; and no vacuum with optical bench stabilisation on. The results are shown in figure 3 in the form of power spectral density, which shows the level of force noise at different frequencies. The noise floor above  $3 \text{ Hz}$  remains at  $\sim 10^{-8} \text{ N}$  for all cases. The noise floor with the table on at both low vacuum and atmospheric pressure remain similar at frequencies below  $3 \text{ Hz}$ , moving from  $10^{-7} \text{ N}$  at  $0.1 \text{ Hz}$  to almost  $1 \times 10^{-6} \text{ N}$  at  $0.03 \text{ Hz}$ . The noise floor with the table off at low vacuum shows a significantly lower noise floor, moving from  $10^{-8} \text{ } \mu\text{N}$  at  $0.1 \text{ Hz}$  to almost  $10^{-9} \text{ N}$  at  $0.03 \text{ Hz}$ . The results indicate that the noise environment is generally better with the stabilisation off. Further tests are required to show how noise changes from atmospheric pressure to high vacuum.

# Experimental Design

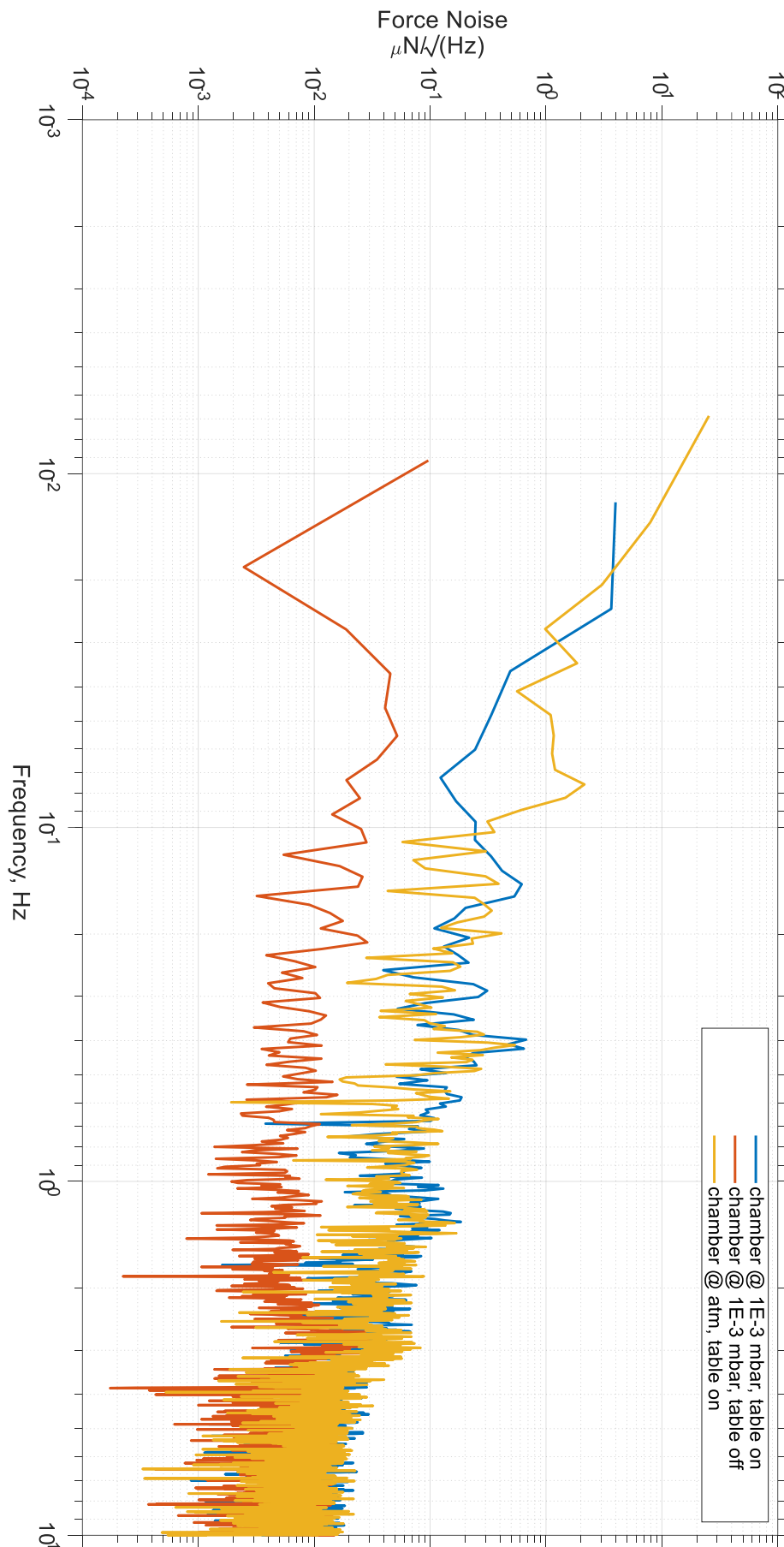
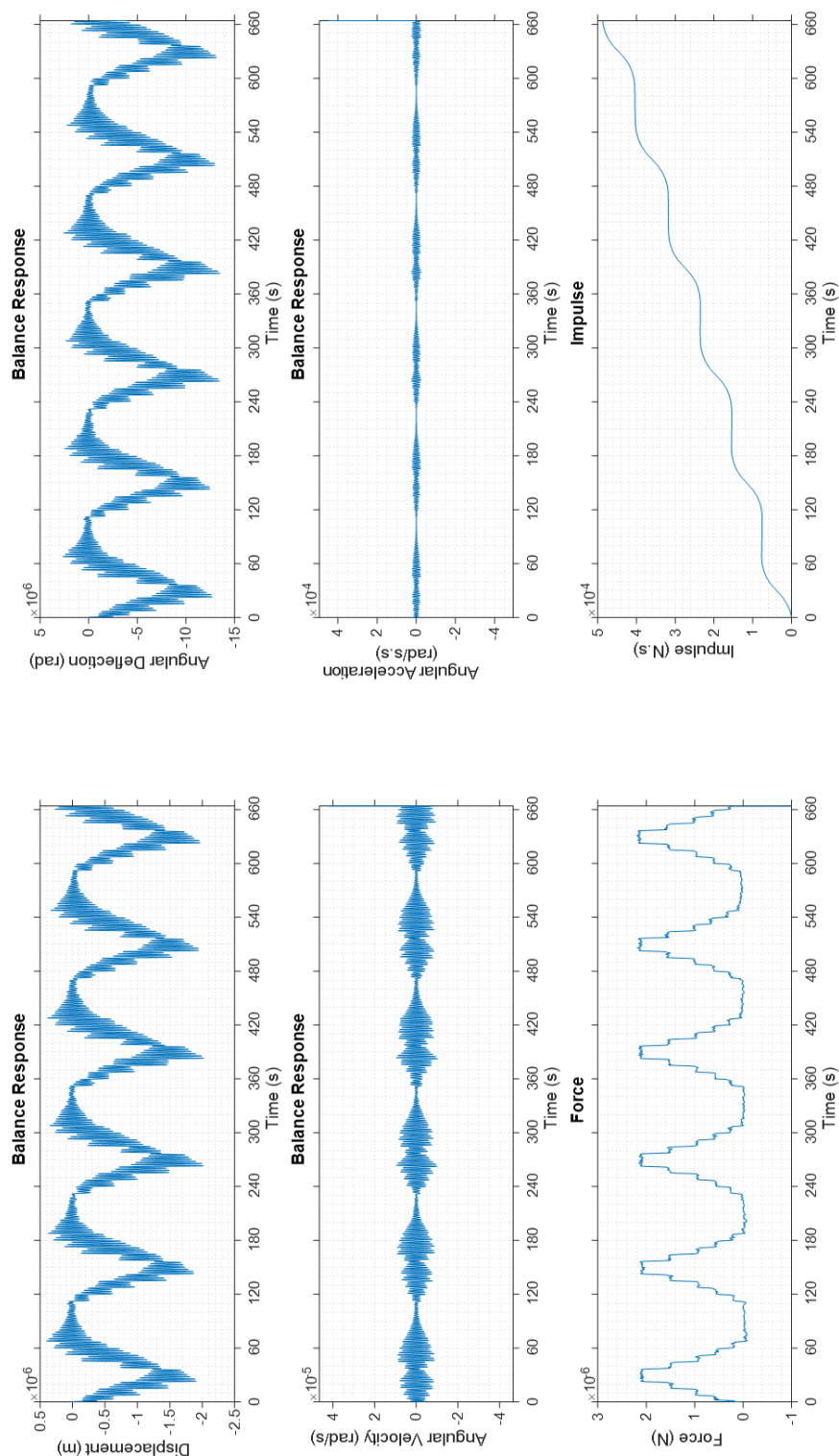


Figure 33. Balance noise floor measurements taken when no forces are applied to the balance.

## Experimental Design

### 6.1.4. Repeatability

This has yet to be determined, as an insufficient quantity of data has been gathered. The normal approach used to determine repeatability in propulsion testing is to produce a ramp up and ramp down force input over extended periods of time. This is demonstrated in figure 34 using ramps with varying forces between 150 nN and 2000 nN and a period of 120 s.



**Figure 34.** A force and impulse measurement taken with the balance.

## Experimental Design

### 6.1.5. Range

On the lower end this is dependent on the noise floor, which ranges from  $1 \times 10^{-9}$  N to  $1 \times 10^{-6}$  N. Under typical experimental conditions under atmospheric pressure with the table off, it is expected that this will be no more than  $5 \times 10^{-8}$  N on average. On the upper end the range is limited by angle at which the beam can move before the electrostatic fin assemblies make contact. This has been experimentally determined using the previously specified moment of inertia of  $0.00491 \text{ kg.m}^2$  to be  $0.0012$  N.

### 6.1.6. Accuracy

**Table 2.** An uncertainty budget for the balance and electrostatic fin system for calibration.

Quantity	Unit	Description
dr	m	Balance beam length from centre to point of action
dM	mg	Mass balance
dm	mg	Traceable mass
dV	V	Electrostatic fin calibration voltage
dg	m	Electrostatic fin gap/width, g/w
dh	m	Electrostatic fin engagement height, l
dl	$\text{kg.m}^2$	Moment of inertia for balance beam and mounted parts
dT	N.m/rad	Effect of temperature on spring rate
dp	N.m/rad	Effect of pressure on spring rate

**Table 3.** An uncertainty budget for balance and logarithmic decrement methods for calibration.

Quantity	Unit	Description
dl	$\text{kg.m}^2$	Moment of inertia for balance beam and mounted parts
dλ	nm	Wavelength
dr	m	Balance beam length from centre to point of action

With respect to dimensional measurement, a Vernier calliper could allow for measurements with  $\pm 0.1$  mm accuracy, whilst a metrology report using a CMM on parts under 300 mm length could produce measurements with  $\pm 0.005$  mm accuracy. The calliper would be suitable for determining the uncertainty in engagement height dl after assembly, whilst the CMM would be more suitable for finding the uncertainty in balance beam length dr and electrostatic fin gap/width dg before assembly.

The electrostatic fin uncertainty will depend on how they are characterised. The simplest and most effective technique will be to mount the fins on a precision mass balance and log its

## Experimental Design

voltage – force response. The mass balance can be calibrated to traceable standards using traceable weights. The overall uncertainty would then be a combination of mass balance uncertainty  $dM$ , and weight uncertainty  $dm$ , both of which can be found on the supplier's website. For example, the uncertainty on a 1 mg /  $1 \times 10^{-6}$  N class 7 mass is  $\pm 0.02$  mg /  $\pm 2 \times 10^{-7}$  N according to Troemner. The uncertainty in electrostatic fin calibration voltage, can be determined using a digital multimeter, which will add its own uncertainty  $2dV$  due to the squared dependence on voltage of the fins according to equation 66.

The uncertainty in moment of inertia  $dI$ , for the balance beam assembly can be calculated using CAD information combined with measurement after manufacturing. The moment of inertia is a product of mass and dimension. An uncertainty in moment of inertia of 5% shall be assumed for any bulky, complex targets mounted to the balance, whilst an uncertainty of 1% shall be assumed for simple targets such as wafers. Even though this is much higher than the combined uncertainty of the callipers and mass balance, counterweights will be required on the opposite side of the balance to centre the balance and their position can only be measured in-situ which compounds errors on both sides of the balance when being input into the CAD system. Also, the measured mass of each component will not take changes in density or centre of mass into account further adding errors.

The uncertainty in natural frequency  $d\omega$  is a function of the uncertainty produced by the interferometer. The uncertainty from the interferometer is however directly proportional to the distance  $r$  and the wavelength of light  $\lambda$  being used. As such the wavelength of the light must be measured and the uncertainty from the spectrometer,  $\delta\lambda$ , assessed. The uncertainty on spring rate due to changes in temperature and pressure can be found by characterising the spring under different conditions and finding the corresponding difference in spring rate. This would be a complex and lengthy undertaking and shall be left out of this analysis. The total uncertainty is the square route of the sum of all uncertainties squared [76], [84], [107], as shown using equation 68 for electrostatic fins and equation 69 for logarithmic decrement. The state of the art  $7 \times 10^{-9}$  nN.s balance previously mentioned has been able to demonstrate a minimum uncertainty of  $\pm 9\%$  [104].

$$\frac{\partial k}{k} = \sqrt{\left(\frac{dI}{I}\right)^2 + \left(\frac{dr}{r}\right)^2 + \left(\frac{dM}{M}\right)^2 + \left(\frac{dm}{m}\right)^2 + \left(\frac{2dV}{V}\right)^2 + \left(\frac{dg}{g}\right)^2 + \left(\frac{dh}{h}\right)^2} \quad (68)$$

$$\frac{\partial k}{k} = \sqrt{\left(\frac{dI}{I}\right)^2 + \left(\frac{dr}{r}\right)^2 + \left(\frac{d\lambda}{\lambda}\right)^2} \quad (69)$$

## Experimental Design

The total uncertainty with electrostatic fins was found to be  $\pm 10.3\%$  as shown in equation 70 below using a HR-200 mass balance, Troemner class 7 mass, AIM-1705 digital multimeter, CMM reports for all manufactured components and an assumed uncertainty of 1% for moment of inertia. This could be reduced to  $\pm 1.8\%$  using a mass balance and calibration weights with an order of magnitude less uncertainty.

$$\frac{\partial k}{k} = \sqrt{\left(\frac{0.5 \times 10^{-4}}{5 \times 10^{-3}}\right)^2 + \left(\frac{5 \times 10^{-6}}{0.3}\right)^2 + \left(\frac{0.1}{1}\right)^2 + \left(\frac{0.02}{1}\right)^2 + \left(\frac{2 \times 0.6}{1000}\right)^2 + \left(\frac{5 \times 10^{-6}}{3 \times 10^{-2}}\right)^2 + \left(\frac{1 \times 10^{-4}}{9 \times 10^{-3}}\right)^2} \quad (70)$$

The wavelength of the selected 632.8 nm, 4 mW helium neon laser was measured over a 6 hour period to determine its value and stability. An Ocean Optics USB4000 spectrometer with an uncertainty of  $\sim 2\%$  was used [108]. It was found that the wavelength did not vary during this period of time and remained at a fixed value of 632.79 nm, shown in figure 35.

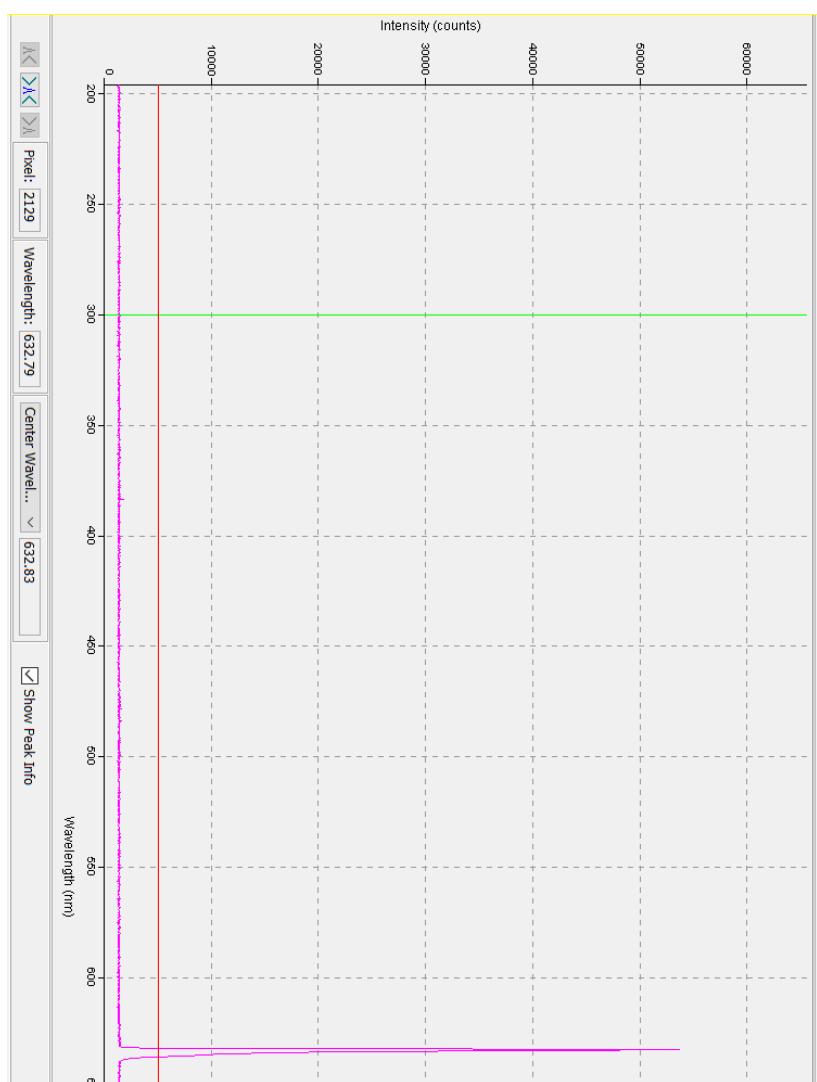


**Figure 35.** Interferometer laser wavelength and stability measurement. Wavelength is displayed on the X axis and intensity count is displayed on the Y axis with 16-bit resolution.

## Experimental Design

The wavelength of the laser shall therefore be taken as  $632.79 \text{ nm} \pm 2\%$ . Using the logarithmic decrement method, the total uncertainty was found to be  $\pm 2.2\%$  as in equation 71, assuming an uncertainty in moment of inertia uncertainty equal to 1%.

$$\frac{\partial k}{k} = \sqrt{\left(\frac{0.5 \times 10^{-4}}{5 \times 10^{-3}}\right)^2 + \left(\frac{5 \times 10^{-6}}{0.3}\right)^2 + \left(\frac{12.7}{632.8}\right)^2} \quad (71)$$

In order to use the electrostatic fin system, it must first be characterised to understand its voltage – force behaviour. As mentioned in 5.1.3, electrostatic fins are chosen over electrostatic plates as they typically do not follow the  $1/L^2$  dependence which unfavourably propagates uncertainty in force. The experimental setup was as follows: a pair of electrostatic fins were constructed using dimensions taken from figure 24. The positive fin is mounted on a 3-axis micrometre stage and aligned above the ground fin which has been firmly mounted to the grounded HR-200 mass scale assembly, as shown in figure 36. A Vernier calliper was then used to align the fins with respect to each other in all 3 axis.

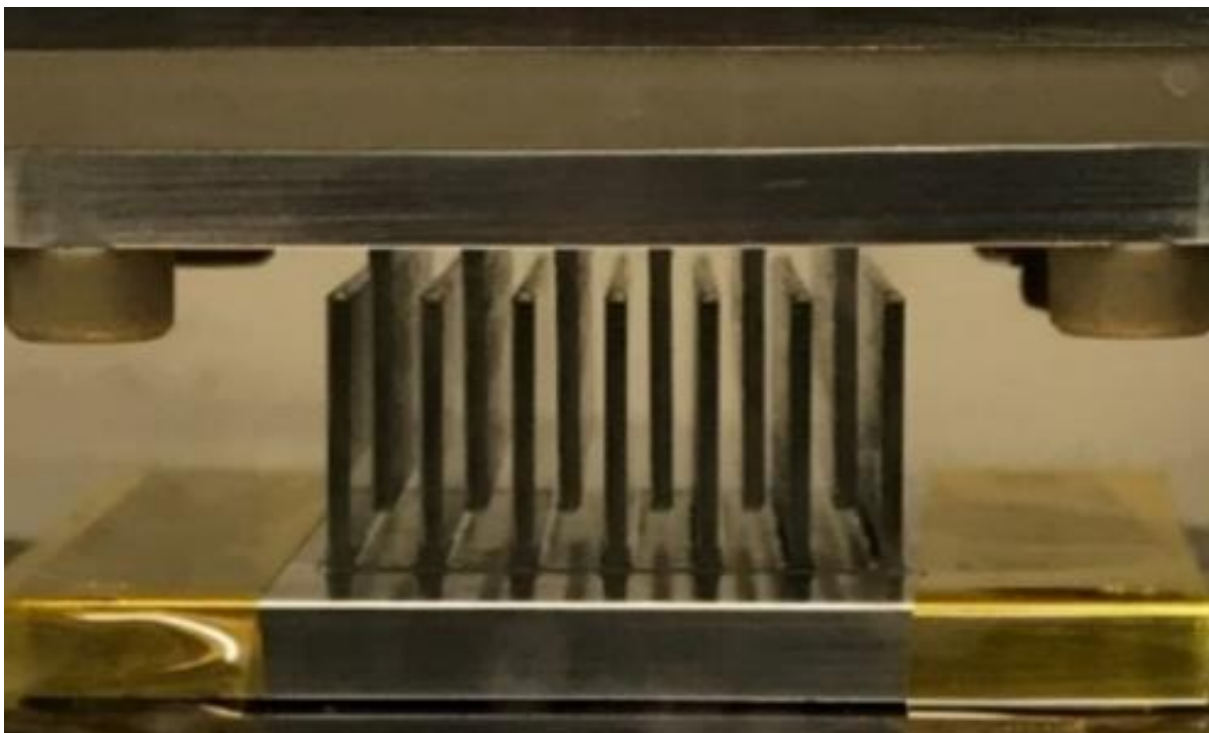


**Figure 36.** An image of the electrostatic fin pairs mounted and engaged.

The driving voltage is provided by a Stanford PS310 power supply and monitored using an Aim TTi 1075 multimeter. As the negative voltage is increased, the repulsive force between the fins increases. The power supply was then used to vary the voltages between 0 V and -1250 V by ramping up and down and in some cases by random selection, which were logged using the multimeter. The force was directly read from the balance and logged. This

## Experimental Design

procedure was repeated 3 times for each engagement height. The results are shown in figure 37. Whilst the relationship between force and voltage increase proportionally as expected the relationship between force and engagement height does not vary linearly.

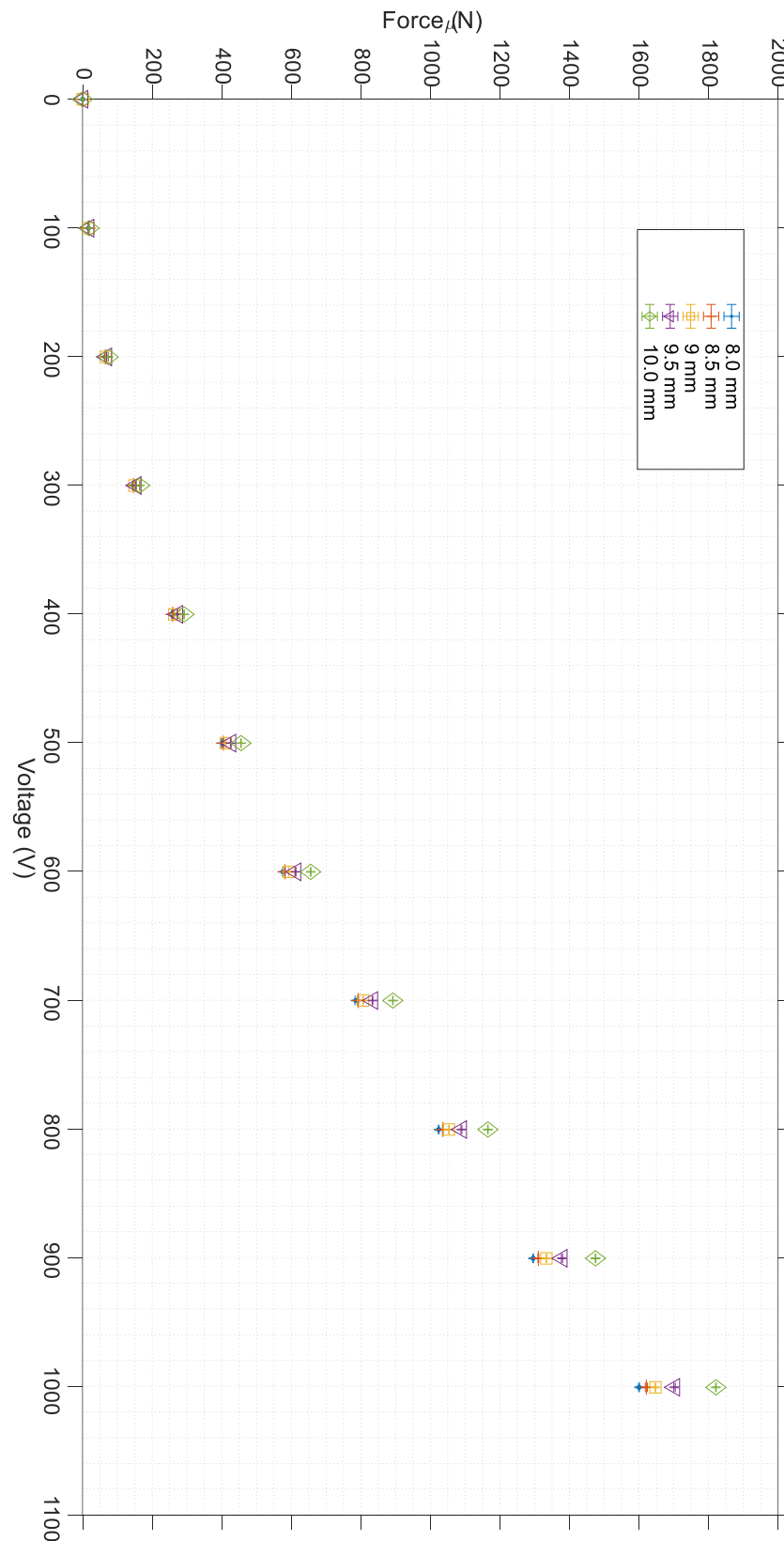


**Figure 37.** A plot of force against voltage at different electrostatic fin engagement heights.

## Experimental Design

Figure 38 illustrates this more clearly as the force at a set voltage does not remain constant for different engagement heights. The dependence therefore lies between  $1/L$  and  $1/L^2$ .

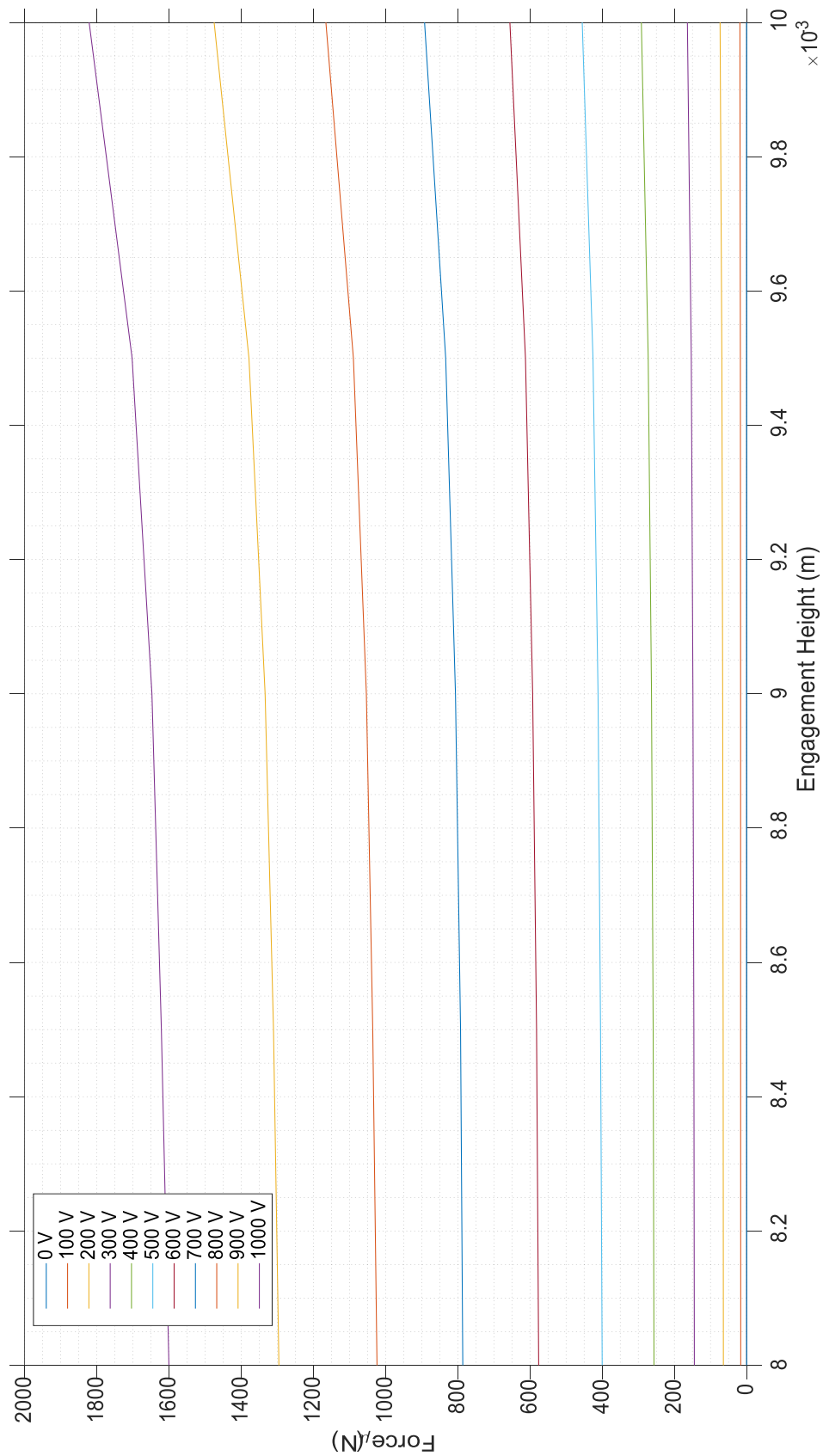


**Figure 38.** A plot of force against engagement height at fixed voltages.

## Experimental Design

An equation was then generated to obtain the specific relationship describing the behaviour of the electrostatic fins. This was achieved using the curve fitting tools available in MATLAB to find the result with the greatest fit and lowest residuals. The electrostatic fins were found to follow a 5<sup>th</sup> order polynomial equation shown below.

$$y = p1*x^5 + p2*x^4 + p3*x^3 + p4*x^2 + p5*x + p6 \quad (72)$$

Where  $y$  represents the force in micronewtons and  $p$  represents the voltage. The polynomial constants are as follows:  $p1 = 7.257e-15$ ,  $p2 = -2.8097e-11$ ,  $p3 = 3.5416e-08$ ,  $p4 = 0.0017282$ ,  $p5 = -0.00119$ ,  $p6 = -0.060258$ . This result indicates that the uncertainty will be higher again than shown in equation 70, but only by  $\pm 0.2\%$  as the measurement uncertainty  $dh$  has in the worst case of  $1/L^2$ , doubled. In any case the logarithmic decrement method shall be used in experiments for ease of use and low uncertainty. Any data presented in the results section shall possess an uncertainty of  $\pm 2.2\%$  which will not be visually represented on graphs due to its low magnitude.

### 6.2. Materials for Processing

In addition to being relevant to the applications described in section 1, the materials used in the processing trials should be both widely used in industry and academia so that general material and processing behaviour is already well understood, useful and relevant. As laser processing is conducted across various industries for a wide range of purposes it will also be important to choose a range of materials which cover different functions e.g. metals, plastics, and semi-conductors. The following materials were selected for their varying properties.

**Table 4.** A summary of materials and their properties to be used in experimental light-matter interaction trials [109]–[111]. The properties are relevant to those discussed in 2.2 which highlight how different properties cause different interaction behaviours.

Material	Structure	Optical Absorption Depth, $d$ @ 1.064 $\mu\text{m}$	Surface Roughness, $R_a$	Refractive Index, $n$	Extinction Coefficient, $k$
Aluminium 1050	Crystal	$10^1$ nm	0.4 $\mu\text{m}$	0.97	10.12
PVC Black	Polymer	$10^5$ nm	0.4 $\mu\text{m}$	1.53	$7.47 \times 10^{-7}$
Silicon <100>	Crystal	$10^5$ nm	0.001 $\mu\text{m}$	3.55	$8.34 \times 10^{-5}$

#### 6.2.1. Aluminium

Aluminium is one of the most abundant metals on Earth. It takes the form of a white-silver metal which is non-magnetic and very ductile in its purer forms. Due to its low density and

## Experimental Design

corrosion resistance, it is typical alloyed, producing some of the most important structural materials used today across countless industries. As a result of its widespread use it is also commonly used in different processes involving lasers: cutting, welding, surface texturing, machining etc. With respect to propulsion, aluminium makes an ideal propellant as it is dense and highly energetic, being able to provide low-thrust but high-efficiency [112]. A set of 3 inch diameter, 2 mm thick, 1000 series aluminium samples were prepared by CNC machining and mechanical automated polishing. The polishing was used to remove the majority of surface scratches and achieve an  $R_a$  of 0.4  $\mu\text{m}$  or better. This value was chosen as it is the same baseline value of  $R_a$  measured on the stock PVC targets in 6.2.2. A sample is shown in figure 39 below.

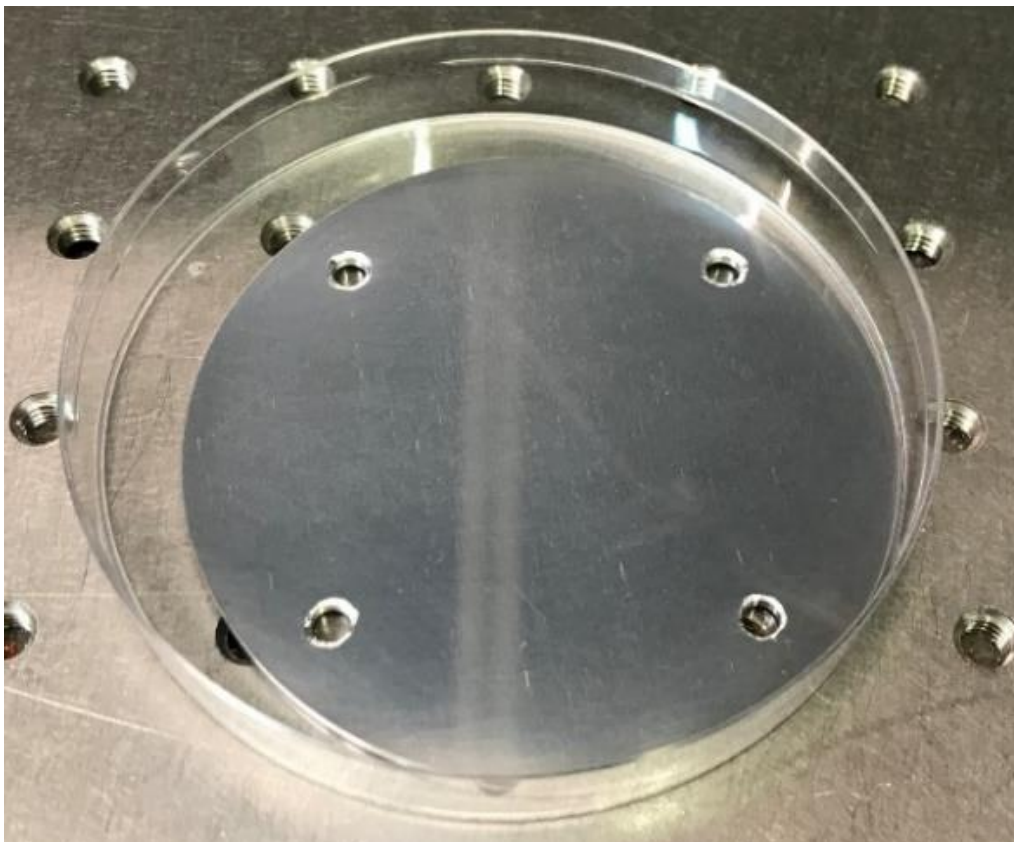


**Figure 39.** Aluminium sample with mounting holes for the force balance arm.

### 6.2.2. Polyvinylchloride (PVC)

PVC is one of the most commonly produced plastics in the World. All-round it is a very useful plastic with modest mechanical strength, melting points and chemical resistance. For this reason, it has a wide range of applications in healthcare, electronics, automotive, aerospace and more. Due to its chemical composition, it does not make a good candidate for laser processing as toxic fumes are produced during thermal processing. It is however a very interesting material for laser propulsion [112], as its lower ablation threshold and deep optical penetration depth enable ablation with lower power lasers. A set of 3 inch diameter, 2 mm

## Experimental Design

thick, black PVC samples were prepared by CNC machining. A sample is shown in figure 40 below.

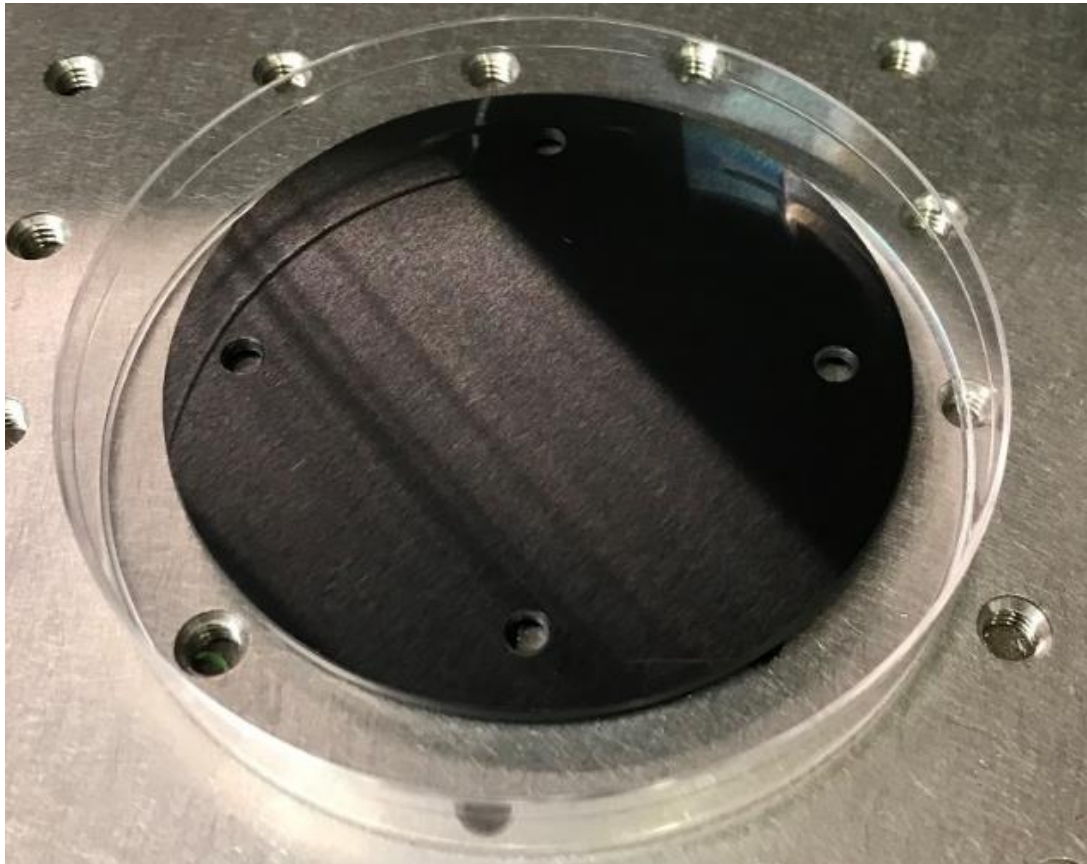


**Figure 40.** PVC sample with mounting holes for the force balance arm.

### 6.2.3. Silicon

Silicon is the second most abundant element on Earth. In its crystalline, processed form, it forms the basis of almost every computer chip and solar cell. It is therefore a very common, but important material. Due to the scale of manufacture required to make the above devices, optical methods are often used for fabrication. This includes laser processing in photolithography. With respect to propulsion, silicon is not an obvious candidate and has never been tested before. As mentioned in 6.1.1, metals often provide high-efficiency, low thrust, and plastics vice-versa. It will be valuable to understand how a semi-conductor behaves under different conditions. A set of 2 inch undoped silicon wafers, single side polished, crystal orientation  $\langle 100 \rangle$  were acquired. A mounting bracket was CNC machined to interface with the force balance arm. Figure 41 shows the setup mounted to the balance.

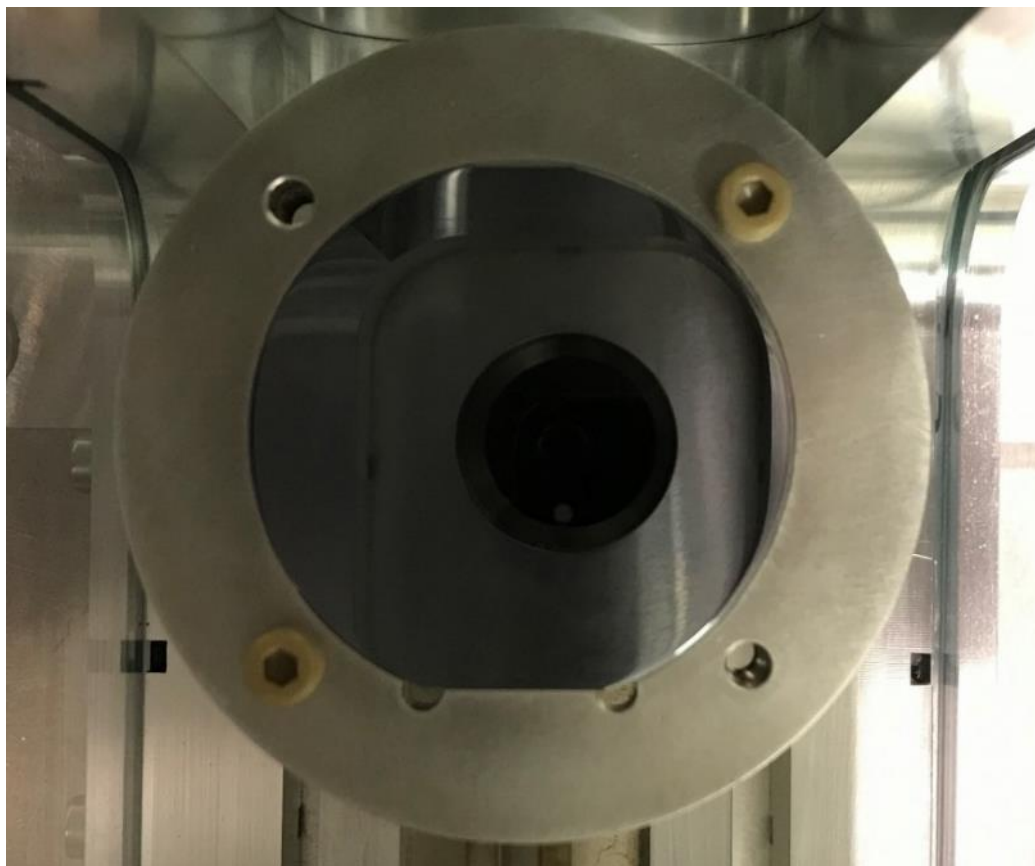


**Figure 41.** A 2 inch silicon wafer mounted to the force balance. Viewed through the laser processing window.

### 6.3. Environment

The type of environment in which a laser-material interaction takes place can have a significant effect on the process and result. The effect of having different gasses during a process is possibly the most industrially relevant. Gases such as nitrogen are often used as shielding gas (gas which protects sensitive equipment close to the processing area and prevents ejected particles from reforming on the substrate surface). This can also have a negative impact on a process, as interactions between the environment and intense laser energy can affect processes by way of producing deposits or altering surface chemistry of a material [113]. Processing gasses can also be used to assist processes [114]. To keep the experiments simple and the outputs relevant the environments in Table 5 have been chosen. The difference in refractive index between the two pressure levels is negligible, suggesting that the same amount of energy and energy density will be delivered to the substrates.

**Table 5.** A summary of processing environments used in experimental light-matter interaction trials. The properties are relevant to those discussed in 2.2.

Medium	Pressure	Temperature	Refractive Index
Air	1013 mbar $\pm$ 10 mbar	294 K $\pm$ 2K.	1.0003
Air	1 x 10 <sup>-8</sup> mbar $\pm$ 5 x 10 <sup>-9</sup> mbar	294 K $\pm$ 2K.	1.0000

## Experimental Design

### 6.3.1. Vacuum

The effect of a very low pressure or vacuum is desirable for applications in space not just because it is a relevant environment and useful for optimising propulsive effects, but also because environments typically offer additional pathways for energy. In terms of laser processing, a vacuum environment is often desirable when conducting ultra-short processes. The high peak power pulses create intense plasmas above samples which can affect machined feature quality and even distort the incoming beam profile [115]. A vacuum environment also helps achieve more precise processing as currents in a liquid or gas media change temperatures and refractive indices etc.

### 6.3.2. Atmospheric Pressure

Atmospheric pressure is the pressure at which most experiments take place because it is the cheapest and easiest environment to use and repeat. 1013.25 mbar is the average pressure in the UK at mean sea level. Experiments shall take place only 6 m above mean sea level.

### 6.3.3. Temperature

As mentioned in 2.2.2.1, an increase in temperature increases optical absorption. Experiments shall be conducted in a laboratory environment with temperature measured at  $294\text{K} \pm 2\text{K}$ .

## 6.4. Laser Systems

Nanosecond pulsed lasers have become the industries' tool of choice for advanced laser processing as they provide many of the benefits that come with short durations, but at low price point relative to picosecond or femtosecond ultrashort alternatives.

### 6.4.1. SPI G4 200 W Nanosecond Fibre Laser

The laser used in this work is based on the SPI G4 platform using a Master Oscillator Power Amplifier (MOPA) fibre architecture. The SP-200P-A-EP-M-L-Y is an experimental laser currently in development for commercial use by SPI. The laser can be evaluated using parameters summarised in 2.1. The lasers overall performance is specified in appendix 6.

The SP-200P-A-EP-M-L-Y has an average power output of 200 W and emits at 1064 nm. The processing wavelength is extremely common because of the gain efficiency of the Nd:YAG gain medium, which allows for significant optical power to be produced. A common wavelength is desirable as it makes the processing results widely relatable. The SP200 is capable of producing pulse energies of up to 5.1 mJ, pulse durations of no less than 2 ns, peak powers as high as 54 kW and repetition rates in the MHz regime. At nanosecond pulse durations the high peak powers make wavelength absorption less of an issue across materials as powers well above ablation threshold can be achieved. This is also desirable as most nanosecond

## Experimental Design

lasers are set to operate in this manner. Furthermore, a high pulse energy and peak power is desirable to produce the maximum possible forces on the force balance with high signal-to-noise ratio measurements above the noise floor.

The laser operates with a degree of polarisation of 20%, and as such shall be considered effectively randomly polarised. The beam quality factor  $M^2$  is between 4 and 6, which means the beam shape differs from an ideal gaussian. However, it shall be assumed that any processing will be done way above ablation threshold and therefore the process shall be driven by pulse energy rather than pulse energy density or peak power density, mitigating the need to measure the lasers spatial profiles.

### 6.4.2. Laser Parameters

The laser parameters are selected to achieve the widest possible range of results so that their effect on kinetic energy ratio, momentum coupling coefficient and mass-loss coefficient can be better understood and linked.

#### 6.4.2.1. Waveform and Pulse Energy

The MOPA configuration enables the system to provide different temporally shaped pulses and therefore different amounts of optical energy delivery over time. The system is able to produce pulse durations between a few nanoseconds and thousands of nanoseconds over a range of pulse energies. As per 2.1.4, this can be effectively used to improve processes. The SP-200P-A-EP-M-L-Y temporal pulse shapes were characterised at 10% output using a Thorlabs DET10A photodetector. A subset of pulse shapes were selected for their wide differences in pulse duration, shown in figure 42.

A selection of waveforms were selected: SW0, SW3, SW5, SW35 and SW40, providing a range of nanosecond pulse shapes with higher peak powers and low pulse duration, through to lower peak powers and higher pulse durations. The highest pulse energy producible across the range of waveforms selected is 2.93 mJ, as per appendix 8 and appendix 9. This pulse energy shall be maintained throughout experiments to maintain an iso-energetic relationship between different parameter sets. The highest possible pulse energy is also picked to ensure the highest signal-to-noise ratio is achieved on the force balance.

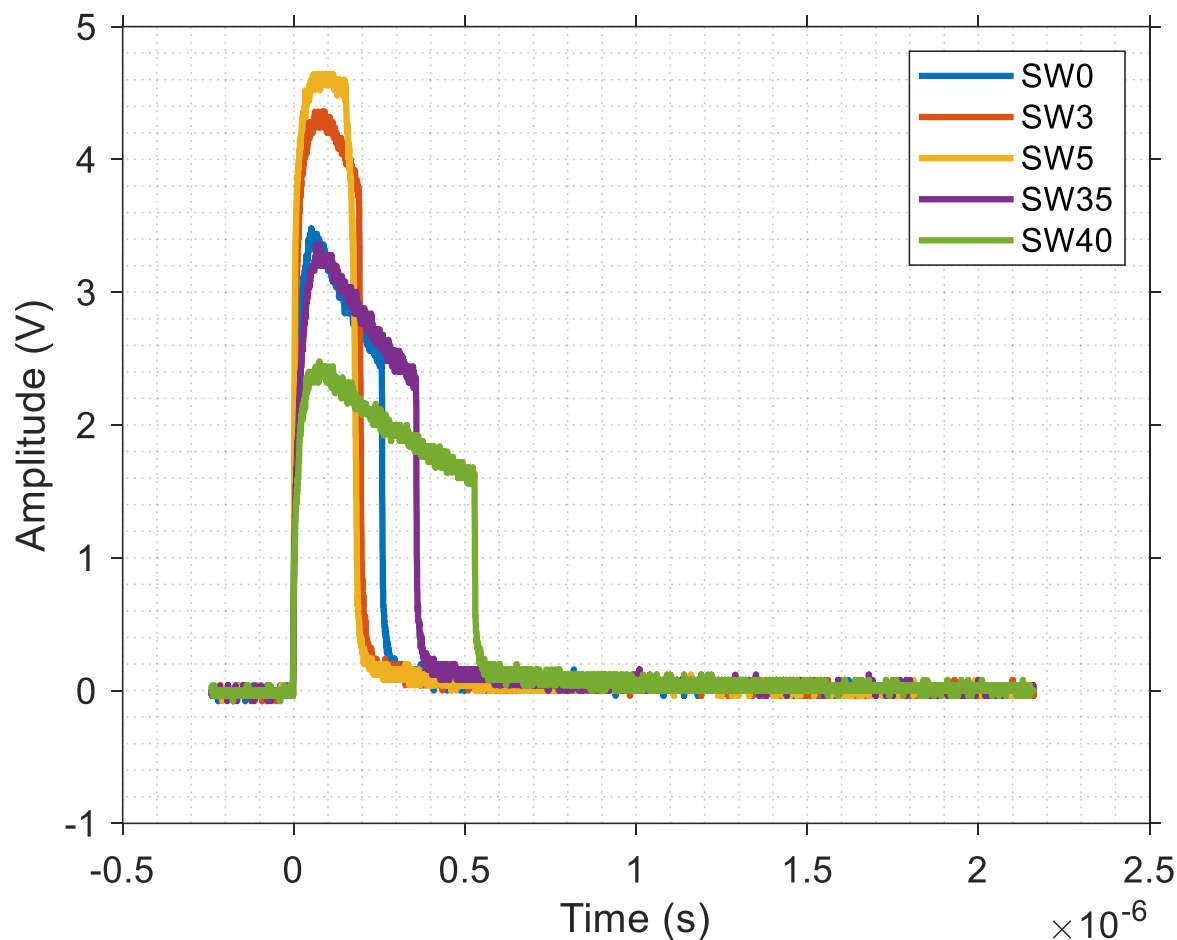


**Figure 42.** A plot showing a subset of pulse shapes measured from the SP-200P-A-EP-M-L-Y laser. The pulse shapes are measured as arbitrary photodiode voltage with respect to time. The pulse shapes were captured using a Thorlabs DET10A photodetector and a 500 MHz Tektronix Oscilloscope.

#### 6.4.2.2. Repetition Rate

According to the datasheet in appendix 6 and 7, and the range of waveforms selected in 6.4.2.1, the highest  $PRF_0$  available is 40 kHz. This shall be maximum repetition rate used in experiments.

#### 6.4.2.3. Total Energy

The number of pulses shall be varied between 20, 40, 80 and 160, giving total energies between 58.6 mJ and 468.8 mJ.

### 6.5. Processing Strategies

It will be useful to compare the kinetic energy ratio, momentum coupling coefficient and ablation efficiency between a process which is always machining over the same spot (similar to laser drilling), and a process which is always machining over virgin material (similar to area machining), whilst changing laser parameters such as pulse duration, pulse shape and repetition rate with the same energy input.

## Experimental Design

The way in which the laser energy is delivered to the substrate is an important factor to consider, as pulses landing on virgin material will interact differently to pulses landing on rough surfaces, melt pools or craters created by a previous pulse. In the former case the energy is spread over a large area which may typically reduce thermal build up and plasma interaction effects. In the latter case many changes to the optical properties of a material may occur as described in 2.2, and if plasma is generated, its physical properties can also cause subsequent pulses to interact as described in 2.3.2. In this case the energy is confined to very small areas, which may allow thermal energy to build up and plasma effects to become more prominent. The above two strategies shall be assessed by comparing:

1. How much input energy is converted into kinetic energy.
2. How effectively momentum is produced.
3. How effectively mass is lost.

Figure 43 below illustrates the two different processing strategies.

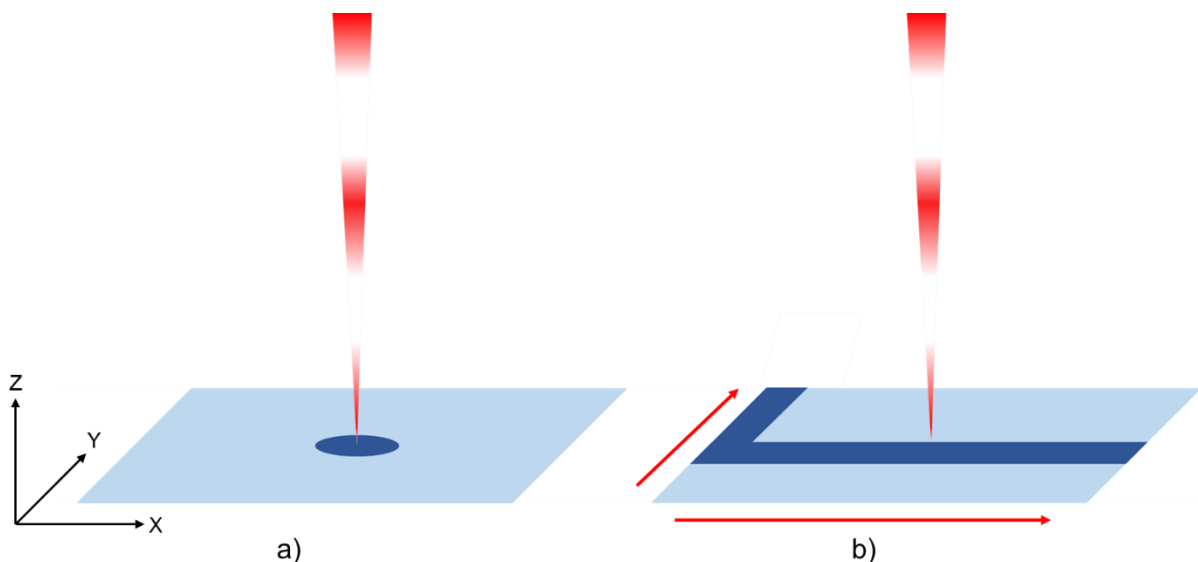


**Figure 43.** A diagram of the proposed processing strategies. A) shows single point processing where the beam is focused into a fixed XYZ position above the substrate. B) shows large area processing where a trench, or multiple trenches are machined to remove an area by scanning the beam in XY position whilst maintaining a fixed focus in Z.

### 6.5.1. Single Point Processing

In this process no constant linear motion is required – the laser must be placed at a fixed focus above the substrate with XYZ adjustment for positioning and re-positioning purposes only. Figure 44 shows an image of the setup.

## Experimental Design

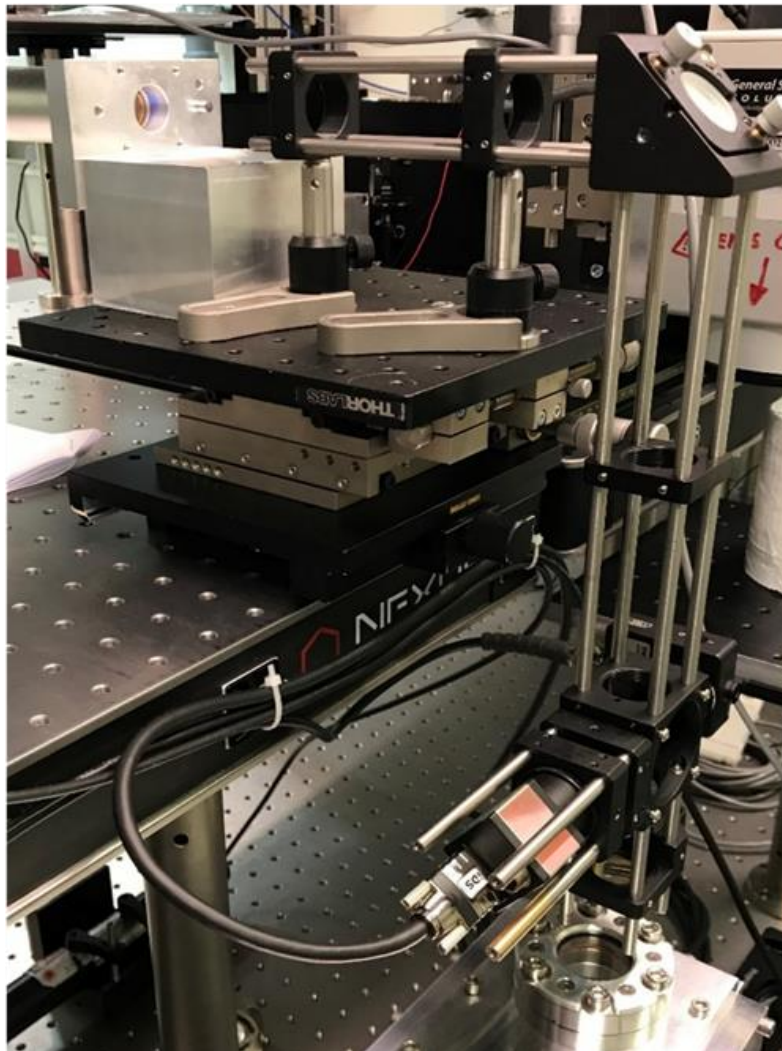
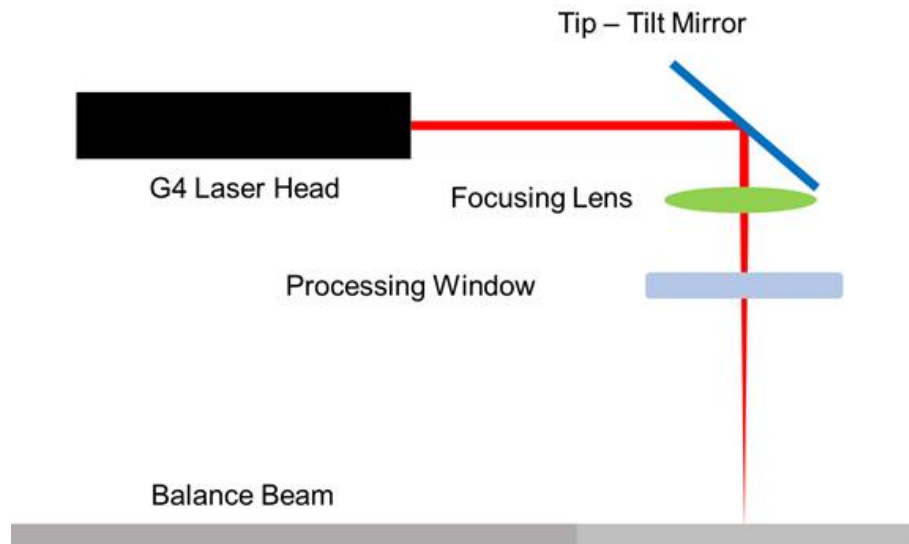


**Figure 44.** An image of the beam delivery system for single point processing. The SPI G4 laser head is inserted into the large aluminium bracket on the top left of the image. The beam (collimated by the laser head) is then reflected through 90 degrees using a mirror, passing through a plano-convex,  $f = 175$  mm focusing lens. The focused beam then travels down into the balance chamber through the laser processing window onto the balance arm where the targets are held. The entire beam delivery system is mounted on a 2-axis linear movement stage for micrometre resolution movement across the sample surface.

## Experimental Design

### 6.5.2. Area Processing

In this process constant linear motion is required in the XY directions, and the laser must be placed at a fixed focus above the substrate with XYZ adjustment for positioning purposes. Figure 45 shows an image of the setup.

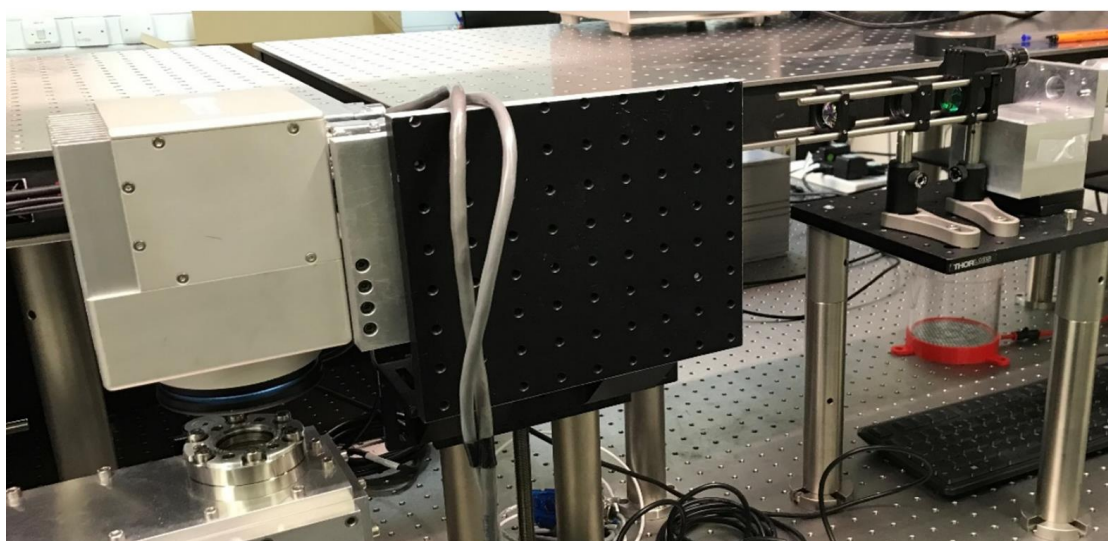
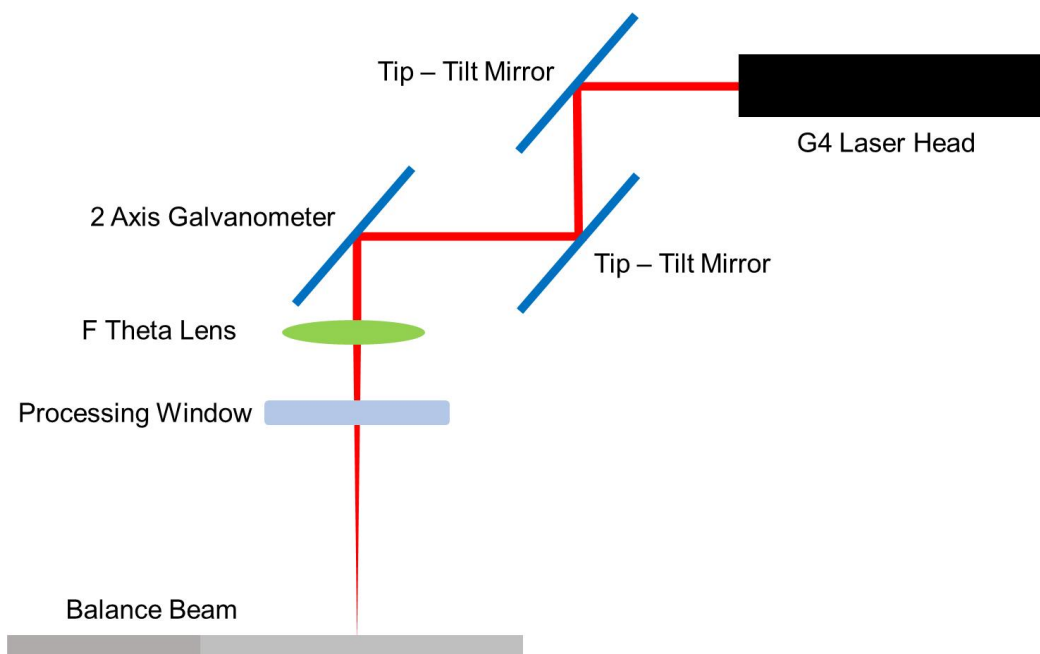


**Figure 45.** An image of the beam delivery system for area processing. The SPI G4 laser head is inserted into the large aluminium bracket on the top right of the image. The beam (already collimated by the laser) is directed into the 2-axis galvanometer mirror head for beam positioning via two mirrors. The beam exits through an  $f = 175$  mm f-theta lens down into the balance chamber through the laser processing window onto the balance arm where the targets are held.

## 6.6. Additional Analysis Tools

### 6.6.1. Optical Microscopy

A stand-alone benchtop microscope was used to inspect samples before and after experiments.

## Experimental Design

### 6.6.2. Scanning Electron Microscopy

A Zeiss cross-beam SEM/FIB system was used to inspect samples after experiments.

## 6.7. Summary of Key Measurement Parameters

The primary output of the force balance is force and mass loss with respect to time. Using these outputs we shall directly assess the following over a range of laser, material and environmental parameters:

- Momentum coupling coefficient,  $C_m$  (N/W). This output describes how effectively force is produced per unit of laser energy in. This parameters is particularly relevant to the energy and space industries where the maximisation of momentum is desirable for triggering reactions or improving the performance of propulsion systems.
- Ablation efficiency,  $C_i$  (kg/W). This output describes how effectively mass is removed from a material per unit of laser energy in. This parameter is particularly relevant to industrial laser based processes which involve laser based material removal on large scales.
- Kinetic energy ratio,  $\beta$ . This output describes the ratio of light-matter interaction plume kinetic energy relative to the laser pulse energy in. This parameter is widely useful as it can be used to determine and compare how well a process has translated laser energy into increased ablation and or momentum.

## 6.8. Experiment 1, Multi-shot Laser Drilling

Assessment of momentum coupling coefficient  $C_m$ , ablation efficiency  $C_i$  and kinetic energy ratio  $\beta$ , according to laser, material, and environmental parameters summarised in 6.

**Table 6.** Experiment 1, single-point, parameter summary. All experiments were repeated 3 times.

<b>Pulse Energy (mJ)</b>	<b>Repetition Rate (kHz)</b>	<b>Waveforms</b>	<b>Number of Pulses</b>	<b>Materials</b>	<b>Environment</b>
2.93	5, 10, 20, 40	0, 3, 5, 35, 40	20, 40, 80, 160	Al, Si, PVC	Air and Vacuum

## 6.9. Experiment 2, Large Area Scanning

Assessment of momentum coupling coefficient  $C_m$ , ablation efficiency  $C_i$  and kinetic energy ratio  $\beta$ , according to laser, material and environmental parameters summarised in 6. This set

## Experimental Design

of experiments focus on a smaller parameter set than in 5.4.7 to reduce the number of data points and experimental workload.

**Table 7.** Experiment 2, areal, parameter summary. All experiments were repeated 3 times.

<b>Pulse Energy (mJ)</b>	<b>Repetition Rate (kHz)</b>	<b>Waveforms</b>	<b>Number of Pulses</b>	<b>Materials</b>	<b>Environment</b>
2.93	5, 10, 20, 40	0, 5, 40	40,000	Al, Si, PVC	Air and Vacuum

The laser and galvo scanner combination are not capable of controlling the number of output pulses. Instead, the marking speed is varied according to the above repetition rate to produce a fixed number of pulses per unit area. The selected processing area is 10 mm x 10 mm, with scanning speeds of 112.5 mm/s, 225 mm/s, 450 mm/s and 900 mm/s corresponding to repetition rates of 5 kHz, 10 kHz, 20 kHz and 40 kHz respectively. The total number of pulses are fixed at 40,000 under this configuration. This produces an 86% overlap which helps ensure significant material removal whilst leaving some virgin material. This is based on a laser spot size of 159  $\mu\text{m}$ , calculated using the laser datasheet in appendix 6 and 7, and processing parameters above.

## 7. Results and Analysis

### 7.1. Effect of Repetition Rate and Pulse Shape

#### 7.1.1. Aluminium

Figure 46 shows  $C_m$  with respect to waveform and repetition rate for the aluminium target in air. Waveforms SW3 and SW5 begin at a value of  $\sim 2.7 \times 10^{-6}$  N/W at 5 kHz and increase to  $\sim 3.7 \times 10^{-6}$  N/W and  $\sim 4.8 \times 10^{-6}$  N/W respectively at 40 kHz. Waveforms SW0, SW35 and SW40 begin at a value of  $\sim 1.6 \times 10^{-6}$  N/W at 5 kHz and increase to  $\sim 2.7 \times 10^{-6}$  N/W,  $\sim 2.3 \times 10^{-6}$  N/W and  $\sim 2.1 \times 10^{-6}$  N/W respectively at 40 kHz. The value of  $C_m$  increases with repetition rate across all waveforms - waveform 5 shows a  $\sim 78\%$  increase in  $C_m$  value from 5 kHz to 40 kHz. Waveforms SW5, SW3, SW0, SW35 and SW40 produce the highest value of  $C_m$  in that order, with the difference in  $C_m$  value between waveforms increasing with repetition rate – there is a  $\sim 1.2 \times 10^{-6}$  N/W difference between SW5 and SW3, and a  $\sim 0.2 \times 10^{-6}$  N/W difference between SW35 and SW40 at 40 kHz. The value of  $C_m$  is therefore dependent on waveform selection and increasing repetition rate for maximum momentum production per unit energy in.

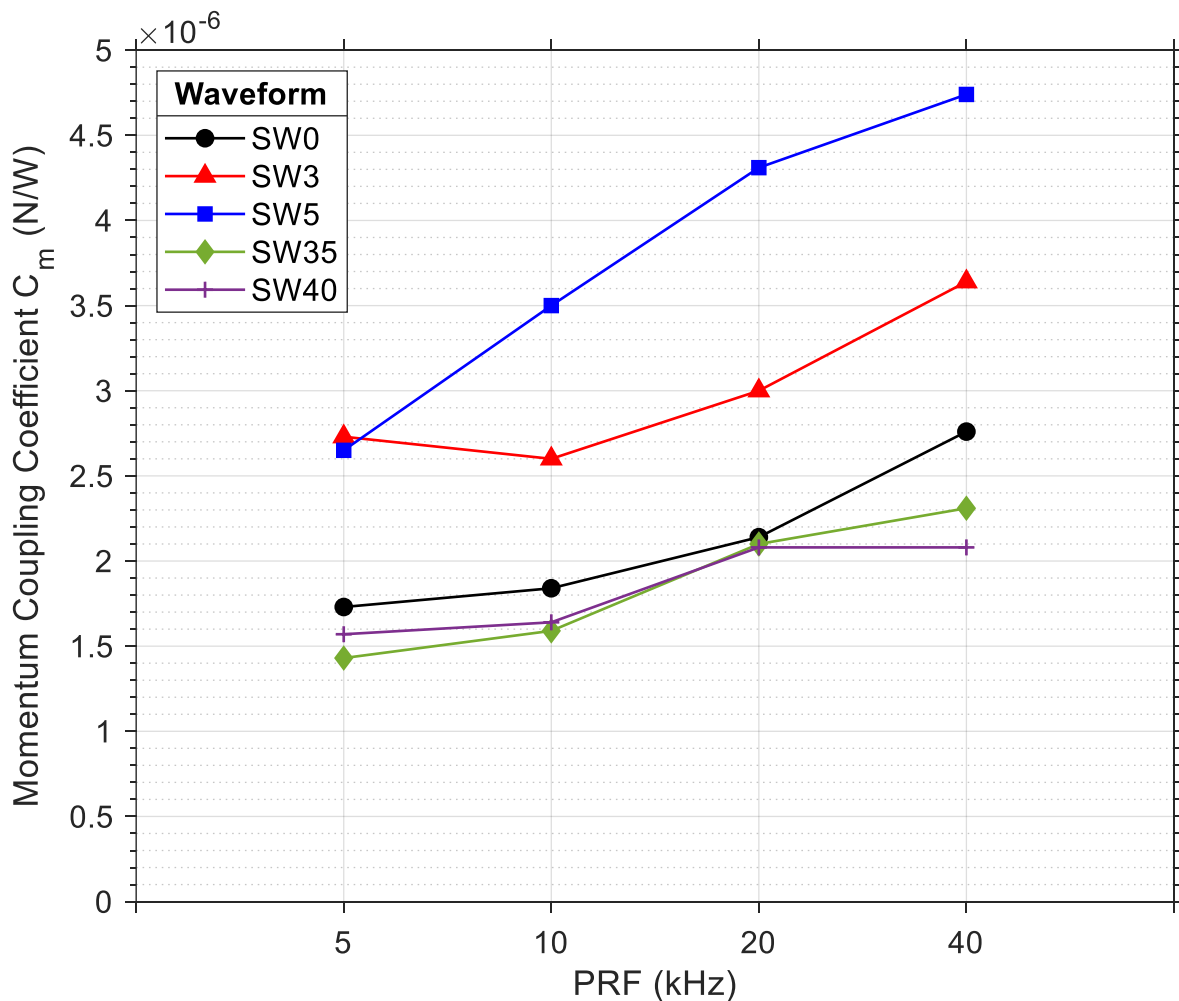


**Figure 46.** A plot of momentum coupling coefficient against waveform and repetition rate for aluminium in air exposed to 160 pulses, or 469 mJ

## Results and Analysis

Figure 47 shows  $C_I$  with respect to waveform and repetition rate for the aluminium target in air. All waveforms approximately begin at a  $C_I$  value of  $0.3 \times 10^{-8} \text{ kg/W} \pm 0.1 \times 10^{-8} \text{ kg/W}$  at 5 kHz. Waveforms SW5, SW3, SW0 and SW35 then reduce in  $C_I$  value at some critical repetition rate before increasing again to  $\sim 1.15 \times 10^{-8} \text{ kg/W}$ ,  $\sim 0.9 \times 10^{-8} \text{ kg/W}$ ,  $\sim 0.75 \times 10^{-8} \text{ kg/W}$  and  $\sim 0.58 \times 10^{-8} \text{ kg/W}$  respectively at 40 kHz. Waveform SW40 does not follow this trend and decreases to a value of  $\sim 0.2 \times 10^{-8} \text{ kg/W}$  at 40 kHz. In general, the value of  $C_I$  therefore increases with repetition rate - waveform 5 shows a  $\sim 283\%$  increase in  $C_I$  value at 40 kHz over 5 kHz. Waveforms SW5, SW3, SW0, SW35 and SW40 produce the highest value of  $C_I$  in that order. The difference in  $C_I$  value between waveforms remains approximately constant at 40 kHz. The value of  $C_I$  is therefore dependent on waveform selection and achieving a critical repetition rate for maximum material removal per unit energy in.

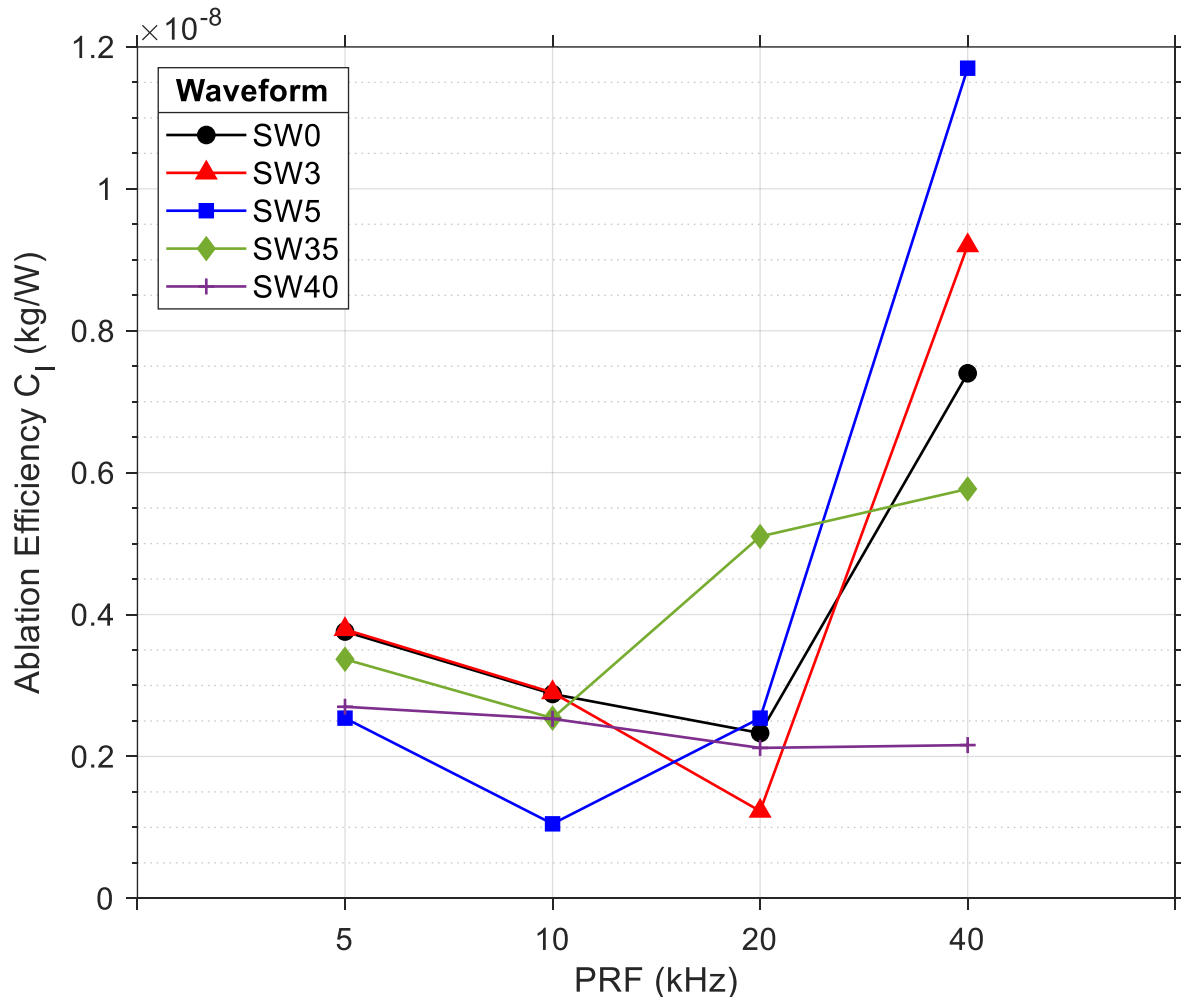


**Figure 47.** A plot of ablation efficiency coefficient against waveform and repetition rate for aluminium in air exposed to 160 pulses, or 469 mJ.

## Results and Analysis

Figure 48 shows  $\beta$  with respect to waveform and repetition rate for the aluminium target in air. Waveforms SW5 and SW3 follow a similar trend, beginning at a  $\beta$  of  $\sim 0.12\%$  between 5 kHz and 10 kHz, before rapidly increasing to  $\sim 0.37\%$  at 20 kHz and dropping to  $\sim 0.19\%$  and  $\sim 0.07\%$  respectively at 40 kHz. SW0 and SW35 follow a different but similar trend, beginning at  $\sim 0.04\%$  at 5 kHz and increasing to  $\sim 0.16\%$  and  $\sim 0.1\%$  respectively at 40 kHz. Waveform SW35 follows a unique trend, whereby an average  $\beta$  of  $\sim 0.04\%$  is maintained throughout all repetition rates except for at 10 kHz where a peak of  $\sim 0.12\%$  is achieved. The value of  $\beta$  is therefore dependent on waveform selection and achieving a critical repetition rate for maximum kinetic energy. The standard deviation has been added to figure 48 to understand if the sudden changes in kinetic energy ratio could be associated to variations in input energy (e.g. pulse train variations, laser thermal stability etc.), rather than variations in the process and interactions. The average standard deviation in the below dataset is 6%, whilst the average across all datasets is  $\sim 4\%$ , with a maximum of  $\sim 8\%$ . Due to the relatively small deviation, this does not seem likely and shall remain out of the remaining data. The instrument uncertainty of  $\pm 2.2\%$  was calculated in 6.1.6 and is also not shown due to its small magnitude.

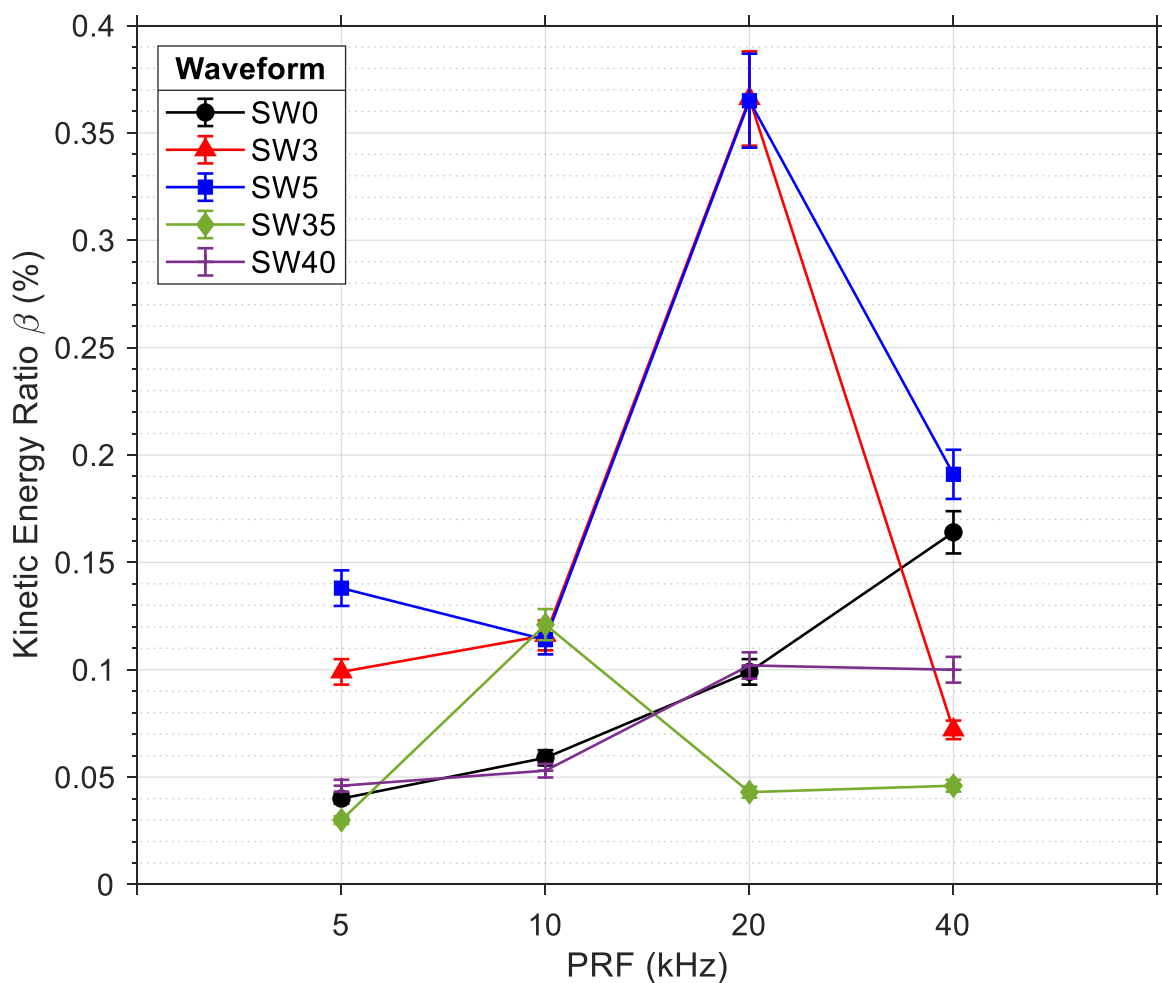


**Figure 48.** A plot of kinetic energy ratio against waveform and repetition rate for aluminium in air exposed to 160 pulses, or 469 mJ.

## Results and Analysis

### 7.1.2. Silicon

Figure 49 shows  $C_m$  with respect to waveform and repetition rate for the silicon target in air. The trend here is very similar to the trend in  $C_m$  for the aluminium target in 7.1.1, whereby the value of  $C_m$  increases with repetition rate - waveform 35 shows a ~54% increase in  $C_m$  value at 40 kHz over 5 kHz. Waveforms SW5, SW3, SW0, SW35 and SW40 produce the highest value of  $C_m$  in that order. The difference in  $C_m$  value between waveforms remains approximately constant from 5 kHz to 40 kHz. The value of  $C_m$  is therefore dependent on waveform selection and increasing repetition rate for maximum momentum production per unit energy in.

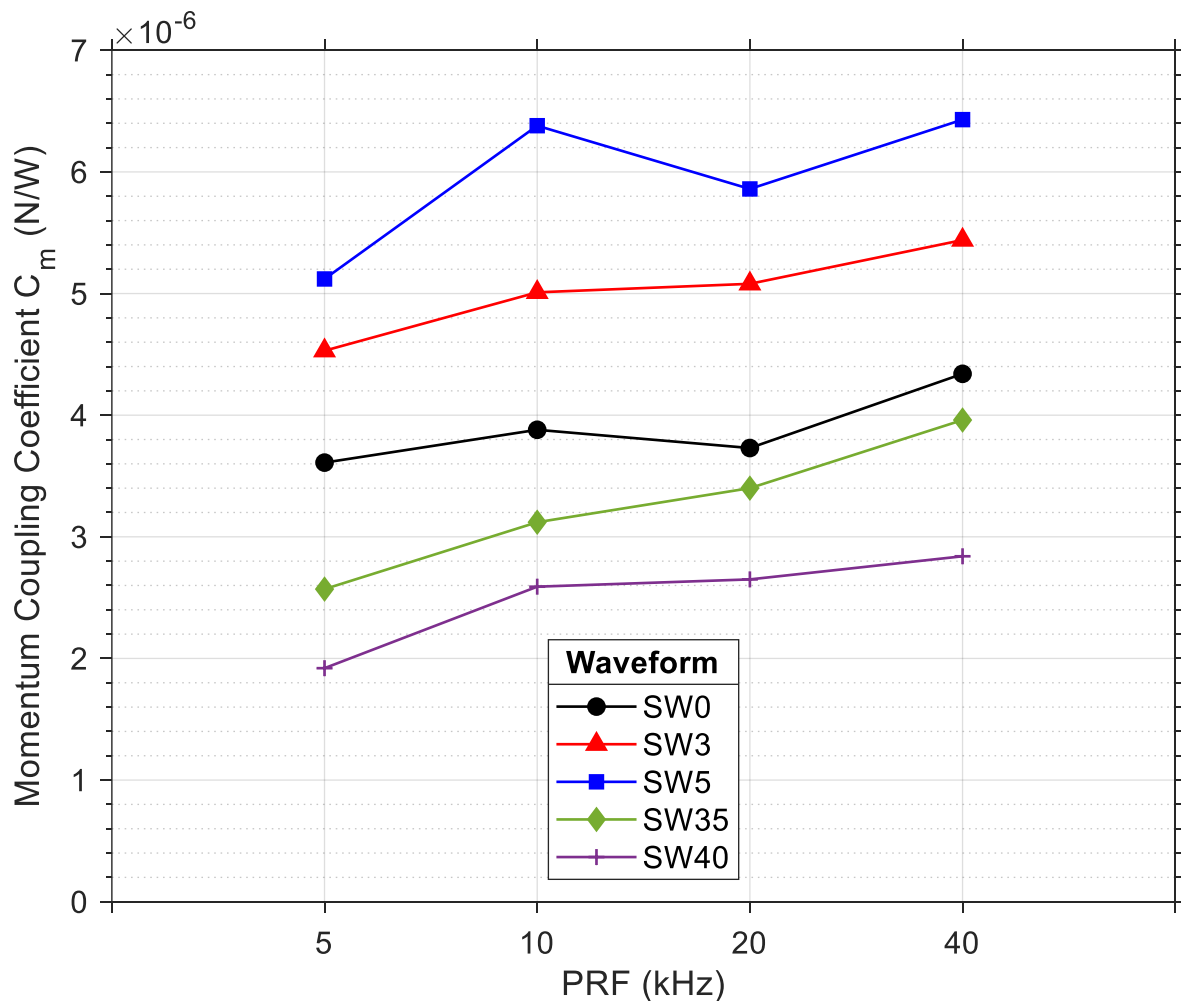


**Figure 49.** A plot of momentum coupling coefficient against waveform and repetition rate for silicon in air exposed to 160 pulses, or 469 mJ.

## Results and Analysis

Figure 50 shows  $C_i$  with respect to waveform and repetition rate for the silicon target in air. Waveforms SW5 and SW35 follow a similar trend, whereby both start at an  $C_i$  value of  $\sim 0.7 \times 10^{-8}$  kg/W at 5 kHz, increasing suddenly to  $\sim 1.1 \times 10^{-8}$  kg/W at 10 kHz and then drop again at 20 kHz where values begin to separate, reaching  $\sim 0.55 \times 10^{-8}$  kg/W and  $\sim 0.4 \times 10^{-8}$  kg/W respectively at 40 kHz. Waveforms SW3 and SW0 following a similar but different trend, whereby both start at a value of  $\sim 0.55 \times 10^{-8}$  kg/W at 5 kHz, decreasing to  $\sim 0.4 \times 10^{-8}$  kg/W at 10 kHz after which the values separate at 20 kHz and come together again at 40 kHz at a value of  $\sim 0.55 \times 10^{-8}$  kg/W. The value of  $C_i$  is therefore dependent on waveform selection and achieving a critical repetition rate for maximum material removal per unit energy in.

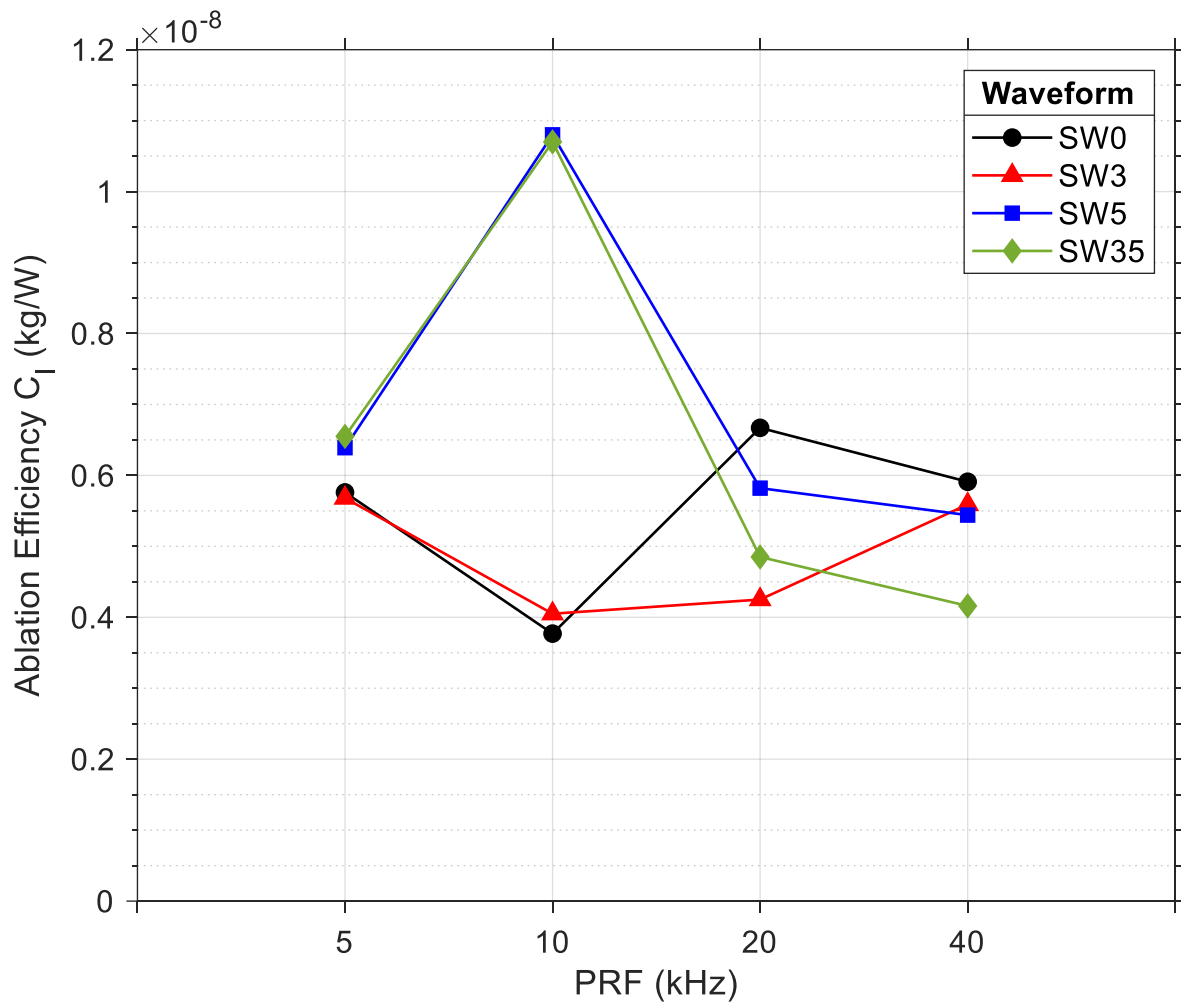


**Figure 50.** A plot of ablation efficiency against waveform and repetition rate for silicon in air exposed to 160 pulses, or 469 mJ. Mass-loss data points for SW40 were not available here.

## Results and Analysis

Figure 51 shows  $\beta$  with respect to waveform and repetition rate for the silicon target in air. The trend between waveforms are varied, with only SW5 and SW35 following a similar trend, beginning at  $\sim 0.2\%$  and  $\sim 0.05\%$  respectively between 5 kHz and 10 kHz, before increasing to  $\sim 0.38\%$  and  $\sim 0.19\%$  respectively at 40 kHz. Meanwhile waveforms SW3 and SW0 increase to a maximum value at some critical repetition rate before dropping again at higher repetition rates. For these waveforms, the critical repetition rate is 10 kHz, whilst for SW5 and SW35 the critical repetition rate seems to be located higher than 40 kHz. The value of  $\beta$  is therefore dependent on waveform selection and achieving a critical repetition rate for maximum kinetic energy.

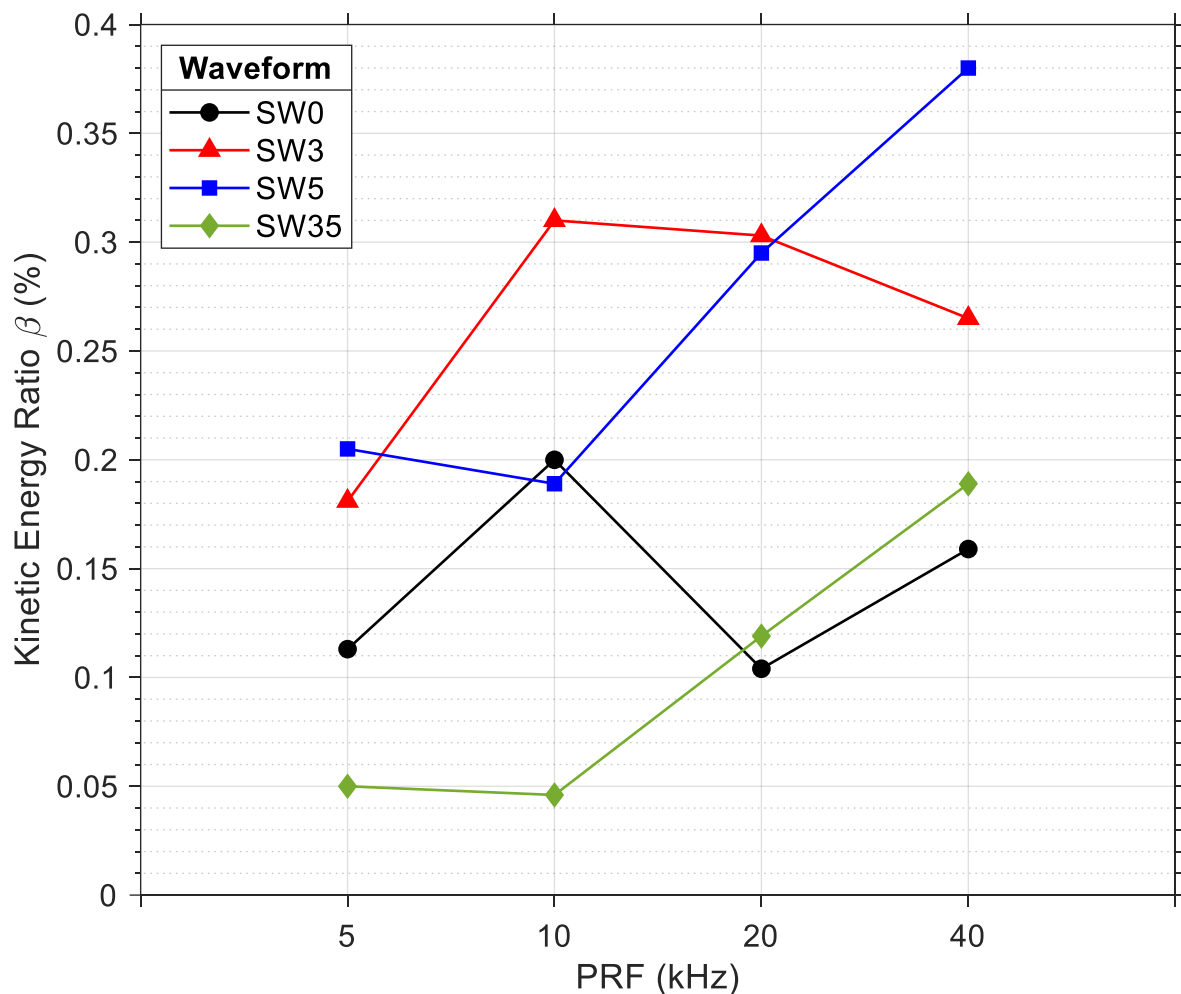


**Figure 51.** A plot of kinetic energy ratio against waveform and repetition rate for silicon in air exposed to 160 pulses, or 469 mJ. Mass-loss data points for SW40 were not available here.

## Results and Analysis

### 7.1.3. PVC

Figure 52 shows  $C_m$  with respect to waveform and repetition rate for the PVC target in air. The trend here is very similar to the trend in  $C_m$  for the aluminium target in 7.1.1 and silicon target in 7.1.2, except here the value of  $C_m$  decreases with increasing repetition rate – on average waveforms show a ~72% decrease in  $C_m$  value from  $\sim 0.9 \times 10^{-5}$  N/W at 5 kHz to  $\sim 0.25 \times 10^{-5}$  N/W at 40 kHz. The order of which waveforms produce the greatest  $C_m$  value varies according to repetition rate. On average waveforms SW5 and SW3 remain greater until between 20 kHz and 40 kHz when they produce the lowest value, and SW35 and SW40 produce the greatest. The difference in  $C_m$  value between waveforms remains approximately constant from 5 kHz to 40 kHz. The value of  $C_m$  is therefore dependent on waveform selection and decreasing repetition rate for maximum momentum production per unit energy in.

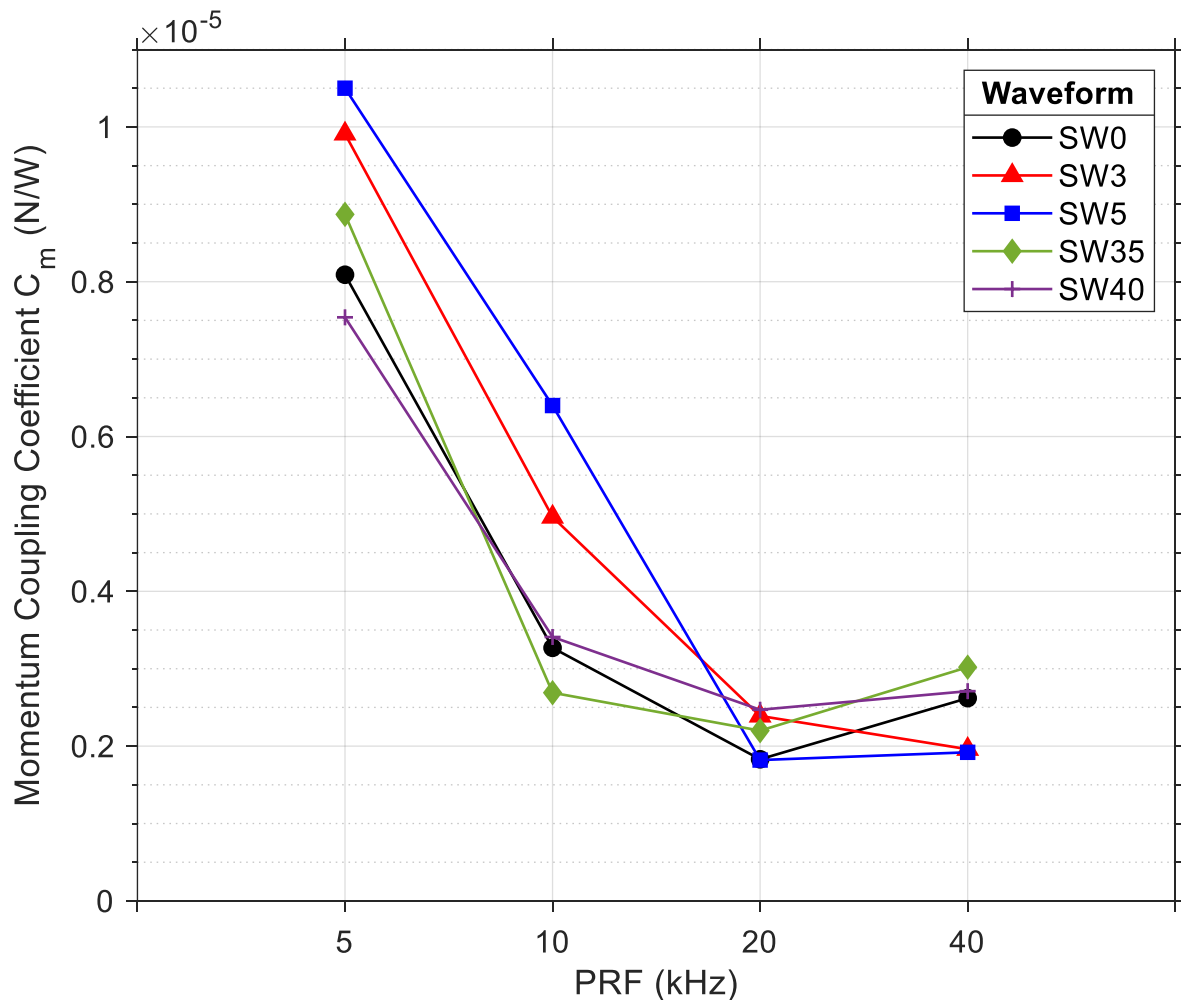


**Figure 52.** A plot of momentum coupling coefficient against waveform and repetition rate for PVC in air exposed to 160 pulses, or 469 mJ.

## Results and Analysis

Figure 53 shows  $C_I$  with respect to waveform and repetition rate for the PVC target in air. No obvious trends can be seen with repetition rate or waveform as data points are sporadically placed. On average most waveforms show almost no change in  $C_I$  value with repetition rate. The value of  $C_I$  is therefore not clearly dependent on waveform selection and repetition rate for PVC.

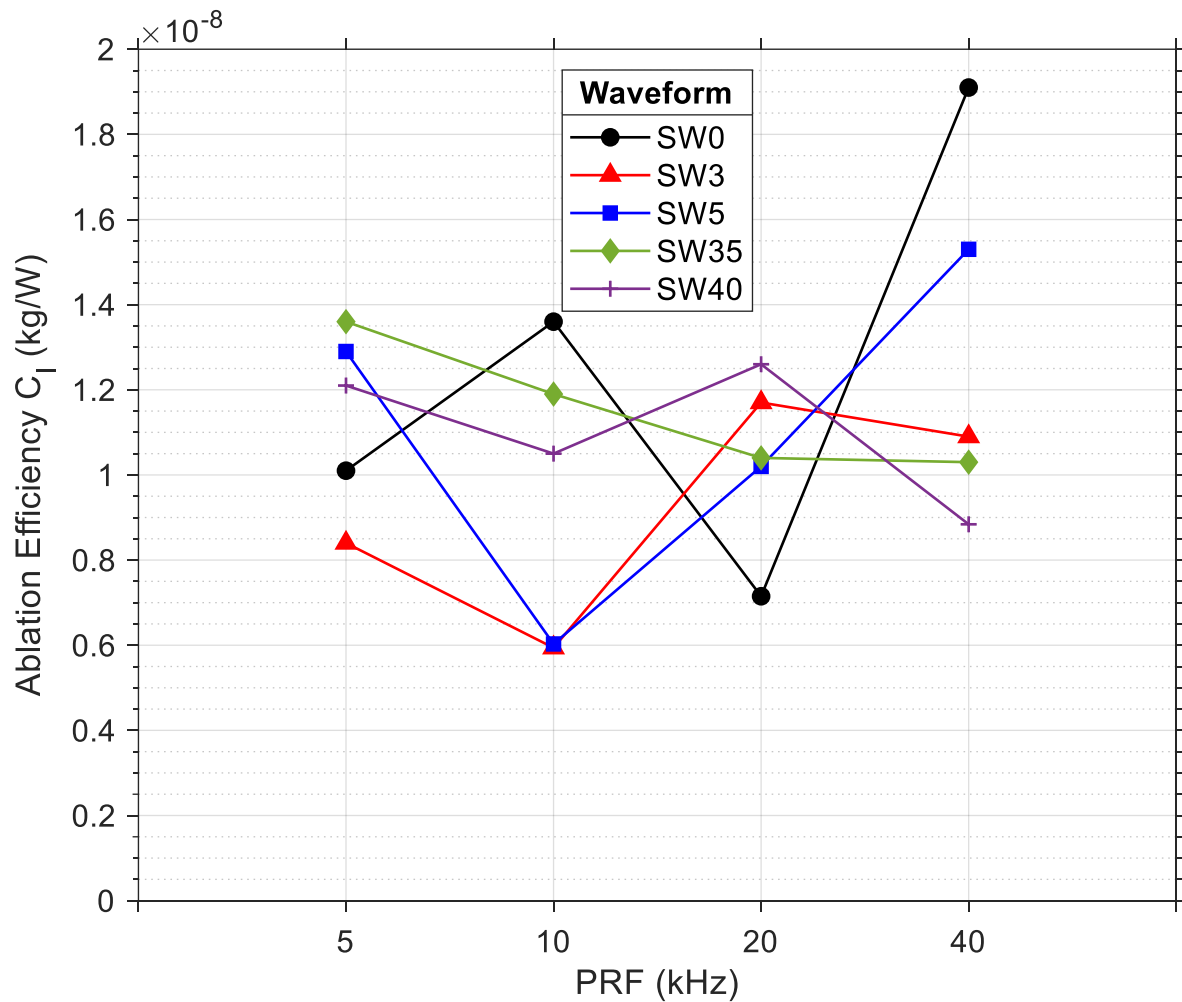


**Figure 53.** A plot of ablation efficiency against waveform and repetition rate for PVC in air exposed to 160 pulses, or 469 mJ.

## Results and Analysis

Figure 54 shows the resulting  $\beta$  with respect to waveform and repetition rate for the PVC target in air. The trend here is very similar to the trend in  $C_m$  for the PVC target, as  $\beta$  decreases with increasing repetition rate – on average waveforms show a large decrease in  $\beta$  from ~0.36% at 5 kHz to ~0.03% at 40 kHz. The order of which waveforms produce the greatest  $C_m$  value varies according to repetition rate. As with the  $C_m$  trend, on average waveforms SW5 and SW3 remain greater until between 20 kHz and 40 kHz when they produce the lowest value, and SW35 and SW40 produce the greatest. The difference in  $\beta$  between waveforms is greater at 5 kHz than 40 kHz. The value of  $\beta$  is therefore dependent on waveform selection and decreasing repetition rate for maximum kinetic energy.

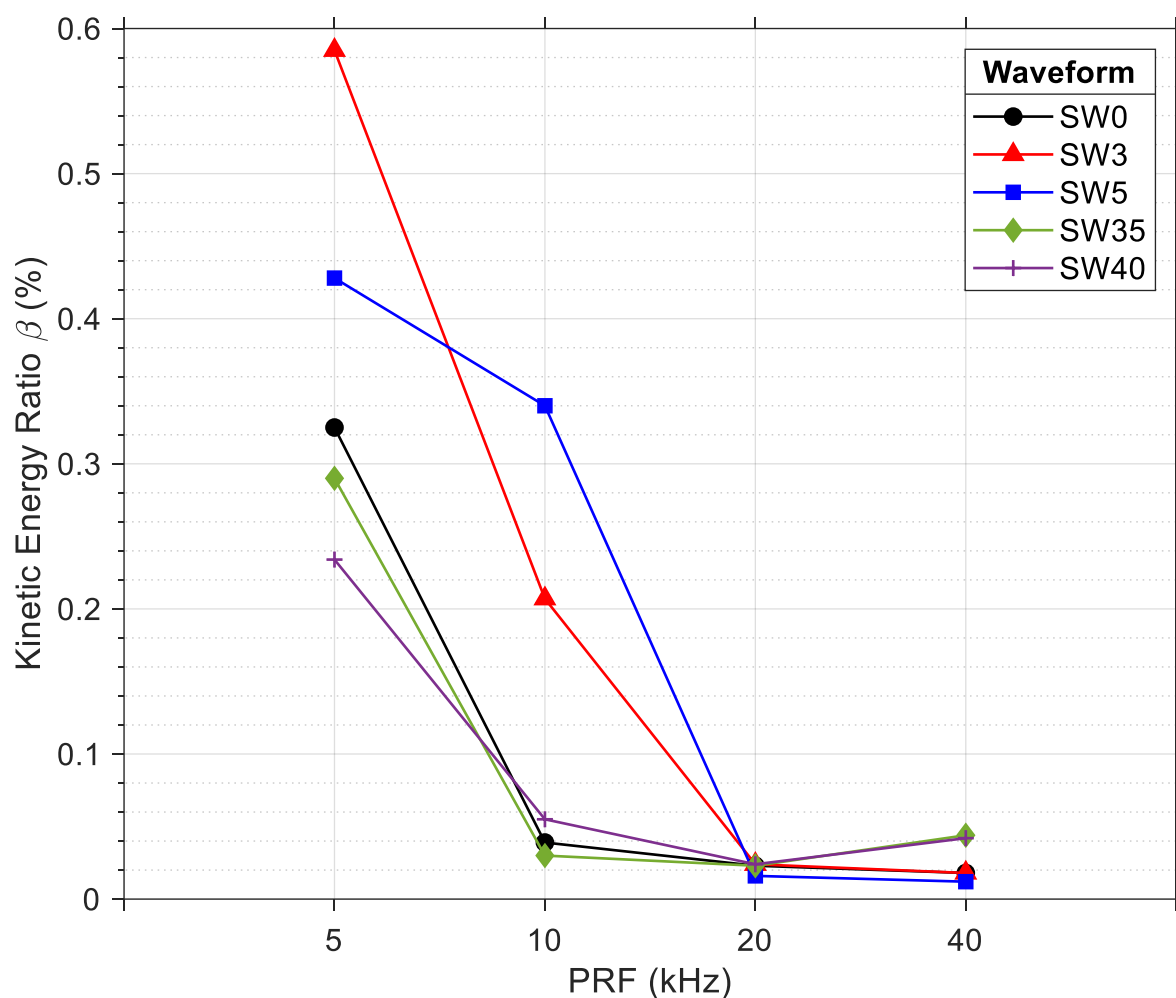


**Figure 54.** A plot of kinetic energy ratio against waveform and repetition rate for PVC in air exposed to 160 pulses, or 469 mJ.

## 7.2. Effect of Total Energy Input and Pulse Shape

### 7.2.1. Aluminium

Figure 55 shows the  $C_m$  with respect to waveform and number of pulses for the aluminium target in air at 40 kHz. The general trend shows a slight increase in  $C_m$  up to 40 pulses which then decreases again after 80 pulses for waveforms SW5, SW0, SW35 and SW40. Waveforms SW0, SW35 and SW40 follow this trend with  $\sim 0.25 \times 10^{-5}$  N/W at 20 pulses, going up to  $\sim 0.35 \times 10^{-5}$  N/W between 40 and 80 pulses before dropping again to  $\sim 0.25 \times 10^{-5}$  N/W at 160 pulses. Waveform SW5 follows the same trend but with values 100% greater than for SW0, SW35 and SW40. Waveform SW3 shows a different trend whereby  $C_m$  decreases with increasing number of pulses,  $\sim 1.25 \times 10^{-5}$  N/W at 20 pulses dropping to  $\sim 0.35 \times 10^{-5}$  N/W at 160 pulses. The value of  $C_m$  is therefore dependent on waveform selection and using a nominal number of pulses for maximum momentum production per unit energy in.

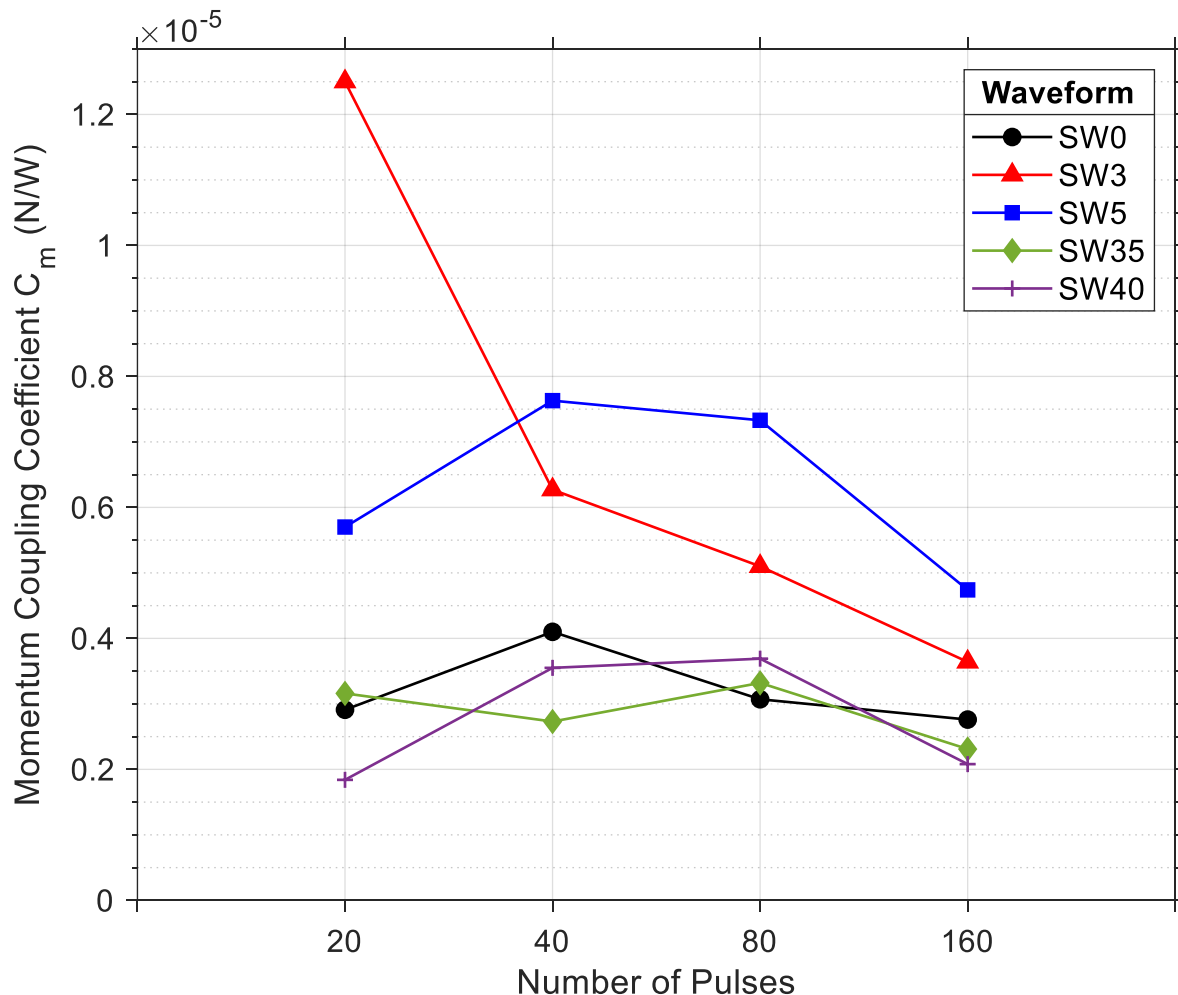


**Figure 55.** A plot of momentum coupling coefficient against number of pulses and waveform for aluminium exposed to air. The repetition rate is 40 kHz and each pulse contains 2.93 mJ.

## Results and Analysis

Figure 56 shows  $C_I$  with respect to waveform and number of pulses for the aluminium target in air at 40 kHz. The general trend is the reduction in  $C_I$  with increasing number of pulses for all waveforms. On average the waveforms see a ~66% reduction in  $C_I$  between from  $\sim 2.2 \times 10^{-8}$  kg/W 20 pulses to  $0.75 \times 10^{-8}$  kg/W at 160 pulses. Another interesting trend is the order of effectiveness of the different waveforms for producing maximum values of  $C_I$ . At 20 pulses the order is SW0, SW40, SW3, SW5 and SW35. By 160 pulses the order is SW5, SW3, SW35, SW0, SW40. The difference in  $C_I$  value between waveforms remains approximately constant from 20 pulses to 160 pulses. The value of  $C_I$  is therefore dependent on waveform selection and decreases repetition rate for maximum material removal per unit energy in.

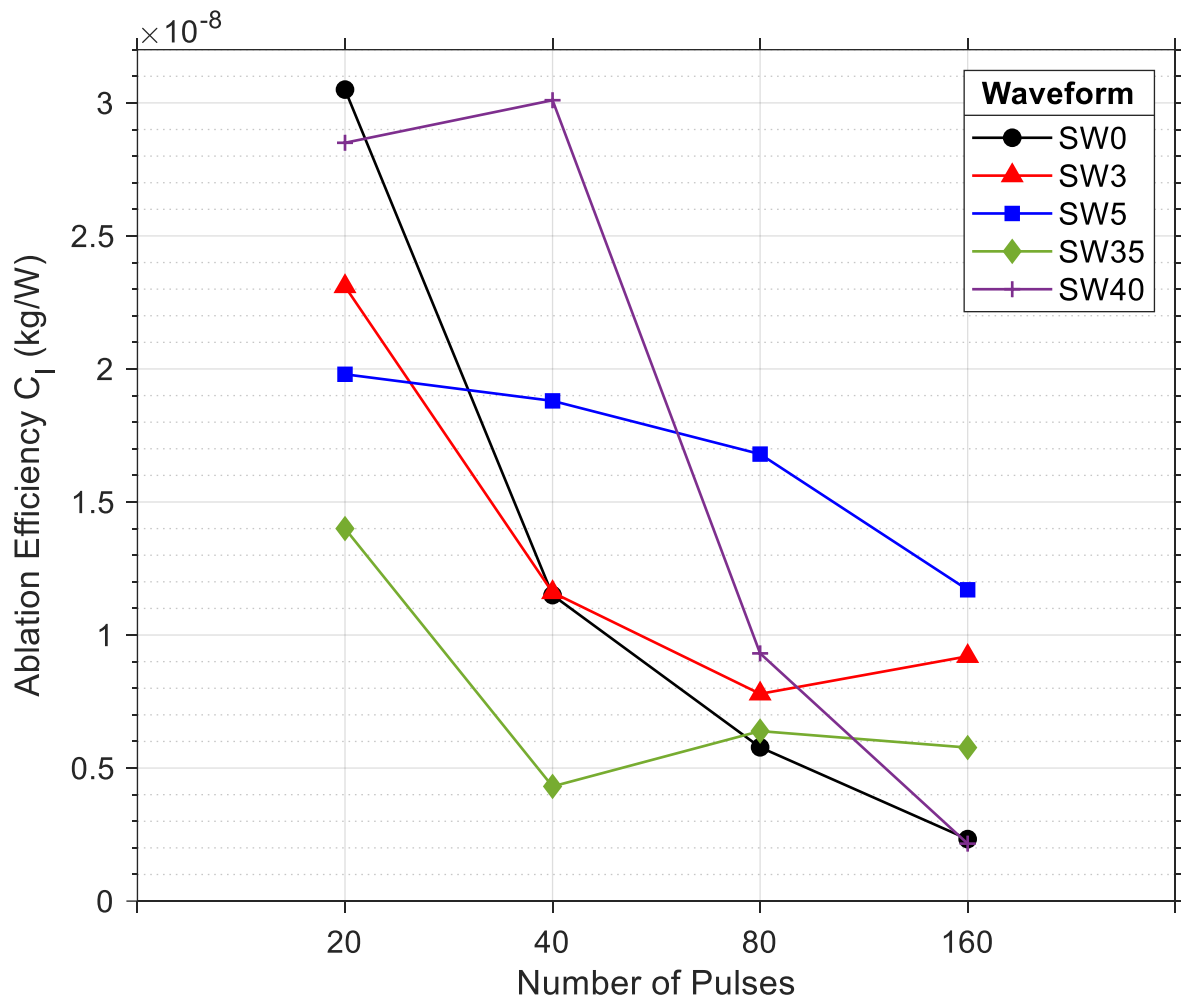


**Figure 56.** A plot of ablation efficiency against number of pulses and waveform for aluminium exposed to air. The repetition rate is 40 kHz and each pulse contains 2.93 mJ.

## Results and Analysis

Figure 57 shows  $\beta$  with respect to waveform and number of pulses for the aluminium target in air at 40 kHz. Here the trend strongly resembles that of  $C_m$  from figure 55, except that waveforms SW5, SW0 and SW40 increase in  $\beta$  after 80 pulses instead of decrease. Waveforms SW3 and SW35 remain generally unchanged. The  $\beta$  value is therefore dependent on waveform selection and using a nominal number of pulses for maximum kinetic energy ratio.

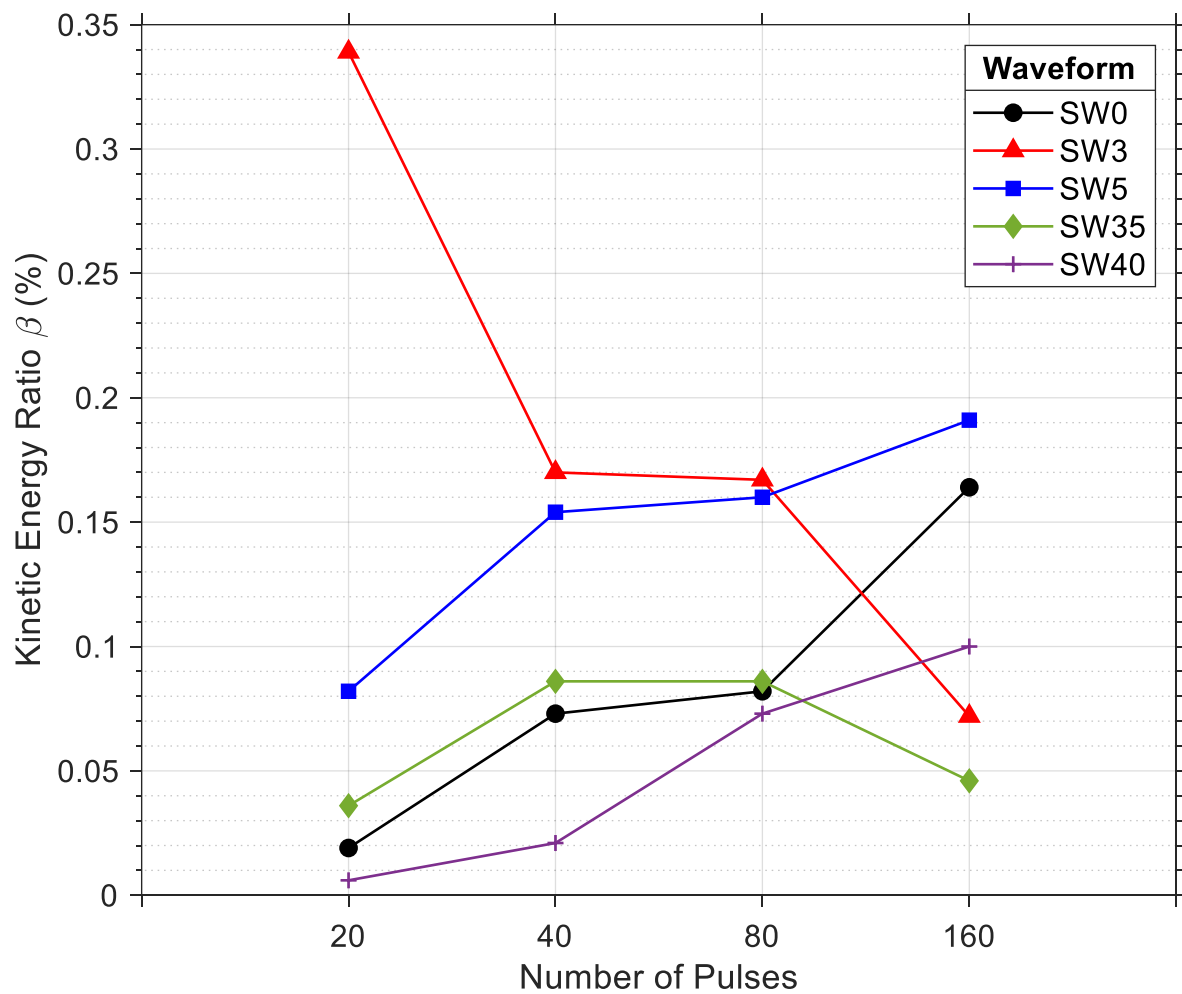


**Figure 57.** A plot of kinetic energy ratio against number of pulses and waveform for aluminium exposed to air. The repetition rate is 40 kHz and each pulse contains 2.93 mJ.

## Results and Analysis

### 7.2.2. Silicon

Figure 58 shows  $C_m$  with respect to waveform and number of pulses for the silicon target in air at 10 kHz. The trend shows a decrease in  $C_m$  with increasing number of pulses – on average waveforms show a ~70% decrease in  $C_m$  value from  $\sim 1.5 \times 10^{-5}$  N/W at 20 pulses to  $\sim 0.45 \times 10^{-5}$  N/W at 160 pulses. Waveforms SW0, SW5, SW3, SW35 and SW40 produce the highest value of  $C_m$  in that order at 20 pulses, and changes to SW5, SW3, SW0, SW35 and SW40 between 40 and 160 pulses. The difference in  $C_m$  value between waveforms remains approximately constant from 20 pulses and 160 pulses. The value of  $C_m$  is therefore dependent on waveform selection and decreasing repetition rate for maximum momentum production per unit energy in.

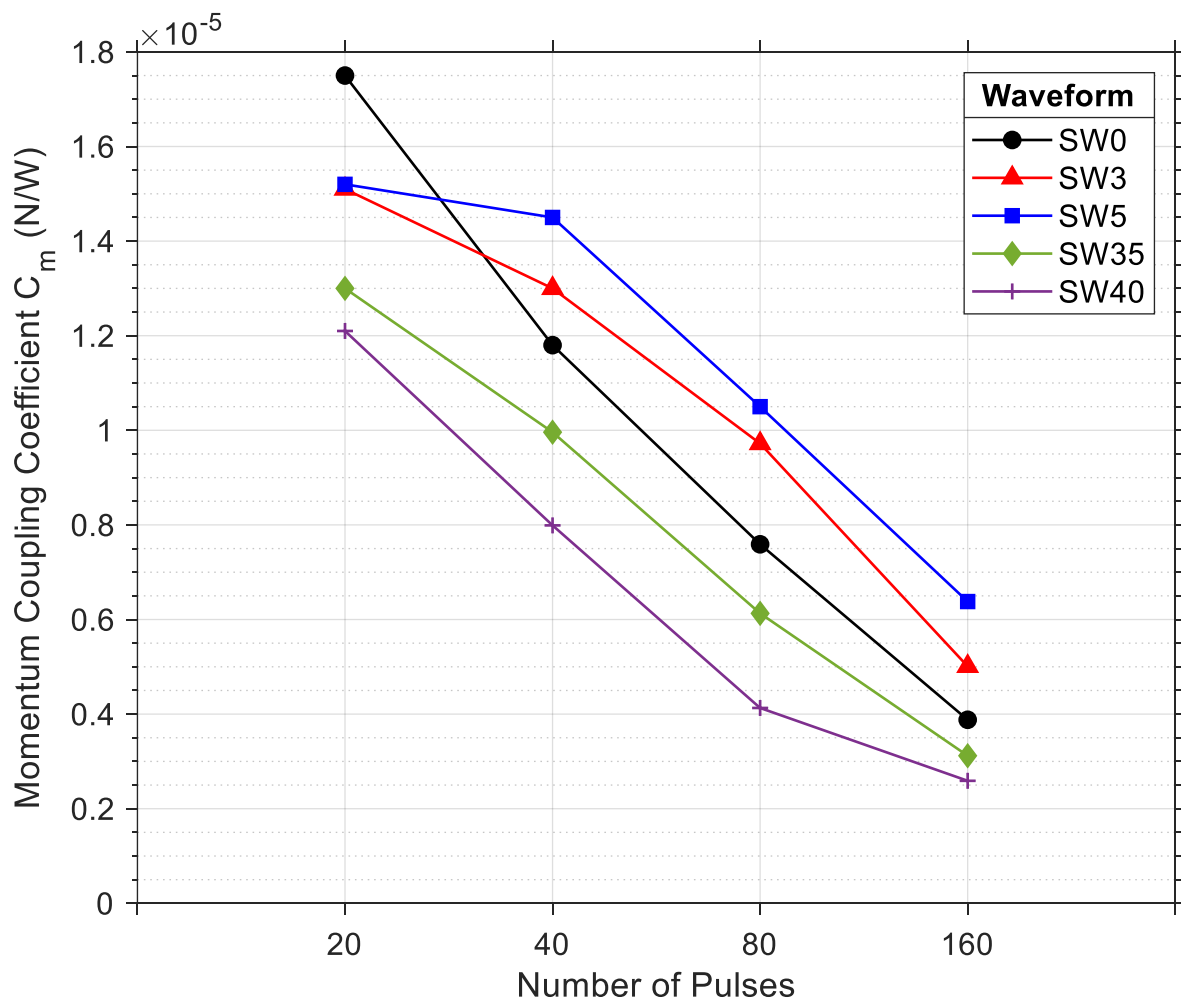


**Figure 58.** A plot of momentum coupling coefficient against number of pulses and waveform for silicon exposed to air. The repetition rate is 10 kHz and each pulse contains 2.93 mJ.

## Results and Analysis

Figure 59 shows  $C_i$  with respect to waveform and number of pulses for the silicon target in air at 10 kHz. The overall trend is similar to that for  $C_m$  in 7.2.2, except with a greater difference in  $C_i$  values at 20 pulses versus 160 pulses. Waveforms SW35, SW5, SW40, SW0 and SW5 produce the highest value of  $C_i$  in that order at 20 pulses, and changes to SW5, SW35, SW40, SW3 and SW0 between 80 and 160 pulses. The value of  $C_i$  is therefore dependent on waveform selection and decreasing repetition rate for maximum material removal per unit energy in.

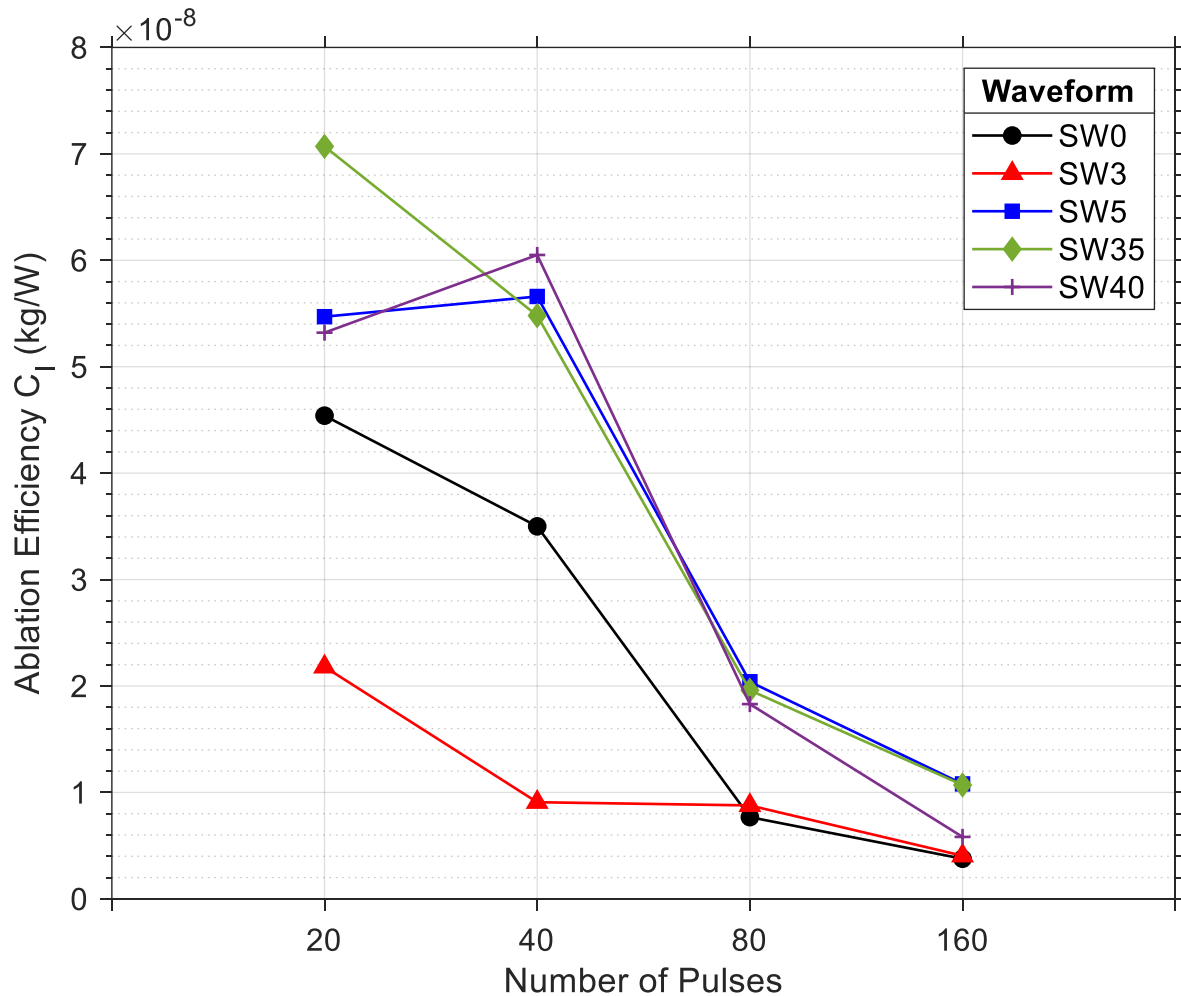


**Figure 59.** A plot of ablation efficiency against number of pulses and waveform for silicon exposed to air. The repetition rate is 10 kHz and each pulse contains 2.93 mJ.

## Results and Analysis

Figure 60 shows  $\beta$  with respect to waveform and number of pulses for the silicon target in air at 10 kHz. Waveforms SW5, SW0, SW35 and SW40 follow a similar trend, whereby they remain at approximately the same value across pulse numbers. There is a slight grouping between waveforms SW0 and SW5 at  $\sim 0.25\%$  and SW35 and SW40 at  $\sim 0.075\%$ . Waveform SW3 follows a different trend which begins at  $\sim 0.52\%$  at 20 pulses, reaching a maximum value of  $\sim 0.94\%$  at 40 pulses before decreasing to  $\sim 0.3\%$  at 160 pulses. The difference in  $\beta$  value between waveforms remains approximately constant from 20 pulses to 160 pulses. The value of  $\beta$  is therefore mostly dependent on waveform selection for maximum kinetic energy.

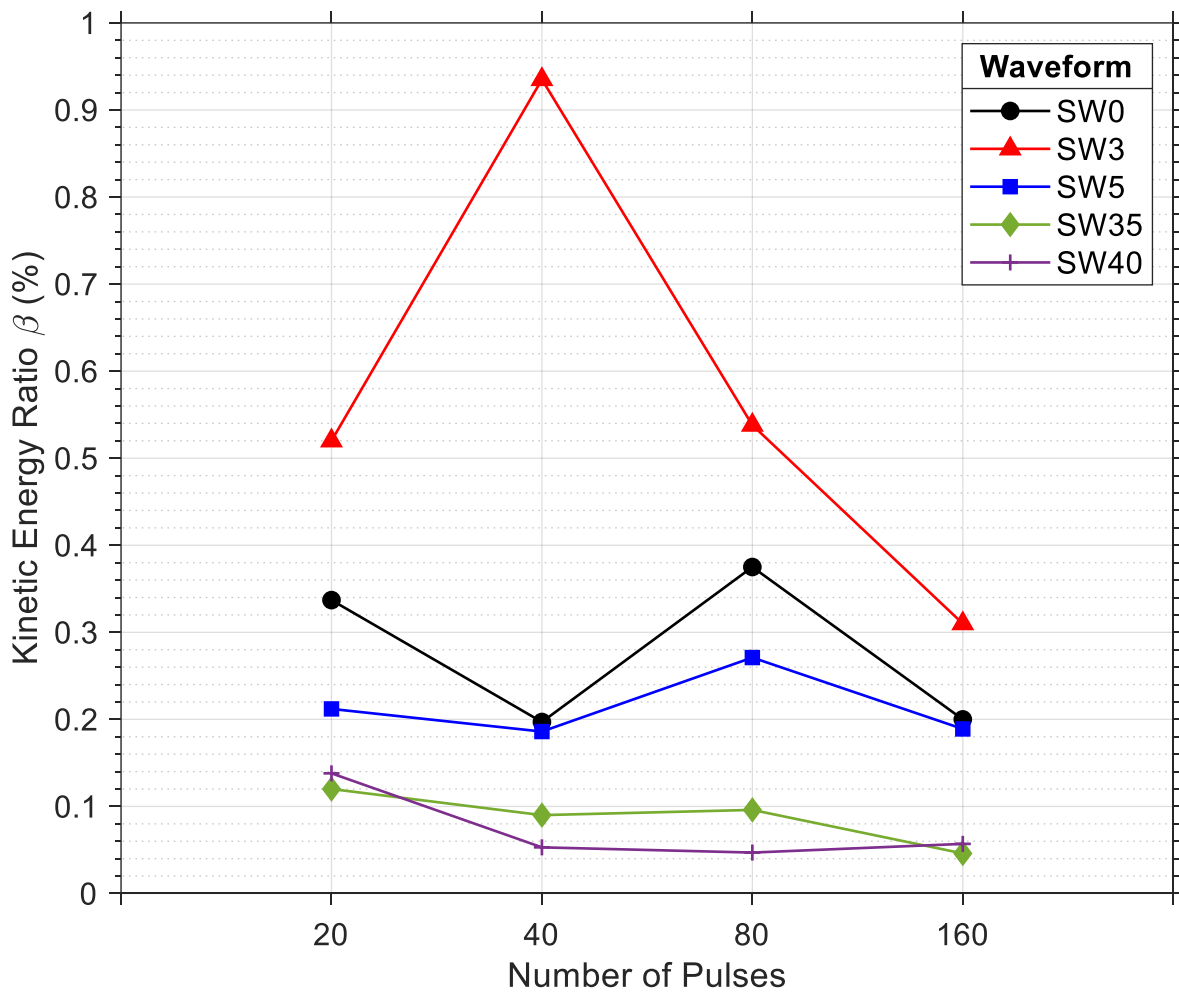


**Figure 60.** A plot of kinetic energy ratio against number of pulses and waveform for silicon exposed to air. The repetition rate is 10 kHz and each pulse contains 2.93 mJ.

## Results and Analysis

### 7.2.3. PVC

Figure 61 shows  $C_m$  with respect to waveform and number of pulses for the PVC target in air at 5 kHz. The trend here is very similar to the trend in  $C_m$  for the aluminium target in 7.1.1 and silicon target in 7.2.2, except here the value of  $C_m$  first decreases with increasing number of pulses and then increases again after some critical pulse number is reached. Waveform SW0 does not follow this trend and remains approximately unchanged with number of pulses. SW40 only follows part of the trend and does not increase in value again after a certain number of pulses. The order of which waveforms produce the greatest  $C_m$  value varies according to number of pulses. On average waveforms SW5 and SW35 remain greater at 20 pulses, SW0 and SW40 at 40 pulses, and SW5 and SW3 at 160 pulses. The difference in  $C_m$  value between waveforms remains approximately constant between 20 and 160 pulses except for waveform SW35 at 20 pulses which remains ~60% higher than the other values. The value of  $C_m$  is therefore dependent on waveform selection and attaining a nominal number of pulses for maximum momentum production per unit energy in.

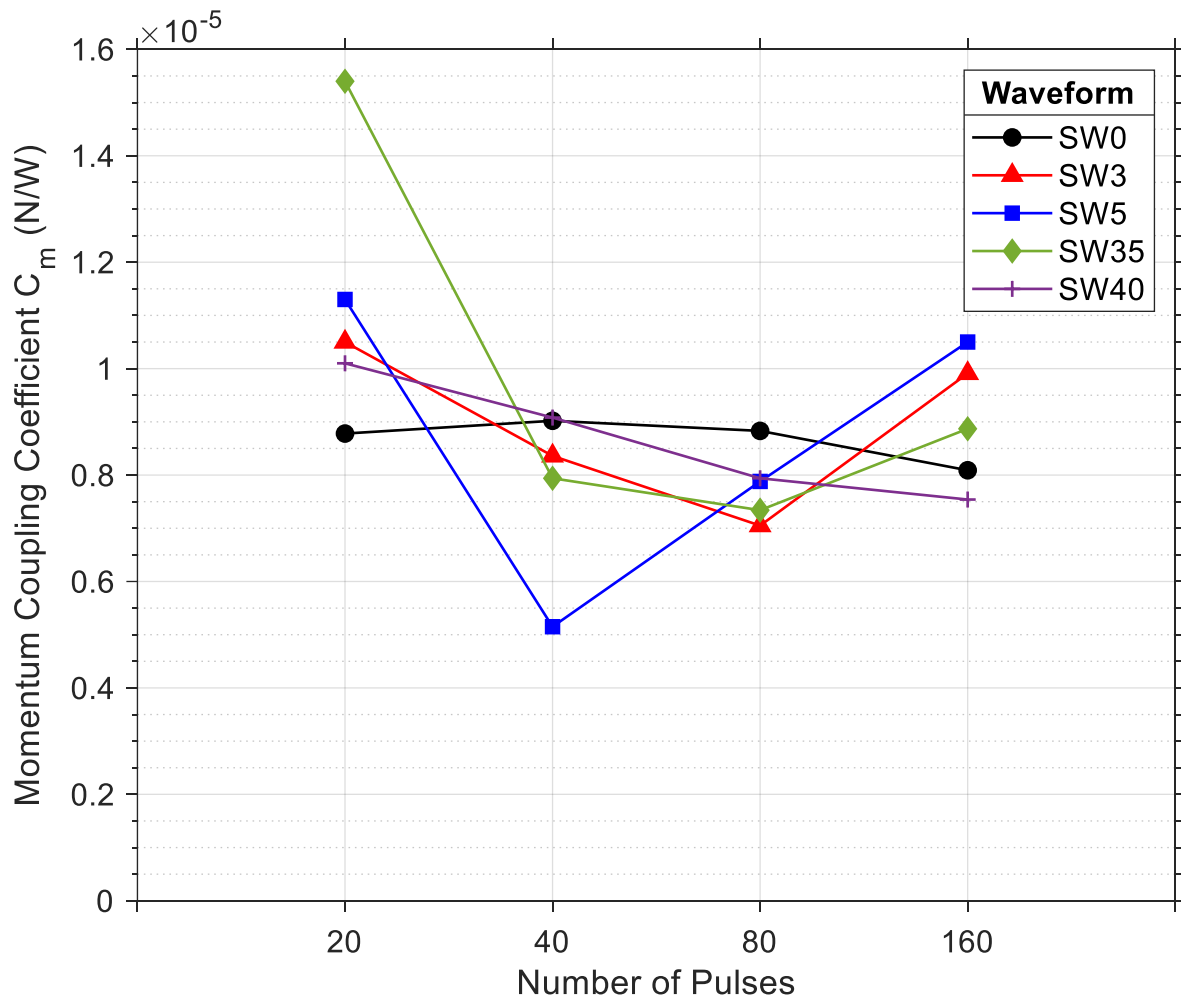


**Figure 61.** A plot of momentum coupling coefficient against number of pulses and waveform for PVC exposed to air. The repetition rate is 5 kHz and each pulse contains 2.93 mJ.

## Results and Analysis

Figure 62 shows  $C_1$  with respect to waveform and number of pulses for the PVC target in air at 5 kHz. The trend shows a decrease in  $C_1$  with increasing number of pulses for all waveforms – on average waveforms show a ~63% decrease in  $C_1$  value from  $\sim 0.9 \times 10^{-7}$  kg/W at 20 pulses to  $\sim 0.33 \times 10^{-7}$  kg/W at 160 pulses. Waveforms SW40, SW3, SW0, SW5 and SW35 produce the highest value of  $C_1$  in that order at 20 pulses, and change to SW35, SW5, SW40, SW0 and SW3 between 20 and 160 pulses. The difference between  $C_1$  values between waveforms decreases with increasing number of pulses by an order of magnitude. The value of  $C_1$  is therefore dependent on waveform selection and decreasing repetition rate for maximum material removal per unit energy in.

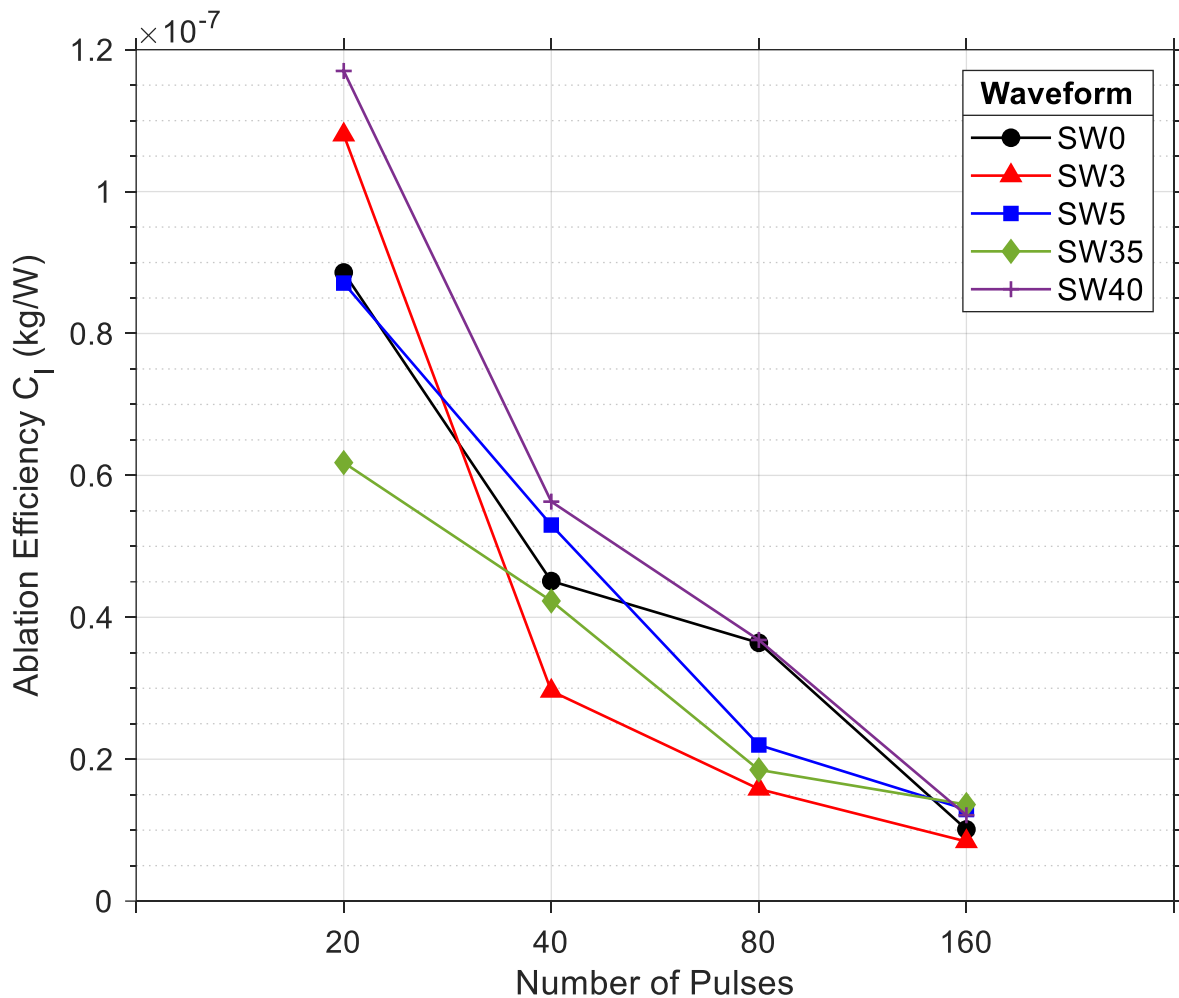


**Figure 62.** A plot of ablation efficiency against number of pulses and waveform for PVC exposed to air. The repetition rate is 5 kHz and each pulse contains 2.93 mJ.

## Results and Analysis

Figure 63 shows  $\beta$  with respect to waveform and number of pulses for the PVC target in air at 5 kHz. The overall trend shows an opposite trend to that for  $C_1$  - a decrease in  $\beta$  between 20 pulses and 40 pulses for waveforms SW5 and SW35 or an increase for waveforms SW3, SW0 and SW40, all followed by rapid rise between 80 pulses and 160 pulses. On average waveforms show a ~200% increase in  $\beta$  from ~0.12% at 20 pulses to ~0.38% at 160 pulses. Waveforms SW35, SW5, SW3, SW40 and SW0 produce the highest  $\beta$  in that order at 20 pulses, and change to SW3, SW5, SW0, SW35 and SW40 at 160 pulses. The value of  $\beta$  is therefore dependent on waveform selection and increasing number of pulses for maximum kinetic energy.

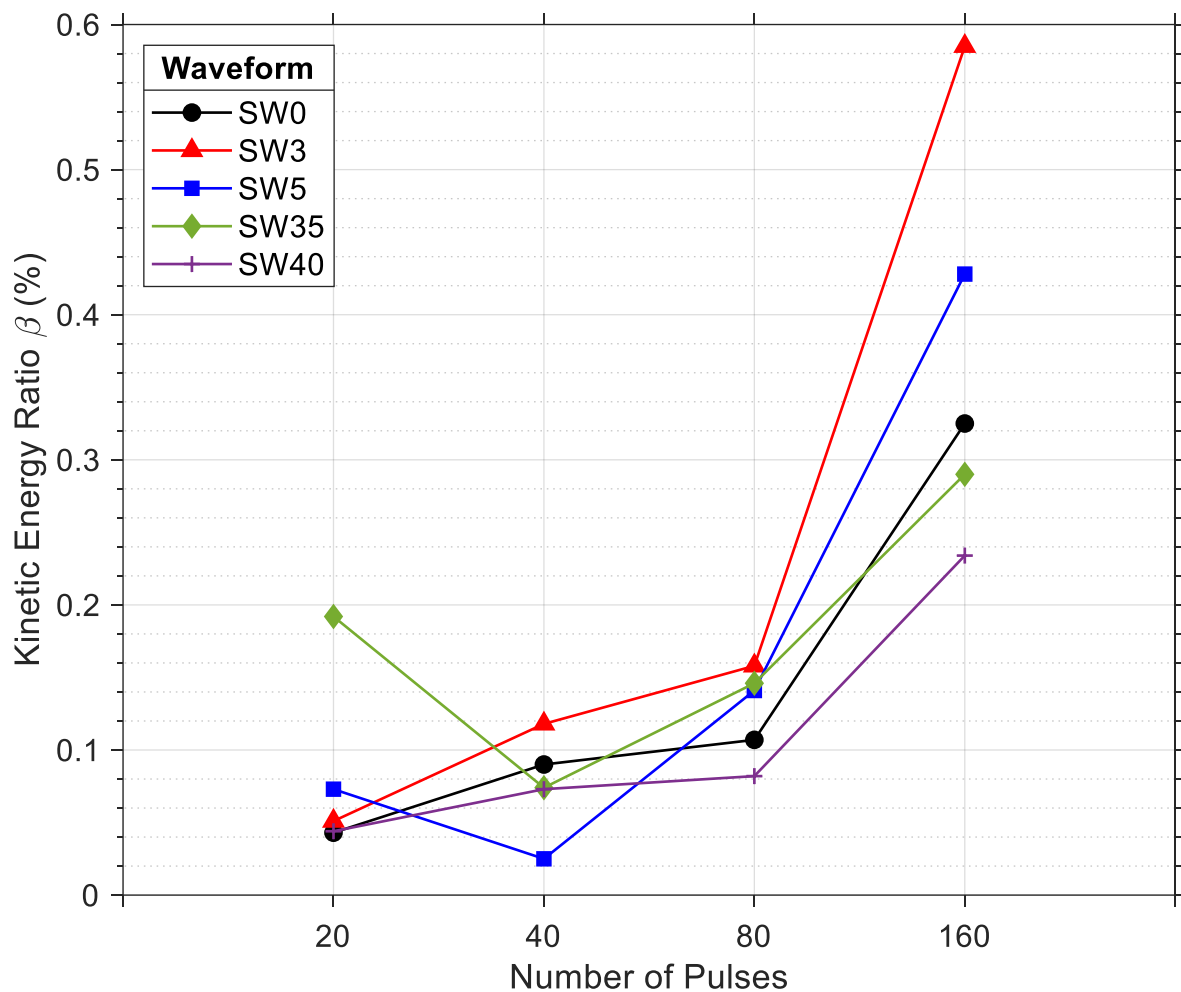


**Figure 63.** A plot of kinetic energy ratio against number of pulses and waveform for PVC exposed to air. The repetition rate is 5 kHz and each pulse contains 2.93 mJ.

### 7.3. Effect of Total Energy Input and Environment

#### 7.3.1. Aluminium

Figure 64 shows the  $C_m$  value with number of pulses for the aluminium target under different environments at 40 kHz and SW40. The  $C_m$  value in air reduces linearly from  $\sim 6 \times 10^{-6}$  N/W at 20 pulses to  $\sim 1.2 \times 10^{-6}$  N/W at 160 shots. The results show that  $C_m$  in vacuum is almost three times greater at 20 pulses than in air. The  $C_m$  value in air increases from  $1.8 \times 10^{-6}$  N/W at 20 pulses to  $3.6 \times 10^{-6}$  N/W at 40 pulses, after which the value remains almost the same until decreasing at 80 pulses to a value of  $\sim 2 \times 10^{-6}$  N/W at 160 pulses. The  $C_m$  value in vacuum drops below that in air after approximately 60 pulses. The selection of environment for optimal  $C_m$  is therefore dependent on a critical value for number of pulses.

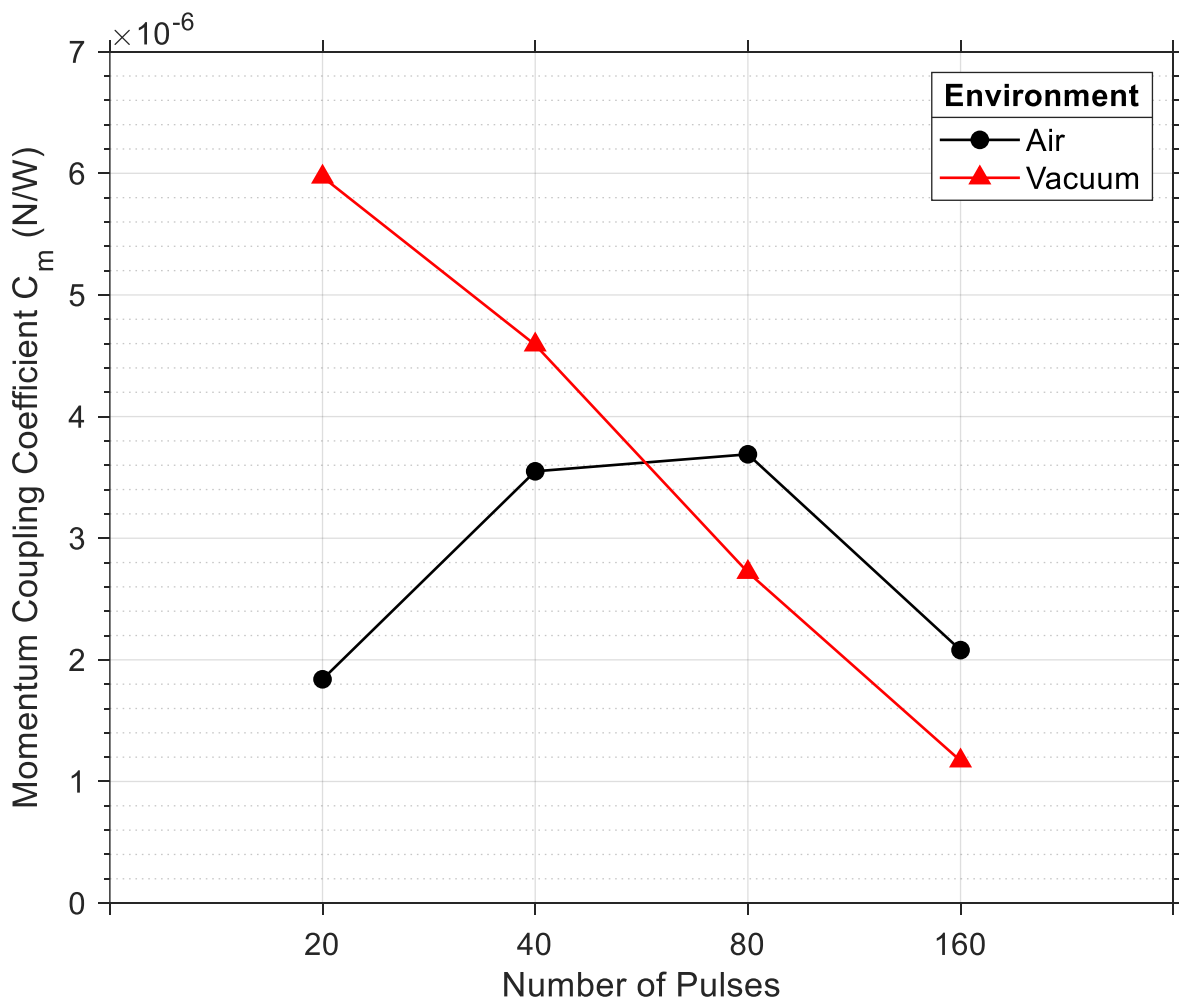


**Figure 64.** A plot of momentum coupling coefficient against number of pulses and environment for aluminium. The repetition rate is 40 kHz, the waveform is SW40 and each pulse contains 2.93 mJ.

## Results and Analysis

Figure 65 shows the  $C_i$  value with number of pulses for the aluminium target under different environments at 40 kHz and SW40. The  $C_i$  value in air remains at a value of  $\sim 2.9 \times 10^{-8}$  kg/W between 20 and 40 pulses, after which it linearly decreases to  $\sim 0.2 \times 10^{-8}$  kg/W at 160 pulses. The results show that  $C_i$  in air is almost 30 times greater at 20 pulses than in vacuum. The  $C_i$  value in vacuum remains at a value of  $\sim 0.1 \times 10^{-8}$  kg/W between 20 and 40 pulses, after which it linearly increases to  $\sim 0.4 \times 10^{-8}$  kg/W at 160 pulses. The  $C_i$  value in air drops below that in vacuum after approximately 140 pulses. The selection of environment for optimal  $C_i$  is therefore dependent on a critical value for number of pulses.

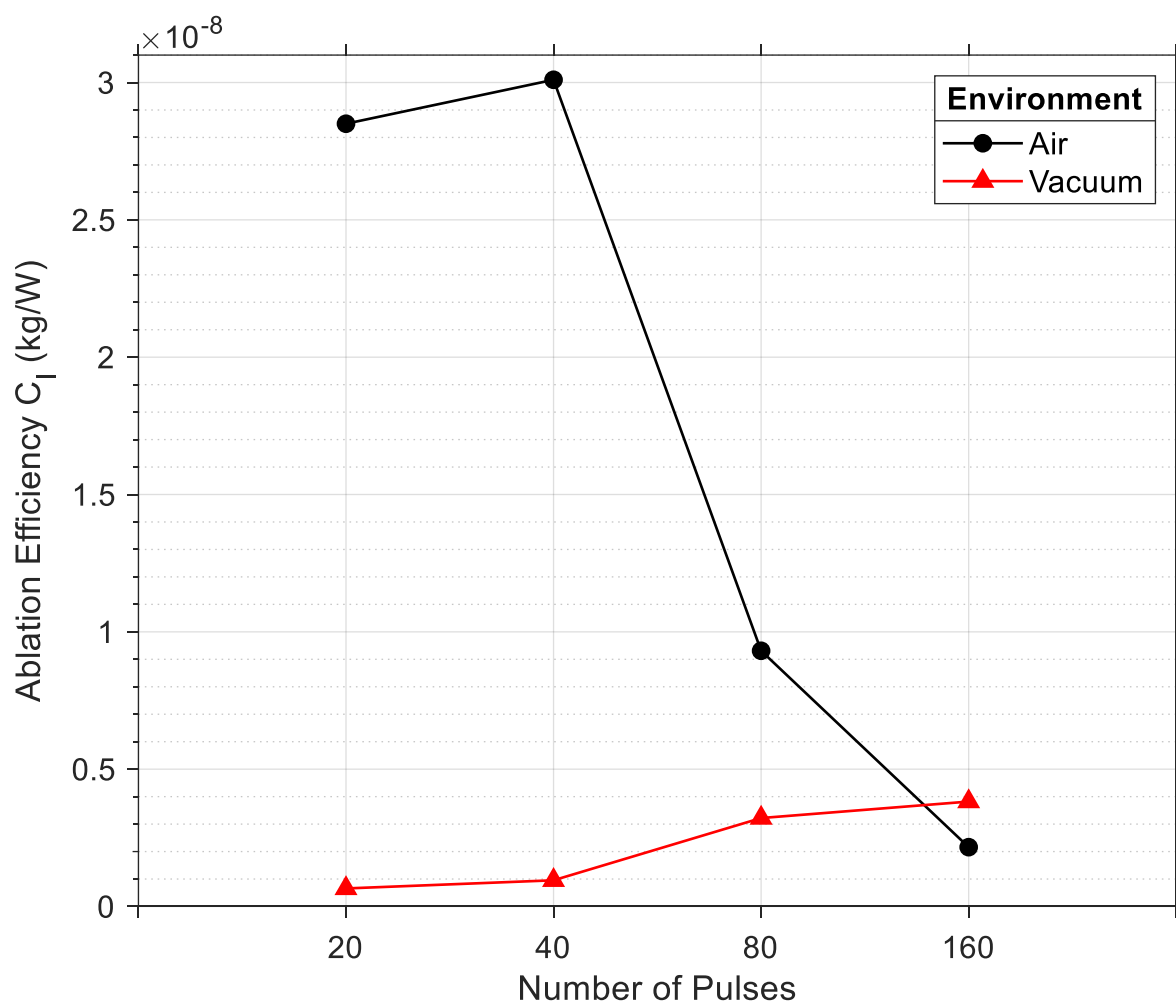


**Figure 65.** A plot of ablation efficiency against number of pulses and environment for aluminium. The repetition rate is 40 kHz, the waveform is SW40 and each pulse contains 2.93 mJ.

## Results and Analysis

Figure 66 shows the  $\beta$  value with number of pulses for the aluminium target under different environments at 40 kHz and SW40. Here, the result in vacuum shows a decrease in  $\beta$  with increasing number of pulses. An initial value of  $\sim 2.7\%$ , reducing to  $\sim 0.1\%$  after 160 pulses. The result in air shows a small increase in  $\beta$  from almost 0% to 0.1% after 160 pulses. The  $\beta$  in vacuum becomes smaller than in air after about 100 pulses. The selection of environment for optimal  $\beta$  is therefore dependent on a critical value for number of pulses.

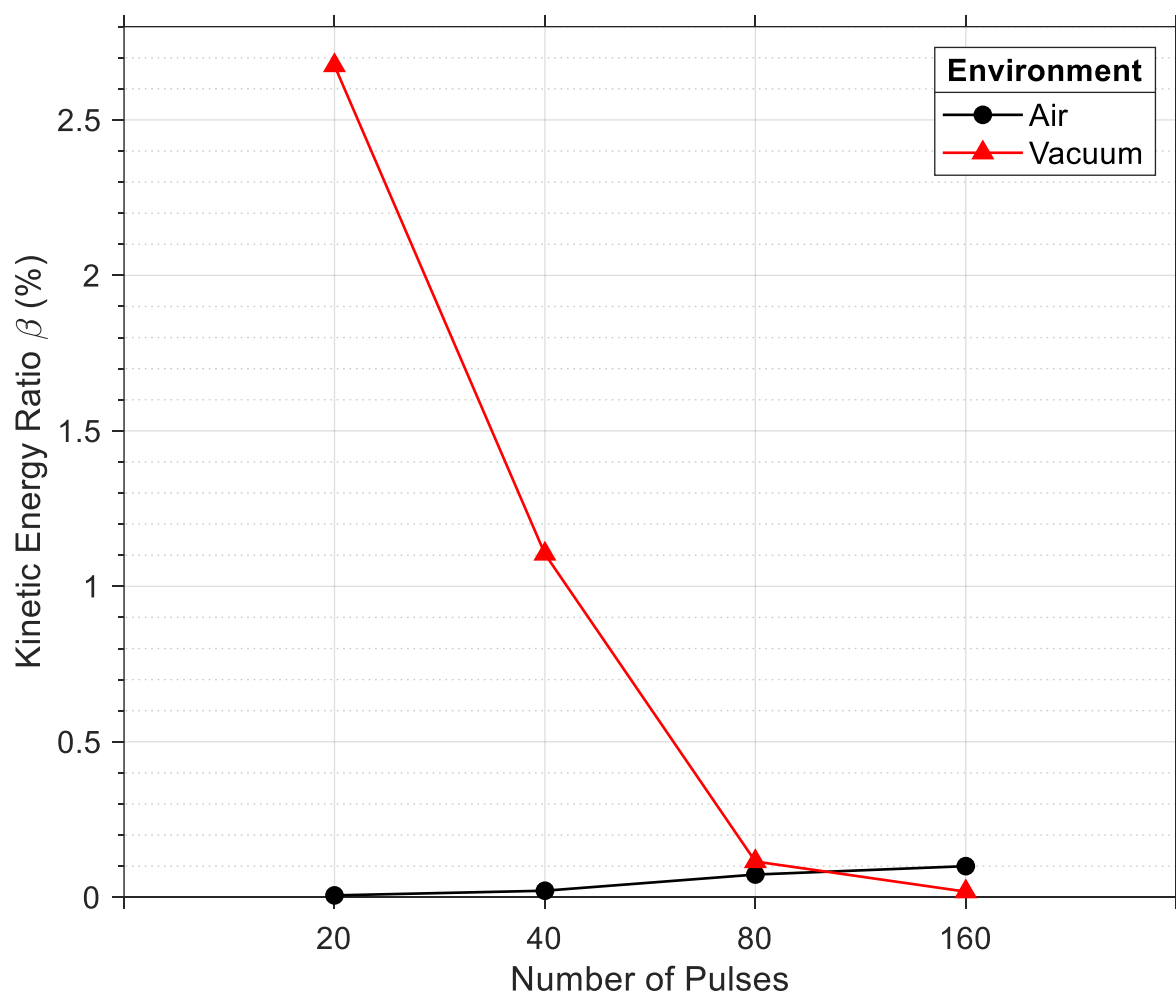


**Figure 66.** A plot of kinetic energy ratio against number of pulses and environment for aluminium. The repetition rate is 40 kHz, the waveform is SW40 and each pulse contains 2.93 mJ.

## Results and Analysis

### 7.3.2. Silicon

Figure 67 shows the  $C_m$  value with number of pulses for the silicon target under different environments at 10 kHz and SW40. Here the trends for both air and vacuum environments are similar. Both show a linear reduction of  $C_m$  with increasing number of pulses. The vacuum results begin at  $\sim 1.4 \times 10^{-5}$  N/W at 20 pulses and reduce to  $\sim 0.5 \times 10^{-5}$  N/W at 160 pulses, whilst in air starts at  $\sim 1.2 \times 10^{-5}$  N/W at 20 pulses and reduces to  $\sim 0.25 \times 10^{-5}$  N/W at 160 pulses. The results in vacuum always remain higher than in air and as such the selection of environment for optimal  $C_m$  is not highly dependent on number of pulses.

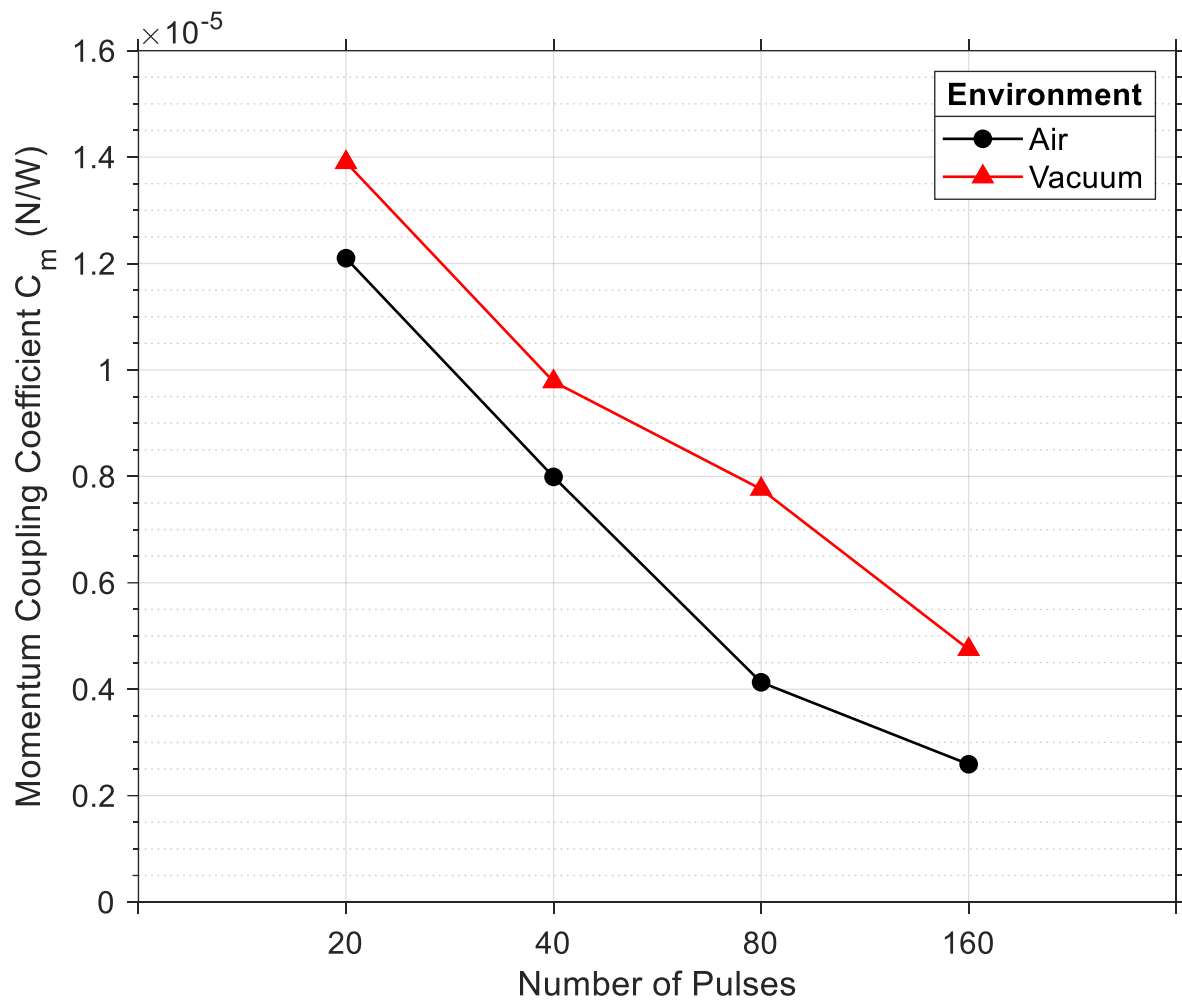


**Figure 67.** A plot of momentum coupling coefficient against number of pulses and environment for silicon. The repetition rate is 10 kHz, the waveform is SW40 and each pulse contains 2.93 mJ.

## Results and Analysis

Figure 68 shows the  $C_i$  value with number of pulses for the silicon target under different environments at 10 kHz and SW40. The trend for the results in vacuum show an almost linear reduction in  $C_i$  with increasing number of pulses, from  $\sim 3 \times 10^{-8}$  kg/W at 20 pulses down to  $\sim 1.4 \times 10^{-8}$  kg/W at 160 pulses. The results in air are quite different. The value increases from  $\sim 5.4 \times 10^{-8}$  kg/W to  $6 \times 10^{-8}$  kg/W between 20 and 40 pulses before dropping to  $0.6 \times 10^{-8}$  kg/W after 160 pulses, crossing the vacuum values at around 80 pulses. The selection of environment for optimal  $C_i$  is therefore dependent on a critical value for number of pulses.

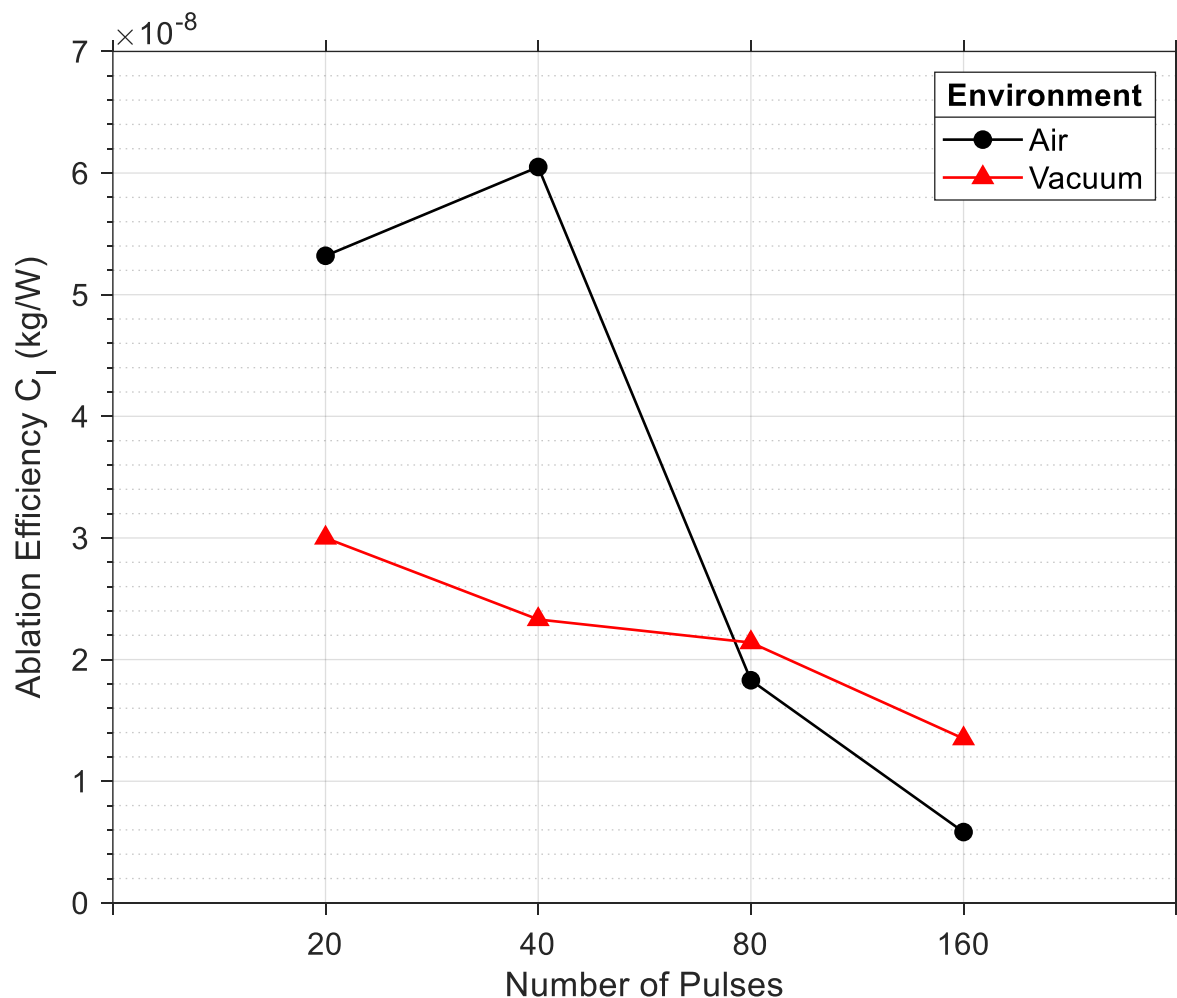


**Figure 68.** A plot of ablation efficiency against number of pulses and environment for silicon. The repetition rate is 10 kHz, the waveform is SW40 and each pulse contains 2.93 mJ.

## Results and Analysis

Figure 69 shows the  $\beta$  value with number of pulses for the silicon target under different environments at 10 kHz and SW40. In vacuum the  $\beta$  value drops linearly with increasing number of pulses, from ~0.32% at 20 pulses to 0.08% at ~160 pulses. The  $\beta$  value in air begins by dropping from ~0.14% at 20 pulses to 0.05% at 40 pulses after which the value remains approximately the same up to 160 pulses. The results in vacuum always remain higher than in air and as such the selection of environment for optimal  $\beta$  is not highly dependent on number of pulses.

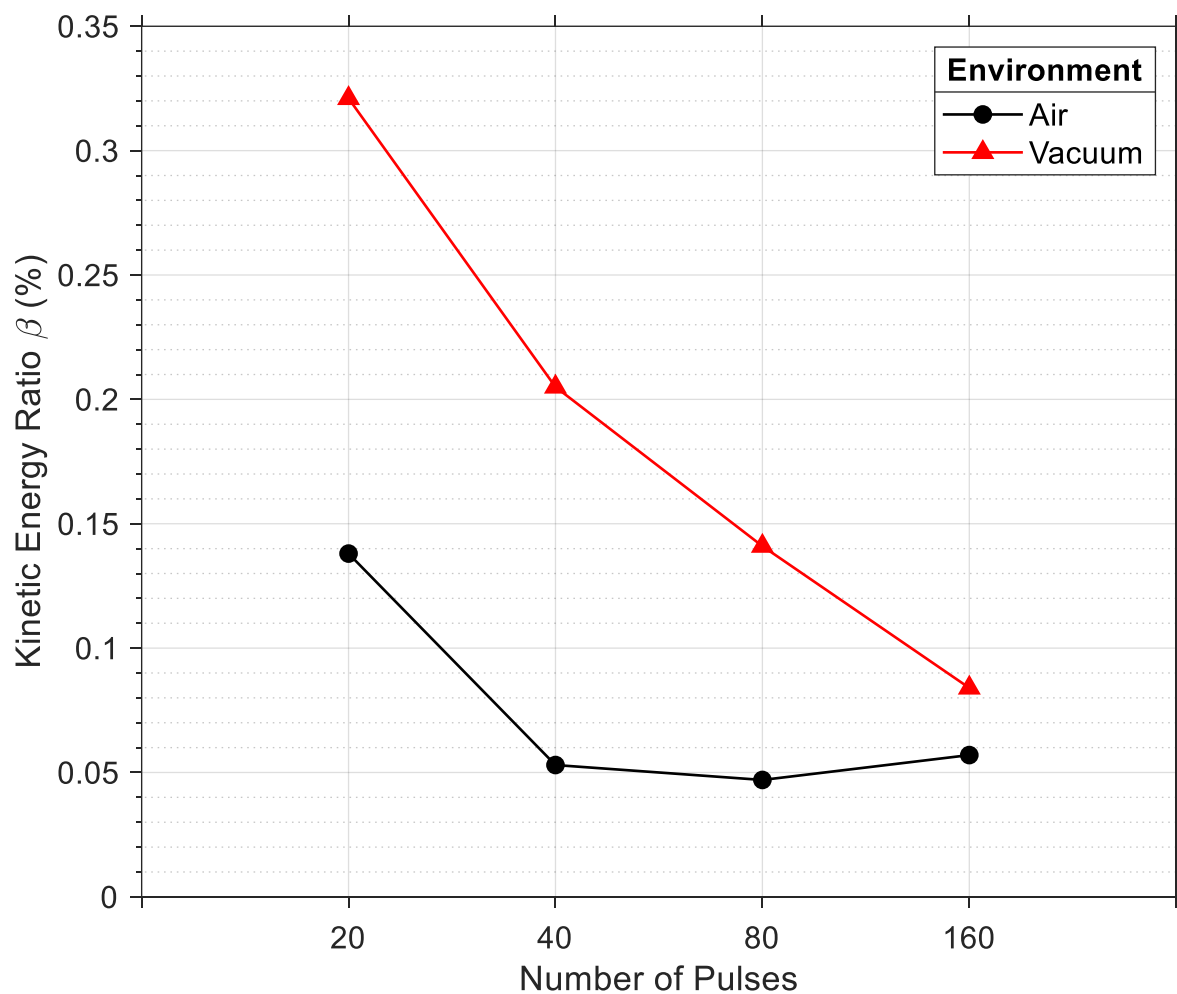


**Figure 69.** A plot of kinetic energy ratio against number of pulses and environment for silicon. The repetition rate is 10 kHz, the waveform is SW40 and each pulse contains 2.93 mJ.

## Results and Analysis

### 7.3.3. PVC

Figure 70 shows the  $C_m$  value with number of pulses for the PVC target under different environments at 5 kHz and SW40. At 20 pulses both environments produce a similar  $C_m$  value of about  $0.125 \times 10^{-4}$  N/W. The results in air stay at approximately the same value until 160 pulses. The values in vacuum increase to  $\sim 1.5 \times 10^{-4}$  N/W at 40 pulses and then drop slightly to  $\sim 1.3 \times 10^{-4}$  N/W until 160 pulses. After 40 pulses the values in vacuum remain almost 13 times greater than air. The results in vacuum always remain higher than in air and as such the selection of environment for optimal  $C_m$  is not highly dependent on number of pulses.

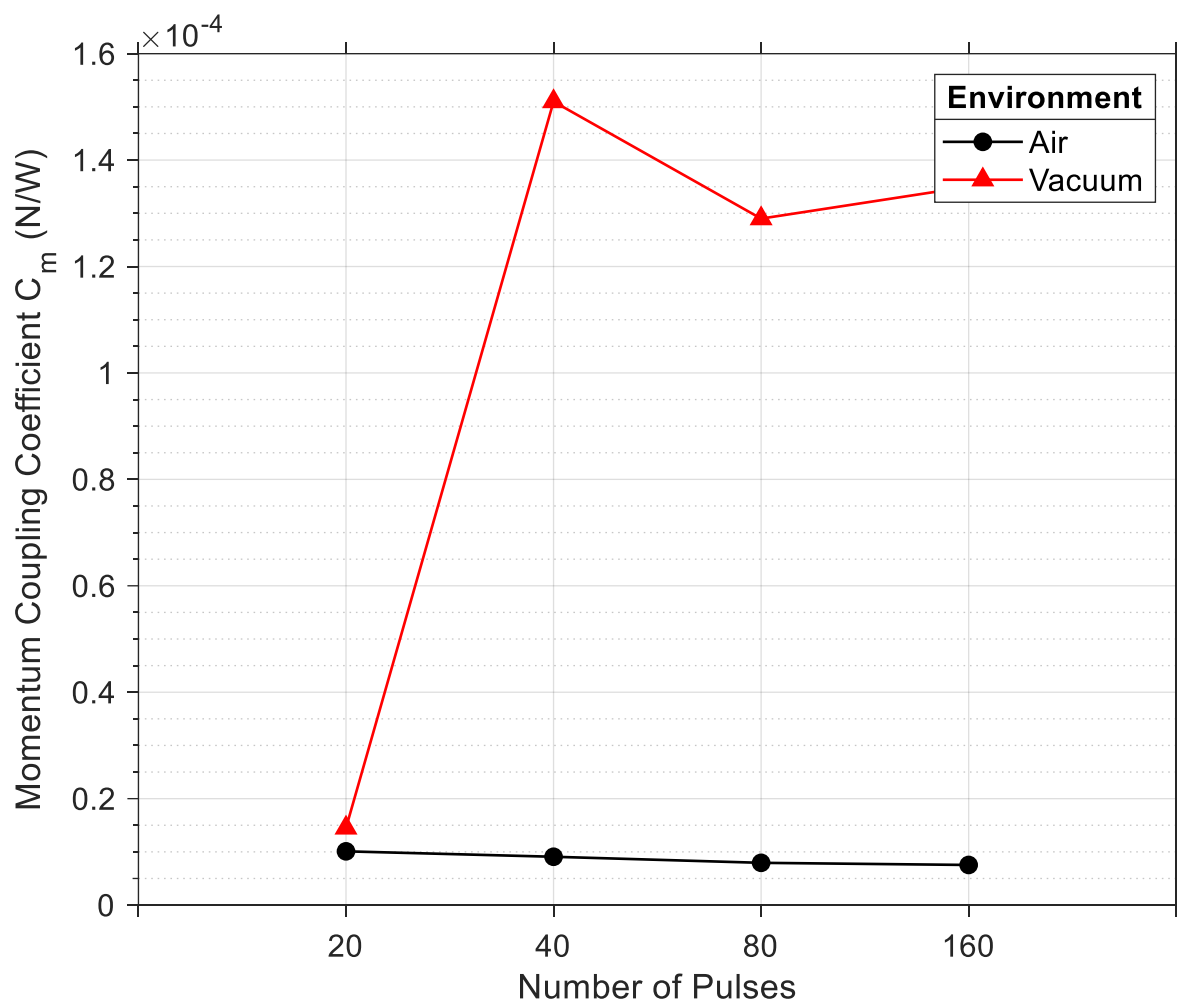


**Figure 70.** A plot of momentum coupling coefficient against number of pulses and environment for PVC. The repetition rate is 5 kHz, the waveform is SW40 and each pulse contains 2.93 mJ.

## Results and Analysis

Figure 71 shows the  $C_I$  value with number of pulses for the PVC target under different environments at 5 kHz and SW40. Results for vacuum and air follow a similar trend and values, showing a non-linear decrease of  $C_I$  with increasing number of pulses. Overall, the values in vacuum are higher than those in air, following a fairly consistent difference of ~40%. In vacuum the  $C_I$  values are  $\sim 1.65 \times 10^{-7}$  kg/W at 20 pulses and reduce to  $\sim 0.15 \times 10^{-7}$  kg/W at 160 pulses. This trend is broken once at 80 pulses whereby the value for air exceeds that for vacuum by the same percentage difference. The selection of environment for optimal  $C_I$  is therefore dependent on a critical value for number of pulses.

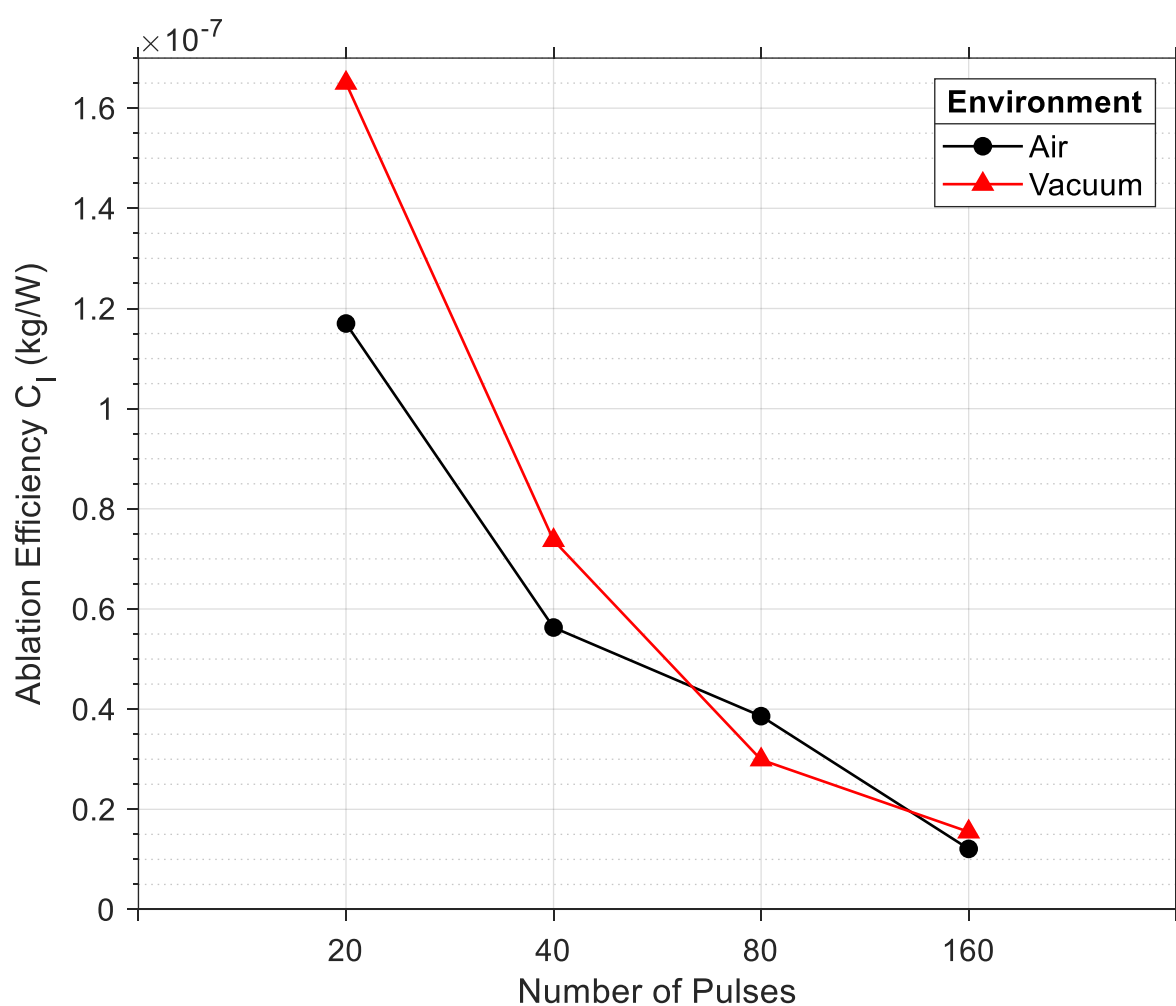


**Figure 71.** A plot of ablation efficiency against number of pulses and environment for PVC. The repetition rate is 5 kHz, the waveform is SW40 and each pulse contains 2.93 mJ.

## Results and Analysis

Figure 72 shows the  $\beta$  value with number of pulses for the PVC target under different environments at 5 kHz and SW40. The results are plotted on a semi-log scale due to the vast difference in values. The values in vacuum are on average two orders of magnitude greater than the values achieved in air. Results for vacuum and air follow a linear trend of increasing  $\beta$  with number of pulses. In vacuum this begins at ~5% and increases to ~50% at 160 pulses. The results in vacuum always remain higher than in air and as such the selection of environment for optimal  $\beta$  is not highly dependent on number of pulses.

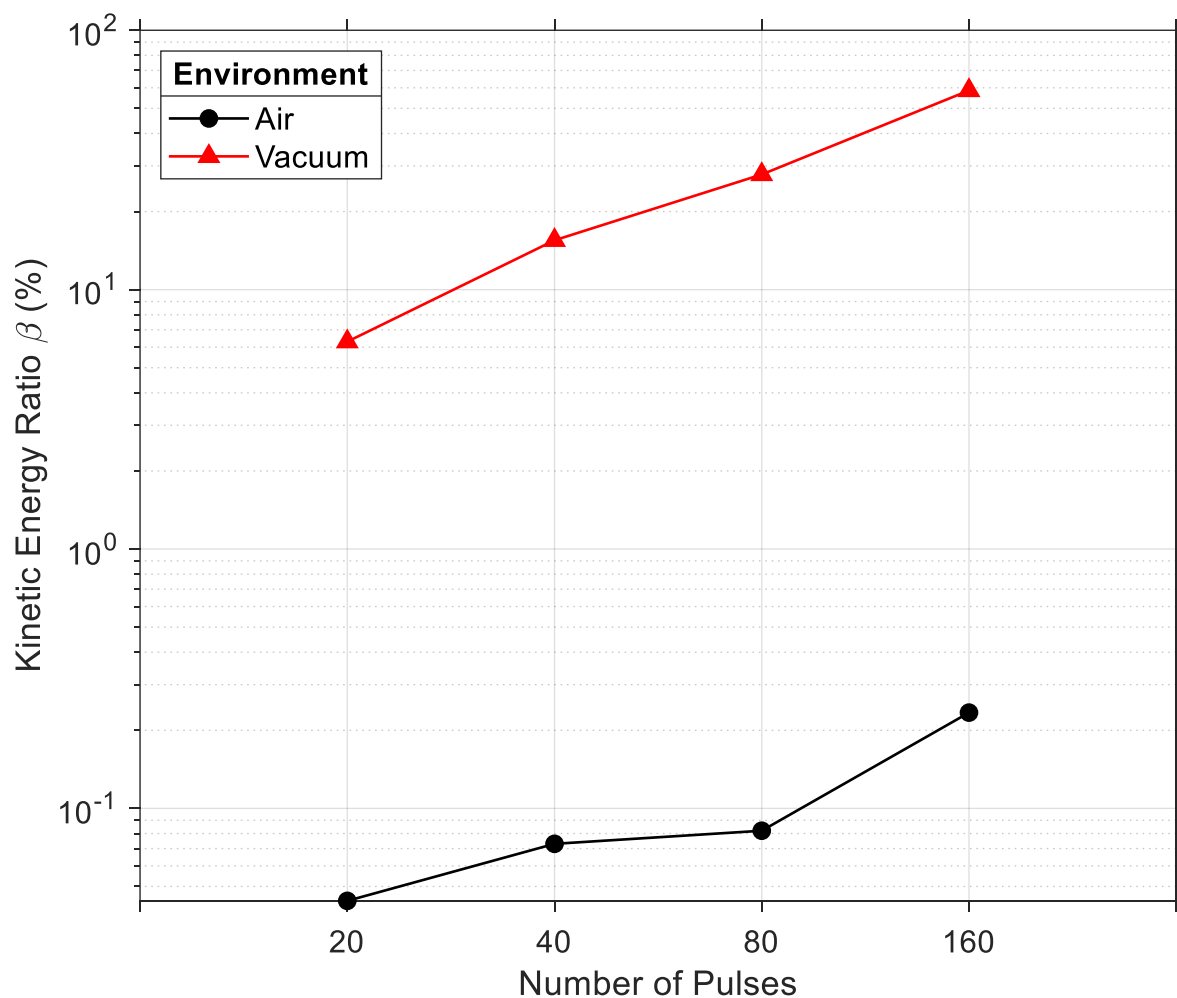


**Figure 72.** A semi-log plot of kinetic energy ratio against number of pulses and environment for PVC. The repetition rate is 5 kHz, the waveform is SW40 and each pulse contains 2.93 mJ.

## 7.4. Effect of Processing Strategy

### 7.4.1. Aluminium

Figure 73 shows the  $C_m$  value with varying repetition rate for different processing strategies on the aluminium target in vacuum using waveform SW5. Overall, the results for single point processing are two orders of magnitude greater than for area processing. The trend in single point processing on the semi-log scale is linear, with the  $C_m$  value increasing from  $\sim 1 \times 10^{-6}$  N/W at 5 kHz to  $3 \times 10^{-6}$  N/W at 40 kHz. The trend in area processing is not linear, as the value increases from  $0.1 \times 10^{-8}$  N/W to  $1 \times 10^{-8}$  N/W between 5 and 10 kHz before dropping to  $0.8 \times 10^{-9}$  N/W at 20 kHz and then increasing again to  $\sim 1 \times 10^{-8}$  N/W at 40 kHz. The results for single point always remain higher than area processing and as such the selection of processing type for optimal  $C_m$  is not highly dependent on repetition rate.

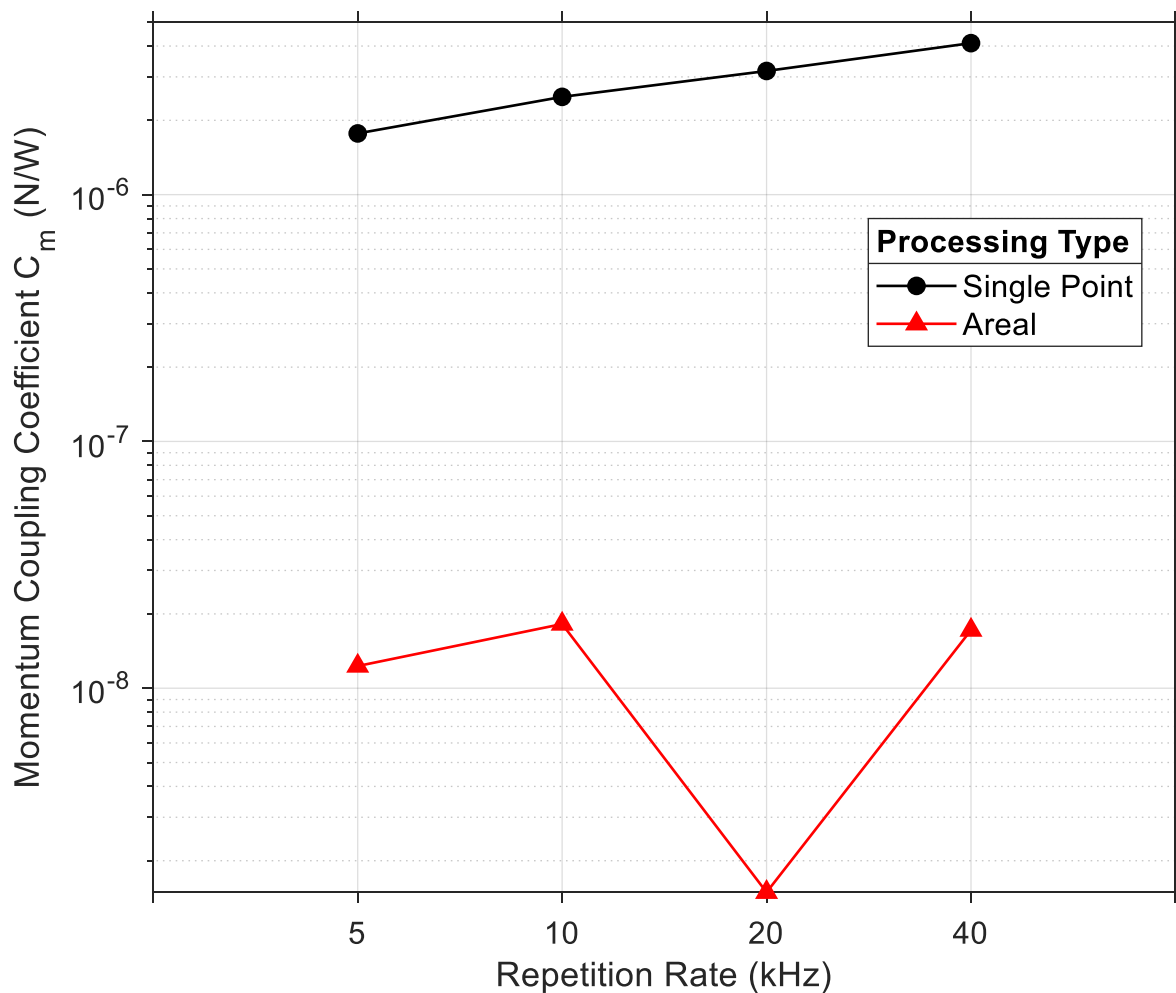


**Figure 73.** A semi-log plot of momentum coupling coefficient against repetition rate and processing type for aluminium in vacuum. The waveform used is SW5 and the number of pulses is 160 and 40,000 for single point and area respectively.

## Results and Analysis

Figure 74 shows the  $C_I$  value with varying repetition rate for different processing strategies on the aluminium target in vacuum using waveform SW5. The overall trend for both processing strategies shows almost no change in  $C_I$  with repetition rate. The values for single point processing are almost 3 orders of magnitude greater than for area processing. The average value for single point processing is  $\sim 2 \times 10^{-9}$  kg/W and  $6 \times 10^{-12}$  kg/W for area processing. The trend is briefly broken at 10 kHz for area processing where the  $C_I$  value increases to  $3 \times 10^{-11}$  kg/W. The results for single point always remain higher than area processing and as such the selection of processing type for optimal  $C_I$  is not highly dependent on repetition rate.

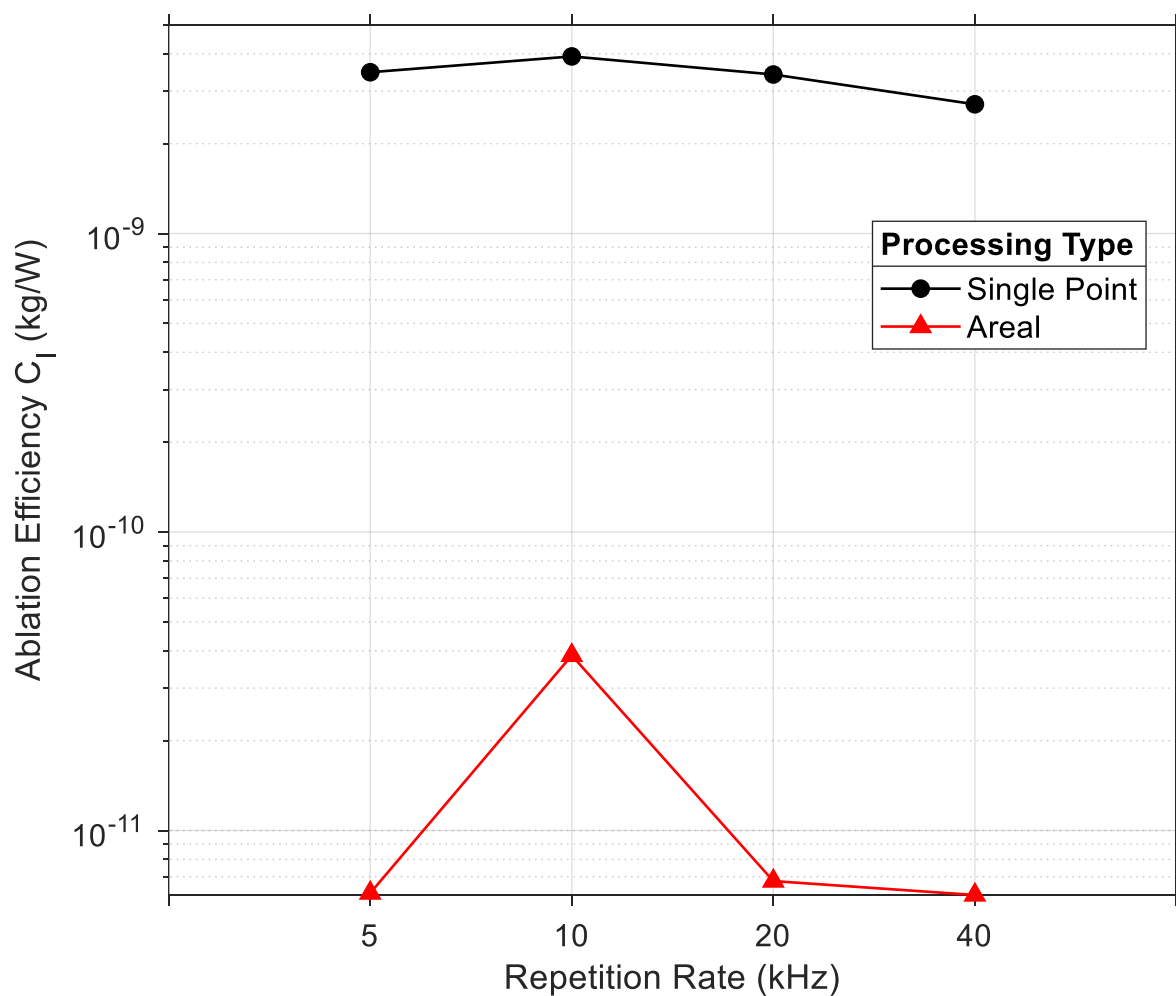


**Figure 74.** A semi-log plot of ablation efficiency against repetition rate and processing type for aluminium in vacuum. The waveform used is SW5 and the number of pulses is 160 and 40,000 for single point and areal respectively.

## Results and Analysis

Figure 75 shows  $\beta$  with varying repetition rate for different processing strategies on the aluminium target in vacuum using waveform SW5. Both trends show an increase of  $\beta$  with increasing repetition rate. The single point processing values are almost two orders of magnitude higher, starting at 0.03% at 5 kHz increasing to 0.2% at 40 kHz. The area processing value begin at 0.0005% at 5 kHz and increase to 0.001% at 40 kHz. As with the previous results for CM and CL, the trend is broken in area processing. In this case there is a drop in  $\beta$  to 0.0004% at 10 kHz after which it rises again. The results for single point always remain higher than area processing and as such the selection of processing type for optimal  $\beta$  is not highly dependent on repetition rate.

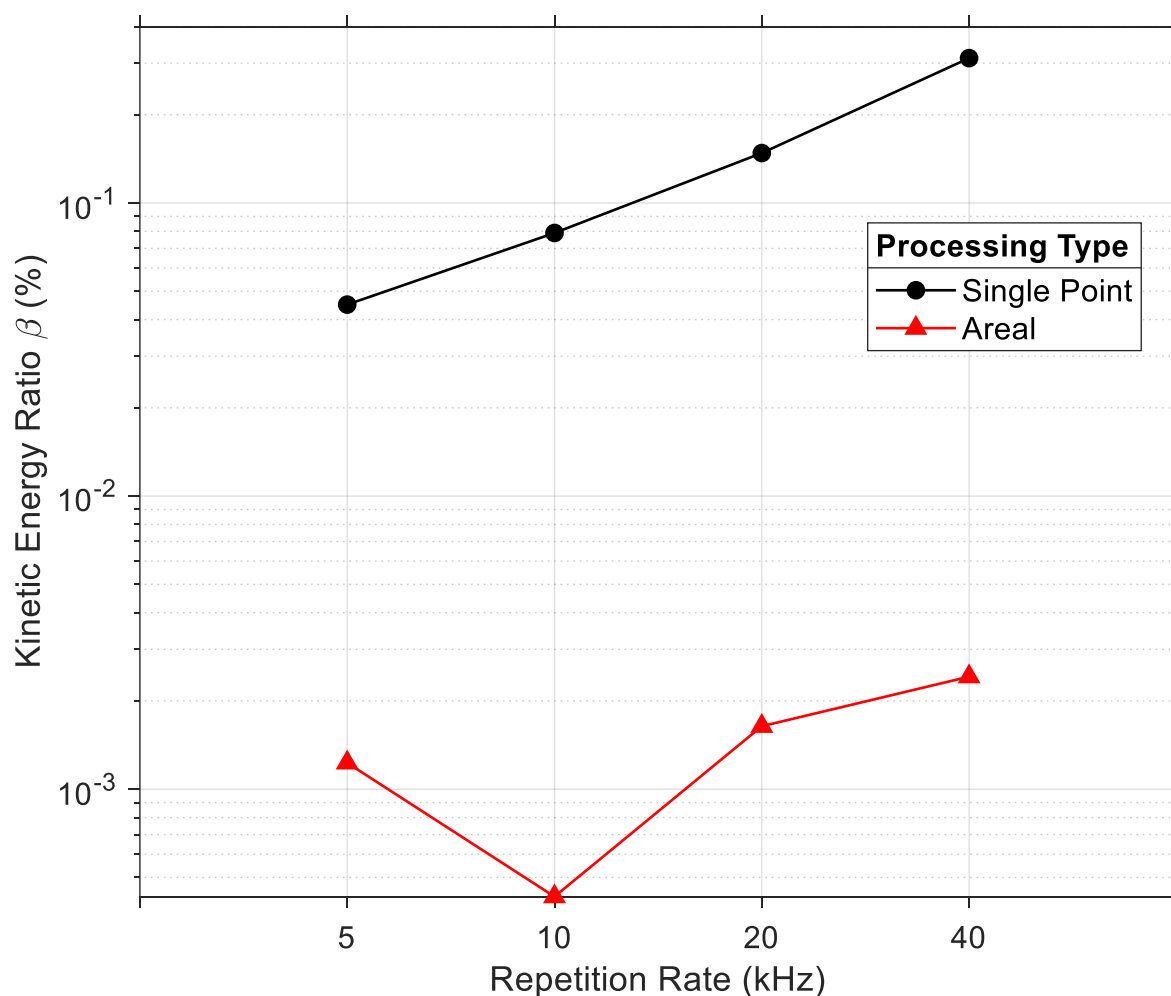


**Figure 75.** A semi-log plot of kinetic energy ratio against repetition rate and processing type for aluminium in vacuum. The waveform used is SW5 and the number of pulses is 160 and 40,000 for single point and area respectively.

## Results and Analysis

### 7.4.2. Silicon

Figure 76 shows the  $C_m$  value with varying repetition rate for different processing strategies on the silicon target in vacuum using waveform SW5. The trend for single point processing shows an increase in  $C_m$  with repetition rate from  $\sim 2 \times 10^{-6}$  N/W at 5 kHz to  $\sim 6 \times 10^{-6}$  N/W at 40 kHz. For area processing the trend shows a decrease in  $C_m$  with repetition rate from  $\sim 3 \times 10^{-8}$  N/W at 5 kHz to  $\sim 9 \times 10^{-9}$  N/W at 40 kHz. The single point processing values are over 2 orders of magnitude greater than that for area processing. The results for single point always remain higher than area processing and as such the selection of processing type for optimal  $C_m$  is not highly dependent on repetition rate.

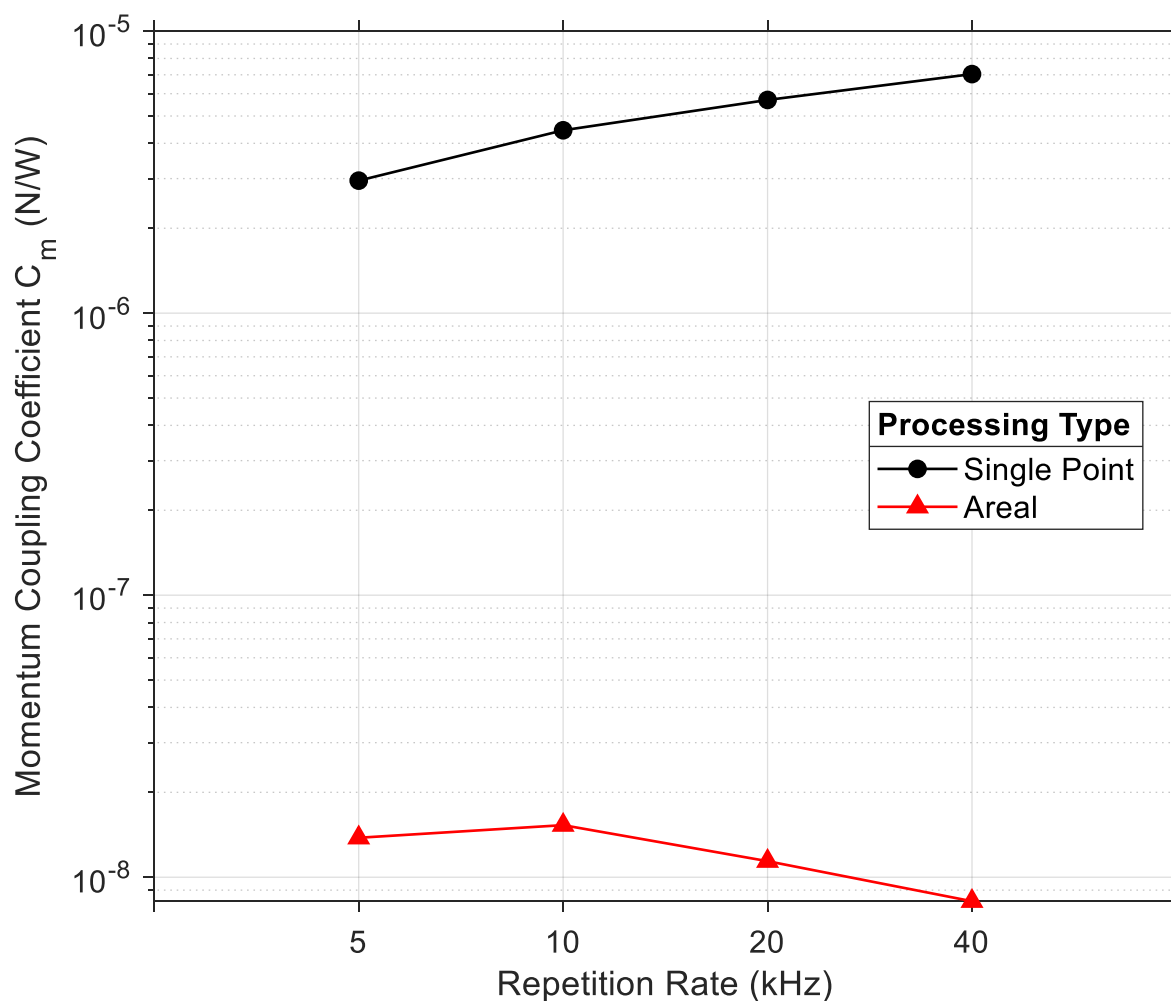


**Figure 76.** A semi-log plot of momentum coupling coefficient against repetition rate and processing type for silicon in vacuum. The waveform used is SW5 and the number of pulses is 160 and 40,000 for single point and area respectively.

## Results and Analysis

Figure 77 shows the  $C_i$  value with varying repetition rate for different processing strategies on the silicon target in vacuum using waveform SW5. Both sets of data follow a similar trend whereby the  $C_i$  value increases from 5 kHz to some critical repetition rate and then reduces again by 40 kHz. For single point processing the  $C_i$  value is  $\sim 1 \times 10^{-8}$  kg/W at 5 kHz, reaching a peak of  $\sim 2 \times 10^{-8}$  kg/W at 10 kHz and then reducing to  $\sim 1.4 \times 10^{-8}$  kg/W at 40 kHz. For area processing, the  $C_i$  value is  $\sim 6 \times 10^{-11}$  kg/W at 5 kHz, reaching a peak of  $\sim 9 \times 10^{-11}$  kg/W at 20 kHz and then reducing to  $\sim 7 \times 10^{-11}$  kg/W at 40 kHz. The single point processing values are over 2 orders of magnitude greater than that for area processing. The results for single point always remain higher than area processing and as such the selection of processing type for optimal  $C_i$  is not highly dependent on repetition rate.

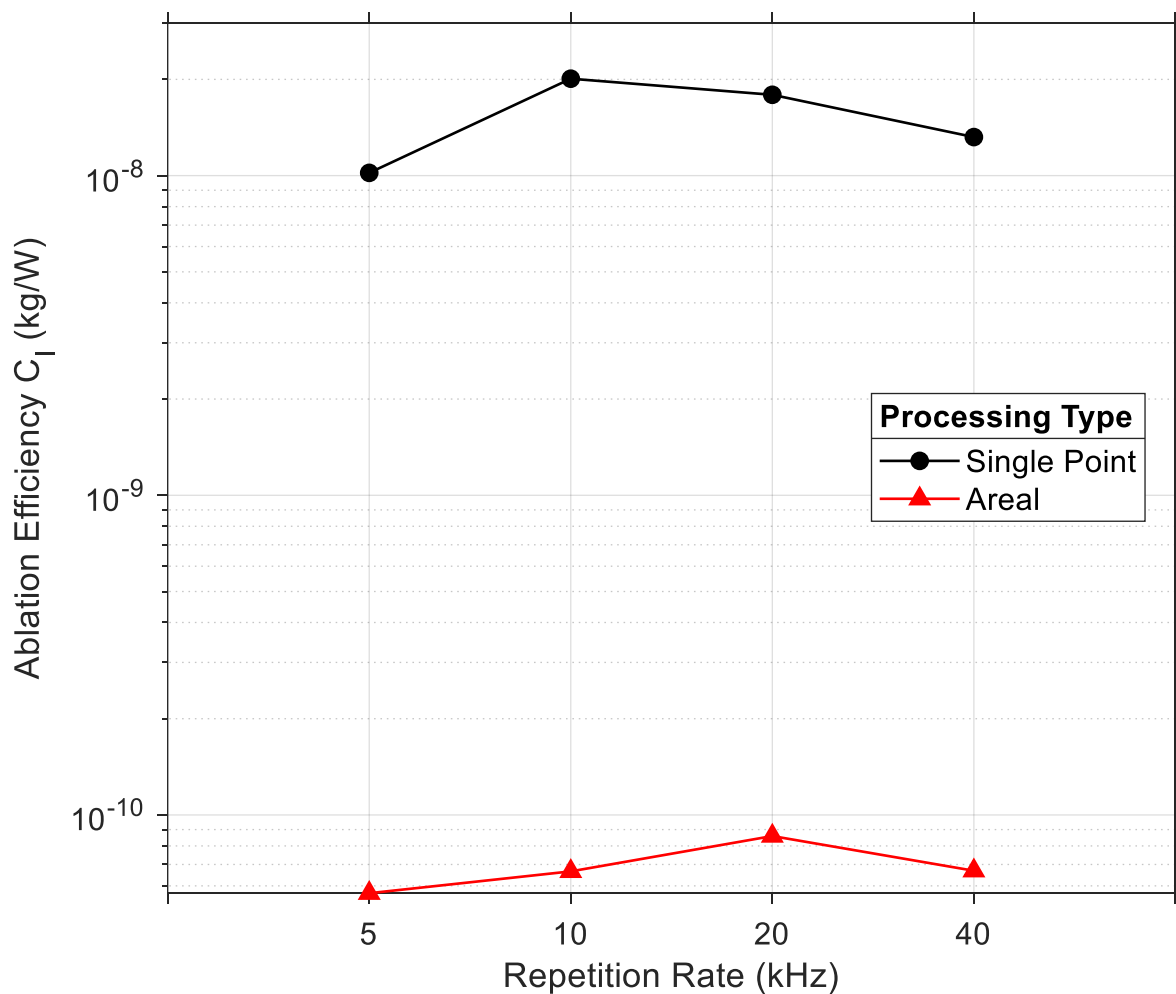


**Figure 77.** A semi-log plot of ablation efficiency against repetition rate and processing type for silicon in vacuum. The waveform used is SW5 and the number of pulses is 160 and 40,000 for single point and area respectively.

## Results and Analysis

Figure 78 shows  $\beta$  with varying repetition rate for different processing strategies on the silicon target in vacuum using waveform SW5. The trend for single point processing shows an increase in  $\beta$  with repetition rate from  $\sim 0.04\%$  at 5 kHz to  $\sim 0.2\%$  at 40 kHz. For area processing, the trend shows a decrease in  $\beta$  with repetition rate from  $\sim 0.0002\%$  at 5 kHz to  $0.00005\%$  at 40 kHz. The single point processing values are over 2 orders of magnitude greater than for area processing. The results for single point always remain higher than area processing and as such the selection of processing type for optimal  $\beta$  is not highly dependent on repetition rate.

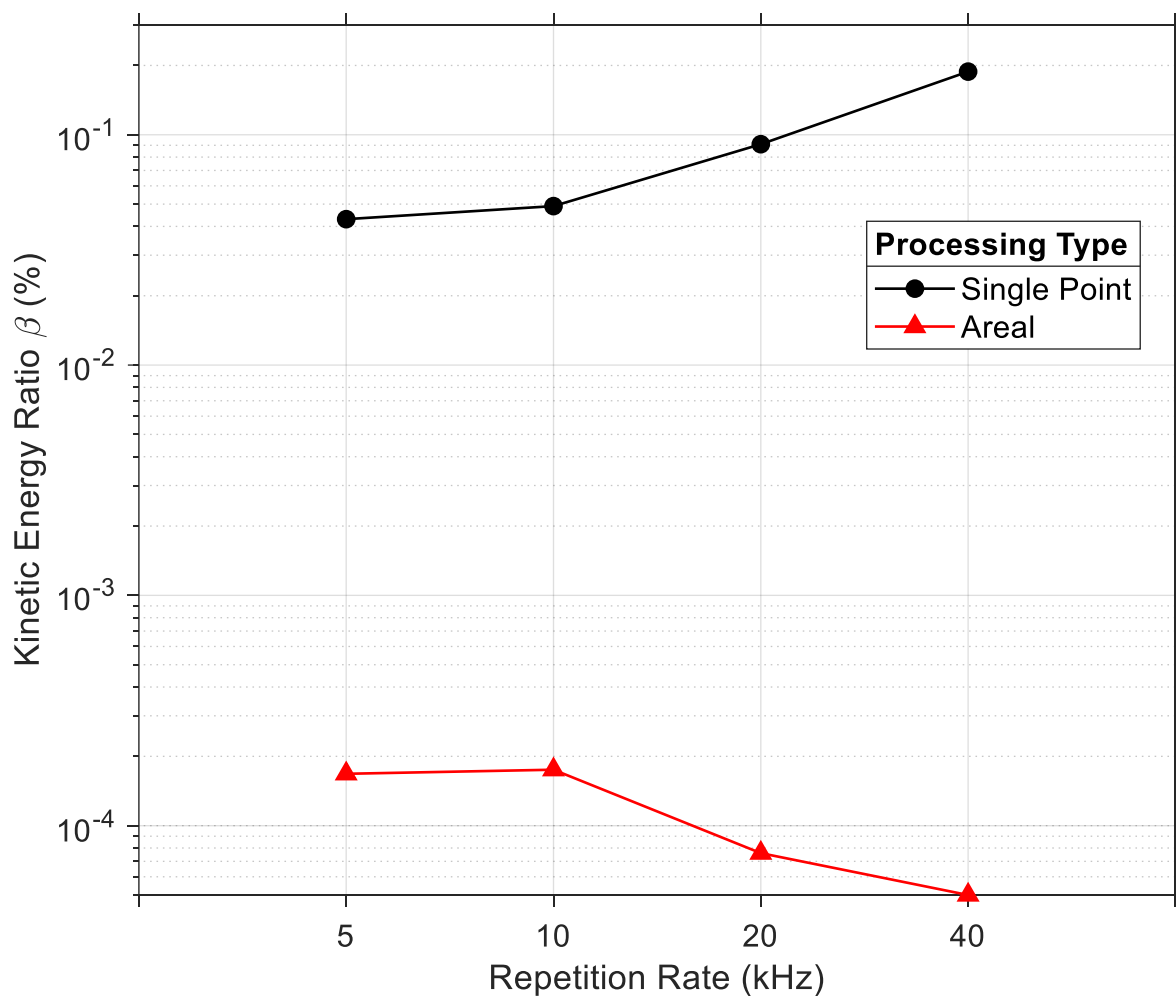


**Figure 78.** A semi-log plot of kinetic energy ratio against repetition rate and processing type for silicon in vacuum. The waveform used is SW5 and the number of pulses is 160 and 40,000 for single point and area respectively.

## Results and Analysis

### 7.4.3. PVC

Figure 79 shows the  $C_m$  value with varying repetition rate for different processing strategies on the PVC target in vacuum using waveform SW5. The trend for single point processing shows a decrease in  $C_m$  with repetition rate from  $\sim 1 \times 10^{-4}$  N/W at 5 kHz to  $\sim 6 \times 10^{-5}$  N/W at 20 kHz where the value approximately remains until 40 kHz. For area processing, the trend shows a rapid decrease in  $C_m$  with repetition rate from  $\sim 1 \times 10^{-5}$  N/W at 5 kHz to  $\sim 2 \times 10^{-6}$  N/W at 10 kHz before rising to  $\sim 2 \times 10^{-5}$  N/W by 40 kHz. The single point processing values are 1 order of magnitude greater than that for area processing. The results for single point always remain higher than area processing and as such the selection of processing type for optimal  $C_m$  is not highly dependent on repetition rate.

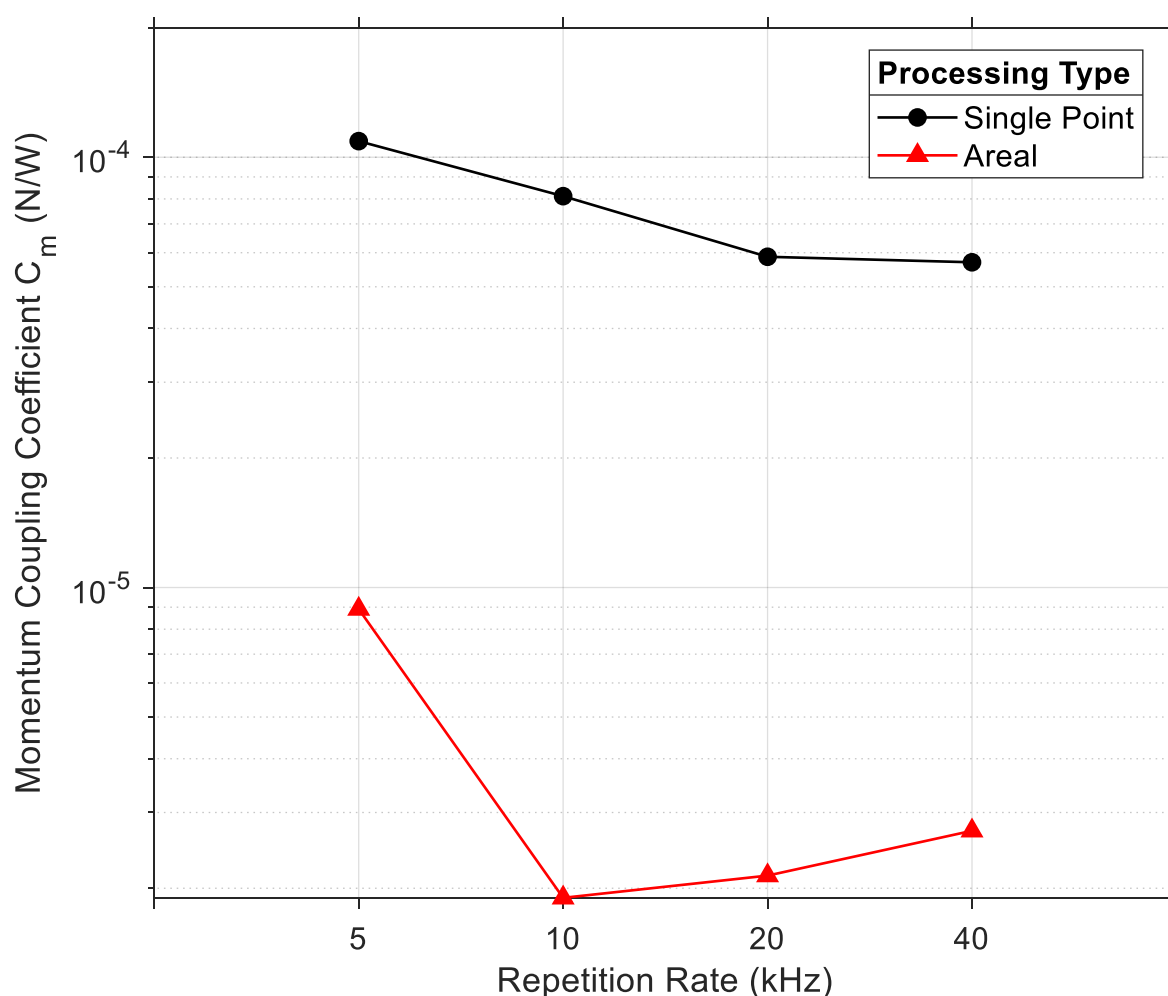


**Figure 79.** A semi-log plot of ablation efficiency against repetition rate and processing type for PVC in vacuum. The waveform used is SW5 and the number of pulses is 160 and 40,000 for single point and area respectively.

## Results and Analysis

Figure 80 shows the  $C_I$  value with varying repetition rate for different processing strategies on the PVC target in vacuum using waveform SW5. The trend in single point processing shows approximately no change in  $C_I$  value with repetition rate, remaining at a value of  $\sim 2 \times 10^{-8}$  kg/W. For area processing, the trend is quite different. Unexpectedly the  $C_I$  value at 5 kHz begins at  $\sim 3 \times 10^{-8}$  kg/W which is above the single point processing value. There is then a sudden drop at 10 kHz to  $\sim 2 \times 10^{-9}$  kg/W before increasing slowly to  $\sim 4 \times 10^{-9}$  kg/W by 40 kHz. The results for single point do not always remain higher than area processing and as such the selection of processing type for optimal  $C_I$  is dependent on repetition rate.

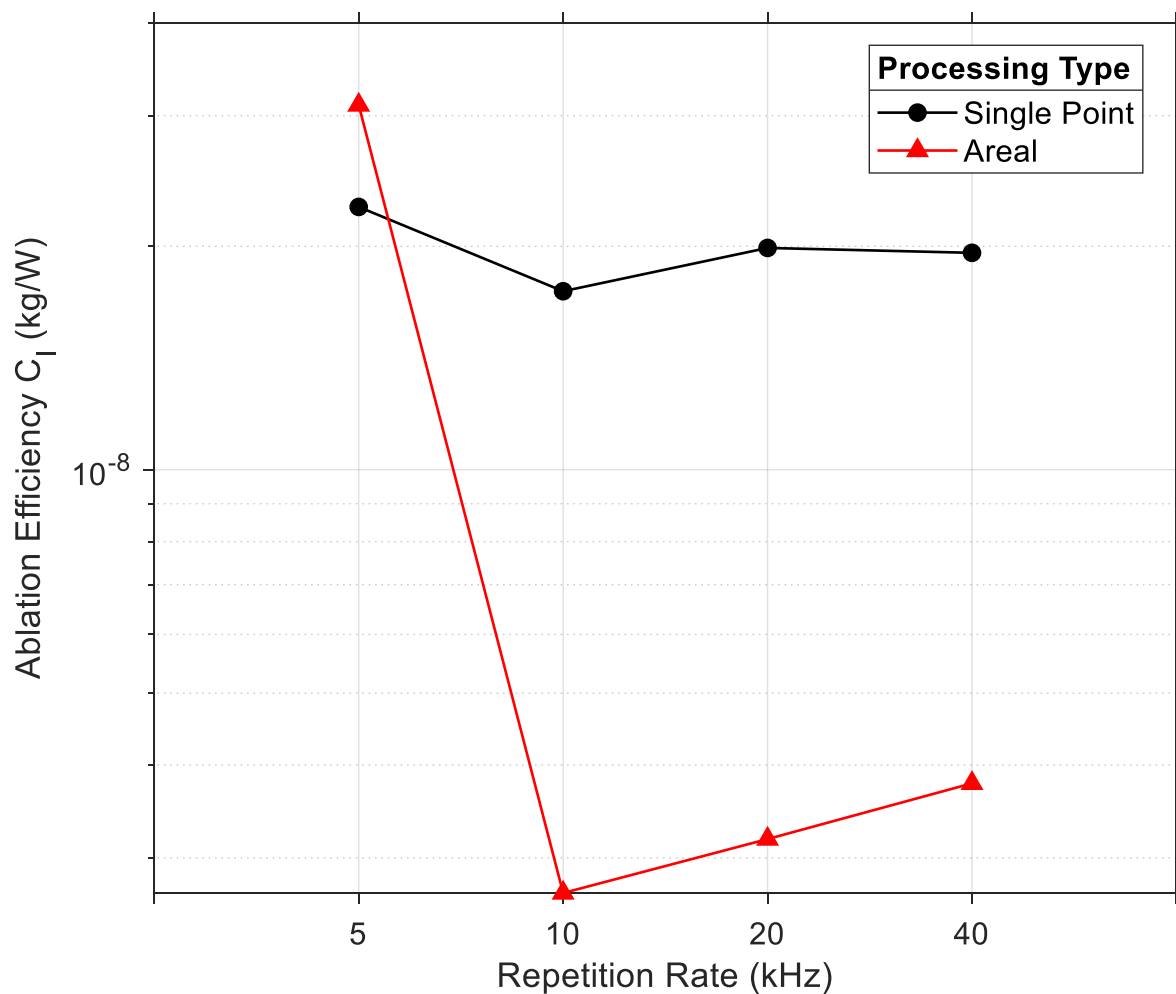


**Figure 80.** A semi-log plot of ablation efficiency against repetition rate and processing type for PVC in vacuum. The waveform used is SW5 and the number of pulses is 160 and 40,000 for single point and area respectively.

## Results and Analysis

Figure 81 shows  $\beta$  with varying repetition rate for different processing strategies on the PVC target in vacuum using waveform SW5. The trend for single point processing shows a decrease in  $\beta$  with repetition rate from ~12% at 5 kHz to ~0.9% at 20 kHz after which the value remains the same until 40 kHz. For area processing, the trend shows a decrease in  $\beta$  with repetition rate from ~0.15% at 5 kHz to 0.007% at 10 kHz which remains the same until 20 kHz, after which the value increase to ~0.1%. The single point processing values are almost 2 orders of magnitude greater than for area processing. The results for single point always remain higher than area processing and as such the selection of processing type for optimal  $\beta$  is not highly dependent on repetition rate.

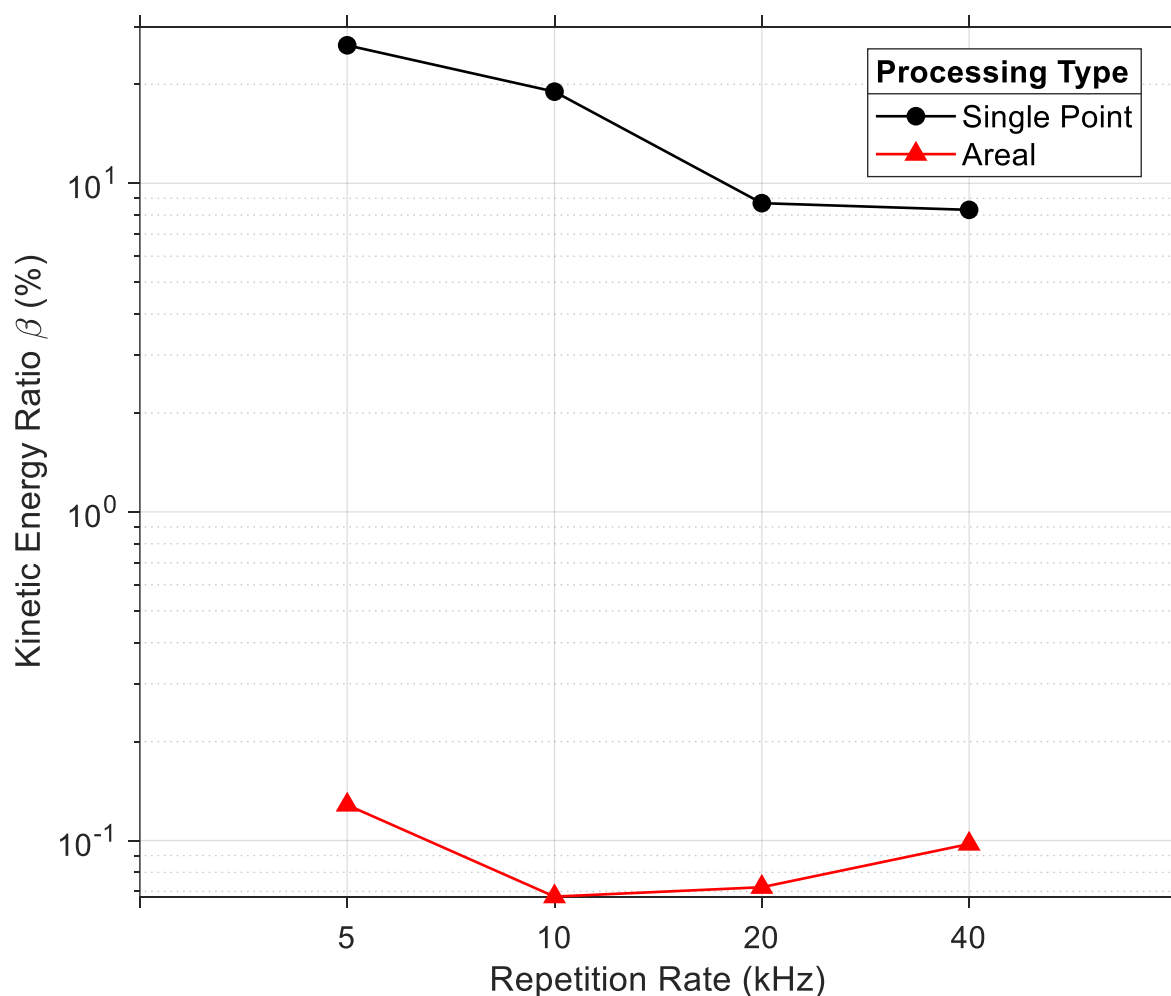


**Figure 81.** A semi-log plot of kinetic energy ratio against repetition rate and processing type for PVC in vacuum. The waveform used is SW5 and the number of pulses is 160 and 40,000 for single point and area respectively.

## 8. Discussion

The force balance was used to analyse the behaviour of varying laser, material, and environmental parameters on three different performance parameters. This was done to understand how well the selected performance parameters can be related to well-known phenomenon (as the force balance is a novel, unproven diagnostic tool) and then to understand and measure how efficiently and effectively laser energy has been used in a process, as required by research objective 2b.

As a first-iteration novel diagnostic tool the balance performed as designed in 5, and evaluated in 6.1. The force balance was able to exhibit its high sensitivity and range as per 6.1, evaluating the three key performance parameters which provided results over 7 orders of magnitude changing parameters such as total energy, repetition rate, waveform, pulse shape, material and environment. The balance did not require any maintenance or changes in hardware, software or calibration scheme. The experiments were conducted in a semi-automated fashion so that the user was only required to perform start-up and power-down procedures such as substrate loading, unloading, vacuum system pumping and laser operation. The high resolution of the force balance was not the most useful performance attribute in these experiments as measurements were generally far from the noise floor of the balance and had an extremely wide spread due to the wide range of laser, material and environmental parameters being tested. The resolution will however be important for conducting repeatability tests or tests where range of each parameter sets are significantly reduced, such as when trying to iterate on a particular region of high performance. The accuracy and repeatability of the system were shown to be very important as many results, such as in figures 47-50, show trends with many values within a similar range with complicated trends which vary discretely between parameter sets.

The results in 7.1 look at the effect of repetition and pulse shape on performance parameters. The majority of the results can be explained by looking at similar phenomenon in laser drilling at low frequencies [116]–[118], where increases in repetition rate are associated with increased ablation and removal of molten material. This is shown across the materials, as in general, performance parameters ( $C_i$ ,  $C_m$  and  $\beta$ ) increase in value with increasing repetition rate. The increased ablation is a result of higher average temperatures within the absorption region of the material, reducing the energy required for melting and evaporation. The increased removal of molten material from the melt front is due to an increased frequency of shockwaves being generated by recoil pressure from each light-matter interaction whilst a higher average temperature and more molten material exists. The theory is briefly described in 2.3.1 and 2.3.2, for when the pulse duration is longer than electron cooling and lattice

## Discussion

heating times so that thermal equilibrium is assumed, and all experiments are assumed to be well above ablation threshold.

The trend between repetition rate and hole morphology is reported in literature which suggests that in general, the depth and diameter, and therefore expelled mass of ablated holes increases with respect to repetition rate up to a critical value, and then begins to decrease [119]–[121]. Above a certain critical value, plasma shielding occurs which absorbs significant laser energy and reduces material removal. This is reflected in values of  $C_I$  across materials. Generally, the critical repetition rates for the performance coefficients decrease from aluminium to silicon to PVC. This also means that a higher average energy accumulation per unit time eventually becomes detrimental to material ejection. This is due to the residual cumulative heat causing significant interaction between pulses and material ejecta [122].

A trend also exists between the performance coefficients and waveforms - the waveforms, shown in figure 42, maintain the same total pulse energy, but differ in energy with respect to time. It is commonly reported in literature that the speed, quality and efficiency of laser drilling operations can be improved by increasing peak power and reducing pulse duration [123], [124]. This is clearly shown by many of the trends in 7.1 where waveforms with a shorter duration and higher peak power produce higher values of performance coefficient. The pulse durations decrease and peak power increase in order: SW5, SW3, SW0, SW35, SW40 as described in figure 42. This result can also be explained by an association with increased ablation through increased temperatures at higher peak powers. It is interesting to note that as the results move away from the region of optimum performance coefficient values, the order of the waveforms change and often reverse entirely or equalise, suggesting parameters sets exist where waveform and repetition rate become irrelevant to performance coefficients. This means they must be in thermally dominated regimes which occur over longer time scales and thus do not follow short pulse behaviours any longer. This also explains that whilst the trends between materials varies with repetition rate and waveform, the performance parameter values do not significantly differ between materials, which is surprising considering their very different properties (see 6.2). The values of  $\beta$  in 7.1 never exceed 0.6%. This suggests that only 0.6% of the laser energy has been converted into kinetic energy. The value is not surprising as the experiments were not designed to find optimum efficiency, but do indicate that a significant amount of energy is being wasted as heat.

The results in 7.2 look at the effect of total energy input and pulse shape on performance parameters. It was expected that more pulses and therefore more total energy input into a material would correspond to a higher plume momentum (mass loss and or velocity) until some critical number of pulses before dropping again. This decrease would be expected as ablation

## Discussion

sites or holes develop non-linearly in diameter and depth - as the depth increases, the plasma becomes confined within the hole which leads to attenuation of incoming optical energy through scattering and inverse Bremsstrahlung absorption into the plasma plume. This is shown in literature for nanosecond laser ablation for up to 100 pulses [125]–[127]. As the crater depths increase with pulse number, the larger area becomes available for energy loss by heat conduction, causing recondensation within the crater [125]. The trends in  $C_m$  and  $C_i$  in 7.2 show this trend across all materials, but much earlier than expected, with the critical pulse number at 40.

An SEM image, shown in figure 82, partially confirms this result by an increase in melt pool volume and slight decrease in diameter with increased number of pulses. It also shows that crater diameters vary with repetition rate. The effects of different waveforms on performance coefficients remain the same as discussed earlier in this section. However, it seems that the value of performance coefficients are less dependent on waveform when looking at total number of pulses – the data in 7.2 shows the waveforms are generally organised by increasing peak power and to a limited extent, reducing pulse duration. The values of  $\beta$  in 7.2 never exceed 1%. This again suggests that very little laser energy has been converted into kinetic energy and that a significant amount of energy is being wasted as heat. This also shows that varying pulse number, repetition rate and waveform in an iso-energetic manner does not have a significant effect on performance parameters in a thermally dominated regime.

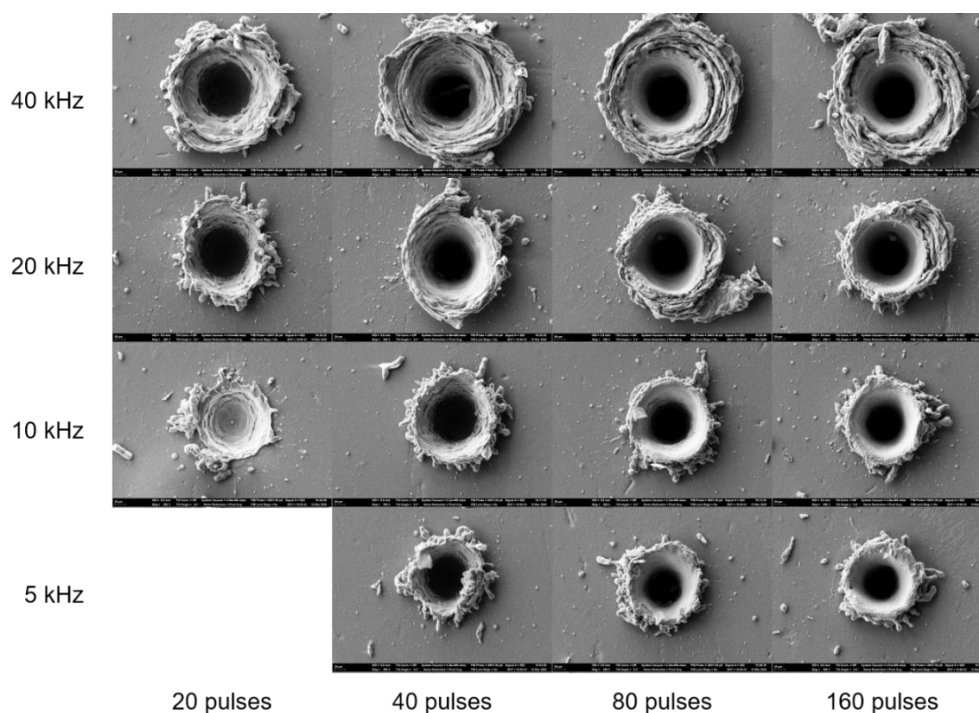


**Figure 82.** A stitched array of SEM images taken using the system described in 6.6.2. At a working distance of 5 mm, magnification of x286 and EHT = 10 kV using the SE2 detector. The SEM images reflect the ablation sites for aluminium in air using waveform SW0, where the X axis represents number of pulses (20, 40, 80, 160) and the Y axis represent the repetition rate (5 kHz, 10 kHz, 20 kHz, 40 kHz).

## Discussion

The results in 7.3 look at the effect of total energy input and environment on performance parameters. With respect to performance coefficients, it was expected that in general, operation in vacuum was to produce higher values than in air. With respect to geometry, an increasing pressure difference between the growing hole or crater and the atmosphere should increase momentum if treated as a supersonic nozzle in a choked flow condition. In a high-vacuum the mean free path is many orders of magnitudes higher which leads to far fewer collisions between particles, allowing for greater momentum to be maintained. The lack of environment also means the types of energy transfer are limited, such as no heat loss via convection. Additionally, no chemical reaction can be initiated in vacuum between target material and environment, such as combustion in air, which potentially diverts energy from the desired processes.

Across all materials, the  $C_m$  values start at a maximum at 20 pulses, but then drop below the values for air at some critical number of pulses after which the values for both environments continue dropping together. The values for  $C_l$  tend to follow the same trend, but with air starting at a maximum and then dropping below values for vacuum after some critical number of pulses. This response is likely due to plasma shielding effects dominating the process at different points. Below the critical pulse numbers, the results suggest that momentum coupling is more efficient in vacuum, whilst material ejection is more efficient in air. The latter result was not expected, as it suggests that the presence of air increases material removal efficiency before the effects of plasma shielding take place. This could be due to laser induced combustion of expelled aluminium particles with air (see 2.3.2).

The  $\beta$  values in air and vacuum for aluminium and silicon show a reduction in value with increasing number of pulses, with PVC showing the opposite trend. It is possible that PVC shows the opposite trend as the effects of plasma shielding begin at a lower critical number of pulses and are overcome by 20 pulses. The  $\beta$  value for vacuum in figure 79 is two orders of magnitude higher than air, reaching a maximum of almost 60% at 160 pulses, which is the highest across all results assessed thus far. This suggests that PVC benefits significantly from being processed in vacuum and that performance parameters suddenly become very sensitive with respect to total energy input when in a different environment. It also shows that far less laser energy is being wasted as heat.

The results in 7.4 look at the effect of processing strategy on performance parameters. The results across all performance parameters and materials show that single point processing using 160 pulses or 0.47 J in the same location is approximately two orders of magnitude more effective than area processing using 40,000 pulses (117.2 J) over an area in vacuum. This can primarily be explained by the earlier analysis which explains how effectively energy is

## Discussion

used, accumulated, and consumed within a drilling-like process. This is reflected by the poor  $\beta$  values across 7.4, which are orders of magnitude lower than all previously examined  $\beta$  values from any material and process parameter. It could be theorised that the ablation threshold is not being reached because there is lots of heat energy vs. kinetic energy, however there is still mass loss being shown which suggests material removal is still taking place. The reason for this could be that the laser was operating in a non-thermally dominated regime, whereby the interaction creates a plume predominantly consisting of a plasma (not a thermally dominated regime) with a high velocity and very low mass loss, showing a low overall kinetic energy.

As generally shown the repetition rate for area processing does effect performance parameters, as consecutive pulses overlap 86%, therefore still allowing for more thermal accumulation to take place. If the pulses did not overlap at all, the performance parameters would not change with repetition rate. In any case the results in this section show, that with respect to momentum coupling, material removal, it is far more energy efficient to drill arrays of holes rather than ablate large areas repeatedly. This also means that it is likely to be more time efficient as well, as less time is required to remove the same mass or volume of material. This is an interesting result as typical industrial laser processing machines scan large areas quickly layer by layer, rather than process small volumes at a time. This kind of analysis would not easily be possible without in-situ mass measurement.

The results in 7.1 – 7.4 highlight many different, non-linear trends between laser, material, environmental, and performance parameters. As required by research objective 2b, the force balance should also be capable of finding relationships that can be used to optimise a process with respect to performance and efficiency. The results as shown are useful for researching very specific combinations of laser, materials, environmental and performance parameters, however this is not usually the case used in academia and industry because the areas of interest for mass removal are usually not well defined and span large areas as shown in figure 1.

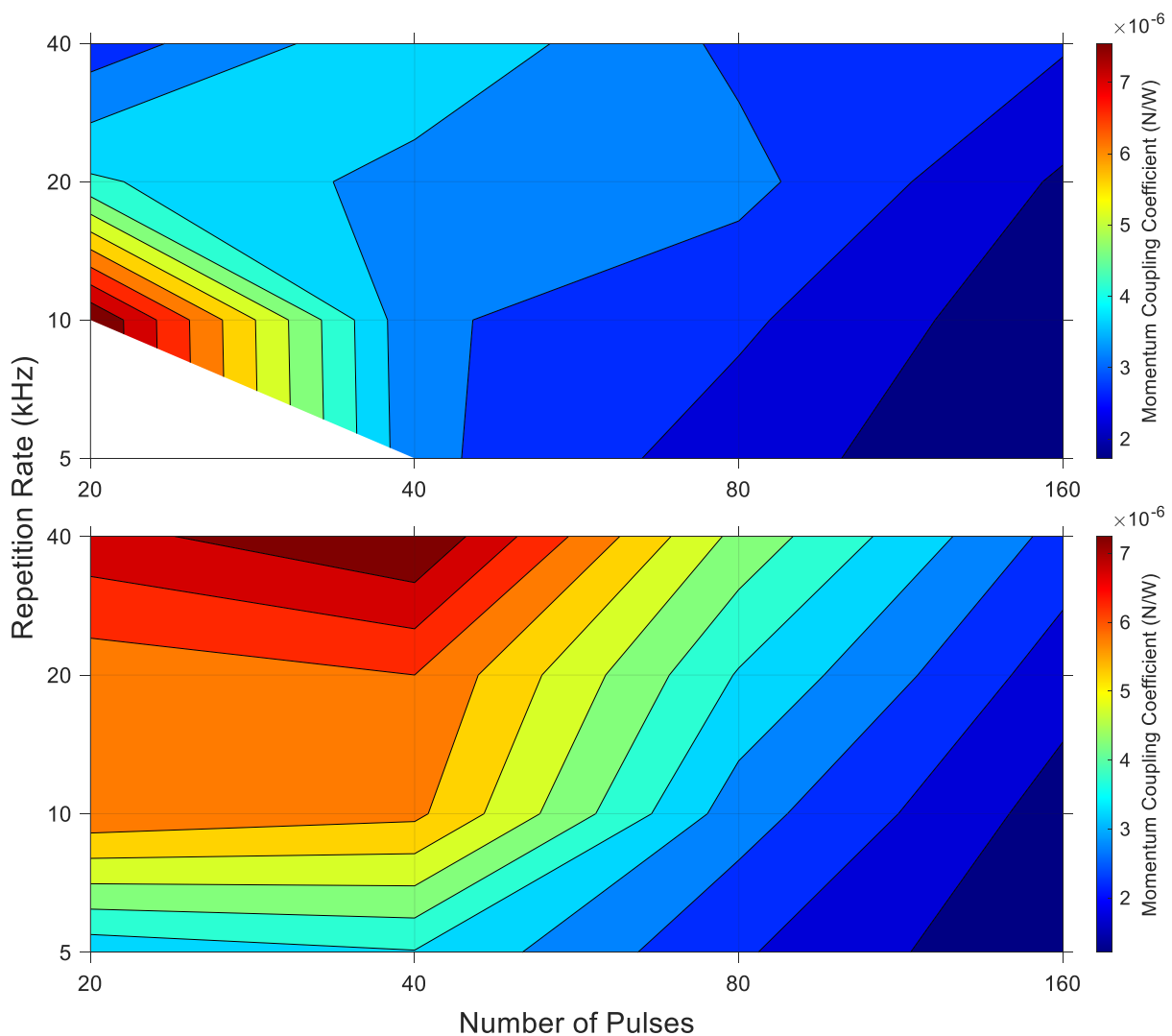
The general approach for achieving this objective will be to combine quantitative and qualitative data in 3D, with the aim of producing a map for every combination of laser, material, environment, and performance used in the system. These should offer the possibility of being stitched together to produce a 'master' map and contribute toward research question 2c, on producing a light-matter interaction framework.

Figure 83 is used as a baseline example. It shows the value of  $C_m$  for aluminium in air and vacuum against repetition rate and number of pulses using waveform SW0. In general, figure 83 shows that the  $C_m$  value decreases with increasing number of pulses. It shows that

## Discussion

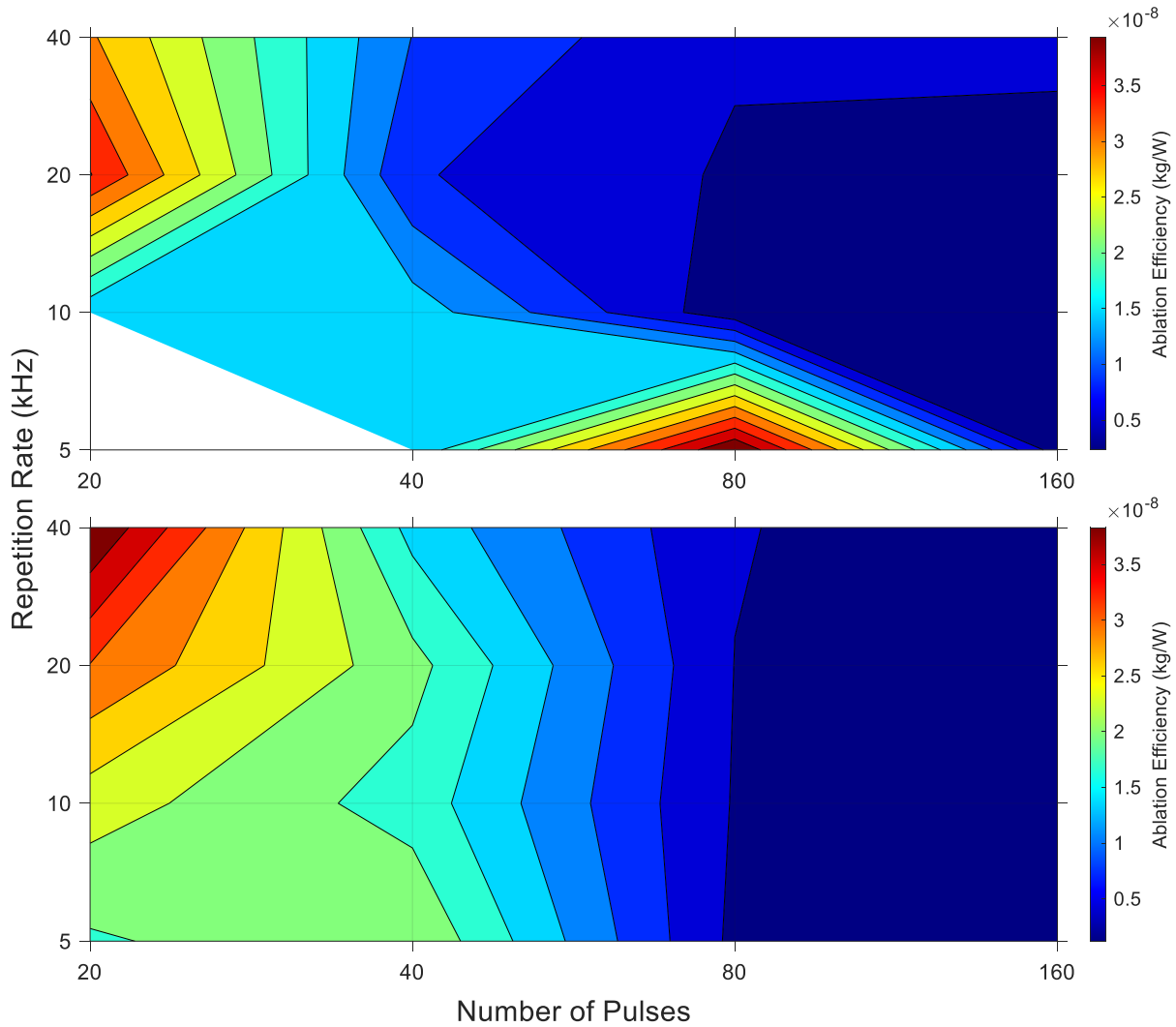
in vacuum, a higher repetition rate is desirable for optimum performance, and vice-versa for air. The data also shows that it is easier to produce a higher  $C_m$  in vacuum than in air given the same laser and material parameters.

Figure 84 shows the corresponding  $C_i$  values for the same parameters used to produce figure 83. A comparison between the two show that in air, the parameter set for optimum  $C_i$  does not overlap much with the parameter set for optimum  $C_m$ . Meanwhile in vacuum, these show a much stronger overlap, which mean that a change in environment can potentially provide multiple performance advantages using the same laser and material parameters. In any case, the results in figure 83 and 84 could be convoluted to find the best parameter for combined overall performance.



**Figure 83 (above).** A filled contour plot of  $C_m$  against repetition rate and number of pulses on the aluminium target in air using waveform SW0. **Figure 83 (below).** A filled contour plot of the  $C_m$  value against repetition rate and number of pulses on the aluminium target in vacuum using waveform SW0.

## Discussion



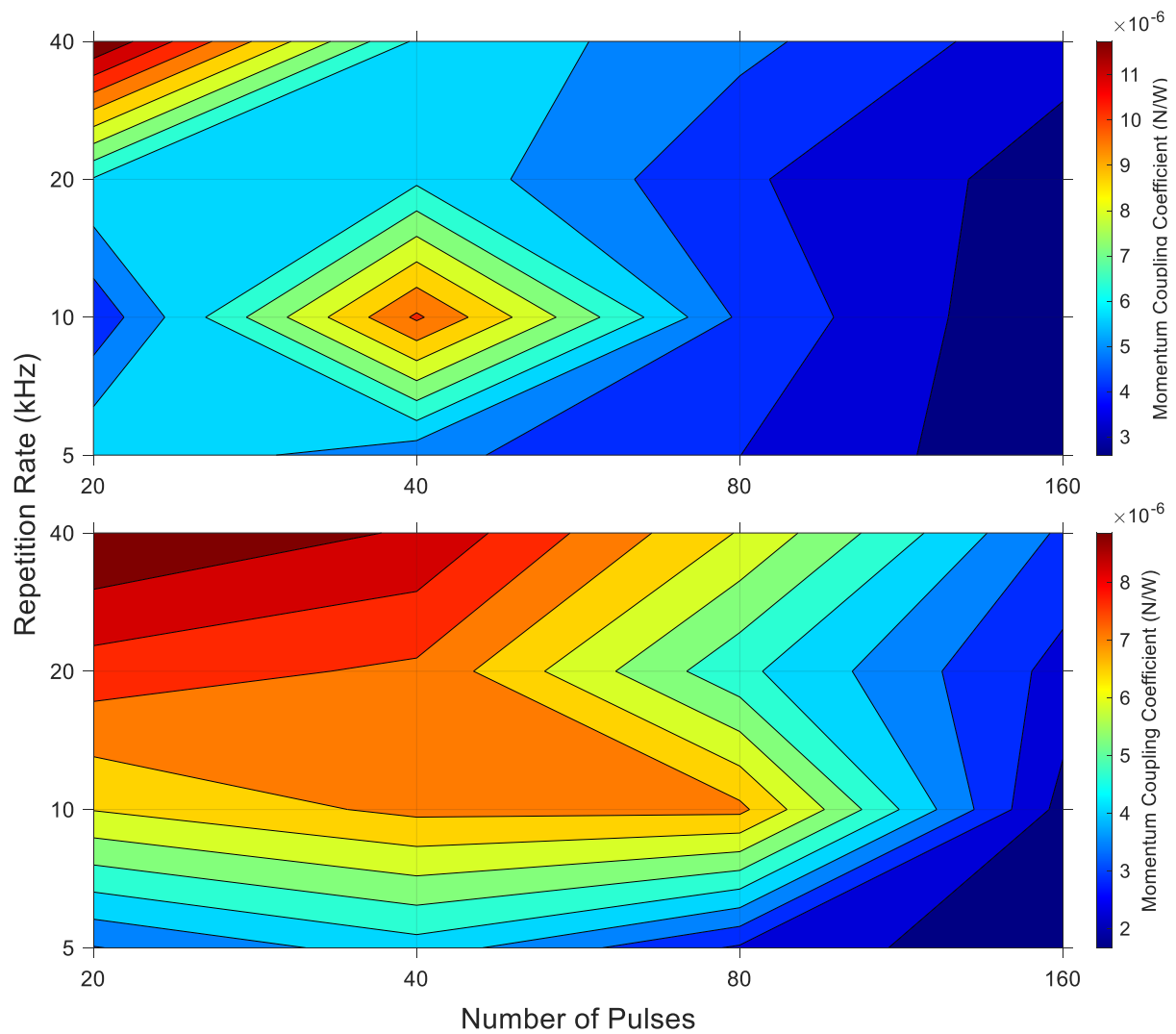
**Figure 84 (above).** A filled contour plot of the  $C_i$  value against repetition rate and number of pulses on the aluminium target in air using waveform SW0. **Figure 84 (below).** A filled contour plot of the  $C_i$  value against repetition rate and number of pulses on the aluminium target in vacuum using waveform SW0.

Figure 85 shows the corresponding  $C_m$  values for aluminium in air and vacuum against repetition rate and number of pulses using waveform SW3 instead of SW0. This map has been produced to highlight the difference in  $C_m$  produced by changing waveform. In comparison to figure 83, the region of optimum performance in air is now found at a higher repetition rate and low pulse number, with an additional area of higher performance appearing at 10 kHz and 40 pulses. Whilst in vacuum, the differences are far less notable, apart from an increase in the area of higher performance between 20 kHz and 40 kHz and 40 pulses to 80 pulses.

Figure 86 shows the corresponding  $C_m$  values for silicon in air and vacuum against repetition rate and number of pulses using waveform SW0. This map has been produced to highlight the differences in performance between materials. In comparison to figure 83 in air, there is a larger area of higher performance with  $C_m$  values of up to two times greater. The performance decreases rapidly with increasing pulse number but is more consistent with increasing

## Discussion

repetition rate. The area in vacuum is not significantly different. This approach can be used to compare the 'processability' of different materials using the same laser and environmental parameters.



**Figure 85 (above).** A filled contour plot of the  $C_m$  value against repetition rate and number of pulses on the aluminium target in air using waveform SW3. **Figure 85 (below).** A filled contour plot of the  $C_m$  value against repetition rate and number of pulses on the aluminium target in vacuum using waveform SW3.

## Discussion

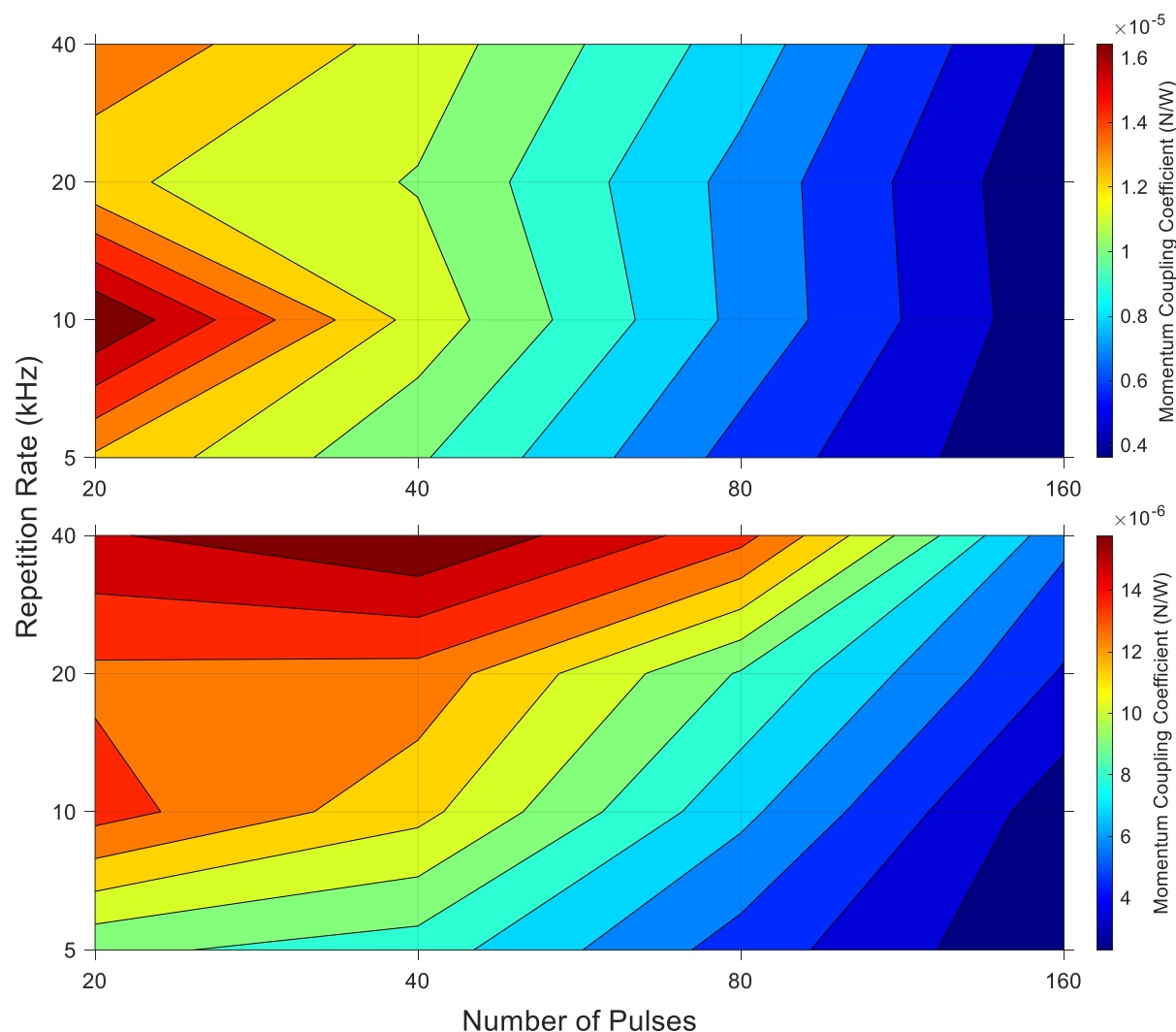


**Figure 86 (above).** A filled contour plot of the  $C_m$  value against repetition rate and number of pulses on the silicon target in air using waveform SW0. **Figure 86 (below).** A filled contour plot of the  $C_m$  value against repetition rate and number of pulses on the silicon target in vacuum using waveform SW0.

These kinds of information rich assessments could be useful for rapid optimisation of processes, which could be performed and computed in very short periods of time - data points from each graph were produced and processed in 16 minutes. The trends in the data could be followed to find processing 'sweet' spots which would otherwise not be seen by coarse or random parameter sweeps. Other types of information could be added to produce a more complete picture of process efficiency, such as using the holographic camera from 3.7, with new performance parameters created for assessment.

For example, the previous sections have focused on optimisation and assessment of performance parameters of light-matter interactions. However, this type of information does not always satisfy all requirements. The quality of resulting ablation sites or surface modifications may also be important. Figure 87 helps illustrate this by showing the corresponding ablation sites used to produce figures 83 and 84, allowing for direct comparison

## Discussion

between performance parameter and physical quality. The images were captured using an SEM described in 6.6.3 - a similar result could be achieved in-situ with the addition of an inline microscope. The general correlation between the figures show that optimum  $C_m$  is achieved at low repetition rate and pulse numbers, where the ablation sites are smaller in diameter and have vastly smaller areas of melt pooling – less energy is going into melting and material removal, and more into exhaust velocity. Optimum  $C_i$  is mostly achieved at high repetition rates and low pulse numbers, where the ablation sites have the largest diameters with relatively small melt pools – less energy is going into melting and exhaust velocity, and more into material removal. Figures 82 and 83 could also be combined as shown in figure 87 below, further linking qualitative and quantitative data.

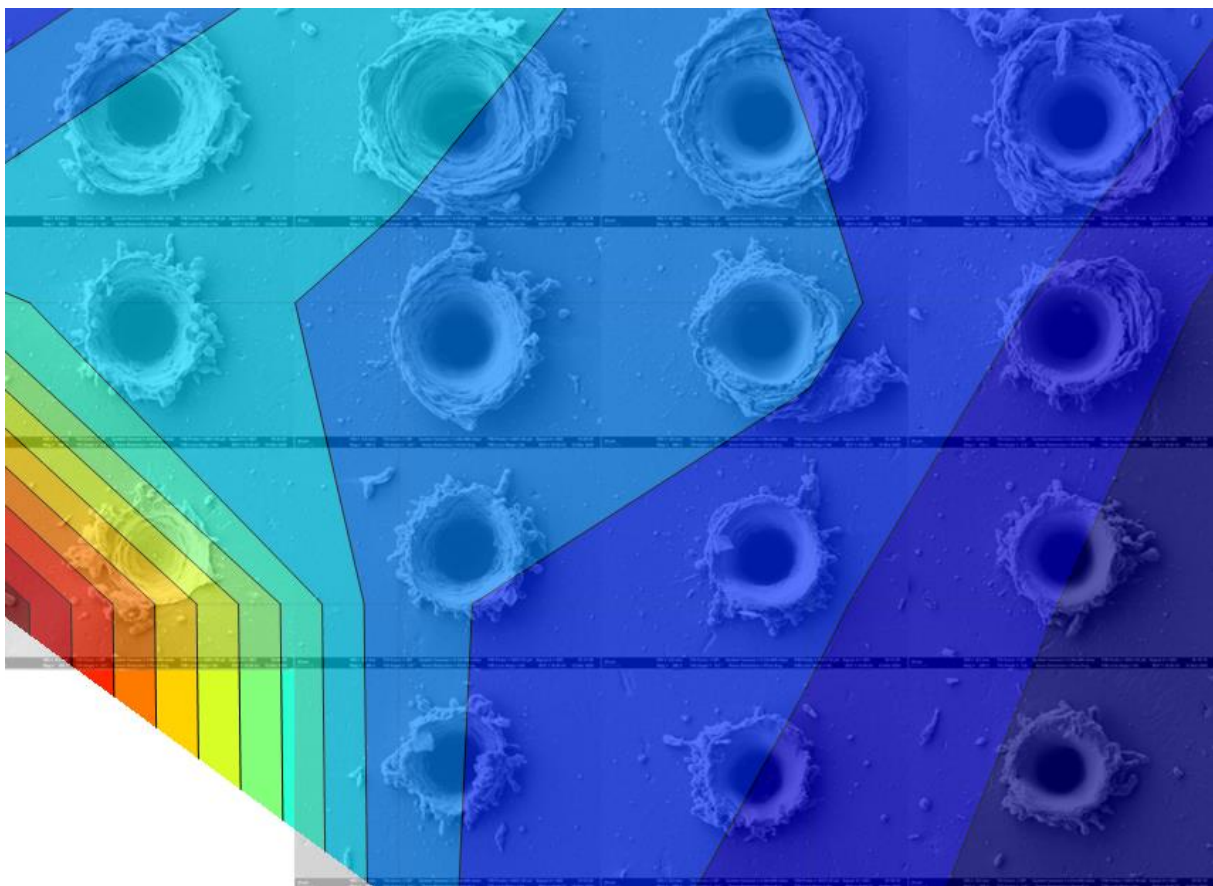


**Figure 87.** An overlay of figures 81 and 82, showing the combination of qualitative data from the force balance and quantitative data from the SEM.

Using the force balance technique could therefore enable a process to be effectively controlled and optimised providing a parameter sweep has taken place. Although this means that the assessment of light-matter interactions remains empirical, it could bring the experimental time down by orders of magnitude compared to conventional techniques, whilst giving new insights into efficiency and energy transfer.

## Discussion

The non-optimised experimental data gathered in this thesis is broad, yet detailed enough to guide decisions according to a specific application e.g. spacecraft propulsion or energy efficient material removal. For spacecraft propulsion,  $C_m$  would be the most useful term as it defines how large an impulse is produced per unit input energy. Using the processing maps from 7.5.1 it has been made obvious that a moderate number of pulses (40), high repetition rate (40 kHz), using SW3 (vs. SW0) in vacuum on silicon is the best choice. Whilst for energy efficient material removal, the  $C_i$  would be most useful term to follow as it defines how much material is removed per unit input energy.

### 9. Conclusions

Light-matter interactions are complex, non-linear processes sensitive to the properties of the source, material, mechanisms, and environment in which they interact. In order to control a process, its key features must be quantifiable and the process understood. To date, most efforts toward doing so usually follow either empirical or theoretical approaches, or less often, a combination of both. However, this has still left existing users and potential users of laser technology operating within unknown grey areas, incurring large time, cost, and energy barriers to find parameter sets which work 'first time'. The aim of the thesis is to reduce this burden using a novel force balance instrument.

The reason for highly academic and or highly empirical study is due to the immense complexity, and non-linear, interdependent behaviour of light-matter interactions dependent on a large number of light, material, and environmental parameters. This is particularly true for short (ns) and ultra-short (<ps) interactions which additionally require measurement tools of equal or faster time resolution, with incredible range and sensitivity due to relatively low output powers. The main disadvantage to academic studies in this field is the number of assumptions and simplifications that must be made for models to be of practical use. Whilst with empirical studies, the time required to cover even small parameter sets is normally enormous and does not usually contribute to building useful models. Comparing these approaches in state of the art in light-matter interaction research provided some understanding of which measurement parameters were useful for consideration across industry and academia, and highlighted the vast measurement ranges, high sensitivity and time resolution required of the tools used.

With this it was possible to assess different balance configurations according to their performance and capability in chapter 4. A vertical torsion balance was selected as it simultaneously provided force and mass-loss data required for the selected performance parameters. Chapter 5 focused on the design and construction of the tool - this chapter represents a significant body of engineering work, covering the development of complex ultra-precise electro-opto-mechanical system drawing on multiple sources of knowledge from electric propulsion testing through to laser processing. The key to the whole system was the novel integration of a phase shifting, angular interferometric displacement sensor which could provide sub-nm resolution at near MHz output frequencies. This system heavily influenced the mechanical, electrical and optical designs, particularly requirements driving data capture rate, bandwidth and processing which were more complicated and demanding than expected.

The empirical work provided by the force balance has shown that for the first time it has been possible to optimise a light-matter interaction without the use of heavily empirical or theoretical

## Conclusions

methods. By tracking performance specific outputs, it has become possible to generically optimise a relevant process or technology very easily, quickly, and efficiently as required by research objective 2b e.g. maximum momentum coupling coefficient for spacecraft propulsion or maximum ablation efficiency for energy efficient material removal (ablation, drilling etc.).

For any given material and environment, a dataset could be captured in as little as 16 minutes. As datasets are presented visually in 3 or more dimensions, trends in data are easily and quickly followed toward 'sweet' spots which would otherwise not be seen by coarse, random, or non-generic sweeps. If required, microscope images can be overlaid to provide a cross-over of qualitative and quantitative information. This enables high parameter resolution, light-matter-environmental parameter maps to be produced within hours, instead of months or years. The end result could be the production of a process map for any given laser or material with low uncertainty. This could revolutionize the way lasers are used and completely change where time and energy is spent in academia and industry.

In general, the instrument and techniques demonstrated had multiple benefits:

- New insights into well understood laser processes by evaluation of force and mass-loss.
- Is sensitive to a large number of variables - laser, material, and environmental.
- Is capable of working within wide parameter ranges, with 7 orders of magnitude demonstrated.
- Is a semi-empirical process producing qualitative and quantitative data.
- Data can be provided with high temporal resolution (MHz demonstrated).
- Data can be traceable to national standards.
- Lends well to commercial implementation.

Whilst the data from experiments are accurate and precise, it is not broad enough by itself to produce a framework from as it only meets a small part of the equation from research question 1d, shown below again.

$$E_{\text{pulse}} - E_{\text{transmitted}} - E_{\text{reflected}} = E_{\text{absorbed}} = E_{\text{shockwave}} + E_{\text{plasma}} + E_{\text{kinetic}} + E_{\text{RF}} + E_{\text{material } \Delta T} + E_{\text{everything else}}$$

The main reason for this is the limited type of data the force balance provides – in this thesis the force balance is assumed to measure the energy being transferred into kinetic energy. In this case, the losses or remainder of the laser energy is assumed to mostly represent thermal coupling into the substrate causing surface modifications, melting and increases in temperature. This re-iterates the requirements for the addition of a digital holographic system which is able to measure such events.

## 10. Future Work

This thesis shows early promise for the use of in-situ force and mass loss measurement for light-matter interactions. Due to the level of technical difficulty in the design, construction and characterisation of the balance system, a significant proportion of time initially dedicated to experiments and analysis was taken up. There is a significant amount of work left to do before the proposed approach is validated.

Ideally, the processing maps discussed in chapter 8 would have been produced for all the data points covered in chapter 7, and then compared to better understand the trends and sensitivity between performance parameters and variables. This is necessary as the processing maps have more dimensions and more detail than the 2D plots, which could lose focus when presented in multiple dimensions. Furthermore, assessing the sensitivity of variables on performance parameters could be another useful analysis, giving users an idea of which operating regimes are easy or hard to attain, or where a wide performance range could be attained. A higher resolution parameter sweep may be required to achieve this e.g. repetition rate going from 5 kHz to 40 kHz in 40 steps instead of 4, or pulse number going from 20 to 160 in 20 steps instead of 4.

Then, with a full set of processing maps a few case studies should be produced. These could for example, cover the applications mentioned in chapter 8 for spacecraft propulsion and laser ablation. By setting requirements with respect to performance parameters, the proposed approach in this thesis could be more thoroughly tested by attempting to optimise a process or technology. Within each case study, which would include theory on a specific application, the balance theory and direct measurement outputs discussed at the beginning of chapter 4 could be more deeply linked to laser matter interaction theory from chapter 2. A direct comparison between balance measurements, theory and empirical studies could then be made and compared.

Following this body of work, the integration, characterisation, and calibration of a digital holographic imaging system from 3.7 would be required to create the proposed diagnostic platform. Then a very simple, well understood process should be selected for analysis. The goal would be to measure as many parts of the equation from research question 1d as possible to understand if a framework for energy efficient and effective technologies/processes can be created using a performance parameter / energy budget approach. Figure 88 shows what the proposed platform would look like.

## Future Work

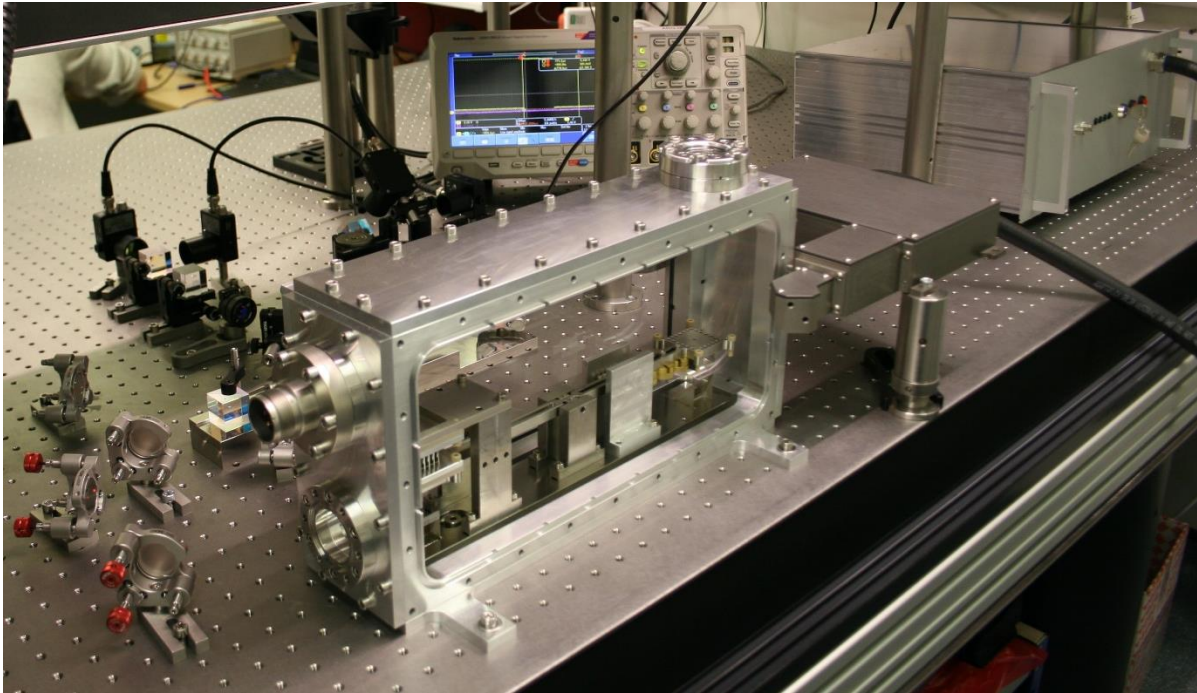


**Figure 88.** A photograph showing early test fits of the balance system and Falcon GHz digital holographic system developed by Pangovski et al. [47], [73], [128]. The Falcon system is shown on the right hand side mounting around the balance chamber, so that its optical path is directly above the balance substrate mount. When combined the two systems, including auxiliary equipment fit within the volume of a typical optical bench (1m x 2m) and do not require any specialist noise isolation, HVAC, or power systems.

The primary challenge expected is conducting experiments with a comparable accuracy, precision, and repeatability to the balance system. This may require extremely rigorous calibration and traceability work, perhaps requiring national or international organisation levels of support e.g. NPL or NIST and strictly controlled environments e.g. atmospheric control or vibration free-environments.

The secondary challenge expected is in data processing and analysis, as extraordinary amounts and types of data would be produced per experiment. This would require significant additional human resources possessing a wide range of multi-disciplinary knowledge. This work could also benefit from the use of machine learning for data analysis as the numerous inputs, outputs, variables, non-linearities make laser matter interaction studies among the most intellectually and physically demanding, requiring deep theoretical and empirical application which any one person rarely possesses.

## References

- [1] D. Bäuerle, *Laser Processing and Chemistry*. Berlin, Heidelberg: Springer Berlin Heidelberg, 2011. doi: 10.1007/978-3-642-17613-5.
- [2] *Laser Material Processing | William Steen | Springer*. Accessed: Apr. 21, 2017. [Online]. Available: <http://www.springer.com/us/book/9781849960618>
- [3] J. Han and Y. Li, 'Interaction Between Pulsed Laser and Materials', in *Lasers - Applications in Science and Industry*, K. Jakubczak, Ed. InTech, 2011. doi: 10.5772/25061.
- [4] M. S. Brown and C. B. Arnold, 'Fundamentals of Laser-Material Interaction and Application to Multiscale Surface Modification', in *Laser Precision Microfabrication*, vol. 135, K. Sugioka, M. Meunier, and A. Piqué, Eds. Berlin, Heidelberg: Springer Berlin Heidelberg, 2010, pp. 91–120. doi: 10.1007/978-3-642-10523-4\_4.
- [5] A. H. Hamad, 'Effects of Different Laser Pulse Regimes (Nanosecond, Picosecond and Femtosecond) on the Ablation of Materials for Production of Nanoparticles in Liquid Solution', *High Energy Short Pulse Lasers*, Sep. 2016, doi: 10/gg7r7r.
- [6] K. Sugioka and Y. Cheng, 'Ultrafast lasers—reliable tools for advanced materials processing', *Light Sci. Appl.*, vol. 3, no. 4, p. e149, Apr. 2014, doi: 10.1038/lsa.2014.30.
- [7] Z. Zhang, Q. Nian, C. C. Dumanidis, and Y. Liao, 'First-principles modeling of laser-matter interaction and plasma dynamics in nanosecond pulsed laser shock processing', *J. Appl. Phys.*, vol. 123, no. 5, p. 054901, Feb. 2018, doi: 10.1063/1.5021894.
- [8] B. Guo, J. Sun, Y. Hua, N. Zhan, J. Jia, and K. Chu, 'Femtosecond Laser Micro/Nano-manufacturing: Theories, Measurements, Methods, and Applications', *Nanomanufacturing Metrol.*, vol. 3, no. 1, pp. 26–67, Mar. 2020, doi: 10.1007/s41871-020-00056-5.
- [9] J. Ion, *Laser Processing of Engineering Materials: Principles, Procedure and Industrial Application*. Butterworth-Heinemann, 2005.
- [10] R. Fabro, 'Laser shock-hardening, physics and applications', in *Conference on Lasers and Electro-Optics Europe*, Amsterdam Netherlands, 1994, pp. 6–6. doi: 10.1109/CLEOE.1994.635761.

## References

- [11] A. Vogel and V. Venugopalan, 'Mechanisms of Pulsed Laser Ablation of Biological Tissues', *Chem. Rev.*, vol. 103, no. 2, pp. 577–644, Feb. 2003, doi: 10.1021/cr010379n.
- [12] S. Svanberg, 'Some Medical and Biological Applications of Ultrafast Lasers', in *Ultrafast Optics IV*, vol. 95, F. Krausz, G. Korn, P. Corkum, and I. A. Walmsley, Eds. New York, NY: Springer New York, 2004, pp. 437–448. doi: 10.1007/978-0-387-34756-1\_55.
- [13] E. Fogarassy, S. Lazare, and Summer School on Laser Ablation of Electronic Materials, Eds., *Laser ablation of electronic materials: basic mechanisms and applications*. Amsterdam: North-Holland, 1992.
- [14] R. Russo, 'Laser ablation in analytical chemistry—a review', *Talanta*, vol. 57, no. 3, pp. 425–451, May 2002, doi: 10.1016/S0039-9140(02)00053-X.
- [15] G. Yang, 'Laser ablation in liquids: Applications in the synthesis of nanocrystals', *Prog. Mater. Sci.*, vol. 52, no. 4, pp. 648–698, May 2007, doi: 10.1016/j.pmatsci.2006.10.016.
- [16] R. S. Craxton *et al.*, 'Direct-drive inertial confinement fusion: A review', *Phys. Plasmas*, Nov. 2015, doi: 10.1063/1.4934714.
- [17] K. Tanaka *et al.*, 'Study on behaviors of laser produced plumes for fusion material ablation', Jun. 2011, pp. 1–1. doi: 10.1109/PLASMA.2011.5993080.
- [18] *Laser Additive Manufacturing*. Elsevier, 2017. doi: 10.1016/C2014-0-03891-9.
- [19] H. J. Booth *et al.*, 'Laser micromachining techniques for industrial MEMS applications', Apr. 2005, p. 190. doi: 10.1117/12.599414.
- [20] C. Phipps *et al.*, 'A Review of Laser Ablation Propulsion', 2010, pp. 710–722. doi: 10.1063/1.3507164.
- [21] M. Keidar *et al.*, 'Electric propulsion for small satellites', *Plasma Phys. Control. Fusion*, vol. 57, no. 1, p. 014005, Jan. 2015, doi: 10.1088/0741-3335/57/1/014005.
- [22] S. Sumida, H. Horisawa, and I. Funaki, 'Experimental Investigation of  $\mu\text{N}$ -class Laser Ablation Thruster', *Trans. Jpn. Soc. Aeronaut. SPACE Sci. SPACE Technol. Jpn.*, vol. 7, no. ists26, p. Pb\_159-Pb\_162, 2009, doi: 10.2322/tstj.7.Pb\_159.

## References

- [23] H. Kuramoto, 'Fundamental Study of a Forward Laser Plasma Accelerator for Space Propulsion Applications', 2004, vol. 702, pp. 493–502. doi: 10.1063/1.1721026.
- [24] C. P. Fernando, 'Nano Satellite Propulsion using FEEP Thrusters', in *Smaller Satellites: Bigger Business?*, vol. 6, M. Rycroft and N. Crosby, Eds. Dordrecht: Springer Netherlands, 2002, pp. 373–376. doi: 10.1007/978-94-017-3008-2\_48.
- [25] D. Bock and M. Tajmar, 'Highly miniaturized FEEP propulsion system (NanoFEEP) for attitude and orbit control of CubeSats', *Acta Astronaut.*, vol. 144, pp. 422–428, Mar. 2018, doi: 10.1016/j.actaastro.2018.01.012.
- [26] M. Tajmar, A. Genovese, and W. Steiger, 'Indium Field Emission Electric Propulsion Microthruster Experimental Characterization', *J. Propuls. Power*, vol. 20, no. 2, pp. 211–218, Mar. 2004, doi: 10.2514/1.9247.
- [27] D. Krejci and P. Lozano, 'Space Propulsion Technology for Small Spacecraft', *Proc. IEEE*, vol. 106, no. 3, pp. 362–378, Mar. 2018, doi: 10.1109/JPROC.2017.2778747.
- [28] H. Yu, H. Li, Y. Wang, L. Cui, S. Liu, and J. Yang, 'Brief review on pulse laser propulsion', *Opt. Laser Technol.*, vol. 100, pp. 57–74, Mar. 2018, doi: 10.1016/j.optlastec.2017.09.052.
- [29] F. Apostolos, S. Panagiotis, S. Konstantinos, and C. George, 'Energy Efficiency Assessment of Laser Drilling Process', *Phys. Procedia*, vol. 39, pp. 776–783, 2012, doi: 10.1016/j.phpro.2012.10.100.
- [30] K. Kellens, G. C. Rodrigues, W. Dewulf, and J. R. Duflou, 'Energy and Resource Efficiency of Laser Cutting Processes', *Phys. Procedia*, vol. 56, pp. 854–864, 2014, doi: 10.1016/j.phpro.2014.08.104.
- [31] 'World Bank Assessment and Action Plan for electricity services in Palestine - WB report', *Question of Palestine*. <https://www.un.org/unispal/document/auto-insert-200068/> (accessed Dec. 20, 2020).
- [32] R. Stoian, M. Boyle, A. Thoss, A. Rosenfeld, G. Korn, and I. V. Hertel, 'Dynamic temporal pulse shaping in advanced ultrafast laser material processing', *Appl. Phys. A*, vol. 77, no. 2, pp. 265–269, Jul. 2003, doi: 10.1007/s00339-003-2112-x.

## References

- [33] R. Le Harzic *et al.*, 'Processing of metals by double pulses with short laser pulses', *Appl. Phys. A*, vol. 81, no. 6, pp. 1121–1125, Nov. 2005, doi: 10.1007/s00339-005-3307-0.
- [34] Peh Siong TEH, 'High Performance Pulsed Fiber Laser Systems for Scientific & Industrial Applications.', Southampton, 2015. [Online]. Available: [https://eprints.soton.ac.uk/383623/1/\\_\\_soton.ac.uk\\_ude\\_personalfiles\\_users\\_jo1d13\\_mydesktop\\_PST%2520thesis.pdf](https://eprints.soton.ac.uk/383623/1/__soton.ac.uk_ude_personalfiles_users_jo1d13_mydesktop_PST%2520thesis.pdf)
- [35] J. Bonse, S. Baudach, J. Krüger, W. Kautek, and M. Lenzner, 'Femtosecond laser ablation of silicon—modification thresholds and morphology', *Appl. Phys. A*, vol. 74, no. 1, pp. 19–25, Jan. 2002, doi: 10.1007/s003390100893.
- [36] M. Kumar Kuntumalla, K. Rajamudili, N. Rao Desai, and V. V. S. S. Srikanth, 'Polarization controlled deep sub-wavelength periodic features written by femtosecond laser on nanodiamond thin film surface', *Appl. Phys. Lett.*, vol. 104, no. 16, p. 161607, Apr. 2014, doi: 10.1063/1.4873139.
- [37] E. Kannatey-Asibu, *Principles of Laser Materials Processing*. Hoboken, NJ, USA: John Wiley & Sons, Inc., 2009. doi: 10.1002/9780470459300.
- [38] W. M. Haynes, *CRC Handbook of Chemistry and Physics, 96th Edition*. CRC Press, 2015.
- [39] Krste Pangovski, 'Temporal pulse design and analysis of silicon ablation using advanced pulse shaping and digital holography in the nanosecond domain', PhD Thesis, University of Cambridge, 2014.
- [40] B. N. Chichkov, C. Momma, S. Nolte, F. von Alvensleben, and A. Tünnermann, 'Femtosecond, picosecond and nanosecond laser ablation of solids', *Appl. Phys. A*, vol. 63, no. 2, pp. 109–115, Aug. 1996, doi: 10.1007/BF01567637.
- [41] B. Rethfeld, A. Kaiser, M. Vicanek, and G. Simon, 'Ultrafast dynamics of nonequilibrium electrons in metals under femtosecond laser irradiation', *Phys. Rev. B*, vol. 65, no. 21, May 2002, doi: 10.1103/PhysRevB.65.214303.
- [42] A. Tilke, L. Pescini, A. Erbe, H. Lorenz, and R. H. Blick, 'Electron-phonon interaction in suspended highly doped silicon nanowires', *Nanotechnology*, vol. 13, no. 4, pp. 491–494, Jun. 2002, doi: 10.1088/0957-4484/13/4/310.

## References

- [43] W. O'Neill and Kun Li, 'High-Quality Micromachining of Silicon at 1064 nm Using a High-Brightness MOPA-Based 20-W Yb Fiber Laser', *IEEE J. Sel. Top. Quantum Electron.*, vol. 15, no. 2, pp. 462–470, 2009, doi: 10.1109/JSTQE.2009.2012269.
- [44] K.-H. Leitz, B. Redlingshöfer, Y. Reg, A. Otto, and M. Schmidt, 'Metal Ablation with Short and Ultrashort Laser Pulses', *Phys. Procedia*, vol. 12, pp. 230–238, Jan. 2011, doi: 10.1016/j.phpro.2011.03.128.
- [45] Jr. G. E. J. R. F. Wood, 'Time-resolved reflectivity measurements on silicon and germanium using a pulsed excimer KrF laser heating beam.', *Phys. Rev. B*, vol. 34(4), pp. 25, 27, 126, 1986.
- [46] M. von Allmen, 'Laser drilling velocity in metals', *J. Appl. Phys.*, vol. 47, no. 12, pp. 5460–5463, Dec. 1976, doi: 10.1063/1.322578.
- [47] A. G. Demir, K. Pangovski, W. O'Neill, and B. Previtali, 'Investigation of pulse shape characteristics on the laser ablation dynamics of TiN coatings in the ns regime', *J. Phys. Appl. Phys.*, vol. 48, no. 23, p. 235202, Jun. 2015, doi: 10.1088/0022-3727/48/23/235202.
- [48] M. von Allmen and A. Blatter, *Laser-Beam Interactions with Materials*, vol. 2. Berlin, Heidelberg: Springer Berlin Heidelberg, 1995. doi: 10.1007/978-3-642-57813-7.
- [49] D. J. Lee and S. H. Jeong, 'Analysis of recoil force during Nd:YAG laser ablation of silicon', *Appl. Phys. A*, vol. 79, no. 4–6, pp. 1341–1344, Sep. 2004, doi: 10.1007/s00339-004-2767-y.
- [50] R. K. Singh and J. Narayan, 'Pulsed-laser evaporation technique for deposition of thin films: Physics and theoretical model', *Phys. Rev. B*, vol. 41, no. 13, pp. 8843–8859, May 1990, doi: 10.1103/PhysRevB.41.8843.
- [51] W. Zhang, Z. Wei, Y. B. Wang, and G. Y. Jin, 'Numerical simulation of laser-supported combustion wave induced by millisecond-pulsed laser on aluminum alloy', *Laser Phys.*, vol. 26, no. 1, p. 015001, Jan. 2016, doi: 10.1088/1054-660X/26/1/015001.
- [52] K. Shimamura, J. A. Ofori, K. Komurasaki, and H. Koizumi, 'Predicting propagation limits of laser-supported detonation by Hugoniot analysis', *Jpn. J. Appl. Phys.*, vol. 54, no. 1, p. 016201, Jan. 2015, doi: 10.7567/JJAP.54.016201.

## References

- [53] I. H. Hutchinson, 'Principles of Plasma Diagnostics: Second Edition', *Plasma Phys. Control. Fusion*, vol. 44, no. 12, pp. 2603–2603, Dec. 2002, doi: 10.1088/0741-3335/44/12/701.
- [54] A. A. Ovsyannikov and M. F. Zhukov, *Plasma Diagnostics*. Cambridge Int Science Publishing, 2000.
- [55] I. O. Misiruk, O. I. Timoshenko, V. S. Taran, and I. E. Garkusha, 'Data acquisition system based on Arduino platform for Langmuir probe plasma measurements', Oct. 2016, pp. 128–131. doi: 10.1109/YSF.2016.7753818.
- [56] 'Holographic Interferometry (Pure & Applied Optics) by Charles M. Vest: Wiley-Blackwell 9780471906834 - Anybook Ltd.' <https://www.abebooks.co.uk/Holographic-Interferometry-Pure-Applied-Optics-Charles/17929753407/bd> (accessed Apr. 28, 2017).
- [57] Mazumdar, Amrita, 'Principles and Techniques of Schlieren Imaging Systems', *Dep. Comput. Sci. Columbia Univ.*, 2013, [Online]. Available: <http://hdl.handle.net/10022/AC:P:20839>
- [58] P. K. Panigrahi and K. Muralidhar, 'Laser Schlieren and Shadowgraph', in *Schlieren and Shadowgraph Methods in Heat and Mass Transfer*, New York, NY: Springer New York, 2012, pp. 23–46. doi: 10.1007/978-1-4614-4535-7\_2.
- [59] 'Synthetic schlieren: Determination of the density gradient generated by internal waves propagating in a stratified fluid', *ResearchGate*. [https://www.researchgate.net/publication/230971921\\_Synthetic\\_schlieren\\_Determination\\_of\\_the\\_density\\_gradient\\_generated\\_by\\_internal\\_waves\\_propagating\\_in\\_a\\_stratified\\_fluid](https://www.researchgate.net/publication/230971921_Synthetic_schlieren_Determination_of_the_density_gradient_generated_by_internal_waves_propagating_in_a_stratified_fluid) (accessed Apr. 28, 2017).
- [60] J. M. D. R. Deron, 'Shadow, Schlieren and Color Interferometry.', [Online]. Available: <http://www.aerospacelab-journal.org/al1/Shadow-Schlieren-and-Color-Interferometry>
- [61] Y. A Leslie, 'Interferograms, Schlieren, and Shadowgraphs Constructed from Real- and Ideal-Gas, Two- and Three-Dimensional Computed Flowfields'. <http://www.worldlibrary.org/eBooks/WPLBN0002209127-Interferograms-Schlieren-and-Shadowgraphs-Constructed-from-Real-and-Ideal-Gas-Two-and-Thre-by-Yates-Leslie-A.aspx> (accessed Apr. 28, 2017).

## References

- [62] J.-M. Desse, P. Picart, and P. Tankam, 'Digital three-color holographic interferometry for flow analysis', *Opt. Express*, vol. 16, no. 8, p. 5471, Apr. 2008, doi: 10.1364/OE.16.005471.
- [63] G. Pedrini, W. Osten, and M. E. Gusev, 'High-speed digital holographic interferometry for vibration measurement', *Appl. Opt.*, vol. 45, no. 15, p. 3456, May 2006, doi: 10.1364/AO.45.003456.
- [64] R. Doleček, V. Kopecký, P. Psota, and V. Lédl, 'Digital Holographic setup for Measurement of Asymmetric Temperature Field and Tomographic Reconstruction', *EPJ Web Conf.*, vol. 48, p. 00003, 2013, doi: 10.1051/epjconf/20134800003.
- [65] G. Nehmetallah, P. P. Banerjee, and S. Praharaj, 'Digital Holographic Tomography for 3-D Visualization', 2011, p. DWE3. doi: 10.1364/DH.2011.DWE3.
- [66] G. Nehmetallah and P. P. Banerjee, 'SHOT: single-beam holographic tomography', Nov. 2010, p. 78510I. doi: 10.1117/12.873083.
- [67] H. G. Tompkins and W. A. McGahan, *Spectroscopic Ellipsometry and Reflectometry: A User's Guide*. Wiley, 1999.
- [68] R. H. Huddlestone and S. L. Leonard, *Plasma diagnostic techniques*. Academic Press, 1965.
- [69] D. Robinson and P. D. Lenn, 'Plasma Diagnostics by Spectroscopic Methods', *Appl. Opt.*, vol. 6, no. 6, pp. 983–1000, Jun. 1967, doi: 10.1364/AO.6.000983.
- [70] J. B. Ahmed and F. Fouad, 'Effect of Spectral Line Self-Absorption on the Laser-Induced Plasma Diagnostics', *IEEE Trans. Plasma Sci.*, vol. 42, no. 8, pp. 2073–2078, Aug. 2014, doi: 10.1109/TPS.2014.2331851.
- [71] F. Rezaei and S. H. Tavassoli, 'Developing the model of laser ablation by considering the interplay between emission and expansion of aluminum plasma', *Phys. Plasmas*, vol. 20, no. 1, p. 013301, Jan. 2013, doi: 10.1063/1.4773036.
- [72] 'A holographic method for optimisation of laser-based production processes : Advanced Optical Technologies', Apr. 01, 2016.  
<https://www.degruyter.com/view/j/aot.2016.5.issue-2/aot-2015-0057/aot-2015-0057.xml>  
(accessed May 01, 2017).

## References

- [73] K. Pangovski *et al.*, 'Investigation of plume dynamics during picosecond laser ablation of H13 steel using high-speed digital holography', *Appl. Phys. A*, vol. 123, no. 2, Feb. 2017, doi: 10.1007/s00339-016-0589-3.
- [74] A. G. Demir, K. Pangovski, W. O'Neill, and B. Previtali, 'Laser micromachining of TiN coatings with variable pulse durations and shapes in ns regime', *Surf. Coat. Technol.*, vol. 258, pp. 240–248, Nov. 2014, doi: 10.1016/j.surfcoat.2014.09.021.
- [75] K. Pangovski *et al.*, 'Control of Material Transport Through Pulse Shape Manipulation&#x2014;A Development Toward Designer Pulses', *IEEE J. Sel. Top. Quantum Electron.*, vol. 20, no. 5, pp. 51–63, Sep. 2014, doi: 10.1109/JSTQE.2014.2302441.
- [76] J. E. Polk *et al.*, 'Recommended Practice for Thrust Measurement in Electric Propulsion Testing', *J. Propuls. Power*, pp. 1–17, Apr. 2017, doi: 10.2514/1.B35564.
- [77] F. G. Hey, A. Keller, C. Braxmaier, M. Tajmar, U. Johann, and D. Weise, 'Development of a Highly Precise Micronewton Thrust Balance', *IEEE Trans. Plasma Sci.*, vol. 43, no. 1, pp. 234–239, Jan. 2015, doi: 10.1109/TPS.2014.2377652.
- [78] 'Thrust Measurements with the ONERA Micronewton Balance', *ResearchGate*.  
[https://www.researchgate.net/publication/242185203\\_Thrust\\_Measurements\\_with\\_the\\_ONERA\\_Micronewton\\_Balance](https://www.researchgate.net/publication/242185203_Thrust_Measurements_with_the_ONERA_Micronewton_Balance) (accessed May 02, 2017).
- [79] E. Canuto and A. Rolino, 'Nanobalance: An automated interferometric balance for micro-thrust measurement', *ISA Trans.*, vol. 43, no. 2, pp. 169–187, Apr. 2004, doi: 10.1016/S0019-0578(07)60028-7.
- [80] A. Kodys, R. Murray, L. Cassady, and E. Choueiri, 'An Inverted-Pendulum Thrust Stand for High-Power Electric Thrusters', 東京工業大学附属図書館 文献データベース.  
<http://tdl.libra.titech.ac.jp/journaldocs/recordID/article.bib-02/ZR000000181773>  
(accessed May 02, 2017).
- [81] R. Lee, B. D'Souza, T. Lilly, and A. Ketsdever, 'Thrust Stand micro-Mass Balance Diagnostic Techniques for the Direct Measurement of Specific Impulse', Jul. 2007. doi: 10.2514/6.2007-5300.
- [82] 'A Torsional Balance that Resolves Sub-micro-Newton Forces'.  
[https://www.researchgate.net/publication/268424190\\_A\\_Torsional\\_Balance\\_that\\_Resolves\\_Sub-micro-Newton\\_Forces](https://www.researchgate.net/publication/268424190_A_Torsional_Balance_that_Resolves_Sub-micro-Newton_Forces) (accessed Jan. 09, 2017).

## References

- [83] T. Lilly, A. Pancotti, A. Ketsdever, M. Young, and J. Duncan, 'Development of a Specific Impulse Balance for a Pulsed Capillary Discharge', Jul. 2008. doi: 10.2514/6.2008-4740.
- [84] 'Development and Verification of a  $\mu\text{N}$  Thrust Balance for High Voltage Electric Propulsion Systems', *ResearchGate*.  
[https://www.researchgate.net/publication/269993886\\_Development\\_and\\_Verification\\_of\\_a\\_mN\\_Thrust\\_Balance\\_for\\_High\\_Voltage\\_Electric\\_Propulsion\\_Systems](https://www.researchgate.net/publication/269993886_Development_and_Verification_of_a_mN_Thrust_Balance_for_High_Voltage_Electric_Propulsion_Systems) (accessed May 03, 2017).
- [85] J. Liu, D. G. Blair, and L. Ju, 'Near-shore ocean wave measurement using a very low frequency folded pendulum', *Meas. Sci. Technol.*, vol. 9, no. 10, pp. 1772–1776, Oct. 1998, doi: 10.1088/0957-0233/9/10/018.
- [86] D. G. Blair, J. Liu, E. F. Moghaddam, and L. Ju, 'Performance of an ultra low-frequency folded pendulum', *Phys. Lett. A*, vol. 193, no. 3, pp. 223–226, Oct. 1994, doi: 10.1016/0375-9601(94)90587-8.
- [87] J. P. L. B. Hughes, 'Development Status of the ESA Micro-Newton Thrust Balance', *IEPC-2011-011*, 2011, [Online]. Available: [http://erps.spacegrant.org/uploads/images/images/iepc\\_articledownload\\_1988-2007/2011index/IEPC-2011-011.pdf](http://erps.spacegrant.org/uploads/images/images/iepc_articledownload_1988-2007/2011index/IEPC-2011-011.pdf)
- [88] H. Brito, R. Garay, R. Duelli, and S. Maglione, 'A compact, low-cost test stand for PPT impulse bit measurements', Jul. 2000. doi: 10.2514/6.2000-3435.
- [89] Capt. J. P. L. Michael J. Dulligan, 'RESONANT OPERATION OF A MICRO-NEWTON THRUST STAND', [Online]. Available: <http://www.dtic.mil/docs/citations/ADA411147>
- [90] B. D'Souza and A. Ketsdever, 'Direct Impulse Measurements of Ablation Processes from Laser-Surface Interactions', Jun. 2005. doi: 10.2514/6.2005-5172.
- [91] A. D. Ketsdever, B. C. D'Souza, and R. H. Lee, 'Thrust Stand Micromass Balance for the Direct Measurement of Specific Impulse', *J. Propuls. Power*, vol. 24, no. 6, pp. 1376–1381, 2008, doi: 10/fxg2m4.
- [92] B. C. D'Souza and A. D. Ketsdever, 'Investigation of time-dependent forces on a nano-Newton-second impulse balance', *Rev. Sci. Instrum.*, Dec. 2004, doi: 10.1063/1.1834707.

## References

- [93] B. C. D'Souza, 'Development of impulse measurement techniques for the investigation of transient forces due to laser-induced ablation', Ph.D., University of Southern California, United States -- California, 2007. Accessed: May 03, 2017. [Online]. Available:  
<http://search.proquest.com/docview/304827104/abstract/21AB070FCEF1440CPQ/1>
- [94] C. Phipps *et al.*, 'Giant Momentum Coupling Coefficients from Nanoscale Laser-Initiated Exothermic Compounds', presented at the 41st AIAA/ASME/SAE/ASEE Joint Propulsion Conference & Exhibit, Tucson, Arizona, Jul. 2005. doi: 10/gg7r8v.
- [95] S. R. Davide Nicolini, 'Micro-Thrust Balance Testing and Characterization', *IEPC-2005-126*, 2005, [Online]. Available:  
[http://erps.spacegrant.org/uploads/images/images/iepc\\_articledownload\\_1988-2007/2005index/126.pdf](http://erps.spacegrant.org/uploads/images/images/iepc_articledownload_1988-2007/2005index/126.pdf)
- [96] 'Laser Interferometry.pdf'. Accessed: Aug. 06, 2018. [Online]. Available:  
<https://www.physics.nus.edu.sg/~L3000/Level3manuals/Laser%20Interferometry.pdf>
- [97] M. A. V. C. W. Lee, 'Interferometric angle measurement and the hardware options available from Renishaw', *Tech. White Pap. TE326*, [Online]. Available:  
<http://resources.renishaw.com/en/download/white-paper-interferometric-angle-measurement-and-the-hardware-options-available-from-renishaw--81981>
- [98] A. J. J. E.P. Muntz1, 'Accurate Measurement of Nano-Newton Thrust for Micropropulsion System Characterization', *IEPC-01-236*, 2001, [Online]. Available:  
[http://erps.spacegrant.org/uploads/images/images/iepc\\_articledownload\\_1988-2007/2001index/236\\_1.pdf](http://erps.spacegrant.org/uploads/images/images/iepc_articledownload_1988-2007/2001index/236_1.pdf)
- [99] 'Gas dynamic calibration of a nano-Newton thrust stand', *ResearchGate*.  
[https://www.researchgate.net/publication/234909028\\_Gas\\_dynamic\\_calibration\\_of\\_a\\_nano-Newton\\_thrust\\_stand](https://www.researchgate.net/publication/234909028_Gas_dynamic_calibration_of_a_nano-Newton_thrust_stand) (accessed May 08, 2017).
- [100] 'Performance measurements using a sub-microNewton resolution thrust stand', *ResearchGate*.  
[https://www.researchgate.net/publication/228537331\\_Performance\\_measurements\\_using\\_a\\_sub-microNewton\\_resolution\\_thrust\\_stand](https://www.researchgate.net/publication/228537331_Performance_measurements_using_a_sub-microNewton_resolution_thrust_stand) (accessed May 08, 2017).
- [101] Y.-X. Yang, L.-C. Tu, S.-Q. Yang, and J. Luo, 'A torsion balance for impulse and thrust measurements of micro-Newton thrusters', *Rev. Sci. Instrum.*, vol. 83, no. 1, p. 015105, Jan. 2012, doi: 10.1063/1.3675576.

## References

- [102]M. Gamero-Castaño, 'A torsional balance for the characterization of microNewton thrusters', *Rev. Sci. Instrum.*, vol. 74, no. 10, pp. 4509–4514, Oct. 2003, doi: 10.1063/1.1611614.
- [103]Z. He, J. Wu, D. Zhang, G. Lu, Z. Liu, and R. Zhang, 'Precision electromagnetic calibration technique for micro-Newton thrust stands', *Rev. Sci. Instrum.*, vol. 84, no. 5, p. 055107, May 2013, doi: 10.1063/1.4804285.
- [104]N. P. Selden and A. D. Ketsdever, 'Comparison of force balance calibration techniques for the nano-Newton range', *Rev. Sci. Instrum.*, vol. 74, no. 12, pp. 5249–5254, Dec. 2003, doi: 10.1063/1.1623628.
- [105]B. D'Souza and A. Ketsdever, 'Development of a Nano-Impulse Balance for Micropropulsion Systems', Jul. 2005. doi: 10.2514/6.2005-4080.
- [106]J. Soni and S. Roy, 'Design and characterization of a nano-Newton resolution thrust stand', *Rev. Sci. Instrum.*, vol. 84, no. 9, p. 095103, Sep. 2013, doi: 10.1063/1.4819252.
- [107]S. Ciaralli, M. Coletti, and S. B. Gabriel, 'An impulsive thrust balance for applications of micro-pulsed plasma thrusters', *Meas. Sci. Technol.*, vol. 24, no. 11, p. 115003, Nov. 2013, doi: 10.1088/0957-0233/24/11/115003.
- [108]H. Lee, C. Oh, and J. W. Hahn, 'Calibration and Uncertainty Analysis of an Optical Emission Spectrometer Measuring the Absolute Spectral Radiant Exitance of UV Signatures', *Propellants Explos. Pyrotech.*, vol. 37, no. 1, pp. 116–121, Feb. 2012, doi: 10.1002/prop.201000157.
- [109]H.-J. Hagemann, W. Gudat, and C. Kunz, 'Optical constants from the far infrared to the x-ray region: Mg, Al, Cu, Ag, Au, Bi, C, and Al<sub>2</sub>O<sub>3</sub>', *J. Opt. Soc. Am.*, vol. 65, no. 6, p. 742, Jun. 1975, doi: 10.1364/JOSA.65.000742.
- [110]M. A. Green, 'Self-consistent optical parameters of intrinsic silicon at 300 K including temperature coefficients', *Sol. Energy Mater. Sol. Cells*, vol. 92, no. 11, pp. 1305–1310, Nov. 2008, doi: 10.1016/j.solmat.2008.06.009.
- [111]X. Zhang, J. Qiu, X. Li, J. Zhao, and L. Liu, 'Complex refractive indices measurements of polymers in visible and near-infrared bands', *Appl. Opt.*, vol. 59, no. 8, p. 2337, Mar. 2020, doi: 10.1364/AO.383831.

## References

- [112]C. Phipps *et al.*, 'Review: Laser-Ablation Propulsion', *J. Propuls. Power*, vol. 26, no. 4, pp. 609–637, Jul. 2010, doi: 10.2514/1.43733.
- [113]S. Katayama, D. Yoshida, and A. Matsunawa, 'Effect of Nitrogen Shielding Gas on Laser Weldability of Austenitic Stainless Steel', *J. High Temp. Soc.*, vol. 30, no. 2, pp. 93–99, 2004, doi: 10.7791/jhts.30.93.
- [114]A. Riveiro *et al.*, 'Laser Cutting: A Review on the Influence of Assist Gas', *Materials*, vol. 12, no. 1, p. 157, Jan. 2019, doi: 10/gg7r54.
- [115]J. J. J. Nivas, Z. Song, R. Fittipaldi, A. Vecchione, R. Bruzzese, and S. Amoroso, 'Direct ultrashort laser surface structuring of silicon in air and vacuum at 1055 nm', *Appl. Surf. Sci.*, vol. 417, pp. 149–154, Sep. 2017, doi: 10/gg7r55.
- [116]S. Döring, T. Ullsperger, F. Heisler, S. Richter, A. Tünnermann, and S. Nolte, 'Hole Formation Process in Ultrashort Pulse Laser Percussion Drilling', *Phys. Procedia*, vol. 41, pp. 431–440, 2013, doi: 10/gg7r8n.
- [117]T. V. Kononenko, C. Freitag, D. N. Sovyk, A. B. Lukhter, K. V. Skvortsov, and V. I. Konov, 'Influence of pulse repetition rate on percussion drilling of Ti-based alloy by picosecond laser pulses', *Opt. Lasers Eng.*, vol. 103, pp. 65–70, Apr. 2018, doi: 10/gg7r8m.
- [118]S. T. Hendow, R. Romero, S. A. Shakir, and P. T. Guerreiro, 'Percussion drilling of metals using bursts of nanosecond pulses', *Opt. Express*, vol. 19, no. 11, p. 10221, May 2011, doi: 10/d6nqt5.
- [119]W. Zhao, X. Shen, H. Liu, L. Wang, and H. Jiang, 'Effect of high repetition rate on dimension and morphology of micro-hole drilled in metals by picosecond ultra-short pulse laser', *Opt. Lasers Eng.*, vol. 124, p. 105811, Jan. 2020, doi: 10/gg7r8k.
- [120]A. Ancona, F. Röser, K. Rademaker, J. Limpert, S. Nolte, and A. Tünnermann, 'High speed laser drilling of metals using a high repetition rate, high average power ultrafast fiber CPA system', *Opt. Express*, vol. 16, no. 12, p. 8958, Jun. 2008, doi: 10/fj2tw7.
- [121]J. Finger and M. Reininghaus, 'Effect of pulse to pulse interactions on ultra-short pulse laser drilling of steel with repetition rates up to 10 MHz', *Opt. Express*, vol. 22, no. 15, p. 18790, Jul. 2014, doi: 10/gg7r8j.

## References

- [122]M.-K. Wei and H. Yang, 'Cumulative Heat Effect in Excimer Laser Ablation of Polymer PC and ABS', *Int. J. Adv. Manuf. Technol.*, vol. 21, no. 12, pp. 1029–1034, Sep. 2003, doi: 10/chn6pn.
- [123]G. K. L. Ng and L. Li, 'The effect of laser peak power and pulse width on the hole geometry repeatability in laser percussion drilling', *Opt. Laser Technol.*, vol. 33, no. 6, pp. 393–402, Sep. 2001, doi: 10/c42btx.
- [124]W. Han and R. J. Pryputniewicz, 'Investigations of laser percussion drilling of small holes on thin sheet metals', Denver, CO, Sep. 2004, p. 31. doi: 10/d862kb.
- [125]I. Vladiou, M. Stafe, C. Negutu, and I. M. Popescu, 'Influence of the pulse number and fluence of a nanosecond laser on the ablation rate of metals, semiconductors and dielectrics', *Eur. Phys. J. Appl. Phys.*, vol. 47, no. 3, p. 30702, Sep. 2009, doi: 10/dr62zs.
- [126]Y. Wang, D. Diaz, and D. W. Hahn, 'Ablation Characteristics of Nanosecond Laser Pulsed Ablation of Aluminum', in *Volume 2: Advanced Manufacturing*, Pittsburgh, Pennsylvania, USA, Nov. 2018, p. V002T02A086. doi: 10/gg7r8b.
- [127]N. Ren, L. Jiang, D. Liu, L. Lv, and Q. Wang, 'Comparison of the simulation and experimental of hole characteristics during nanosecond-pulsed laser drilling of thin titanium sheets', *Int. J. Adv. Manuf. Technol.*, vol. 76, no. 5–8, pp. 735–743, Feb. 2015, doi: 10/f6xkqv.
- [128]K. Pangovski, 'Temporal pulse design and analysis of silicon ablation using advanced pulse shaping and digital holography in the nanosecond domain', The University of Cambridge, 2014.

## Appendices

**Appendix 1.** MATLAB model used to model the torsion balance.

```
function torsion_balance_23012018
close all; clear all; clc;

%----- FORCE INPUT VARIABLES -----%
F = 5.00E-8; %Nominal Input Force, (N).
rr = 0.0001; %Repetition Rate, (Hz).
pw = 1; %Pulse Width, (s).
T = 1/rr; %Period, (s).
N = pw/T; %Duty Cycle, (s).

if N > 1; fprintf('Duty Cycle above 100 percent');
    return;
    end; %Duty cycle can not exceed 100%.

g = 9.80665; %Standard Acceleration of Gravity, (m/s^2).
mdot = 0.000E-07; %Mass Flow Rate, (mg/s). Mass being ejected from from balance in
opposite direction to input force.

function fm = forcem(t)
    ml = (mdot/1000000)*g*t; %Mass loss function.
    fm = ((0.5*F)-(ml)).*(square(2*pi*rr*(t-5),N*100)+1); %Square Wave Pulse Train
Generator with Mass Flow. Assumes mdot<<mtotal and doesn't affect J.
    end

%----- BALANCE MECHANICAL VARIABLES -----%
l = 0.3; %Total Length of Balance from Centre to Centre, (m).
r = l/2; %Distance from Force Centre to Spring Centre, (m).

I = 0.005; %Balance Moment of Inertia, (kg.m^2).
C = 0.0005; %Damping Coefficient, (kg.m^2/s).
K = 0.0066; %Torsional Spring Rate, (N.m/Rad).

%----- SIMULATION VARIABLES -----%
tt = 60; %Total Simulation Time, (s).
ts = pw/1000; %Simulation Step Time, (s). Typically 1/1000 good for accuracy and speed.
t = 0:ts:tt; % Time Scale.
opts = odeset('RelTol',1e-12,'AbsTol',1e-13); %Set error tolerances.

%----- SOLVE DIFFERENTIAL EQUATIONS -----%
initial_x = 0;
initial_dxdt = 0;
```

## Appendices

```
[t,x] = ode45( @rhs, t, [initial_x initial_dxdt], opts ); %Use ODE45 or ODE113. ODE113  
needs tolerances better than 10E-14.
```

```
function dxdt = rhs(t,x)  
    dxdt_1 = x(2);  
    dxdt_2 = -((C/l)*x(2))-((K/l)*x(1))+forcem(t)*(r/l);  
    dxdt = [dxdt_1; dxdt_2];  
end
```

```
%----- CALCULATE CRITICAL VALUES FROM TRACE -----%
```

```
x = x(:,1);
```

```
[pks, locs] = findpeaks(x, t); %Take angular deflection from response trace, find peaks and  
use to identify period and logarithmic decrement.
```

```
Tn = mean(diff(locs));
```

```
Cc = sqrt(4*K*l); %Critical Damping Coefficient, (kg.m2/s).
```

```
dr = C/Cc; %Damping Ratio.
```

```
wd = (2*pi)/(Tn); %Damped Angular Frequency, (rad).
```

```
wo = wd/(sqrt(1-dr2)); %Undamped Angular Frequency, (rad).
```

```
dt = t(2)-t(1);
```

```
[b, c] = sgolay(3, 5);
```

```
dx = zeros(length(x),3);
```

```
for p = 0:2
```

```
    dx(:,p+1) = conv(x, factorial(p)/(-dt)p * c(:,p+1), 'same');
```

```
end
```

```
T = (((l*dx(:,3)))+(C*dx(:,2)))+(K*dx(:,1)))/r;
```

```
Imp = cumtrapz(t, T);
```

```
%----- PRINTS-----%
```

```
fprintf('Period = %f', Tn); fprintf(' s'); fprintf('\n');
```

```
fprintf('Damping Ratio = %f', dr); fprintf('\n');
```

```
fprintf('Undamped Angular Frequency = %f', wo); fprintf(' rad'); fprintf('\n');
```

```
fprintf('Damped Angular Frequency = %f', wd); fprintf(' rad'); fprintf('\n');
```

```
fprintf('Impulse Difference = %f', 100*abs(1-((trapz(forcem(t)))/(trapz(T))))); fprintf(' %%');
```

```
fprintf('\n');
```

```
%----- PLOTS -----%
```

```
figure; subplot(3, 2, 1)
```

```
plot(t, dx(:,1));
```

## Appendices

```
title('Balance Response'); xlabel('Time (s)', 'FontSize', 16); ylabel('Angular Deflection (rad)',  
'FontSize', 16); set(gca,'TickDir','out'); grid minor;  
set(gca,'fontsize', 12);
```

```
subplot(3, 2, 2); plot(t, dx(:,2)); ylim([-2E-6, 2E-6])  
title('Balance Response'); xlabel('Time (s)', 'FontSize', 16); ylabel('Angular Velocity (rad/s)',  
'FontSize', 16); set(gca,'TickDir','out'); grid minor;  
set(gca,'fontsize', 12);
```

```
subplot(3, 2, 3); plot(t, dx(:,3)); ylim([-2E-6, 2E-6])  
title('Balance Response'); xlabel('Time (s)', 'FontSize', 16); ylabel('Angular  
Acceleration(rad/s^2)', 'FontSize', 16); set(gca,'TickDir','out'); grid minor;  
set(gca,'fontsize', 12);
```

```
subplot(3, 2, 4); plot(t, r*(sin(x)));  
title('Balance Response'); xlabel('Time (s)', 'FontSize', 16); ylabel('Displacement (m)',  
'FontSize', 16); set(gca,'TickDir','out'); grid minor;  
set(gca,'fontsize', 12);
```

```
subplot(3, 2, 5); plot(t, T); ylim([0, max(forcem(t)*1.2)]);  
title('Derived Force'); xlabel('Time (s)', 'FontSize', 16); ylabel('Force (N)', 'FontSize', 16);  
set(gca,'TickDir','out'); grid minor;  
set(gca,'fontsize', 12);
```

```
subplot(3, 2, 6); plot(t, Imp); ylim([0, 1E-7])  
title('Impulse'); xlabel('Time (s)', 'FontSize', 16); ylabel('Impulse (N.s)', 'FontSize', 16);  
set(gca,'TickDir','out'); grid minor;  
set(gca,'fontsize', 12);
```

end

## Appendices

**Appendix 2.** MATLAB model used to resolve force, impulse and mass flow rate from the fringe count data produced by the interferometer.

```
close all; clear all; clc; format long;
```

```
%----- LOAD DATA AND CONSTANTS -----%
I = 0.005; %Balance moment of inertia from CAD +
CMM reports, (kg.m^2).
L = 0.3; %Balance length from CAD + CMM
reports, (m).
r = L/2; %Length to pivot point, (m).

f = 20; %Enter encoder output frequency, (Hz).
dt = 1/f; %Convert sampling frequency to time
steps, (s).

fileID = fopen('demo.txt', 'r'); %Open text file with encoder data
%Select the column you are interested in.
formatSpec = '%d %f'; %Define format of the data.
sizeA = [1 Inf]; %Define shape of the data.
A = fscanf(fileID, formatSpec, sizeA); %Read the data and fill out
output array A.
fclose(fileID); %OK to close file now.
A = A'; %Transpose.

xc = A(:,1)+15000; %Pull only the first column. You may
need to add an offset if the encoder count wasnt centred at 0.
xd = (xc/4)*(632.79E-9/2); %Convert count to displacement in
x4 encoder mode using measured laser wavelength, (m).
x = asin(xd/L); %Change displacement to deflection,
(rad).
t = 0:dt:(length(x)-1)*dt; %Generate time data.

%----- PROCESSING AND FILTERING -----%
[g, h] = cheby1(3, 1, 0.5); %Design Chebyshev filter for high-
frequency noise.
x = filter(g, h, x);

[b, c] = sgolay(3, 5); %Design Savitzky-Golay filter for
derivates.

dx = zeros(length(x), 3);
for p = 0:2
    dx(:, p+1) = conv(x, factorial(p)/(-dt)^p*c(:, p+1), 'same'); %Derive angular velocity
and acceleration from deflection trace.
end
```

## Appendices

```

%----- CALCULATIONS -----%
[pks, locs] = findpeaks(x);
tl = t(locs);
locs = locs';
dl = diff(tl);
pl = dl > 2.0 & dl < 2.7;
Tn = mean(dl(pl));

pm = mean(x);
pr = pks > 1.2*pm;
from noise.
peaks = pks(pr);
ps = size(peaks);

i = 1;
s = peaks(1:end-1);
for n = 2:size(s)-1
    decr(i) = (1/n)*(log(s(1)/s(n+1)));
from peaks.
    i = i + 1;
end

ldec = mean(decr);
decrement.

dr = 1/(sqrt(1+((2*pi)/(ldec))^2));
wd = (2*pi)/Tn;
wo = wd/(sqrt(1-(dr^2)));
(rad/s).
K = l*wo^2;
C = dr*2*l*wo;
Cc = C/dr;
(kg.m^2/s).

T = (l*dx(:, 3)+C*dx(:, 2)+K*dx(:, 1))/r;
respect to time, (N).
[q,w] = butter(2, 0.02);
T = filter(q, w, T);

Imp = cumtrapz(t, T);
to time, (N.s).

%----- PRINTS -----%
fprintf('Period = %f', Tn); fprintf(' s'); fprintf('\n');
fprintf('Damping Ratio = %f', dr); fprintf('\n');
fprintf('Damping Coefficient = %f', C); fprintf(' kg.m^2/s'); fprintf('\n');
fprintf('Spring Constant = %f', K*(pi/180)*8.851); fprintf(' in.lb/deg'); fprintf('\n');
fprintf('Undamped Natural Frequency = %f', wo); fprintf(' rad/s'); fprintf('\n');

```

## Appendices

```
fprintf('Damped Natural Frequency = %f', wd); fprintf(' rad/s'); fprintf('\n');
```

```
%----- PLOTS -----%
```

```
% figure; plot(1:length(decr), decr);  
% title('Logarithmic Decrement');  
% xlabel('n'); ylabel('value');  
% set(gca,'TickDir','out'); grid minor;
```

```
figure; subplot(3, 2, 1); plot(t, r*sin(dx(:,1)));  
title('Balance Response'); xlabel('Time (s)');  
ylabel('Displacement (m)');  
xticks([0:60:max(t)]); xlim([0, max(t)]);  
set(gca,'TickDir','out'); grid minor; fprintf('\n');
```

```
subplot(3, 2, 2); plot(t, dx(:,1));  
title('Balance Response'); xlabel('Time (s)');  
ylabel('Angular Deflection (rad)');  
xticks([0:60:max(t)]); xlim([0, max(t)]);  
set(gca,'TickDir','out'); grid minor;
```

```
subplot(3, 2, 3); plot(t, dx(:, 2));  
title('Balance Response'); xlabel('Time (s)');  
ylabel('Angular Velocity (rad/s)');  
xticks([0:60:max(t)]); xlim([0, max(t)]); ylim([-max(dx(:, 2)*1.3), max(dx(:, 2)*1.3)]);  
set(gca,'TickDir','out'); grid minor;
```

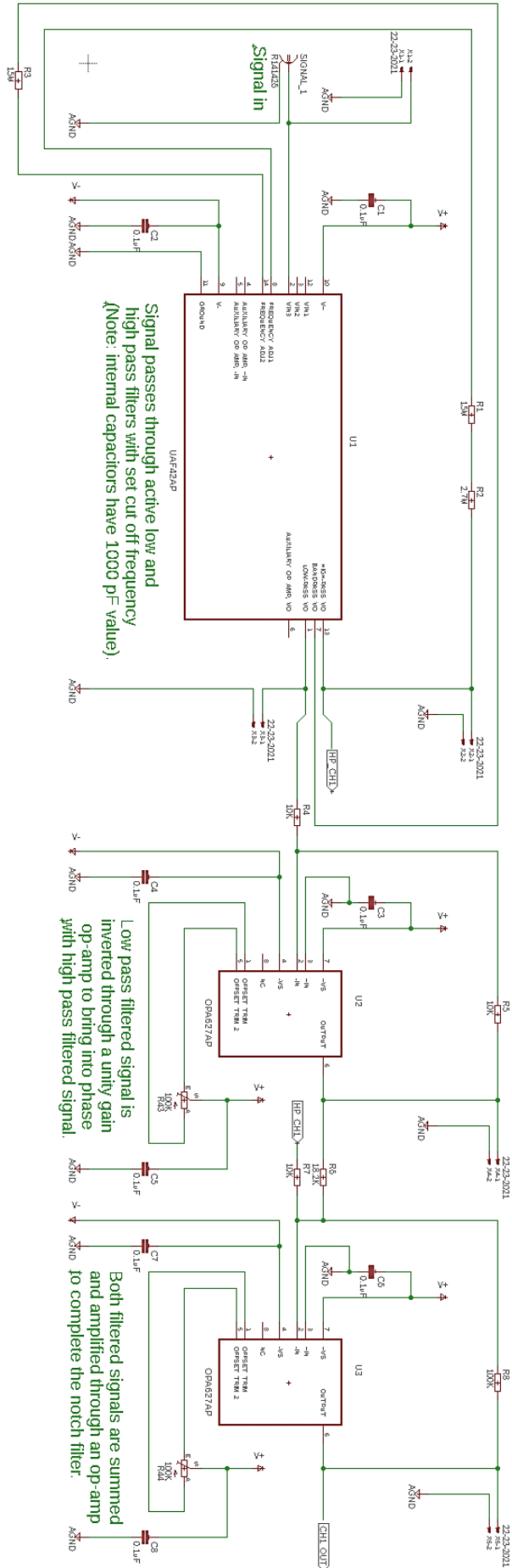
```
subplot(3, 2, 4); plot(t, dx(:, 3));  
title('Balance Response');  
xlabel('Time (s)'); ylabel('Angular Acceleration (rad/s^2)');  
xticks([0:60:max(t)]); xlim([0, max(t)]); ylim([-max(dx(:, 3)*1.1), max(dx(:, 3)*1.1)]);  
set(gca,'TickDir','out'); grid minor;
```

```
subplot(3, 2, 5); plot(t, T);  
title('Force'); xlabel('Time (s)'); ylabel('Force (N)');  
xticks([0:60:max(t)]); xlim([0, max(t)]);  
set(gca,'TickDir','out'); grid minor;
```

```
subplot(3, 2, 6); plot(t, Imp);  
title('Impulse'); xlabel('Time (s)'); ylabel('Impulse (N.s)');  
xticks([0:60:max(t)]); xlim([0, max(t)]);  
set(gca,'TickDir','out'); grid minor;
```

**Appendix 3a.**

The front end of the electronics for the interferometer. The section shown is for a single photodiode channel and is identical for the other three channels. The signal is first passed through a notch filter (UAF42) to remove frequencies related to beam walk off, which occurs when the interference signals move relative to each other due to the movement of the torsional spring in more than one axis. The low-pass output from the filter is passed through an inverting op-amp (OPA627) with unity gain to invert the signal, as the high-pass and low-pass outputs are naturally 180 degrees out of phase. The signals are then summed and amplified in a non-inverting op-amp (OPA627).

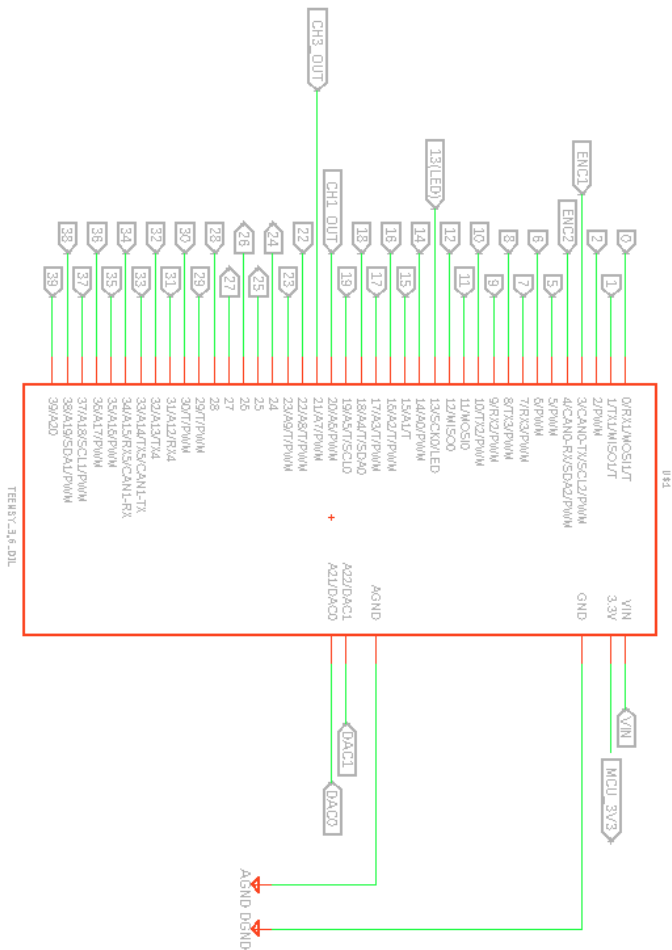
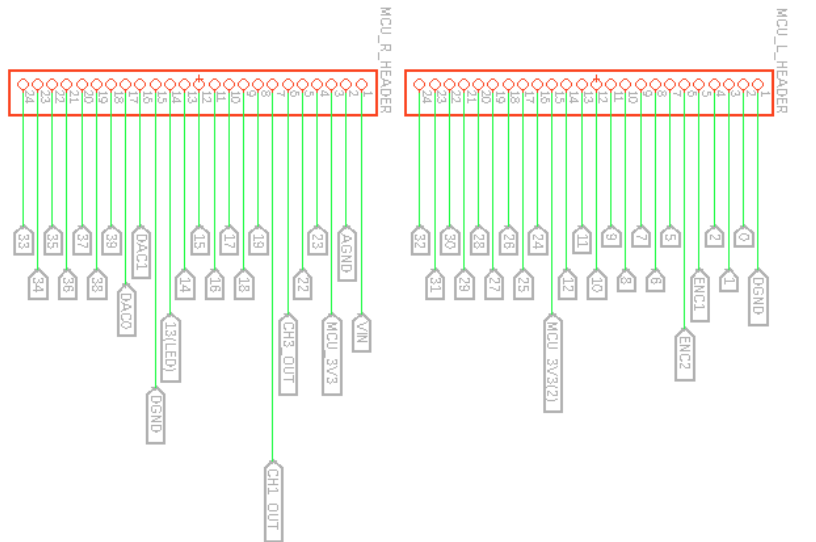




# Appendices

## Appendix 3c.

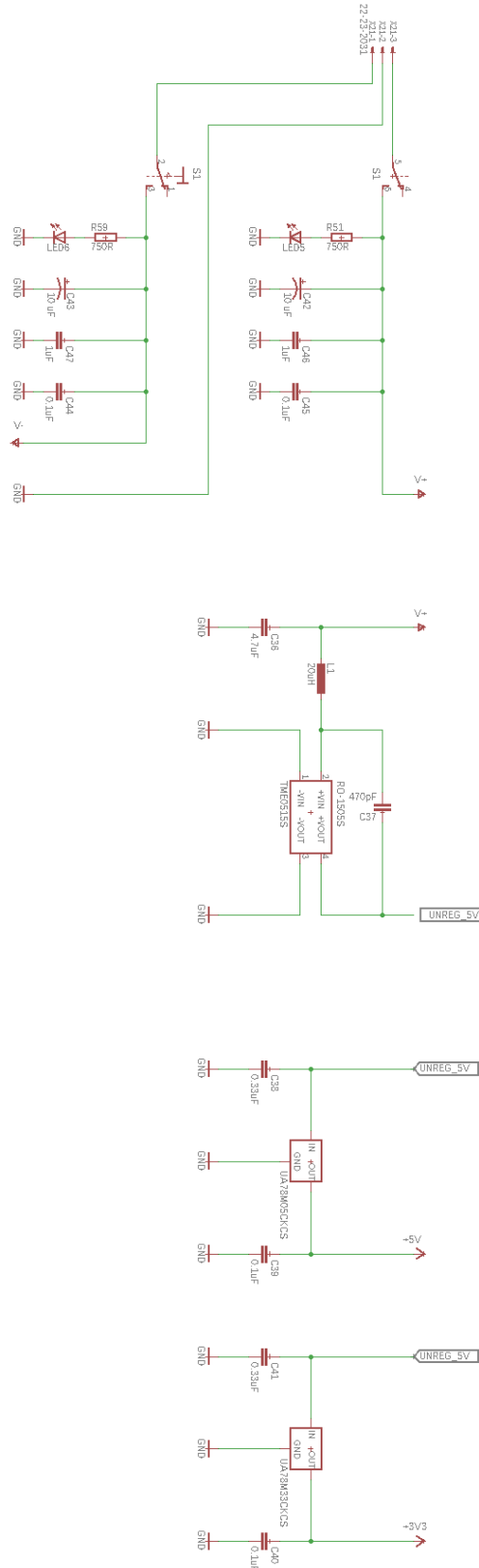
The quadrature encoded signals are passed to a Teensy 3.6 microcontroller which features 32 bit 180 MHz ARM Cortex-M4 processor with floating point unit, quadrature decoder and 13 bit ADC resolution. Channel 1 and Channel 3 are also taken from the front end of the electronics to the Teensy for arctan interpolation.



# Appendices

## Appendix 3d.

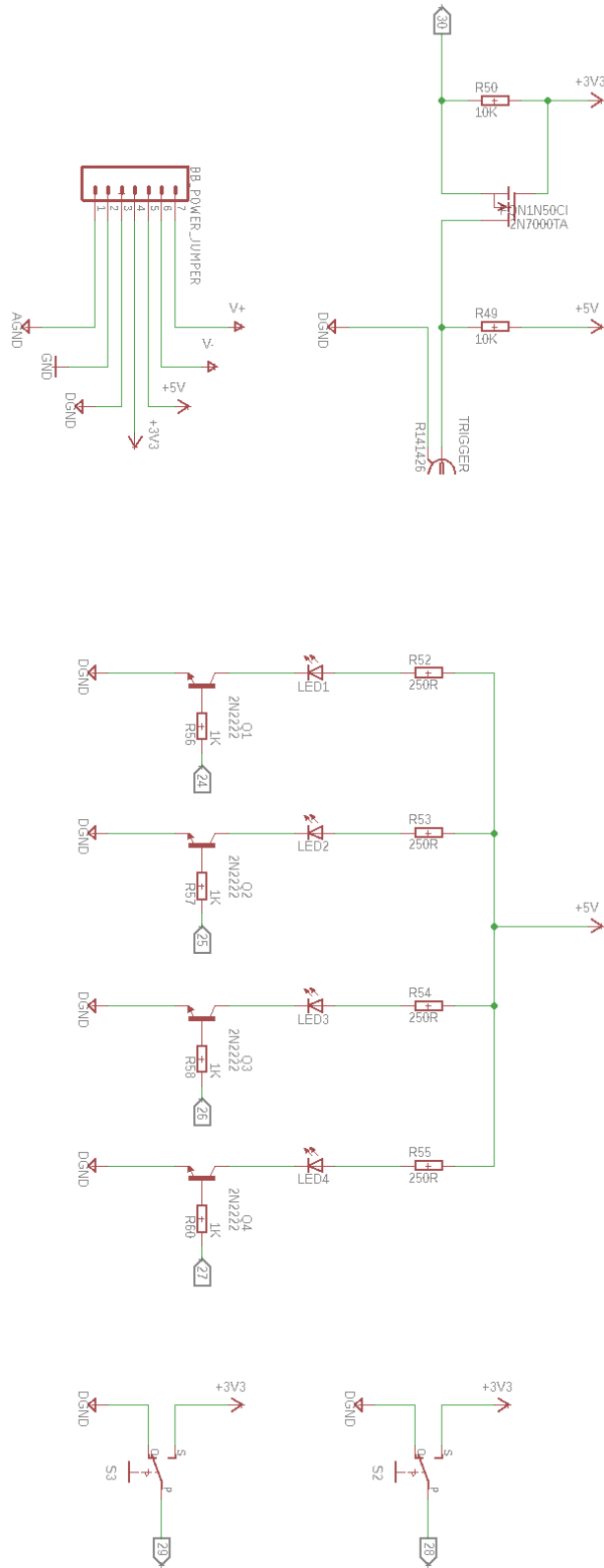
The board is powered using a lab power supply delivering  $\pm 15V$ . This is mainly used to power the front end. This is in turn passed to a 5V and 3.3V regulator for powering the rest of the electronics.



# Appendices

## Appendix 3d.

Miscellaneous support circuitry including a logic level shifter for the trigger (top right), notification LED's (centre) and switches (bottom) for switching between arctan and quadrature measurements.





## Appendices

### Appendix 5.

Bill of materials for the interferometer electronics.

Part	Value	Device	Package	Description
2N7000TA	FQN1N50CI	FQN1N50CI	TO92-INLINE	N MOSFET 500V, 0.4A, 6.0 Ohm
BB1		CONN_24	1X24	Multi connection point.
BB2		CONN_24	1X24	Multi connection point.
BB3		CONN_24	1X24	Multi connection point.
BB4		CONN_24	1X24	Multi connection point.
BB5		CONN_24	1X24	Multi connection point.
BB6		CONN_24	1X24	Multi connection point.
BB7		CONN_24	1X24	Multi connection point.
BB_POWER_JUMPER			CONN_07	1X07 Multi connection point.
C1	0.1uF	C5/3	C5B3	CAPACITOR
C2	0.1uF	C5/3	C5B3	CAPACITOR
C3	0.1uF	C5/3	C5B3	CAPACITOR
C4	0.1uF	C5/3	C5B3	CAPACITOR
C5	0.1uF	C5/3	C5B3	CAPACITOR
C6	0.1uF	C5/3	C5B3	CAPACITOR
C7	0.1uF	C5/3	C5B3	CAPACITOR
C8	0.1uF	C5/3	C5B3	CAPACITOR
C9	0.1uF	C5/3	C5B3	CAPACITOR
C10	0.1uF	C5/3	C5B3	CAPACITOR
C11	0.1uF	C5/3	C5B3	CAPACITOR
C12	0.1uF	C5/3	C5B3	CAPACITOR
C13	0.1uF	C5/3	C5B3	CAPACITOR
C14	0.1uF	C5/3	C5B3	CAPACITOR
C15	0.1uF	C5/3	C5B3	CAPACITOR
C16	0.1uF	C5/3	C5B3	CAPACITOR
C17	0.1uF	C5/3	C5B3	CAPACITOR
C18	0.1uF	C5/3	C5B3	CAPACITOR
C19	0.1uF	C5/3	C5B3	CAPACITOR
C20	0.1uF	C5/3	C5B3	CAPACITOR
C21	0.1uF	C5/3	C5B3	CAPACITOR
C22	0.1uF	C5/3	C5B3	CAPACITOR
C23	0.1uF	C5/3	C5B3	CAPACITOR
C24	0.1uF	C5/3	C5B3	CAPACITOR
C25	0.1uF	C5/3	C5B3	CAPACITOR
C26	0.1uF	C5/3	C5B3	CAPACITOR
C27	0.1uF	C5/3	C5B3	CAPACITOR
C28	0.1uF	C5/3	C5B3	CAPACITOR
C29	0.1uF	C5/3	C5B3	CAPACITOR
C30	0.1uF	C5/3	C5B3	CAPACITOR
C31	0.1uF	C5/3	C5B3	CAPACITOR
C32	0.1uF	C5/3	C5B3	CAPACITOR
C33	0.1uF	C5/3	C5B3	CAPACITOR
C34	0.1uF	C5/3	C5B3	CAPACITOR
C36	4.7uF	C5/3	C5B3	CAPACITOR

## Appendices

C37	470pF	C5/3	C5B3	CAPACITOR
C38	0.33uF	C5/3	C5B3	CAPACITOR
C39	0.1uF	C5/3	C5B3	CAPACITOR
C40	0.1uF	C5/3	C5B3	CAPACITOR
C41	0.33uF	C5/3	C5B3	CAPACITOR
C42	10 uF	CPOL-USE2.5-6	E2,5-6	POLARIZED CAPACITOR,
C43	10 uF	CPOL-USE2.5-6	E2,5-6	POLARIZED CAPACITOR,
C44	0.1uF	C5/3	C5B3	CAPACITOR
C45	0.1uF	C5/3	C5B3	CAPACITOR
C46	1uF	C5/3	C5B3	CAPACITOR
C47	1uF	C5/3	C5B3	CAPACITOR
L1	22uH	L-EU0207/7	0207/7	INDUCTOR, European symbol
LED1		LED5MM	LED5MM	LED
LED2		LED5MM	LED5MM	LED
LED3		LED5MM	LED5MM	LED
LED4		LED5MM	LED5MM	LED
LED5		LED5MM	LED5MM	LED
LED6		LED5MM	LED5MM	LED
MCU_L_HEADER		PINHD-1X24	1X24	PIN HEADER
MCU_R_HEADER		PINHD-1X24	1X24	PIN HEADER
Q1	2N2222	2N2222	TO18	NPN Transistor
Q2	2N2222	2N2222	TO18	NPN Transistor
Q3	2N2222	2N2222	TO18	NPN Transistor
Q4	2N2222	2N2222	TO18	NPN Transistor
R1	15M	R-EU_0207/12	0207/12	RESISTOR, European symbol
R2	2.7M	R-EU_0207/12	0207/12	RESISTOR, European symbol
R3	15M	R-EU_0207/12	0207/12	RESISTOR, European symbol
R4	10K	R-EU_0207/12	0207/12	RESISTOR, European symbol
R5	10K	R-EU_0207/12	0207/12	RESISTOR, European symbol
R6	18.2K	R-EU_0207/12	0207/12	RESISTOR, European symbol
R7	10K	R-EU_0207/12	0207/12	RESISTOR, European symbol
R8	100K	R-EU_0207/12	0207/12	RESISTOR, European symbol
R9	15M	R-EU_0207/12	0207/12	RESISTOR, European symbol
R10	2.7M	R-EU_0207/12	0207/12	RESISTOR, European symbol
R11	15M	R-EU_0207/12	0207/12	RESISTOR, European symbol
R12	10K	R-EU_0207/12	0207/12	RESISTOR, European symbol
R13	10K	R-EU_0207/12	0207/12	RESISTOR, European symbol
R14	18.2K	R-EU_0207/12	0207/12	RESISTOR, European symbol
R15	10K	R-EU_0207/12	0207/12	RESISTOR, European symbol
R16	100K	R-EU_0207/12	0207/12	RESISTOR, European symbol
R17	15M	R-EU_0207/12	0207/12	RESISTOR, European symbol
R18	2.7M	R-EU_0207/12	0207/12	RESISTOR, European symbol
R19	15M	R-EU_0207/12	0207/12	RESISTOR, European symbol
R20	10K	R-EU_0207/12	0207/12	RESISTOR, European symbol
R21	10K	R-EU_0207/12	0207/12	RESISTOR, European symbol
R22	18.2K	R-EU_0207/12	0207/12	RESISTOR, European symbol
R23	10K	R-EU_0207/12	0207/12	RESISTOR, European symbol
R24	100K	R-EU_0207/12	0207/12	RESISTOR, European symbol

## Appendices

R25	15M	R-EU_0207/12	0207/12	RESISTOR, European symbol
R26	2.7M	R-EU_0207/12	0207/12	RESISTOR, European symbol
R27	15M	R-EU_0207/12	0207/12	RESISTOR, European symbol
R28	10K	R-EU_0207/12	0207/12	RESISTOR, European symbol
R29	10K	R-EU_0207/12	0207/12	RESISTOR, European symbol
R30	18.2K	R-EU_0207/12	0207/12	RESISTOR, European symbol
R31	10K	R-EU_0207/12	0207/12	RESISTOR, European symbol
R32	100K	R-EU_0207/12	0207/12	RESISTOR, European symbol
R33	1M	R-EU_0207/12	0207/12	RESISTOR, European symbol
R34	1M	R-EU_0207/12	0207/12	RESISTOR, European symbol
R35	22K	R-EU_0207/12	0207/12	RESISTOR, European symbol
R36	22K	R-EU_0207/12	0207/12	RESISTOR, European symbol
R37	5.23K	R-EU_0207/12	0207/12	RESISTOR, European symbol
R38	2K	R-EU_0207/12	0207/12	RESISTOR, European symbol
R39	1.2K	R-EU_0207/12	0207/12	RESISTOR, European symbol
R40	5.23K	R-EU_0207/12	0207/12	RESISTOR, European symbol
R41	2K	R-EU_0207/12	0207/12	RESISTOR, European symbol
R42	1.2K	R-EU_0207/12	0207/12	RESISTOR, European symbol
R43	100K	TRIM_EU-B64Y	B64Y	POTENTIOMETER
R44	100K	TRIM_EU-B64Y	B64Y	POTENTIOMETER
R45	100K	TRIM_EU-B64Y	B64Y	POTENTIOMETER
R46	100K	TRIM_EU-B64Y	B64Y	POTENTIOMETER
R47	100K	TRIM_EU-B64Y	B64Y	POTENTIOMETER
R48	100K	TRIM_EU-B64Y	B64Y	POTENTIOMETER
R49	10K	R-EU_0207/15	0207/15	RESISTOR, European symbol
R50	10K	R-EU_0207/15	0207/15	RESISTOR, European symbol
R51	750R	R-EU_0207/15	0207/15	RESISTOR, European symbol
R52	250R	R-EU_0207/15	0207/15	RESISTOR, European symbol
R53	250R	R-EU_0207/15	0207/15	RESISTOR, European symbol
R54	250R	R-EU_0207/15	0207/15	RESISTOR, European symbol
R55	250R	R-EU_0207/15	0207/15	RESISTOR, European symbol
R56	1K	R-EU_0207/15	0207/15	RESISTOR, European symbol
R57	1K	R-EU_0207/15	0207/15	RESISTOR, European symbol
R58	1K	R-EU_0207/15	0207/15	RESISTOR, European symbol
R59	750R	R-EU_0207/15	0207/15	RESISTOR, European symbol
R60	1K	R-EU_0207/15	0207/15	RESISTOR, European symbol
R61	100K	TRIM_EU-B64Y	B64Y	POTENTIOMETER
R62	100K	TRIM_EU-B64Y	B64Y	POTENTIOMETER
RO-1505S	TME0515S	TME0515S	TME	DC/DC Converter TME Series
S1	320-938	320-938		TOGGLE SWITCH
S2	EG1218S	EG1218		SLIDING SWITCH
S3	EG1218S	EG1218		SLIDING SWITCH
SIGNAL_1	R141426	R141426	R141426	BNC COAX CONNECTOR
SIGNAL_2	R141426	R141426	R141426	BNC COAX CONNECTOR
SIGNAL_3	R141426	R141426	R141426	BNC COAX CONNECTOR
SIGNAL_4	R141426	R141426	R141426	BNC COAX CONNECTOR
TRIGGER	R141426	R141426	R141426	BNC COAX CONNECTOR
U\$1	TEENSY_3.6_DIL	TEENSY_3.6_DIL	TEENSY_3.6_DIL	Teensy 3.6 DIL

## Appendices

U1	UAF42AP	DIP socket	DIP254P762X508-14	UNIVERSAL ACTIVE FILTER
U2	OPA627AP	OPA627AP	DIP254P762X508-8	OPERATIONAL AMPLIFIER
U3	OPA627AP	OPA627AP	DIP254P762X508-8	OPERATIONAL AMPLIFIER
U4	UAF42AP	UAF42AP	DIP254P762X508-14	UNIVERSAL ACTIVE FILTER
U5	OPA627AP	OPA627AP	DIP254P762X508-8	OPERATIONAL AMPLIFIER
U6	OPA627AP	OPA627AP	DIP254P762X508-8	OPERATIONAL AMPLIFIER
U7	UAF42AP	UAF42AP	DIP254P762X508-14	UNIVERSAL ACTIVE FILTER
U8	OPA627AP	OPA627AP	DIP254P762X508-8	OPERATIONAL AMPLIFIER
U9	OPA627AP	OPA627AP	DIP254P762X508-8	OPERATIONAL AMPLIFIER
U10	UAF42AP	UAF42AP	DIP254P762X508-14	UNIVERSAL ACTIVE FILTER
U11	OPA627AP	OPA627AP	DIP254P762X508-8	OPERATIONAL AMPLIFIER
U12	OPA627AP	OPA627AP	DIP254P762X508-8	OPERATIONAL AMPLIFIER
U13	TL082CP	TL082CP	DIP254P762X508-8	OPERATIONAL AMPLIFIER
TL082CP	1106017	60K6991	PDIP	Texas Instruments
UA78M05CKCS		78XXS	78XXS	VOLTAGE REGULATOR
UA78M33CKCS		78XXS	78XXS	VOLTAGE REGULATOR
X1	22-23-2021	22-23-2021	22-23-2021	.100" (2.54mm) Center Header - 2 Pin
X2	22-23-2021	22-23-2021	22-23-2021	.100" (2.54mm) Center Header - 2 Pin
X3	22-23-2021	22-23-2021	22-23-2021	.100" (2.54mm) Center Header - 2 Pin
X4	22-23-2021	22-23-2021	22-23-2021	.100" (2.54mm) Center Header - 2 Pin
X5	22-23-2021	22-23-2021	22-23-2021	.100" (2.54mm) Center Header - 2 Pin
X6	22-23-2021	22-23-2021	22-23-2021	.100" (2.54mm) Center Header - 2 Pin
X7	22-23-2021	22-23-2021	22-23-2021	.100" (2.54mm) Center Header - 2 Pin
X8	22-23-2021	22-23-2021	22-23-2021	.100" (2.54mm) Center Header - 2 Pin
X9	22-23-2021	22-23-2021	22-23-2021	.100" (2.54mm) Center Header - 2 Pin
X1	22-23-2021	22-23-2021	22-23-2021	.100" (2.54mm) Center Header - 2 Pin
X11	22-23-2021	22-23-2021	22-23-2021	.100" (2.54mm) Center Header - 2 Pin
X12	22-23-2021	22-23-2021	22-23-2021	.100" (2.54mm) Center Header - 2 Pin
X13	22-23-2021	22-23-2021	22-23-2021	.100" (2.54mm) Center Header - 2 Pin
X14	22-23-2021	22-23-2021	22-23-2021	.100" (2.54mm) Center Header - 2 Pin
X15	22-23-2021	22-23-2021	22-23-2021	.100" (2.54mm) Center Header - 2 Pin
X16	22-23-2021	22-23-2021	22-23-2021	.100" (2.54mm) Center Header - 2 Pin
X17	22-23-2021	22-23-2021	22-23-2021	.100" (2.54mm) Center Header - 2 Pin
X18	22-23-2021	22-23-2021	22-23-2021	.100" (2.54mm) Center Header - 2 Pin
X19	22-23-2021	22-23-2021	22-23-2021	.100" (2.54mm) Center Header - 2 Pin
X20	22-23-2021	22-23-2021	22-23-2021	.100" (2.54mm) Center Header - 2 Pin
X21	22-23-2031	22-23-2031	22-23-2031	.100" (2.54mm) Center Header - 3 Pin
X22	22-23-2021	22-23-2021	22-23-2021	.100" (2.54mm) Center Header - 2 Pin
X23	22-23-2021	22-23-2021	22-23-2021	.100" (2.54mm) Center Header - 2 Pin
X25	22-23-2021	22-23-2021	22-23-2021	.100" (2.54mm) Center Header - 2 Pin
X26	22-23-2021	22-23-2021	22-23-2021	.100" (2.54mm) Center Header - 2 Pin

## Appendices

### Appendix 6.

Arduino code used to command the Teensy 3.6 in quadrature and arctan interpolation modes.

```
#include <ADC.h>          // Include relevant libraries
#include <math.h>
#include <stdbool.h>
#include "WProgram.h"
#include "QuadDecode_def.h"

QuadDecode<1> xPosn;    // Using FTM1 timer for hardware quadrature encoder in x4
count mode - pin 3 is Encoder A and pin 4 is encoder B

int sine = A6;         // Use pin 14 on ADC0
int cosine = A7;      // Use pin 38 on ADC1
int toggle = 29;      // Toggle switch pin
int ledW = 24;        // White LED pin
int ledY = 25;        // Yellow LED pin
int ledR = 26;        // Red LED pin
int ledG = 27;        // Green LED pin

int state;            // Toggle switch state
int a1;               // ADC0 values are integers
int b1;               // ADC1 values are integers
int size = 70;        // Look up table vector size

float u;              // Dummy variable for val when troubleshooting interpolator
float a2;              // ADC0 voltage
float b2;              // ADC1 voltage
float val;            // Arctangent value
float x;               // Current interpolated value
float oldx;           // Old interpolated value
float dx;             // Change in position
float count = 0;      // Current position
float oldcount = 0;   // Old position

float in[] = {0, 0.002, 0.224, 0.443, 0.614, 0.737, 0.847, 0.935, 1.011, 1.074, 1.130, 1.199,
1.261, 1.320, 1.388, 1.453, 1.519, 1.578, 1.648, 1.737, 1.845, 1.959, 2.106, 2.252, 2.416,
2.517, 2.652, 2.815, 2.998, 3.141, 3.288, 3.390, 3.480, 3.542, 3.616, 3.669, 3.729, 3.784,
3.828, 3.863, 3.905, 3.930, 3.964, 4.003, 4.033, 4.068, 4.097, 4.124, 4.152, 4.179, 4.204,
4.243, 4.289, 4.346, 4.398, 4.447, 4.489, 4.548, 4.604, 4.684, 4.758, 4.879, 4.985, 5.119,
5.277, 5.444, 5.646, 5.851, 6.0950, 6.283
};          // Input range to be re-mapped

float out[] = {0, 1.020, 3.340, 5.660, 7.980, 10.300, 12.620, 14.940, 17.260, 19.580, 21.900,
24.220, 26.540, 28.860, 31.180, 33.500, 35.820, 38.140, 40.460, 42.780, 45.100, 47.420,
49.740, 52.060, 54.380, 56.700, 59.020, 61.340, 63.660, 65.980, 68.300, 70.620, 72.940,
75.260, 77.580, 79.900, 82.220, 84.540, 86.860, 89.180, 91.500, 93.820, 96.140, 98.460,
```

## Appendices

```
100.780, 103.100, 105.420, 107.740, 110.060, 112.380, 114.700, 117.020, 119.340,  
121.660, 123.980, 126.300, 128.620, 130.940, 133.260, 135.580, 137.900, 140.220,  
142.540, 144.860, 147.180, 149.500, 151.820, 154.140, 156.460, 158.2  
}; // Output range to be mapped to
```

```
float FmultiMap(float val, float in, float out, uint8_t size); // Use multimap() function to do the  
mapping.
```

```
const unsigned long period = 50000; // Time between prints  
unsigned long time_now = 0; // Create time variable for counting
```

```
ADC *adc = new ADC(); // Create ADC object  
ADC::Sync_result result = adc->analogSyncRead(a1, b1); // Initialise sync read of both  
ADC's
```

```
void setup() {  
  Serial.begin(9600); // USB is always 12 Mbit/s  
  pinMode(toggle, INPUT); // Toggle switch is an input  
  pinMode(ledR, OUTPUT); // All LED's are outputs  
  pinMode(ledG, OUTPUT);  
  pinMode(ledY, OUTPUT);  
  pinMode(ledW, OUTPUT);  
  adc->setAveraging(1, ADC_0); // Set number of averages in ADC0  
  adc->setAveraging(1, ADC_1); // Set number of averages in ADC1  
  adc->setResolution(12, ADC_0); // Set ADC resolution in ADC0  
  adc->setResolution(12, ADC_1); // Set ADC resolution in ADC1  
  xPosn.setup(); // Setup quadrature encoder  
  xPosn.start(); // Start quadrature encoder  
  digitalWrite(ledG, HIGH); // Turn on ledG to show successful setup  
}
```

```
void loop() {  
  state = digitalRead(toggle); // Get switch state to decide which counter  
  to use  
  if (state == LOW) {  
    digitalWrite(ledY, LOW);  
    digitalWrite(ledW, HIGH);  
    FmultiMap(); // If switch low, call interpolator function and turn  
    on ledW  
    while (micros() > time_now + period) { // Check we are on time by comparing  
    timer and current time against desired period  
      time_now = micros();  
      Serial.println(count, 0); // Output interpolated count  
    }  
  }  
  else if (state == HIGH) {
```

## Appendices

```
    digitalWrite(ledW, LOW);
    digitalWrite(ledY, HIGH);
    while (micros() > time_now + period) {
// Check we are on time by comparing timer and current time against desired period
        time_now = micros();
        Serial.println(xPosn.calcPosn());
// If switch high, read hardware quadrature which is always running and turn on ledY
    }
}
}
```

```
float FmultiMap() {
    result = adc->analogSynchronizedRead(sine, cosine);
// Read both ADC's at same time
    a1 = result.result_adc0;
    b1 = result.result_adc1;
    double a2 = ((a1 * (3.3 / 4096)) - 2.18);
// Convert ADC values to voltages with double precision, whilst accounting for signal offset
    double b2 = ((b1 * (3.3 / 4096)) - 1.27);
    double val = (atan2(b2, a2)) + 3.1416;
// Calculate arctangent value with double precision and offset to positive range for mapping

    if (val <= in[0]) return out[0];
// Make sure value is within range
    if (val >= in[size - 1]) return out[size - 1];
    uint8_t pos = 1;
// Search right interval
    while (val > in[pos]) pos++;
    if (val == in[pos]) return out[pos];
// Handle any exact points
    x = (val - in[pos - 1]) * (out[pos] - out[pos - 1]) / (in[pos] - in[pos - 1]) + out[pos - 1]; //
    Linearly interpolate

    dx = (x - oldx);
// Calculate change in position (nanometres)
    if ((dx > 20) || (dx < -20)) dx = 0;
// Discard values produced from peak-trough jumps from the arctangent function
    count = oldcount + dx;
// Calculate position

    oldx = x;
// Store and return values as required
    oldcount = count;
    return x;
    return count;
}
```

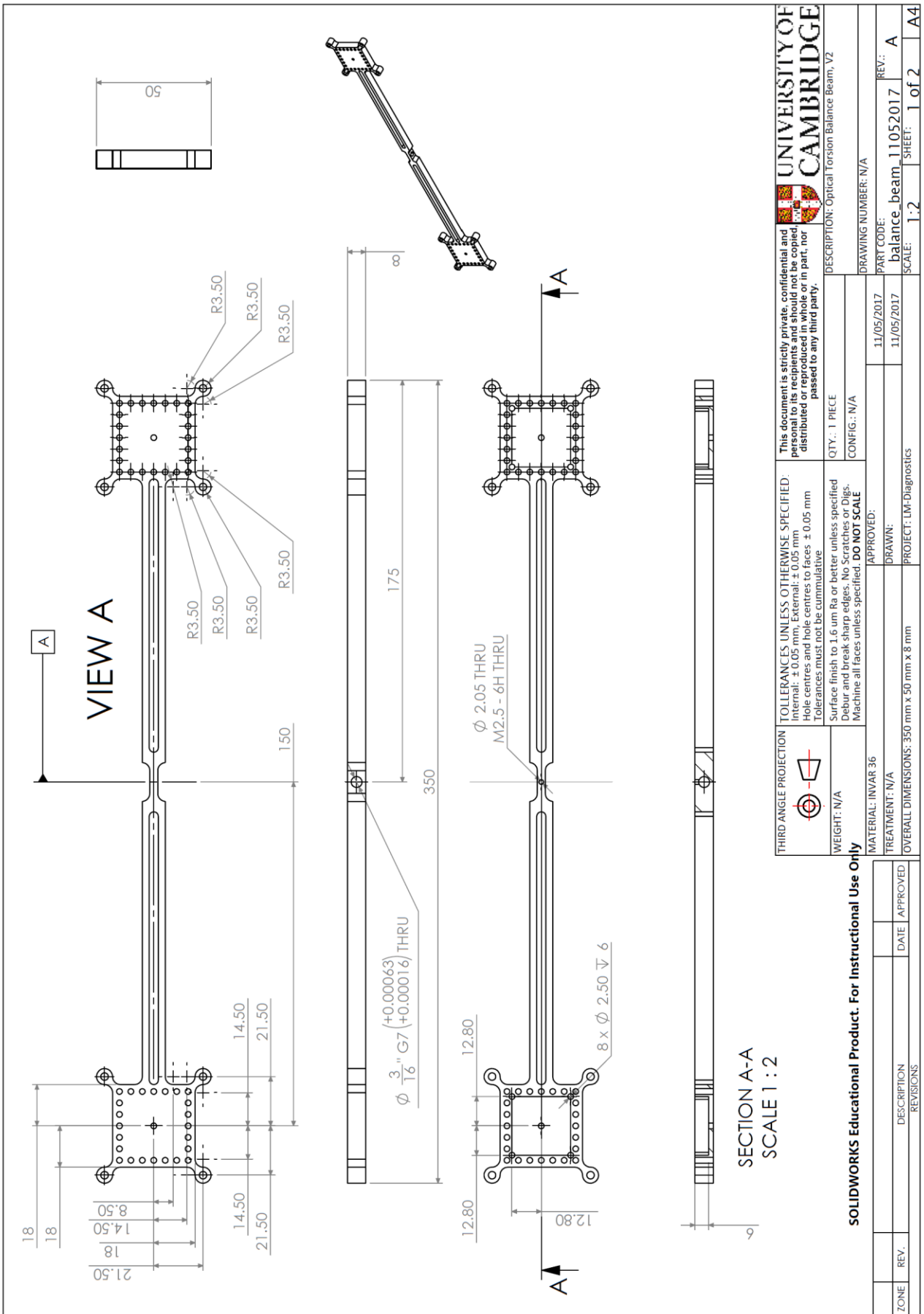
### Appendix 7.

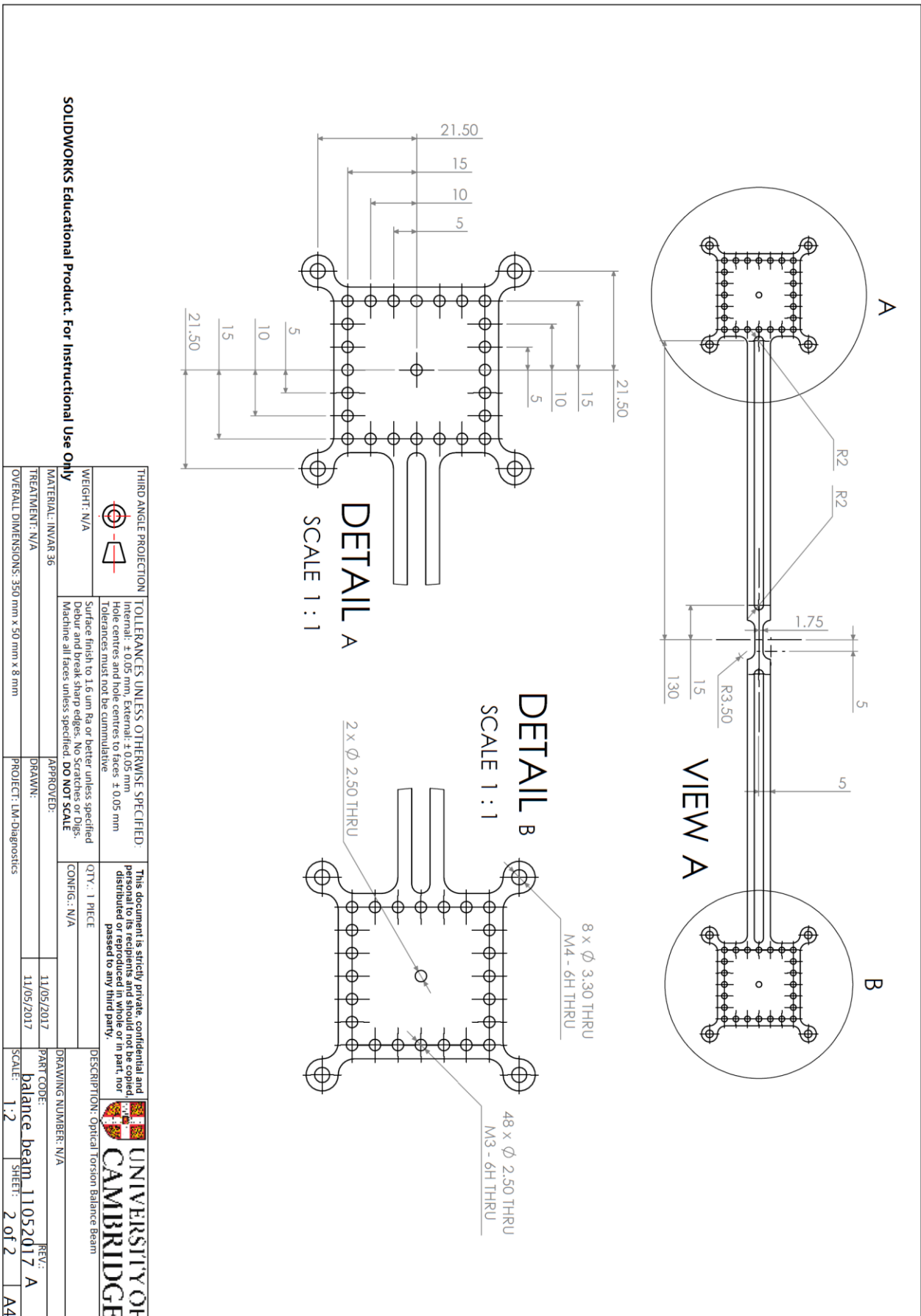
The mechanical design process for the force balance system is outlined here, along with drawings for all CNC machined parts so that work can be replicated. The first step was to extract the desired mechanical properties of the balance such as length, moment of inertia and spring rate. These properties were extracted from the MATLAB model which was iteratively used to achieve a desired response given a set of initial values and constraints. The design of this force balance was driven by range and resolution, as described in 4.2. The main design constraints not mentioned:

- Size. The force balance unit including vacuum chamber must fit within a 450 mm x 250 mm x 150 mm volume.
- Cost. In addition to size, limited funds of approximately £25,000 were available to build the entire system. Generally, cost increases with size and complexity. This also applies to vacuum systems as larger volumes require larger pumps.
- Availability. Not all components could be custom made due to time and cost constraints, therefore as many commercial off-the-shelf components (COTS) we used as possible. The best examples are the torsional springs which are extremely delicate and costly components as they require multiple manufacturing technique to be produced. It was necessary to stick to the specifications of stock models which are somewhat limited. This was difficult considering the importance of spring rate to the system.
- A second important set of limitations apply to the optical assembly side, as standard optical components had to be used e.g beam splitters, mirrors and mounts. It was decided early on to go with standard 1" optics with full kinematic adjustment as they provide the greatest flexibility and allowable error for misalignment later on – this mitigated our requirement for any advanced optical analysis and tolerance stack ups.

The overall system design was based around the balance beam, which most parameters are extracted from (length, moment of inertia and spring rate). The drawings for this component are shown in the figure below. The beam is constructed from Invar 36 which is a low thermal expansion steel. This has been done to reduce the effects of thermal expansion on the centre to centre distances of the retroreflectors with respect to the pivot point. Invar 36 has a CTE of approximately 1.2 ppm/°C, vs. 7075 aluminium which has 23.2 ppm/°C – over the 350 mm length of the beam this corresponds to a length change of 0.42 µm/ °C and 8.1 µm/ °C. The laboratory temperature was measured to fluctuate ±2 °C around the set point.

The target moment of inertia of the beam was 0.005 kg.m<sup>2</sup> from the MATLAB model. The main approach to achieve this whilst keeping the length maximal (to maximise sensitivity) and the high density invar (for thermal control), was to remove mass. The mass of the beam was minimised by cutting slots in the central beam connecting the two centres without reducing the stiffness appreciably. Additional material was removed around mounting holes as well. Below the beam, the balance has ~1" milled slots to locate and bond the retroreflectors into place. They are machined with high precision (± 50 µm) as the distance between centres with respect to the pivot point influences the measurement accuracy. CMM measurements of critical dimensions such as this were taken so that the values are known with even better precision and accuracy.

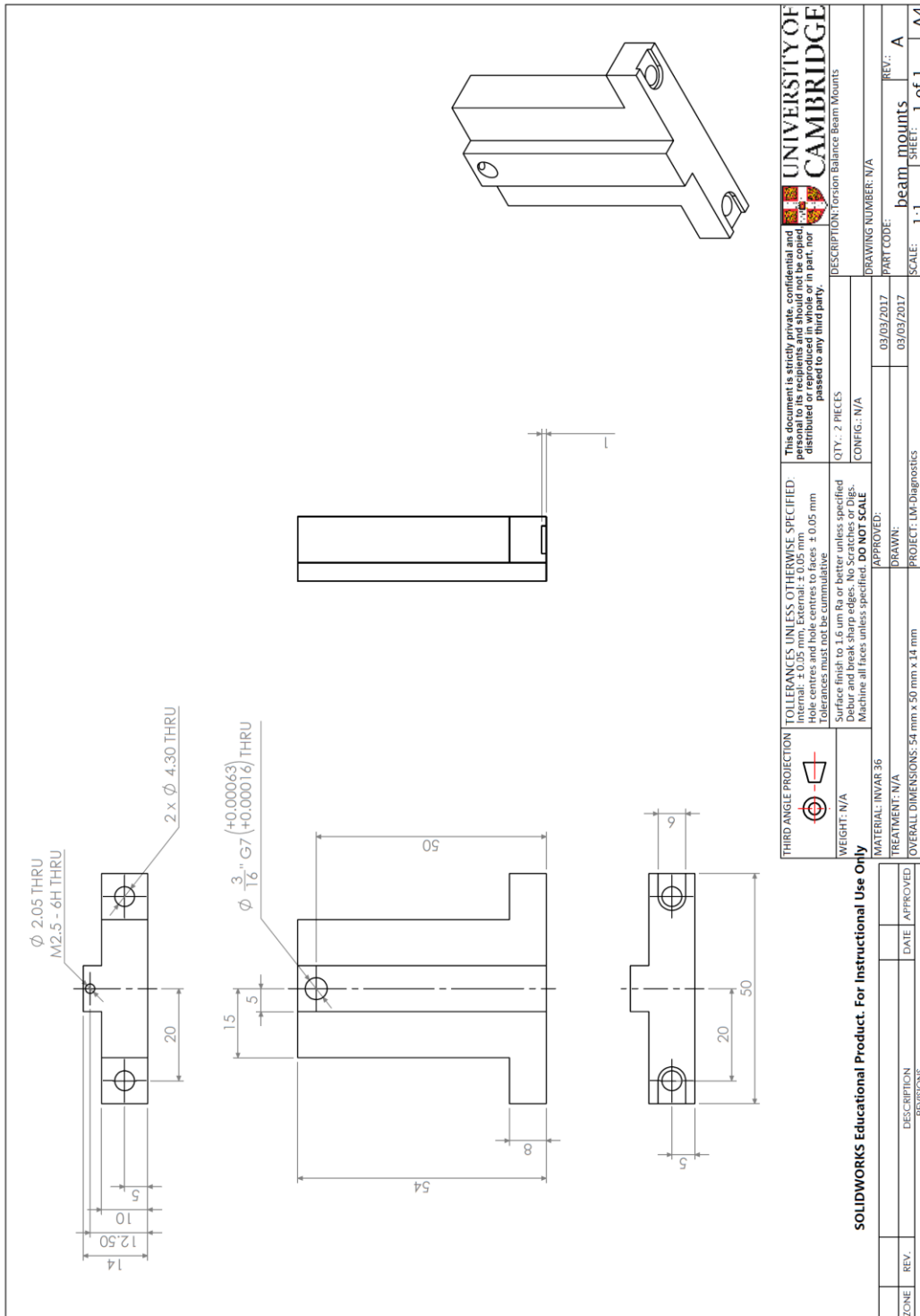




# Appendices

The centre of the balance beam houses a C-Flex CD-20 torsional spring with a nominal torsional spring rate of 0.03884 N.m/rad as described in 6.1.2. This model is a double-ended bearing which has the both outside ends statically mounted, and the inside, middle section the rotating section. The middle section is mounted to the balance beam using grub screws located onto the flats of the bearing. The design for the bearing was challenging due to its small dimensions (3/16" diameter, 0.3" length overall, 0.12" for the middle section). The outside ends are mounted into mounting blocks also constructed from invar 36, shown below.

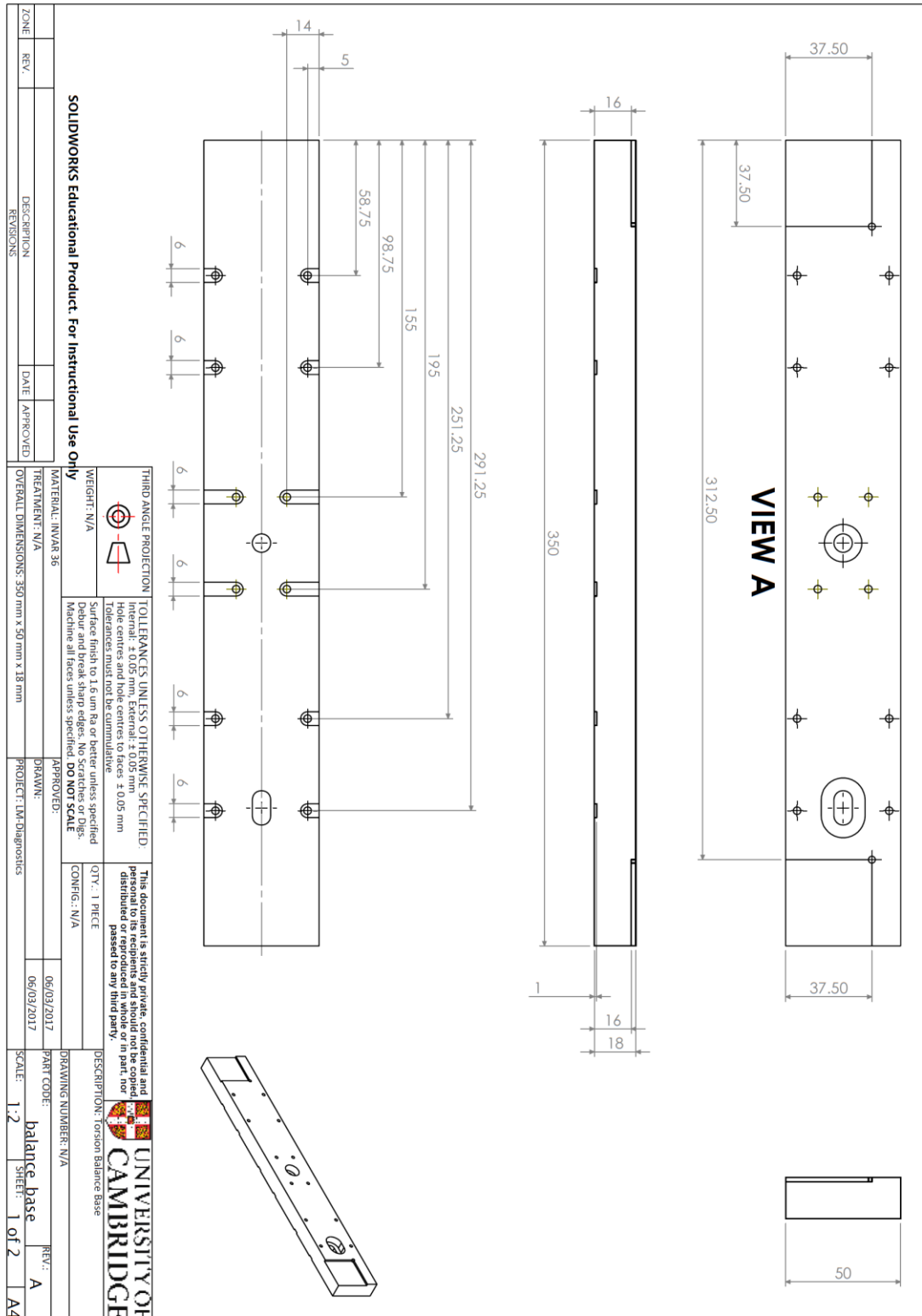
## Balance Beam Mount Drawing



# Appendices

The balance beam mounts, and most other consecutive parts shown which will be in a vacuum environment have features to decrease pumping time. Features include no vented volumes for trapped gas, and high quality surface finish ( $R_a < 1.6 \mu\text{m}$ ) to reduce outgassing load. The balance beam mounts (2x) are connected to the bearing using grub screws and mounted to the balance beam base which is also constructed from invar 36. The drawing is shown below.

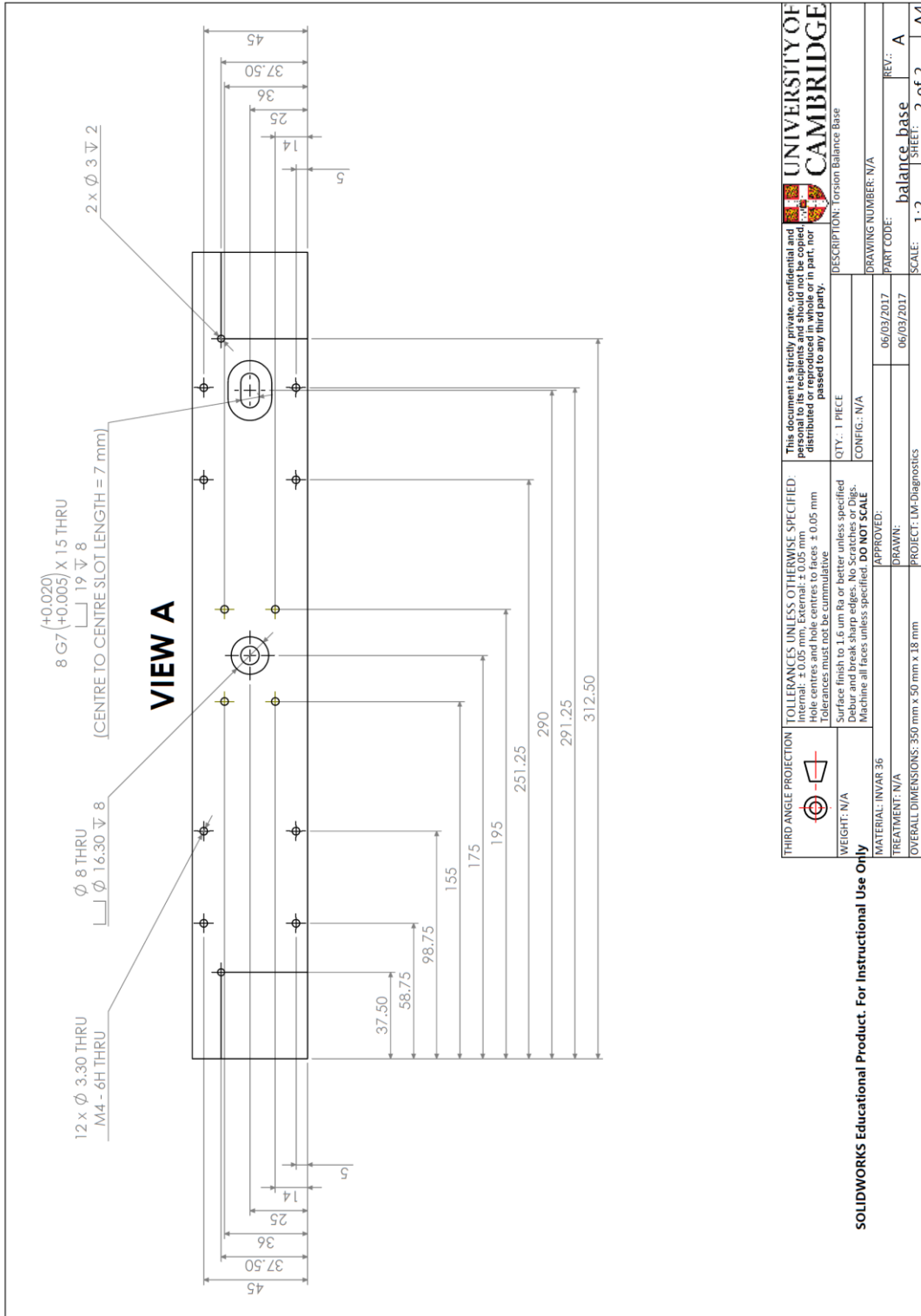
Balance Base Drawing Page 1



# Appendices

This component also contains a slotted hole which is mounted to a base plate use spring washer and shoulder screws to control the direction of thermal expansion so that it more closely matches that of the optics base mount outside the chamber (shown later). The beam base balance has ~1.5" milled slots to locate corner cube reflectors into place. These pass the inbound and outbound laser path from the retroreflectors mounted to the balance beam, to outside the chamber.

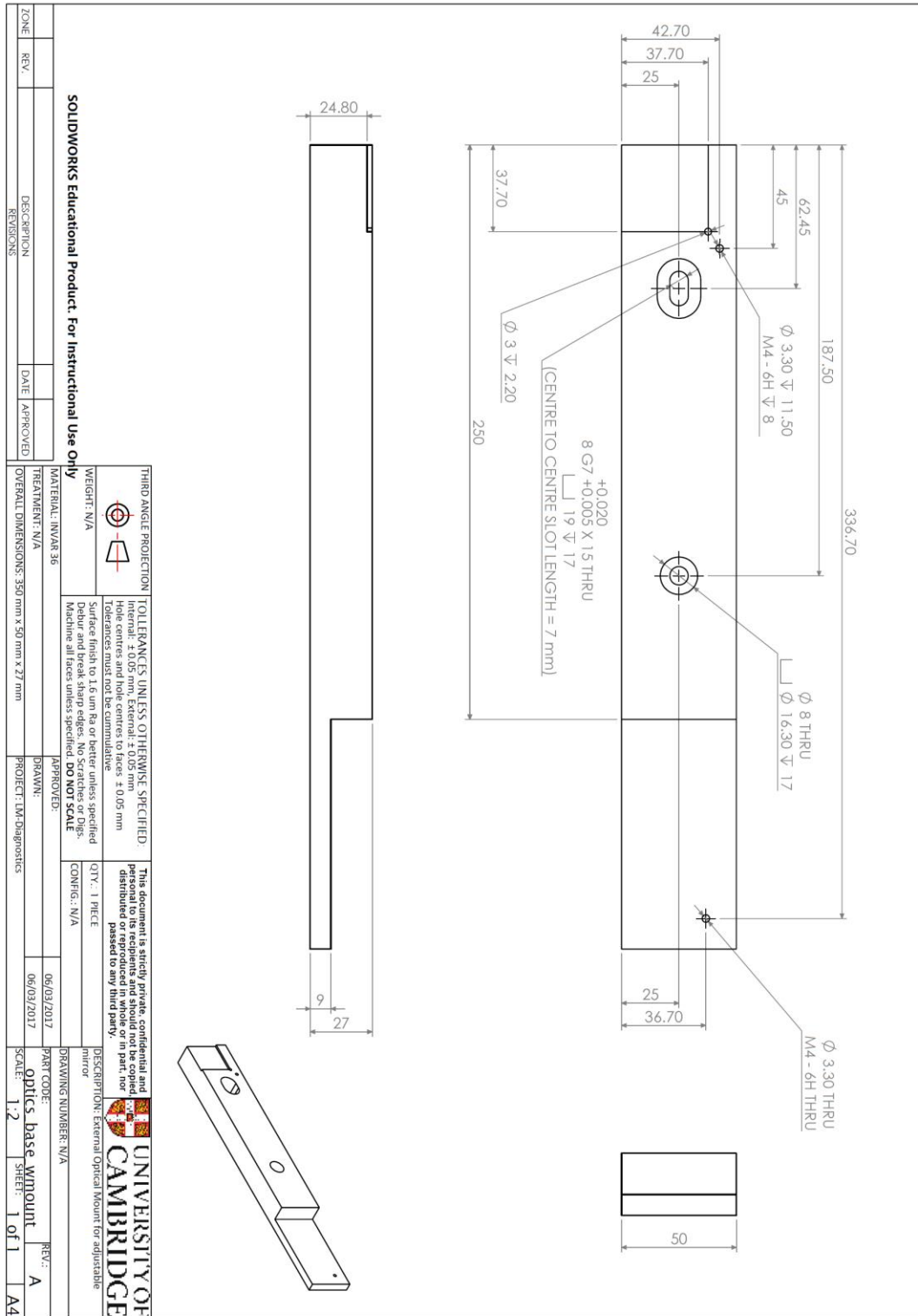
Balance Base Drawing Page 2



# Appendices

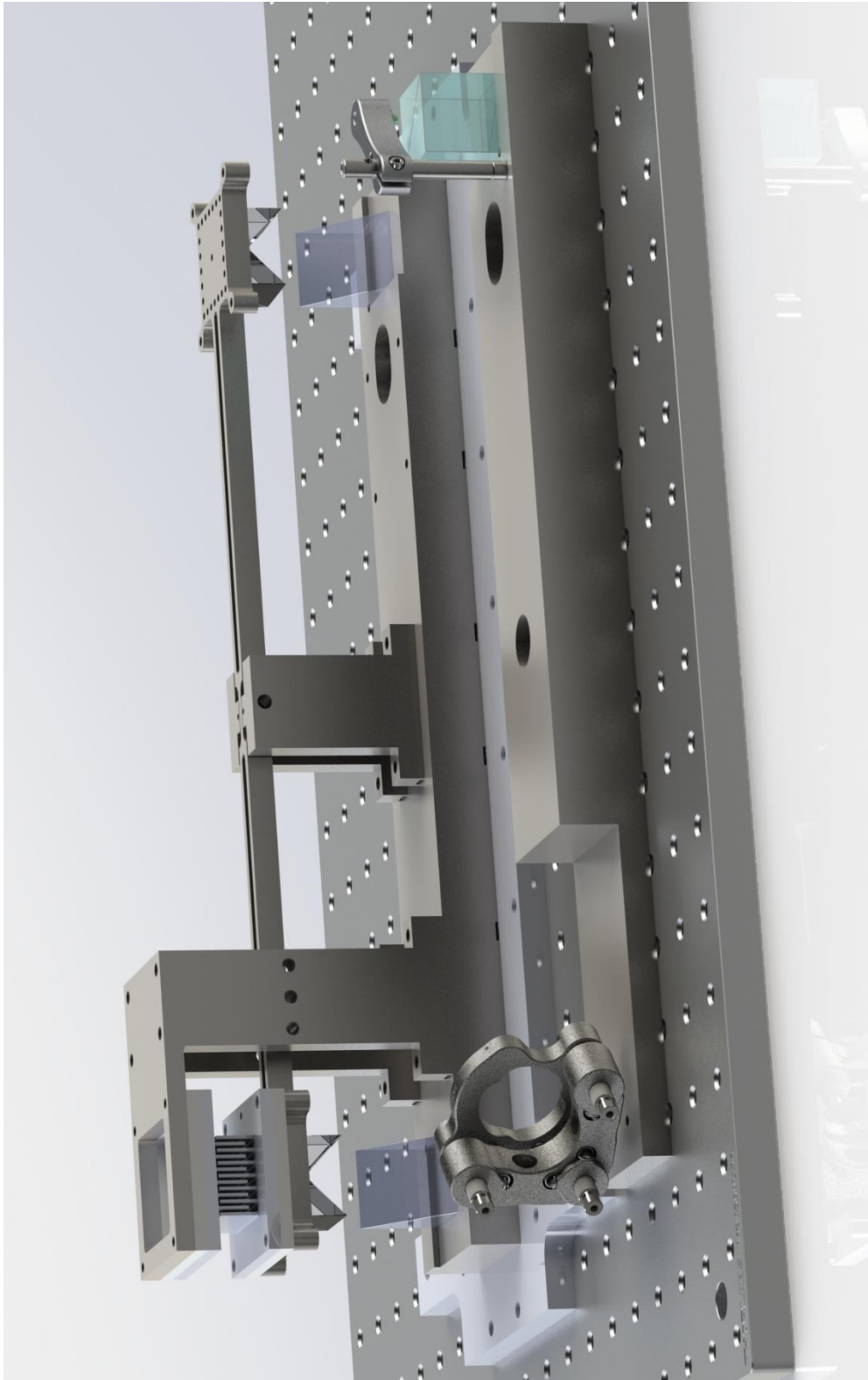
The optics base mount is shown in the drawing below. This mounts a polarising beam splitter cube and kinematic mirror mount with mirror. This component features the same slotted hole, shoulder screw and spring washer mounting system. All mirror mounts used in the optical assembly are precision type with the lowest drift and hysteresis. All mirrors are specified as protected aluminium, which has the highest reflectivity and lowest surface defects and curvature.

Optics Base Drawing.



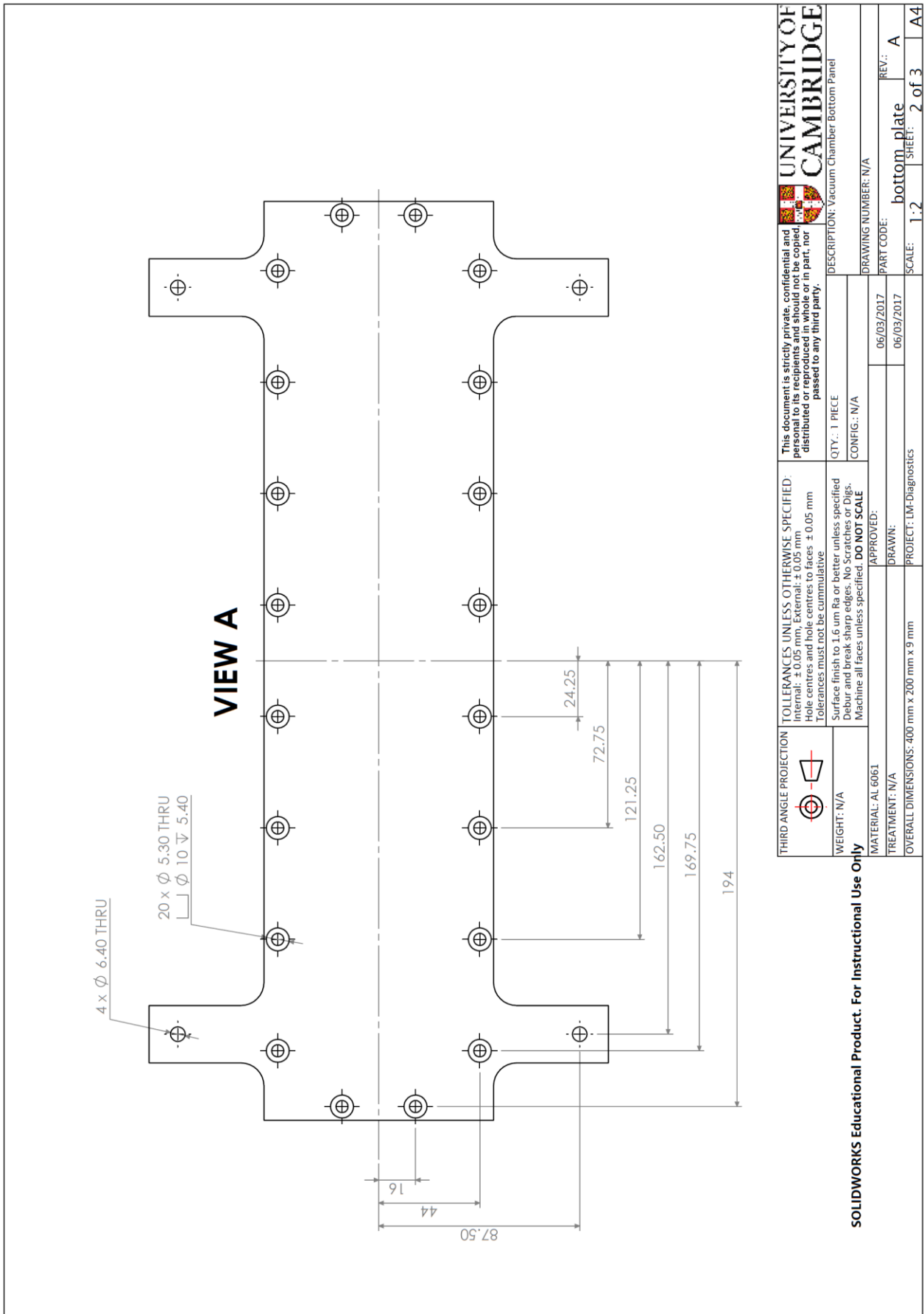
## Appendices

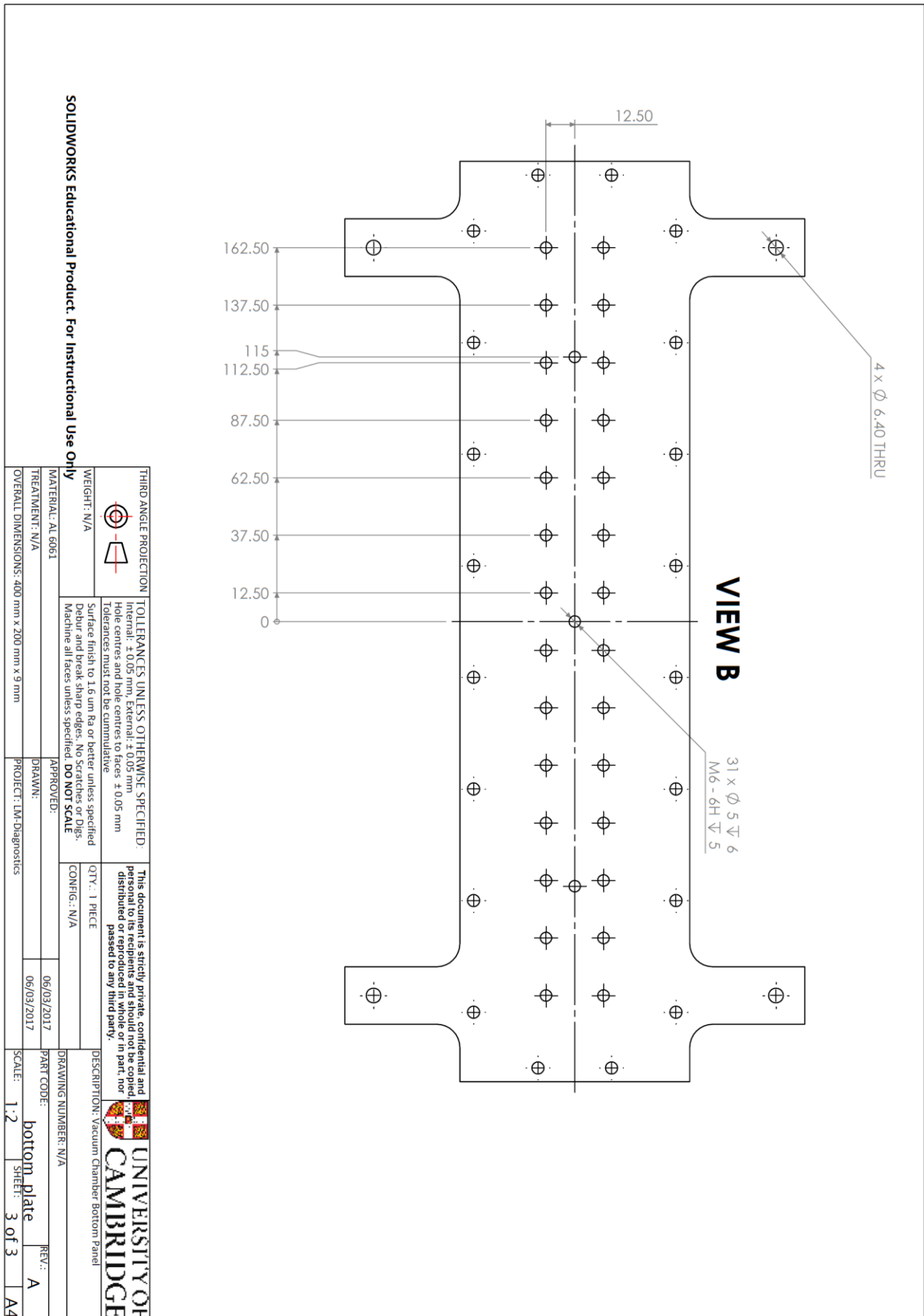
The components described so far can be seen assembled and rendered in the figure below, excluding the electrostatic fin assembly and chamber base plate.



The vacuum chamber baseplate, shown in the drawings below, has two main purposes. It is used to mount the Balance Base and also form the bottom of the modular vacuum chamber assembly. Note the high surface finish required on the side which makes the vacuum seal.



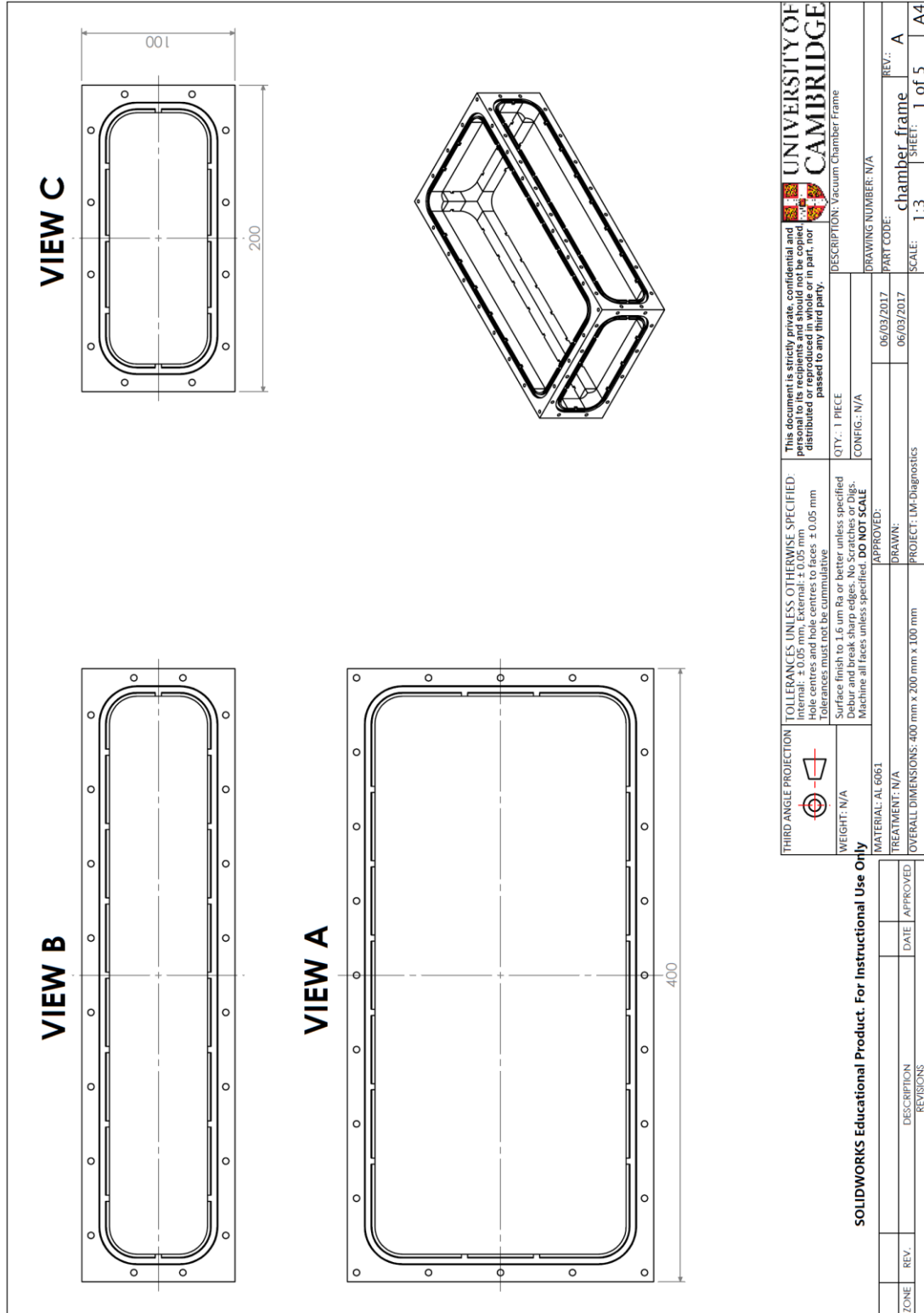




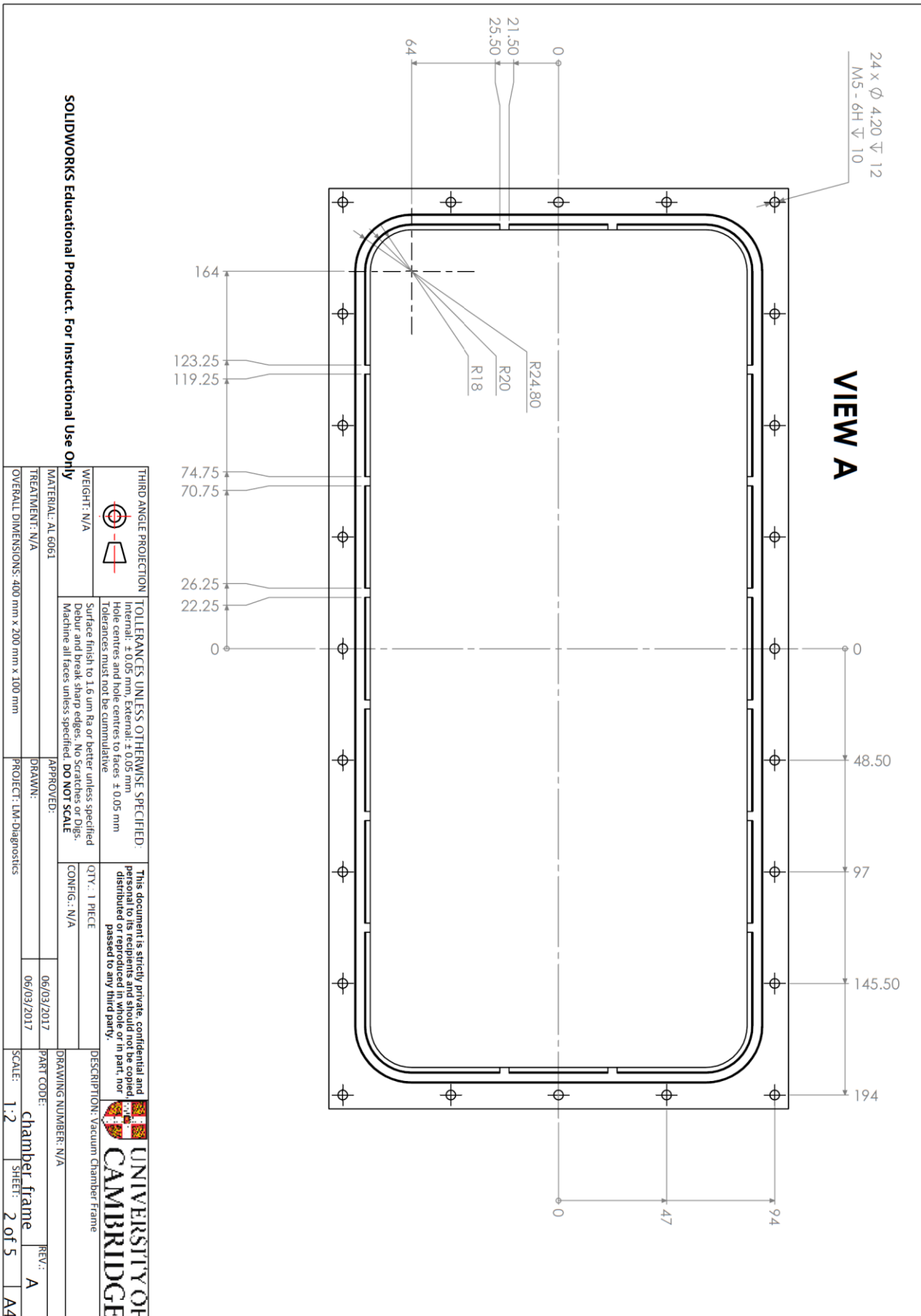
# Appendices

The chamber itself is based around a rectangular one piece frame to which 6 plates mount. This design was selected to maintain modularity so that plates can be swapped on demand for different situations requiring more feedthroughs, volume or sensors. Due to the moderate vacuum level requirement and limited funding, nitrile seals were selected for vacuum seals. The chamber frame drawings are shown below.

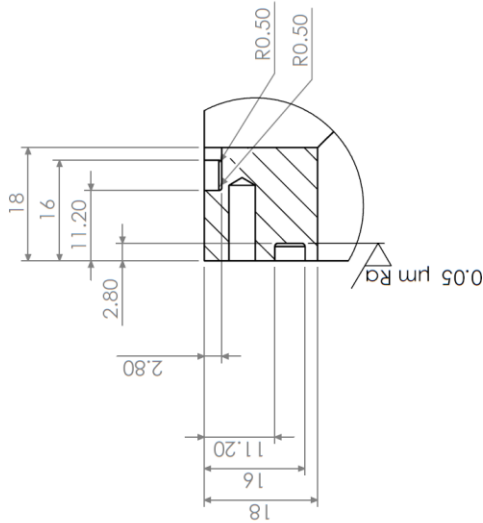
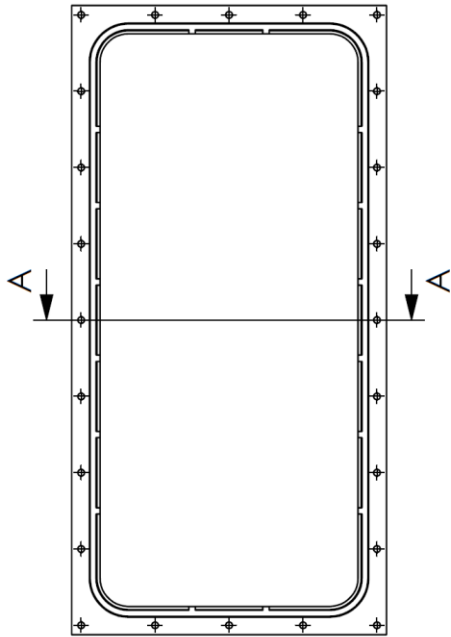
Chamber Frame Drawing Page 1



<p><b>UNIVERSITY OF CAMBRIDGE</b></p> <p>DESCRIPTION: Vacuum Chamber Frame</p>	
<p>TO TOLERANCES UNLESS OTHERWISE SPECIFIED:                  Internals: ± 0.05 mm, External: ± 0.08 mm                  Hole centres and hole centres to faces: ± 0.05 mm                  Tolerances must not be cumulative</p>	
<p>THIRD ANGLE PROJECTION</p>	
<p>WEIGHT: N/A</p>	
<p>MATERIAL: AL 6061</p>	
<p>TREATMENT: N/A</p>	
<p>APPROVED:</p>	
<p>OVERALL DIMENSIONS: 400 mm x 200 mm x 100 mm</p>	
<p>PROJECT: IM-Diagnostics</p>	
<p>DATE APPROVED:</p>	
<p>DESCRIPTION REVISIONS</p>	
<p>QTY.: 1 PIECE</p>	<p>CONFIG.: N/A</p>
<p>DRAWING NUMBER: N/A</p>	<p>REV.: A</p>
<p>PART CODE: chamber frame</p>	<p>SHEET: 1 of 5</p>
<p>SCALE: 1:3</p>	<p>A4</p>



**VIEW A**



**DETAIL J**

SCALE 1 : 1

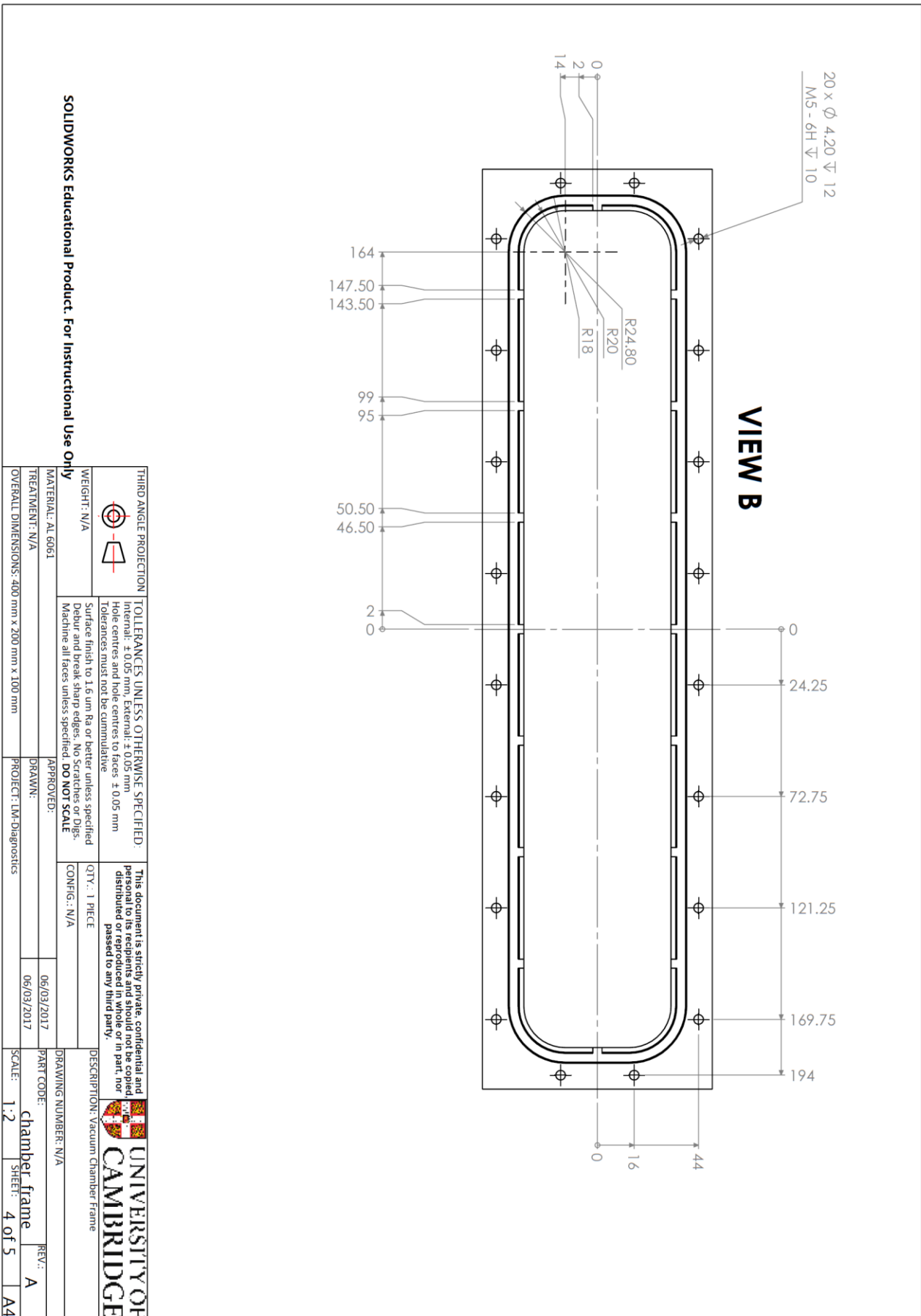
DETAIL J GROOVE PROFILE  
 APPLICABLE TO ALL GROOVES  
 ON ALL FACES, INCLUDING  
 0.05 MICRON RA FINISH ON  
 INSIDE BOTTOM FACE

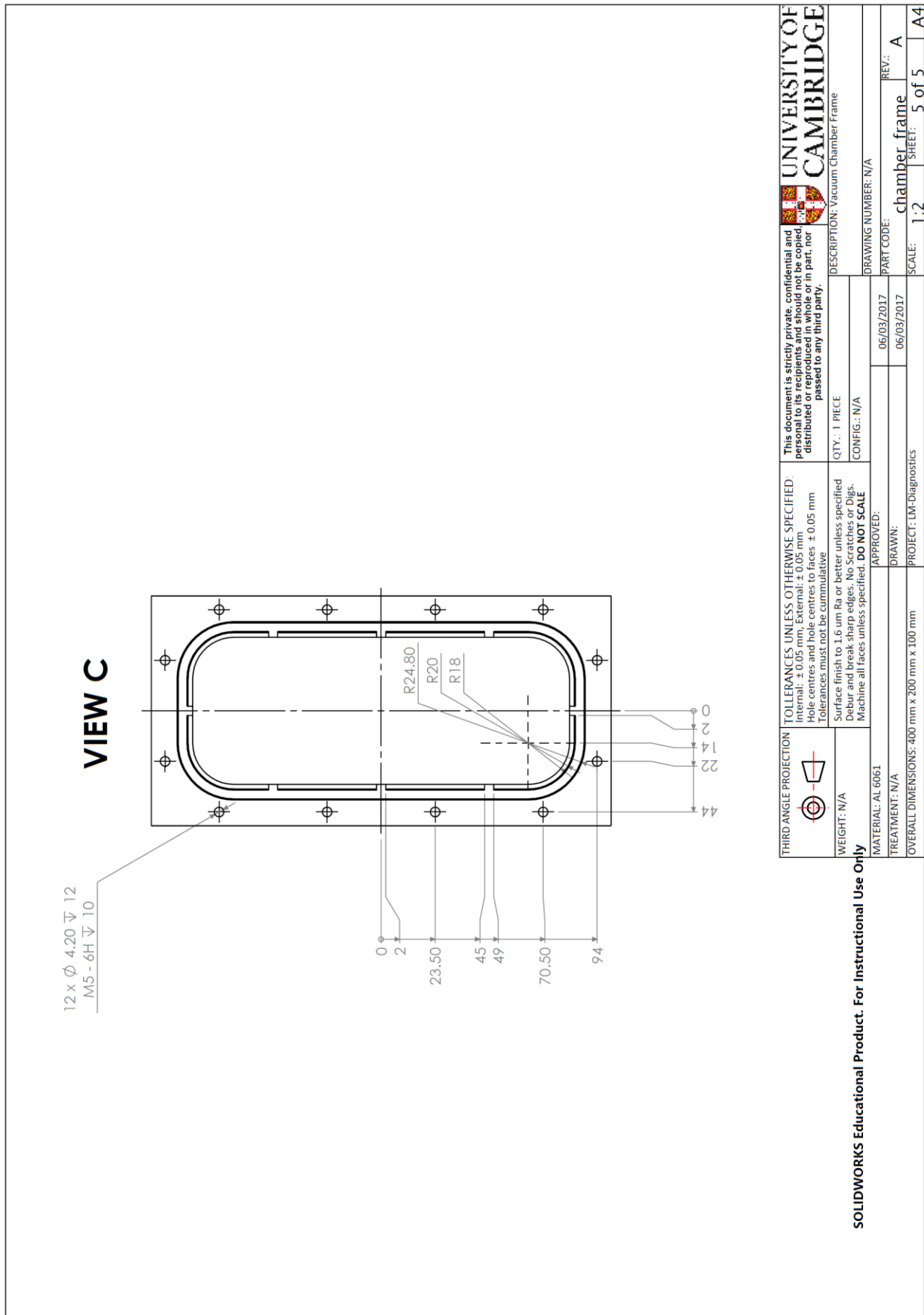
**SECTION A-A**

SCALE 1 : 4

	TOLLERANCES UNLESS OTHERWISE SPECIFIED: Internal: ± 0.05 mm, External: ± 0.05 mm Hole centres and hole centres to faces ± 0.05 mm Tolerances must not be cumulative Surface finish to 1.6 µm Ra or better unless specified Debur and break sharp edges. No Scratches or Digs. Machine all faces unless specified. <b>DO NOT SCALE</b>	This document is strictly private, confidential and personal to its recipients and should not be copied, distributed or reproduced in whole or in part, nor passed to any third party.	UNIVERSITY OF CAMBRIDGE
	WEIGHT: N/A MATERIAL: AL 6061 TREATMENT: N/A OVERALL DIMENSIONS: 400 mm x 200 mm x 100 mm	APPROVED: DRAWN: PROJECT: LM-Diagnostics	QTY.: 1 PIECE CONFIG.: N/A DRAWING NUMBER: N/A PART CODE: chamber frame SCALE: 1:4

**SOLIDWORKS Educational Product. For Instructional Use Only**

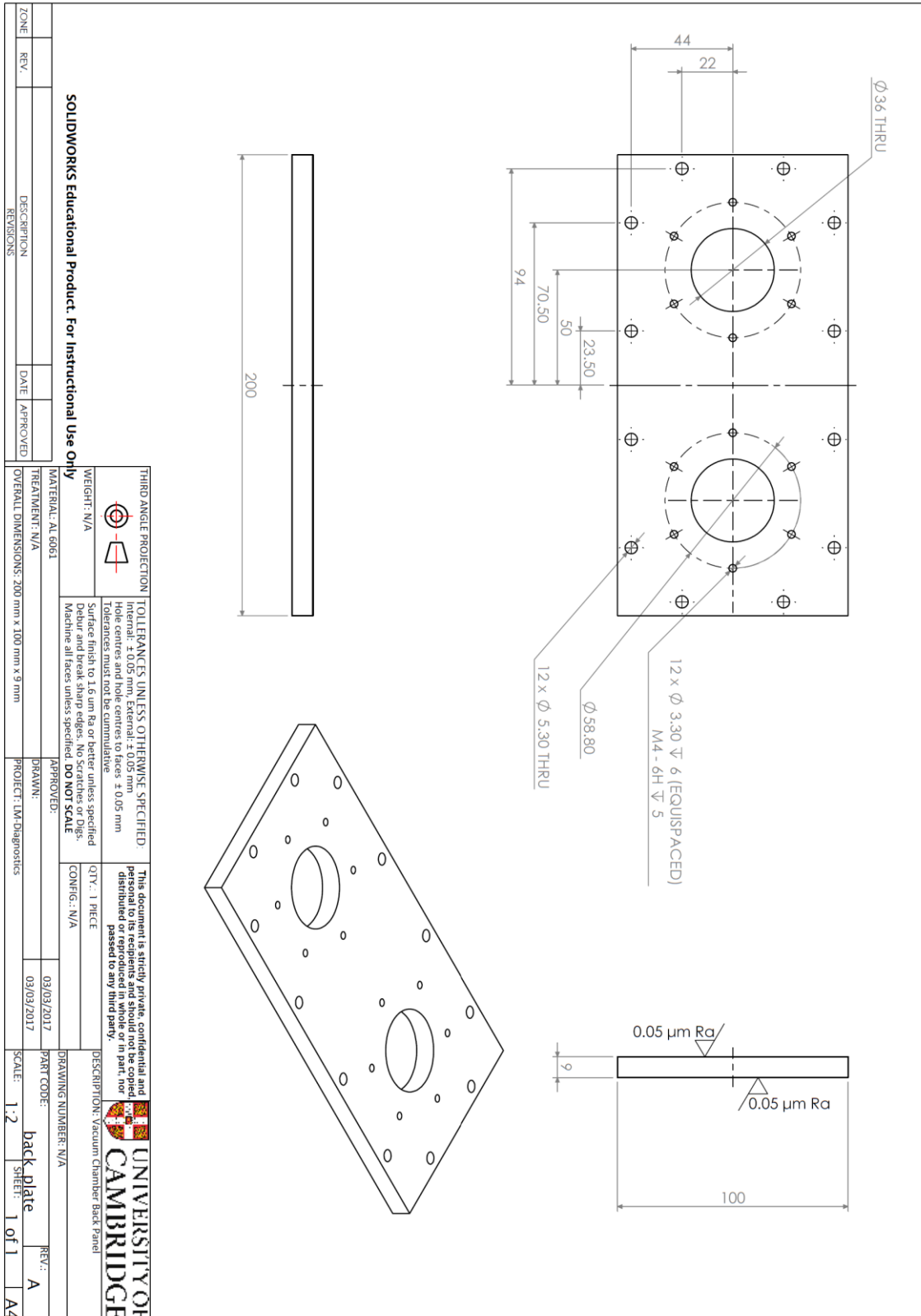




# Appendices

The drawings for the front, back, side and rear plates are shown below. Note the side plates are used with seals to house 10mm thick low-iron toughened glass windows. These were designed for viewing, laser passthrough and eventual integration with the Falcon holographic interferometer.

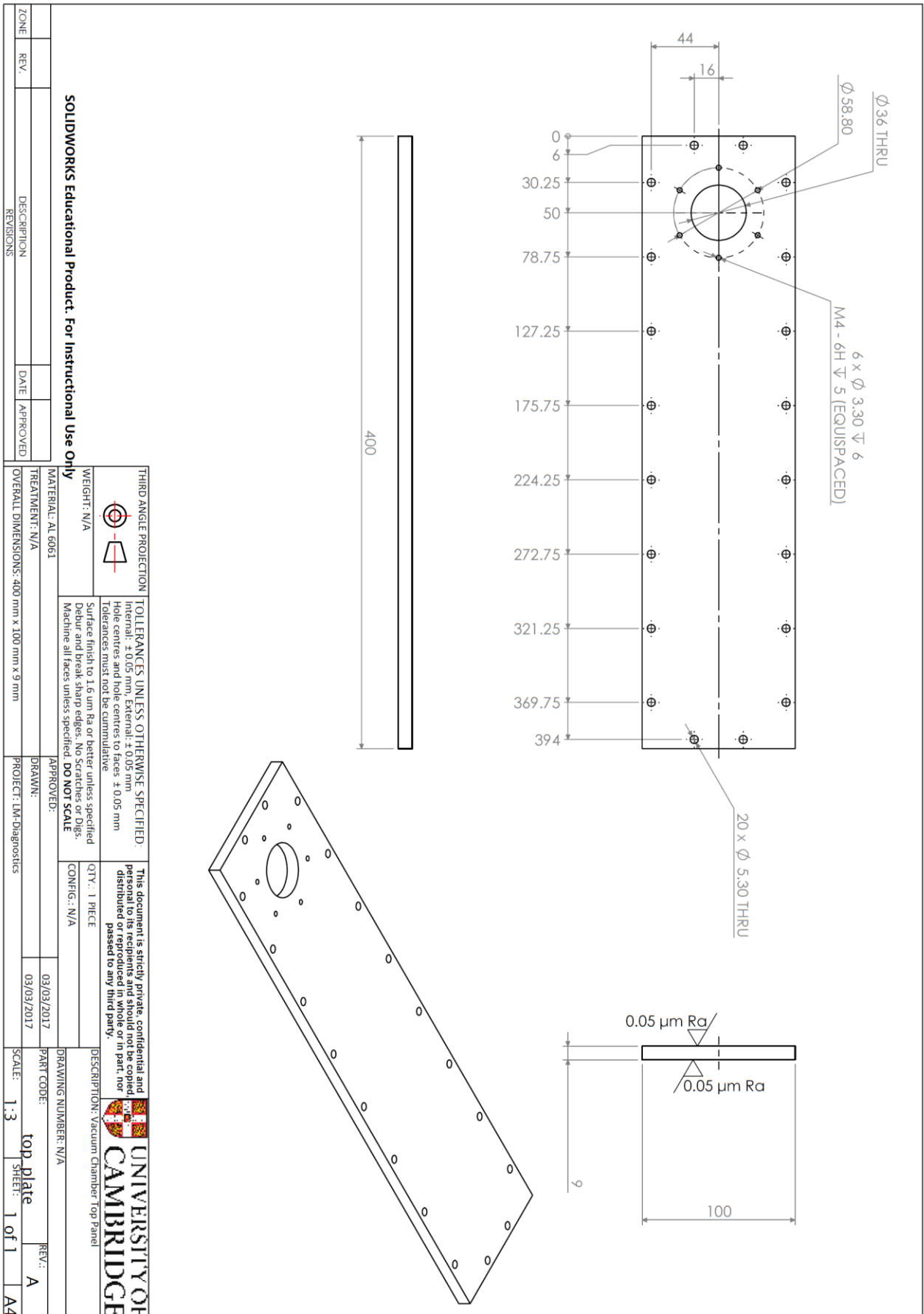
## Chamber Rear Plate Drawing



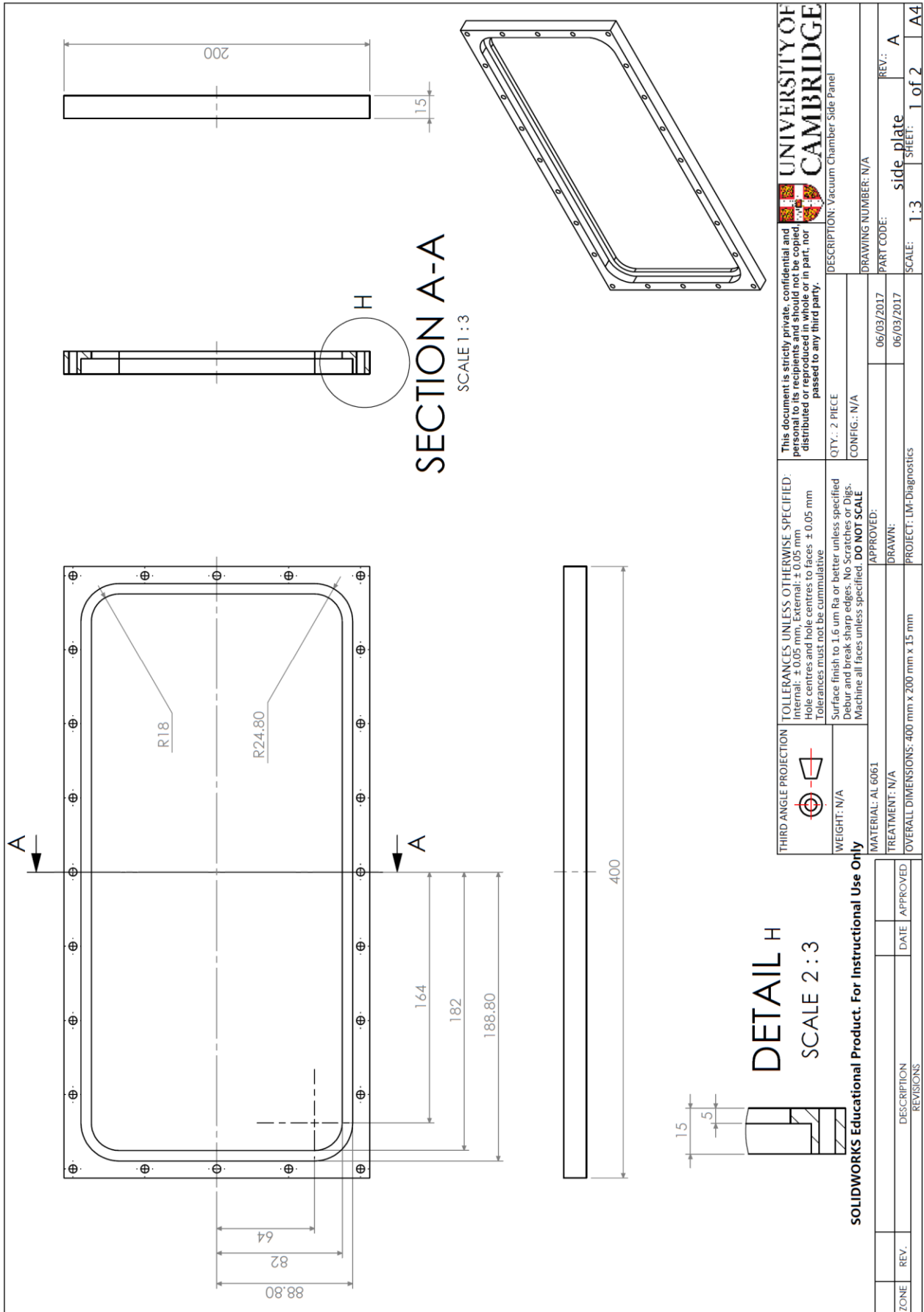


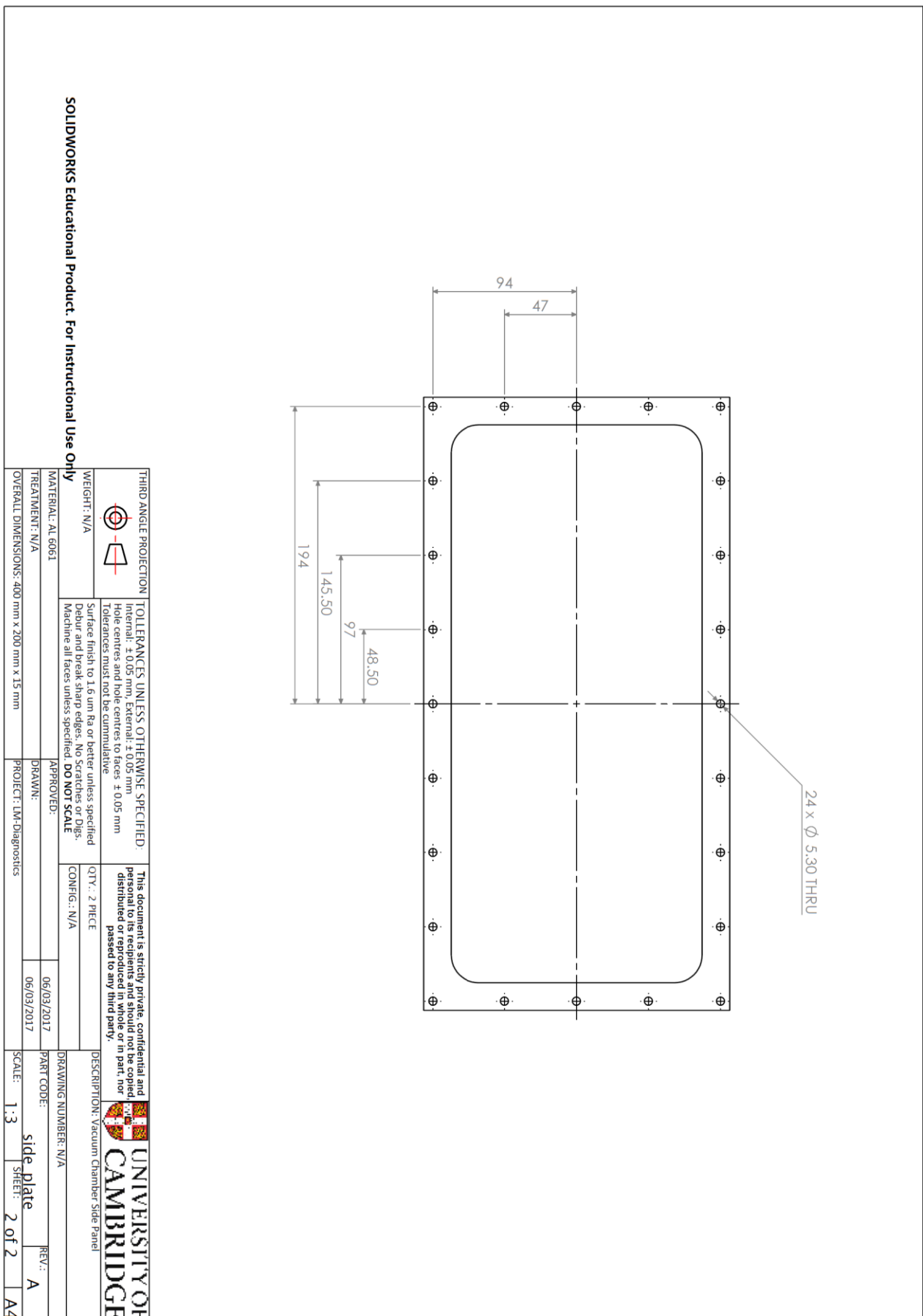
# Appendices

## Chamber Top Plate Drawing



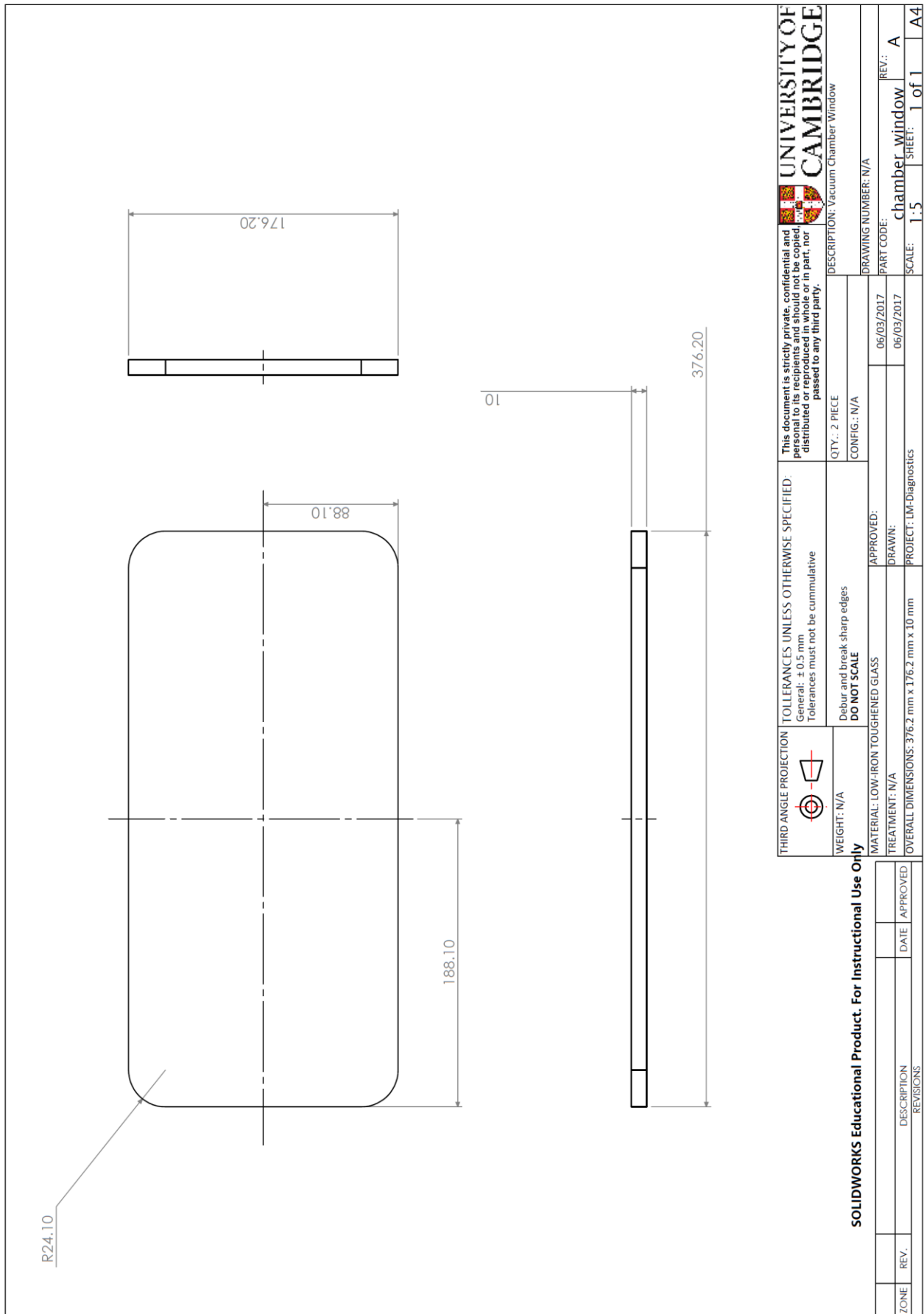
ZONE	REV.	DESCRIPTION	DATE	APPROVED	REVISIONS
<p><b>SOLIDWORKS Educational Product. For Instructional Use Only</b></p>					
MATERIAL: AL 6061		TOLERANCES, UNLESS OTHERWISE SPECIFIED:			
WEIGHT: N/A		Internal: $\pm 0.05$ mm External: $\pm 0.05$ mm Hole centres and hole centres to faces: $\pm 0.05$ mm Tolerances must not be cumulative			
TREATMENT: N/A		Surface finish to 1.5 um Ra or better unless specified Deburr and break sharp edges. No scratches or digs. Machine all faces unless specified. <b>DO NOT SCALE</b>			
OVERALL DIMENSIONS: 400 mm x 100 mm x 9 mm		APPROVED: _____ DRAWN: _____ PROJECT: LM-Diagnostics			
QTY.: 1 PIECE		This document is strictly private, confidential and personal to its recipients and should not be copied, distributed or reproduced in whole or in part, nor passed to any third party.			
CONFIG.: N/A		DESCRIPTION: Vacuum Chamber Top Panel			
DRAWING NUMBER: N/A					
PART CODE: top_plate		DRAWING NUMBER: N/A			
SCALE: 1:3		SHEET: 1 of 1			
REV: A		REV: A			
A4		A4			





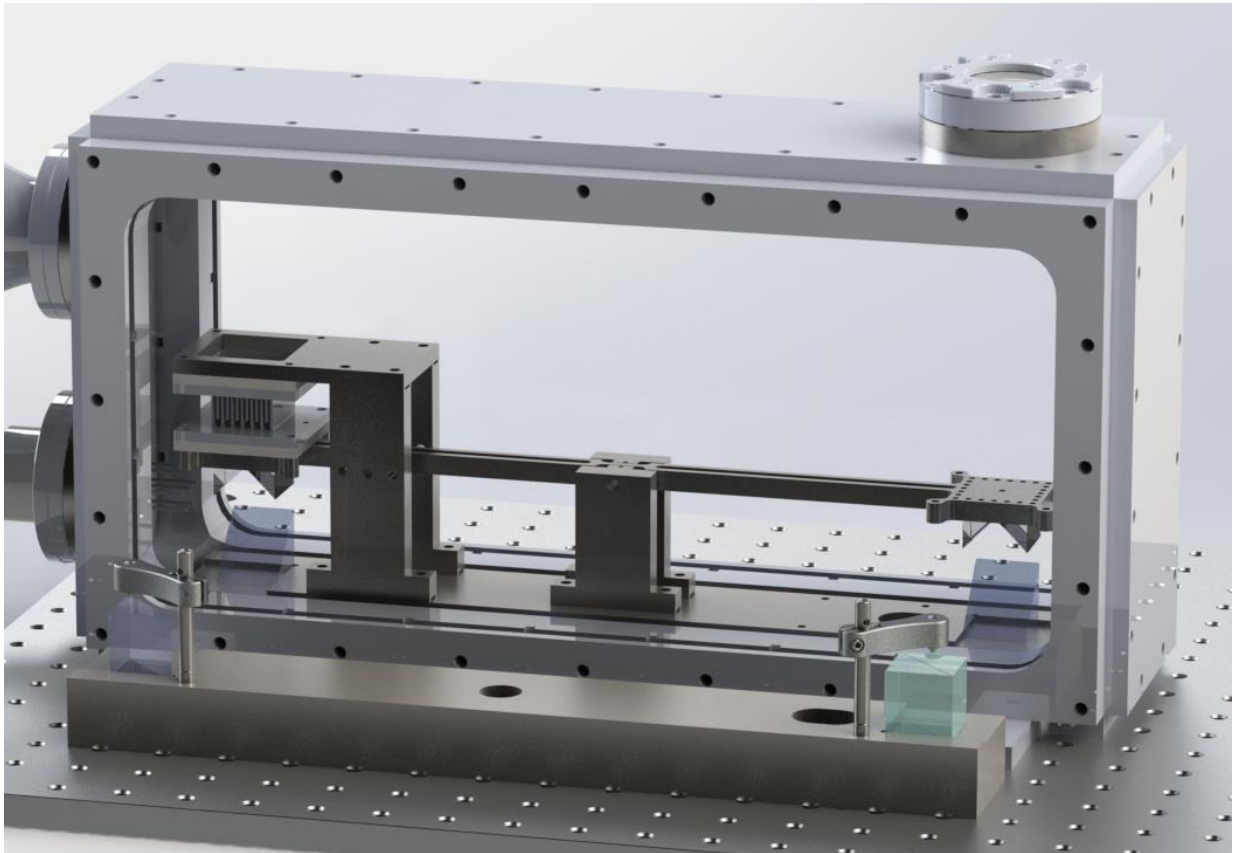
# Appendices

## Chamber Window Drawing



## Appendices

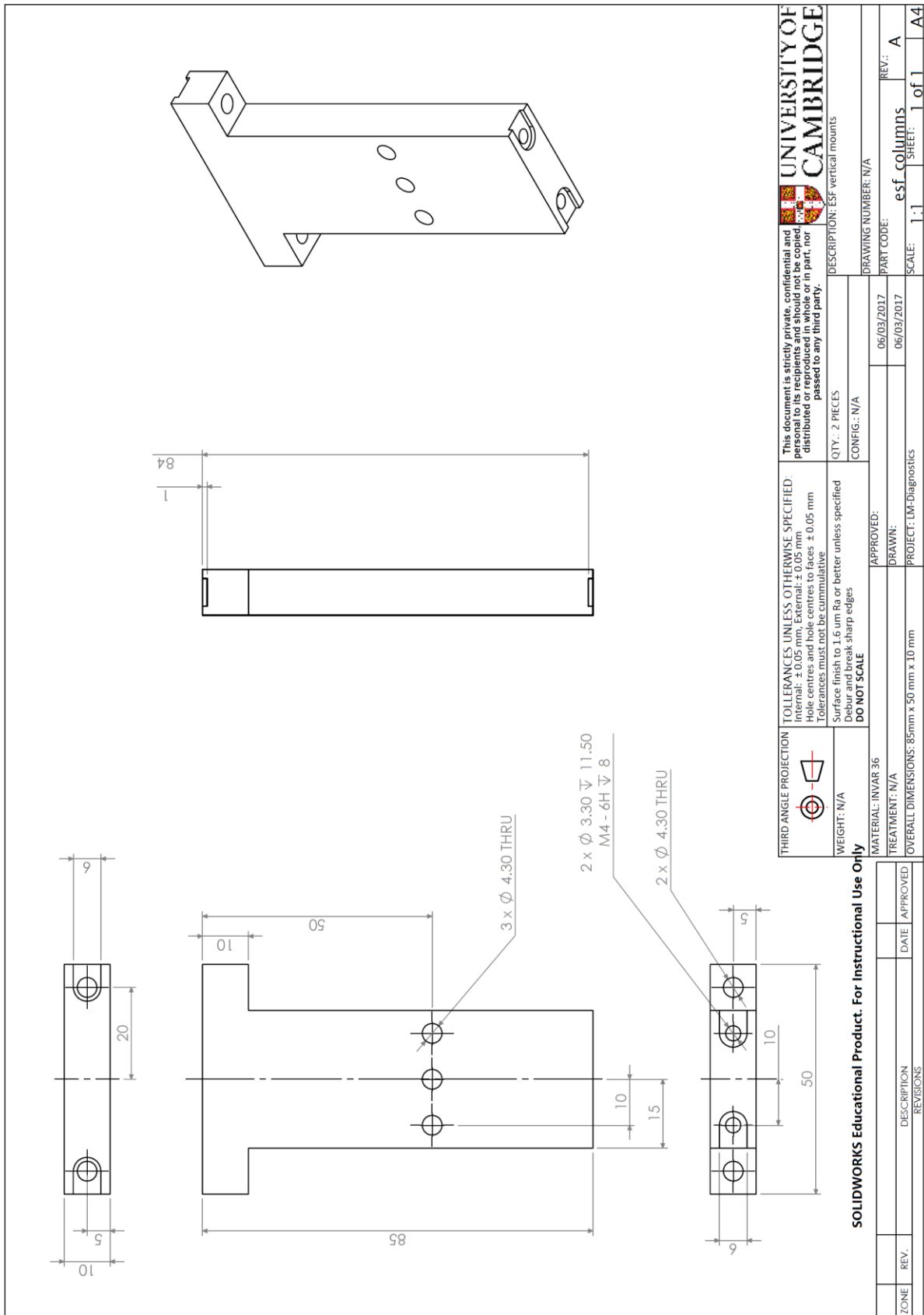
The assembly is shown in the figure below which has been rendered. The vacuum feedthroughs on the left hand side and window on the top right hand size are not included in this description.



# Appendices

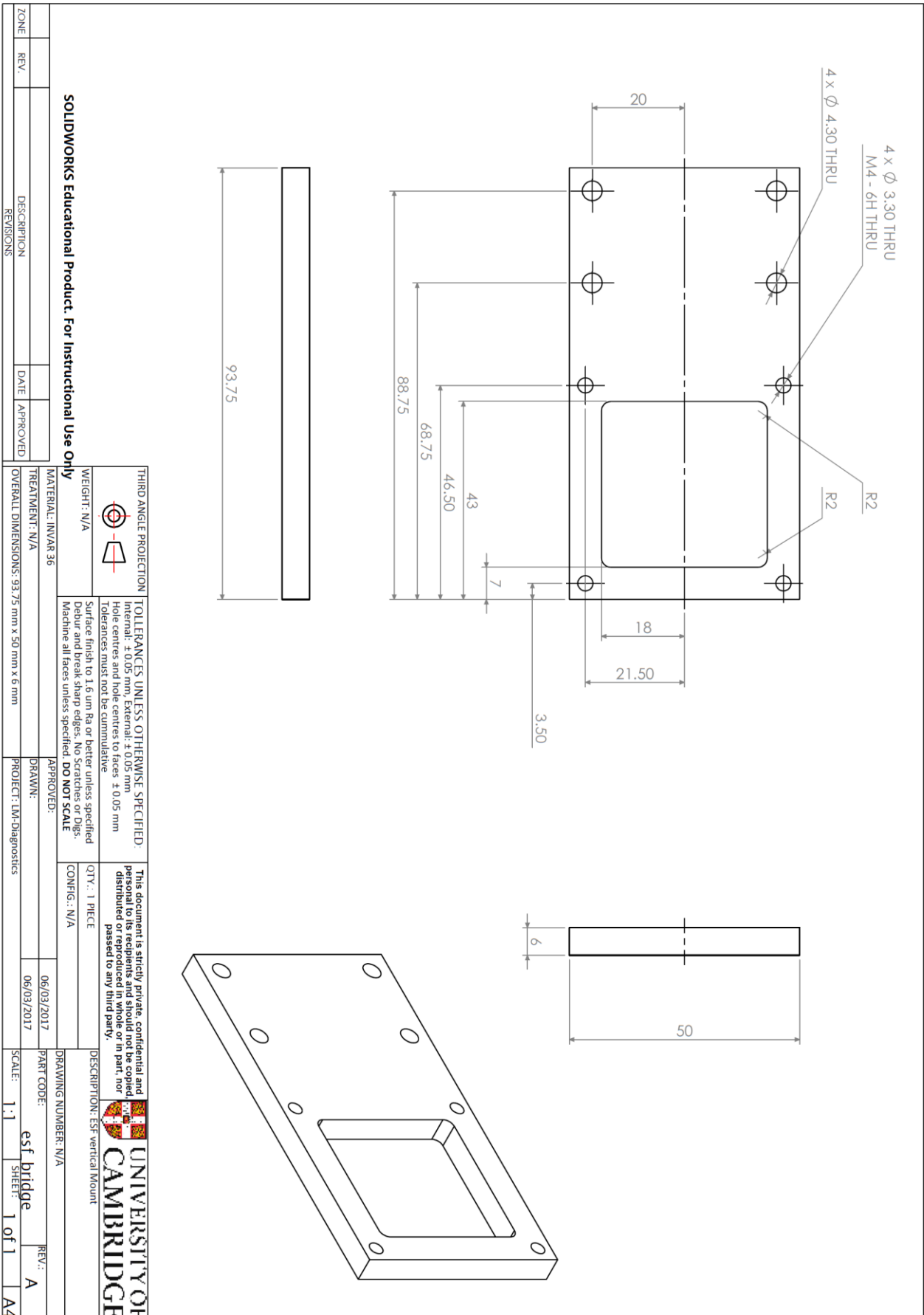
The drawings for the electrostatic fin system (EFS) are included below.

## EFS Vertical Mount Drawing

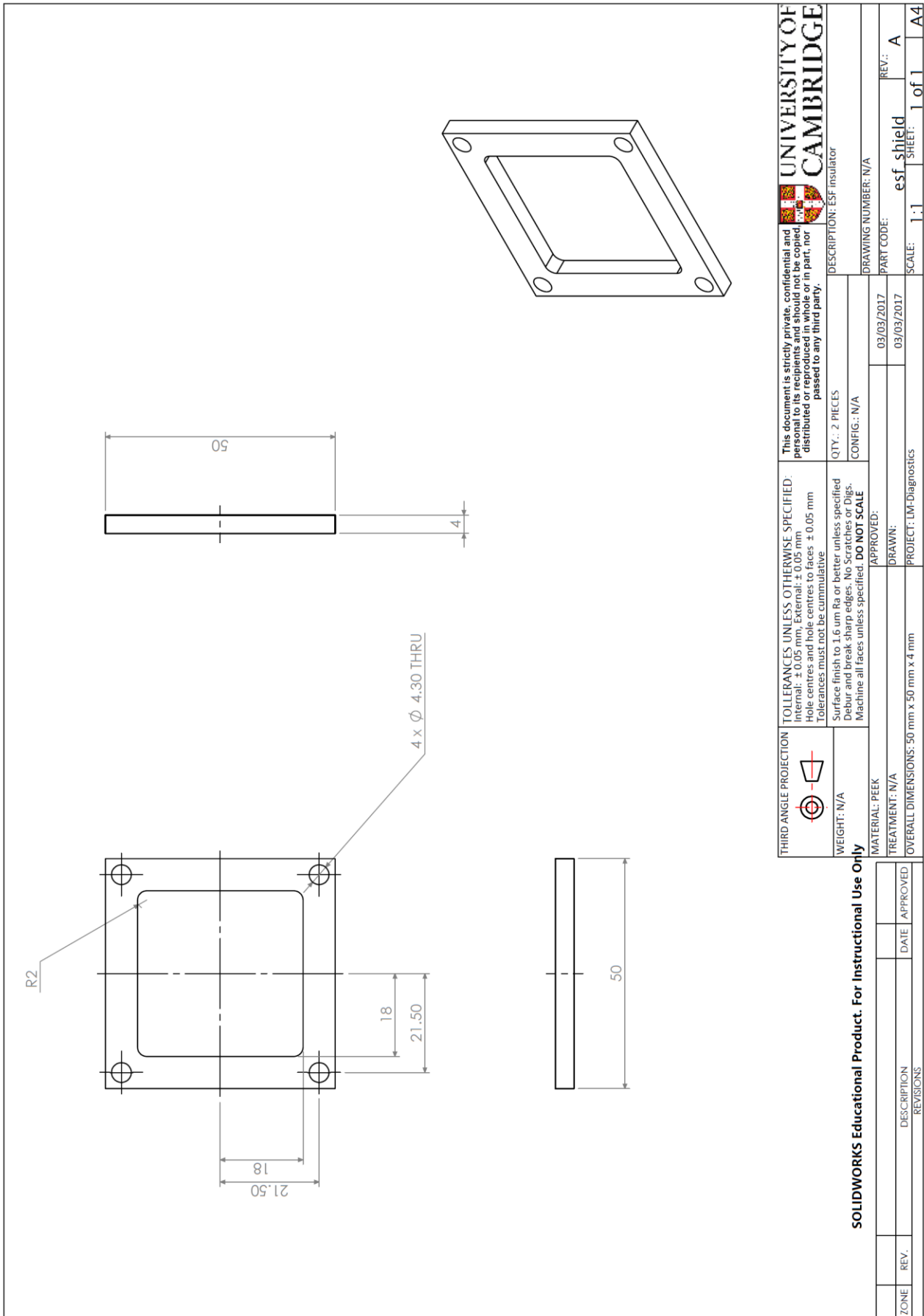


# Appendices

## ESF Horizontal Mount Drawing

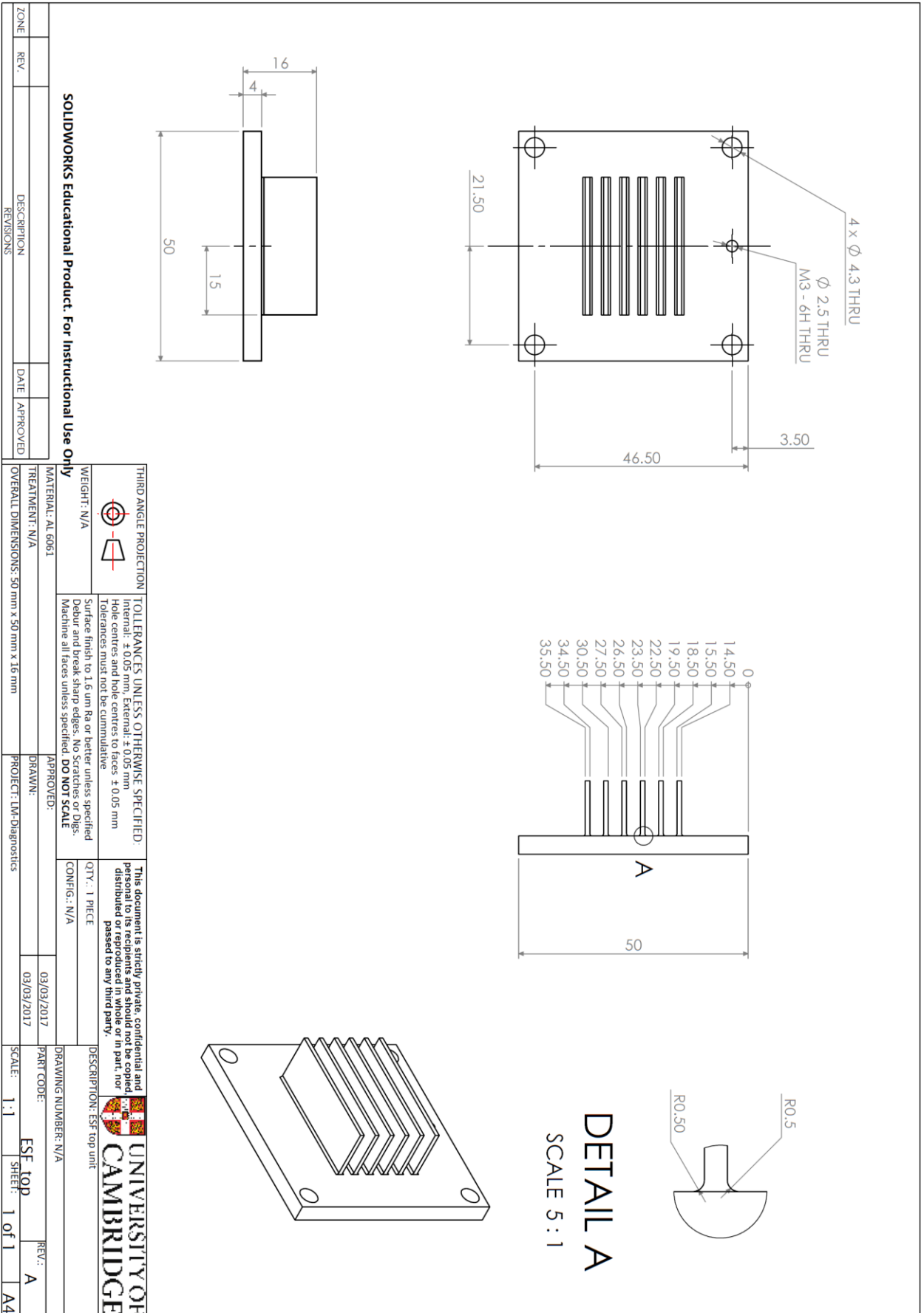


ESF Shield Drawing



# Appendices

## ESF Fin Drawing



Appendix 8.

## Laser Characteristics

All parameters specified for waveform 0 at rated power, PRF<sub>0</sub> (pulse repetition frequency providing maximum pulse energy at rated power) and over full operating temperature range, T<sub>op</sub>, unless otherwise stated.

Parameter	Conditions	Unit	Min.	Typ.	Max.
Central emission wavelength, $\lambda_0$		nm	1059		1065
Emission bandwidth		nm	1		15
Fraction of power within $\lambda_0 \pm 20$ nm		%	90		100
Average output power, P <sub>ave</sub> *		W	195	205	215
Output power adjustment range		%	0		100
Output power stability with temperature	at P <sub>ave</sub> over T <sub>op</sub>	% p-p			5
Maximum pulse energy	see waveform table	mJ			5.1
Pulse-to-Pulse energy stability	at stable temperature	% rms			3
Pulse repetition frequency (PRF)		kHz			3846
Pulse burst length		pulses	1		1000000
Maximum peak power		kW	40	53	
Beam quality, M <sup>2</sup>	averaged over x, y axes		4	5	6
Collimated beam diameter, 2 <sup>nd</sup> moment		mm	8	9.5	11
Full angle divergence, 2 <sup>nd</sup> moment		mrad			±1.2
Beam offset		mm			0.9
Pointing error		mrad			2.15
Circularity (min diameter / max diameter)		%	85		
Astigmatism		Z <sub>R</sub>			0.3
Degree of polarization		%			20
Thermal lens focal shift	Relative to 20% P <sub>ave</sub>	Z <sub>R</sub>		0.5	1.5
CW average output power	Disabled on Alpha units	W		n/a	
CW modulation frequency		kHz		n/a	
Red alignment laser (RAL) power		mW		0.3	

\* Measured using power meters calibrated in accordance with UKAS M3003 to three degrees of freedom from NIST standard.

# Appendices

## Appendix 9.

### Pulse Waveform Table

Waveform	PRF <sub>0</sub> (kHz)	PRF <sub>max</sub> (kHz)	Max. pulse energy, E <sub>max</sub> (mJ)	Typ. FWHM pulse duration at E <sub>max</sub> (ns)	Pulse duration at 10% (ns)	Typ. peak power at E <sub>max</sub> (kW)
0	50	393	4.10	42	270	53
1	51.5	426	3.98	42	250	53
2	55	466	3.73	38	230	53
3	60	537	3.42	38	200	51
4	64.5	589	3.18	37	180	49
5	70	653	2.93	36	160	49
6	74	715	2.77	33	150	49
7	80	770	2.56	32	143	47
8	82	800	2.50	32	130	47
9	86	870	2.38	32	120	46
10	90	953	2.28	32	110	46
11	95	1053	2.16	33	100	48
12	102	1177	2.01	34	90	48
13	106	1306	1.93	34	90	46
14	113	1430	1.81	35	83	45
15	122	1539	1.68	36	77	44
16	130	1667	1.58	37	65	43
17	138	1819	1.49	37	60	42
18	150	2000	1.37	39	55	41
19	163	2173	1.26	39	50	40
20	180	2500	1.14	37	45	39
21	185	2631	1.11	36	50	39
22	200	2941	1.03	33	47	39
23	223	3333	0.92	30	43	37
24	248	3571	0.83	27	40	36
25	282	3846	0.73	24	37	34
26	328	3846	0.63	20	33	32
27	435	3846	0.47	16	17	40
28	545	3846	0.38	12	13	39
29	740	3846	0.28	9	10	38
30	1160	3846	0.18	5	7	36
31	2380	3846	0.09	2	3	39
32	50	364	4.10	53	290	45
33	50	364	4.10	52	310	45
34	50	313	4.10	46	330	46
35	50	278	4.10	44	370	42
36	50	257	4.10	44	400	41
37	50	233	4.10	40	440	41
38	50	209	4.10	36	490	41
39 – 55	50	189	4.10	36	540	39
56	40	157	5.13	28	640	46
57	40	120	5.13	36	840	36
58	40	97	5.13	55	1040	30
59	40	81	5.13	63	1240	25
60	40	70	5.13	73	1440	21
61	40	61	5.13	82	1640	19
62	40	55	5.13	92	1840	17
63	40	50	5.13	102	2040	15

Note: The laser operates at discrete frequencies (multiple of clock cycles), making the spacing between "permissible" frequencies above 2 MHz noticeable. Frequencies at which the laser will operate above 2 MHz are: 2.000, 2.082, 2.173, 2.272, 2.380, 2.500, 2.631, 2.777, 2.941, 3.125, 3.333, 3.571 and 3.846 MHz. If the selected operation frequency is not one of these discrete values, the laser will round to the next frequency up. For instance, if the selected frequency is 3.2 MHz, the laser will operate at 3.333 MHz.

# Appendices

## Appendix 10.

General applications against diagnosable parameters spreadsheet. Where green indicates the measurement can be made, orange where it could be made but may not be relevant, blue where the measurement can be made and either hasn't been made before (NM) or hasn't directly been made (NDM). References have been linked to the spreadsheet directly and are not included within this text.

PRINCIPLE		DIAGNOSABLE PARAMETERS										
		HIGH-SPEED PULSED HOLOGRAPHIC CAMERA					FARADAY CUP	FORCE BALANCE			MASS SPECTROMETRY	LASER SPECTROSCOPY
		DENSITY	MEAN VELOCITY	PRESSURE	TEMPERATURE	MAGNETIC FLUX	CURRENT	FORCE AND IMPULSE	MASS FLOW RATE	SHOCK/ VIBRATION	SPECIES	
CHEMICAL PROPULSION	SOLID	<a href="#">4</a>	<a href="#">1</a>	<a href="#">1</a>	<a href="#">1</a>	N/A	N/A	<a href="#">3</a>	<a href="#">3</a>	<a href="#">5</a>	<a href="#">6</a>	<a href="#">1</a>
	HYBRID	<a href="#">4</a>	<a href="#">1</a>	<a href="#">1</a>	<a href="#">1</a>	N/A	N/A	<a href="#">3</a>	<a href="#">3</a>	<a href="#">5</a>	<a href="#">6</a>	<a href="#">1</a>
	LIQUID	<a href="#">4</a>	<a href="#">1</a>	<a href="#">1</a>	<a href="#">1</a>	N/A	N/A	<a href="#">3</a>	<a href="#">3</a>	<a href="#">5</a>	<a href="#">6</a>	<a href="#">1</a>
	GELS	<a href="#">4</a>	<a href="#">1</a>	<a href="#">1</a>	<a href="#">1</a>	N/A	N/A	<a href="#">3</a>	<a href="#">3</a>	<a href="#">5</a>	<a href="#">6</a>	<a href="#">1</a>
	GAS	<a href="#">4</a>	<a href="#">1</a>	<a href="#">1</a>	<a href="#">1</a>	N/A	N/A	<a href="#">3</a>	<a href="#">3</a>	<a href="#">5</a>	<a href="#">6</a>	<a href="#">1</a>
ELECTRIC PROPULSION	ION	<a href="#">17</a>	<a href="#">15</a>	NDM	<a href="#">20</a>	<a href="#">12</a>	<a href="#">21</a>	<a href="#">24</a>	<a href="#">10</a>	<a href="#">5</a>	<a href="#">27</a>	<a href="#">25</a>
	HALL	<a href="#">16</a>	<a href="#">15</a>	NDM	<a href="#">19</a>	<a href="#">12</a>	<a href="#">11</a>	<a href="#">8</a>	<a href="#">10</a>	<a href="#">5</a>	<a href="#">26</a>	<a href="#">25</a>
	PULSED INDUCTIVE	<a href="#">28</a>	<a href="#">9</a>	<a href="#">1</a>	<a href="#">29</a>	<a href="#">1</a>	<a href="#">1</a>	<a href="#">29</a>	<a href="#">10</a>	NM	<a href="#">30</a>	NM
	MPD	<a href="#">31</a>	<a href="#">32</a>	<a href="#">33</a>	<a href="#">31</a>	<a href="#">34</a>	<a href="#">1</a>	<a href="#">35</a>	<a href="#">10</a>	NM	NM	<a href="#">36</a>
	E-SPRAY	<a href="#">38</a>	<a href="#">37</a>	NDM	NDM	NDM	<a href="#">2</a>	<a href="#">2</a>	<a href="#">10</a>	NM	<a href="#">38</a>	<a href="#">39</a>
	WAVE DRIVE	<a href="#">40</a>	<a href="#">40</a>	NDM	NDM	NDM	<a href="#">40</a>	<a href="#">40</a>	<a href="#">10</a>	NM	NM	NM
	RESISTOJET	<a href="#">41</a>	<a href="#">41</a>	<a href="#">42</a>	<a href="#">42</a>	<a href="#">44</a>	N/A	<a href="#">45</a>	<a href="#">10</a>	NM	<a href="#">46</a>	NM
	ARCJET	<a href="#">47</a>	<a href="#">47</a>	NDM	<a href="#">47</a>	NDM	<a href="#">48</a>	<a href="#">49</a>	<a href="#">10</a>	NM	<a href="#">50</a>	<a href="#">47</a>

# Appendices

	PHOTON	NM	NM	NM	NM	NM	NM	7*	NM	NM	N/A	NM
	VASIMR	NDM	NDM	NDM	52	NDM	51	51	10	NM	53	NM
	PULSED PLASMA	55	54	56	56	58	54	23	54	NM	54	NM
NON-CHEMICAL PROPULSION	FISSION	59	NM	60	59	NM	NM	NM	NM	NM	NM	59
	FUSION	NM	NM	NM	NM	61	NM	61	NM	NM	NM	NM
CHEMICAL DEPOSITION	PVD (+PCVD)	63	62	62	63	NM	62	NM	65	NM	66	68
LITHOGRAPHY	ENERGY BEAM	NM	69	70								
ADDITIVE MANUFACTURING	LASER	NM	NM	NM	71	NM						
	ELECTRON BEAM	NM	NM	NM	72	NM						
SUBTRACTIVE MANUFACTURING	LASER	80	73	80	78	79	74	75*	75*	75*	76	77
	ION BEAM	NM	83	NM	NM	83	81	NM	NM	NM	82	NM
	ELECTRON BEAM	NM	NM	NM	NM	NM	84	NM	NM	NM	N/A	N/A
	SHOCK PEENING	88	87	86	86	85	NM	NM	NM	NDM	NM	NM
ETCHING	ION BEAM	NM	83	NM	NM	83	81	NM	NM	NM	90	NM
	PLASMA	97	98	NM	96	NM	94	NM	NM	NM	89	93
	LASER	NM	NM	NM	NM	NM	95	NM	NM	NM	91	92
FUSION ENERGY	ALL	105	107	106	105	108	110	N/A	N/A	N/A	NM	111
ACCELERATORS	RF/PLASMA ACCEL	100	102	101	100	103	104	NM	NDM	NM	NM	NM

## Appendices

### Appendix 11.

#### General Experimental Procedure

##### Safety

1. The system contains lasers, high-voltage and vacuum systems. Therefore, the laboratory door must be closed and interlocked using appropriate measures at all times during operation.
2. All personal protective equipment should be worn from the beginning.

##### Pre-Experimental Procedure

1. Approximately 60 minutes before experiments the Helium Neon laser must be turned on so that it can reach stable emission.
2. Approximately 30 minutes before experiments the target should be mounted onto the force balance so that the temperature of the target can equalise with the system. The mass of the sample should be noted.
3. An appropriate counter mass should be placed on the opposite arm of the force balance so that the balance settles approximately level. The mass and position of this should be noted and fed back into the CAD model for accurate moment of inertia calculations.
4. All external and internal optics including windows must be inspected for residue, dust etc. and cleaned using IPA and acetone.
5. The chamber door seal should be cleaned of vacuum grease after every experiment and reapplied. The spacers located between the metal frame and glass should be present (2 on each side).
6. The chamber should be sealed and tightened using the star method.
7. Plug the interferometer electronics USB cable into a computer which has a COM port monitor installed.

##### Setup

1. If an atmospheric temperature and pressure is required, make sure all vacuum valves are fully open and vented.
2. If a vacuum is required, follow the vacuum start-up and monitoring procedure.
3. Once a stable environment has been reached, turn on the interferometer power supply, ensuring  $\pm 15$  V is being supplied.
4. Now turn on the interferometer electronics box.
5. Turn on all 4 Thorlabs DET10A photodiodes in the interferometer.
6. Turn on the Tektronix oscilloscope.
7. Ensure the oscilloscope probes are inserted into the four measurement ports on the interferometer electronics box.
8. Four signals should now appear on the oscilloscope.

##### Interferometer Alignment

1. Turn on the Princeton HV power supply and enable it.
2. Turn on the DEI HV signal generator and enable it.

## Appendices

3. Turn on the Tektronix waveform generator and plug the DEI trigger into channel A.
4. The balance should now be set into motion once every 10 seconds, allowing the user to observe continuous interference patterns on the oscilloscope.
5. Use mirror 4 and mirror 7 to adjust the amplitude of the interference signals so that they all have approximately the same amplitude, whilst trying to maximise signal amplitude.
6. Use mirror 8 to further optimise amplitude. Ensure the amplitude exceeds 1Vp-p. A careful alignment can produce 2Vp-p amplitude, which is required for low-force measurements.
7. Each of the 3 mirrors also adjusts the phase between the 4 signals.
8. The easiest way to perform steps 5-7 is to first focus on channels 1 and 2 which should be 180 degrees out of phase. Then channels 3 and 4 which must be 180 degrees out of phase.
9. Finally, when all viewed together, each signal will be 90 degrees out of phase relative to each other.
10. A Lissajous figure can be produced by the oscilloscope to confirm this has been achieved.
11. This can be an iterative process. Repeat until conditions are satisfied.
12. Plug DEI trigger into channel B of the waveform generator. The balance will be set in motion every 180 seconds. This reduces noise which occurs when the balance is meant to be at rest but is being moved by external noise. As a relative measurement this is only important during experimental runs, but not between runs.

## Calibration

1. As the logarithmic method is significantly simpler, less time consuming and uncertain no calibration using the electrostatic system is necessary.

## Operation (Single Point)

1. Turn on delay generator.
2. Turn on laser.
3. Setup the laser parameters (waveform, pulse energy, frequency) using the serial interface in accordance with the G4 laser manual.
4. Setup the delay timing in accordance with the experimental plan, whereby the number of pulses sent is dependent on laser frequency.
5. Open Arduino COM port terminal.
6. The incoming numbers are the quadrature count coming from the interferometer electronics. During the working day this could fluctuate by  $\pm 5$  counts. In the evenings this should remain steady at  $\pm 1$  count. Once every 180 seconds the count will increase significantly, oscillate and decay.
7. The system is now ready to be used, laser can be triggered. Measurements should be taken between the periodic 180 second motion by copy and pasting from the COM terminal into a text or excel file from which it can be analysed later using MATLAB.

## Processing

1. Open MATLAB.
2. Open "force\_balance\_processor".

## Appendices

3. Update the force balance moment of inertia.
4. Run script.
5. Pick the appropriate text or excel file.
6. The script will now run and output balance displacement, velocity, acceleration, impulse and total impulse with respect to time.
7. All variables are available within the workspace for further analysis.